AFRL-ML-WP-TR-2001-4153

LIFE PREDICTION METHODOLOGIES FOR AEROSPACE MATERIALS

N.E. Ashbaugh, R.A. Brockman, D.J. Buchanan,
G.A. Hartman, A.L. Hutson, K. Li, and W.J. Porter

University of Dayton Research Institute
Structural Integrity Division
300 College Park
Dayton, OH 45469-0128

JUNE 2001

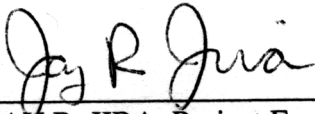**Interim Report for 25 May 2000 – 24 May 2001**

MATERIALS AND MANUFACTURING DIRECTORATE
AIR FORCE RESEARCH LABORATORY
AIR FORCE MATERIEL COMMAND
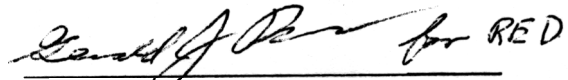**WRIGHT-PATTERSON AIR FORCE BASE, OH 45433-7750**

NOTICE

WHEN GOVERNMENT DRAWINGS, SPECIFICATIONS, OR OTHER DATA ARE USED FOR ANY PURPOSE OTHER THAN IN CONNECTION WITH A DEFINITELY GOVERNMENT-RELATED PROCUREMENT, THE UNITED STATES GOVERNMENT INCURS NO RESPONSIBILITY OR ANY OBLIGATION WHATSOEVER. THE FACT THAT THE GOVERNMENT MAY HAVE FORMULATED OR IN ANY WAY SUPPLIED THE SAID DRAWINGS, SPECIFICATIONS, OR OTHER DATA, IS NOT TO BE REGARDED BY IMPLICATION OR OTHERWISE IN ANY MANNER CONSTRUED, AS LICENSING THE HOLDER OR ANY OTHER PERSON OR CORPORATION, OR AS CONVEYING ANY RIGHTS OR PERMISSION TO MANUFACTURE, USE, OR SELL ANY PATENTED INVENTION THAT MAY IN ANY WAY BE RELATED THERETO.

THIS REPORT IS RELEASABLE TO THE NATIONAL TECHNICAL INFORMATION SERVICE (NTIS). AT NTIS, IT WILL BE AVAILABLE TO THE GENERAL PUBLIC, INCLUDING FOREIGN NATIONS.

THIS TECHNICAL REPORT HAS BEEN REVIEWED AND IS APPROVED FOR PUBLICATION.

JAY R. JIRA, Project Engineer
Metals Branch
Metals, Ceramics & NDE Division

DR. ROLLIE E. DUTTON, Chief
Metals Branch
Metals, Ceramics & NDE Division

DR. WALTER M. GRIFFITH, Chief
Metals, Ceramics & NDE Division
Materials & Manufacturing Directorate

IF YOUR ADDRESS HAS CHANGED, IF YOU WISH TO BE REMOVED FROM OUR MAILING LIST, OR IF THE ADDRESSEE IS NO LONGER EMPLOYED BY YOUR ORGANIZATION, PLEASE NOTIFY, AFRL/MLLMN, WRIGHT-PATTERSON AFB OH 45433-7817 TO HELP US MAINTAIN A CURRENT MAILING LIST.

COPIES OF THIS REPORT SHOULD NOT BE RETURNED UNLESS RETURN IS REQUIRED BY SECURITY CONSIDERATIONS, CONTRACTUAL OBLIGATIONS, OR NOTICE ON A SPECIFIC DOCUMENT.

REPORT DOCUMENTATION PAGE

Form Approved
OMB No. 0704-0188

1. REPORT DATE *(DD-MM-YY)*	2. REPORT TYPE	3. DATES COVERED *(From - To)*
June 2001	Interim	05/25/2000 – 05/24/2001

4. TITLE AND SUBTITLE
LIFE PREDICTION METHODOLOGIES FOR AEROSPACE MATERIALS

5a. CONTRACT NUMBER
F33615-98-C-5214

5b. GRANT NUMBER

5c. PROGRAM ELEMENT NUMBER
62102F

6. AUTHOR(S)
N.E. Ashbaugh, R.A. Brockman, D.J. Buchanan, G.A. Hartman, A.L. Hutson, K. Li, and W.J. Porter

5d. PROJECT NUMBER
4347

5e. TASK NUMBER
52

5f. WORK UNIT NUMBER
01

7. PERFORMING ORGANIZATION NAME(S) AND ADDRESS(ES)
University of Dayton Research Institute
Structural Integrity Division
300 College Park
Dayton, OH 45469-0128

8. PERFORMING ORGANIZATION REPORT NUMBER

9. SPONSORING/MONITORING AGENCY NAME(S) AND ADDRESS(ES)
Materials and Manufacturing Directorate
Air Force Research Laboratory
Air Force Materiel Command
Wright-Patterson Air Force Base, OH 45433-7750

10. SPONSORING/MONITORING AGENCY ACRONYM(S)
AFRL/MLLMN

11. SPONSORING/MONITORING AGENCY REPORT NUMBER(S)
AFRL-ML-WP-TR-2001-4153

12. DISTRIBUTION/AVAILABILITY STATEMENT
Approved for public release; distribution is unlimited.

13. SUPPLEMENTARY NOTES
The appendix contains journal articles and conference papers. This report contains color.

14. ABSTRACT *(Maximum 200 Words)*

Damage tolerance investigations of γ-TiAl alloys have involved assessments of lamellar lath orientations of colonies and defects in large-scale production ingots. An investigation of elastic properties of colonies has continued with conjoint efforts in the experimental evaluation of test specimens containing large colonies and in finite element analysis of modeling of the contiguous colony locations and orientations within the test specimens. Experimental behavior of Nextel TM720/AS ceramic matrix composite was determined under tensile, creep, and thermal exposure conditions. Fracture and creep rupture behavior of MI SiC/SiC and high-cycle fatigue behavior of CVI Cf/SiC have been conducted. Analyses of CMC were conducted to predict strains at notch tips and heat transfer and stresses in a conceptual combustor design and to design rings that were tested on a combustor rig.

Fretting fatigue investigations of Ti-6-4 have focused on the effects of coating fretting pads; the use of dissimilar materials for the fretting pads; the fatigue crack nucleation in fretting pads; the application of an ultrasonic shear wave technique to detect crack initiation; and the effects of specimen thickness and ratios of nominal normal stress to shear stress. High-cycle fatigue tests have continued to evaluate the influence of foreign object damage, mean stress, and previous loading history. A fractographic assessment of load sequences has revealed some surprising results for fatigue crack growth and load interaction in two aluminum alloys.

For the engine rotor life extension program, a broad study of the behavior of residual stresses in nickel-base superalloys has begun. These efforts currently involve the determination of the compressive behavior of materials of interest, the correlation between predicted and measured inelastic strains in bend specimens, and the relaxation of residual stresses due to thermal exposure. Material taken from the rotor components that have experienced service conditions is being evaluated to determine if changes have occurred in the mechanical and microstructural characterizations as a result of usage. A fractographic assessment of crack growth and load interaction in a PM nickel-base superalloy has been initiated to determine the effects of dwell time and fatigue loads. Advances in experimental methodologies include initial implementation of WinMATE test automation software, infrared damage detection enhancements, and improvements in load train alignment equipment and procedures.

15. SUBJECT TERMS
Titanium aluminides, ceramic matrix composites, nickel-base superalloys, turbine blade materials, high-cycle fatigue, fatigue crack growth, elevated temperatures, creep, thermal fatigue, thermomechanical fatigue, fretting fatigue, load interactions, mixed-mode, stress intensity factors, finite element analysis, nondestructive evaluation

16. SECURITY CLASSIFICATION OF:

a. REPORT	b. ABSTRACT	c. THIS PAGE
Unclassified	Unclassified	Unclassified

17. LIMITATION OF ABSTRACT:
SAR

18. NUMBER OF PAGES
250

19a. NAME OF RESPONSIBLE PERSON (Monitor)
Jay R. Jira
19b. TELEPHONE NUMBER *(Include Area Code)*
(937) 255-1358

Standard Form 298 (Rev. 8-98)
Prescribed by ANSI Std. Z39-18

TABLE OF CONTENTS

[1] Notation in square brackets refer to manuscripts in compilation.

TABLE OF CONTENTS (Continued)

SECTION **PAGE**

FOREWORD

The work described in this report was performed at the Ceramic Development & Materials Behavior Branch in the Metals, Ceramics & Nondestructive Evaluation Division of the Materials & Manufacturing Directorate, Air Force Research Laboratory (AFRL/MLLMN) under Contract No. F33615-98-C-5214, "Life Prediction Methodologies for Aerospace Materials." The contract is administered under the direction of AFRL by Lt. Brett Conner. The program is being conducted by the Structural Integrity Division, University of Dayton Research Institute, Dayton, Ohio with Dr. Noel E. Ashbaugh and Mr. Robert J. Andrews acting as the Principal Investigator and Program Manager, respectively. This report is an interim report on the progress of the 5-year contract effort.

In the third year of the contract, the investigations were developed and directed by Drs., Robert Brockman, Geoffrey Frank, Victoria Kramb, and Kezhong Li and Messrs. Dennis Buchanan, George Hartman, James Konicki, David Maxwell, and W. John Porter and Mrs. Alisha Hutson. Mrs. Jacqui Hawkins was responsible for coordinating the input and typing of this document. This interim report covers the work performed during the period of 25 May 2000 to 24 May 2001.

1.0   EXECUTIVE SUMMARY

1.1   g-TiAl-BASE ALUMINIDES

Efforts towards developing models to predict mechanical behavior, especially tensile and fatigue properties, of gamma titanium aluminides were the focus of our efforts over the last year. A three-pronged approach to addressing the modeling of these types of materials was undertaken. First, elastic properties of colonies from large grain gamma samples were experimentally and analytically determined. These findings will result in the ability to accurately deduce the orthotropic properties for gamma titanium aluminide alloys and similar materials. Next, a crystal plasticity model is being developed to predict the anisotropic plastic behavior in polycrystalline gamma titanium aluminides. The understanding of microstructural and loading conditions susceptible to initiating fatigue cracks will be improved through these efforts. Finally, a model that numerically estimates localized stress concentrations in anisotropic polycrystalline materials by incorporating constituent properties into a model based on laminated orthotropic materials was developed. The prediction of locations in structures where microyielding of the local, anisotropic microstructure and, in turn, fatigue crack initiation may occur is the objective for this model.

Work continued in the areas of orientation imaging microscopy (OIM) and in the characterization of defects associated with casting large-diameter, gamma titanium aluminide ingots. The information concerning microstructural orientation gained through OIM and determination of defect types and their probability of occurrence in components will also be used to establish robust models for life prediction.

1.2   CERAMIC MATRIX COMPOSITES

Ceramic matrix composites (CMC) are currently being evaluated as replacement materials in high-temperature environments, such as gas turbine engines. Many of the applications include exhaust wash structures, exhaust nozzle flaps and seals and combustor liners. These structures typically require holes, fillets, and attachment points in their design. Specimen geometries with notches and holes are being used to investigate the material behavior of the CMC in the vicinity of these notches and holes. Creep rupture behavior and damage progression in Nextel™720/AS on semicircular double-notched specimens (DEH(T)), double-notched (DE(T)) and effusion hole geometries are under investigation. As-received, heat-treated, load and unload, fast fracture, and sustained load (creep) experiments on notched specimens are used to determine how damage initiates and progresses at notch tips. Thorough Scanning Electron Microscope (SEM) investigation of notched specimens subjected to different mechanical and thermal loading conditions reveals that damage progression from the notch tips occurs only under sustained load (creep) conditions. In contrast, effusion hole specimens subjected to the same creep loading conditions show no evidence of matrix or fiber damage in the vicinity of the holes.

Through-transmission ultrasonic wave propagation was used to measure the through-thickness modulus (E_{zz}) for Nextel™720/AS. Modulus measurements on steel and aluminum samples of similar dimensions verify the applicability of the ultrasonic measurement technique.

In addition to investigating the fundamental mechanical behavior and damage progression in Nextel™720/AS, several efforts are in progress to evaluate the feasibility of using this composite in a high-temperature environment. Nonlinear orthotropic finite element models are used to evaluate deformation at holes and notches. Steady-state heat transfer and stress analysis calculations are used to simulate combustor engine conditions and investigate combustor conceptual designs using the Nextel™720/AS material. Turbine burner rings made from Nextel™720/AS composite were designed, machined and tested in a prototype combustor under exposure to jet fuel at combustion temperatures.

Tensile, fracture and creep tests were completed on a melt-infiltrated (MI) High-Nicalon-S/SiC ceramic matrix composite. The MI High-Nicalon-S/SiC CMC shows better mechanical properties than the Nextel™720/AS at room and elevated temperatures.

1.3 ENGINE ROTOR MATERIALS IN CURRENT USE

Titanium, nickel and aluminum alloys used in fabricating engine components are being re-examined to assess their behavior under laboratory conditions designed to simulate engine operation. Among the types of loading conditions being simulated are fretting fatigue, as observed in turbine engine blade attachments, foreign object damage (FOD), high-cycle fatigue (HCF) and high-cycle / low-cycle fatigue interactions (HCF/LCF).

The ongoing effort to characterize fretting fatigue phenomena focused on the effects of contact surface composition and morphology, applied clamping stress, applied shear stress, and time required for detrimental fretting fatigue damage. The roughness of a typical blade root coating was identified as the mechanism responsible for improved fretting fatigue life in samples tested against coated pads. Also, no improvement in fretting fatigue behavior was observed in specimens tested against IN100 pads, indicating that the behavior is, in general, insensitive to surface composition.

Applied clamping stress was identified as a parameter influencing the time to fretting fatigue crack nucleation – a parameter critical to component life prediction. However, no trend was observed in the fretting fatigue limit stress either with average applied clamping stress or average applied shear stress. As part of the work to characterize fretting fatigue crack nucleation life, shear wave crack detection was employed with moderate success. Fretting fatigue crack propagation was characterized in a collaborative effort with Purdue University using C-shaped specimens cut from fretting pads, which were used in fretting fatigue tests at Purdue.

Extensive characterizations of laboratory simulated fretting fatigue and FOD damage was conducted using scanning electron microscopy. The observations of fretting fatigue scars revealed lower observable wear than that reported for service components. Investigation of simulated FOD damage revealed no correlation with fatigue strength and FOD depth along simulated airfoil leading edges or residual debris from projectiles used to generate the FOD. These results are being used to define criteria by which detrimental damage may be identified.

An investigation of the effect of compressive mean stress on fatigue behavior was conducted within the elastic compressive regime to identify damage mechanisms related to compressive mean stress loading, often observed in components fabricated with shot peening. This work indicated that the compressive mean stress contributed less than 30 percent to fatigue damage and provided data to extend the Goodman diagram to stress ratios less than -1.

Comprehensive lab support was provided for an investigation of HCF/LCF interaction under uniaxial fatigue conditions. In these experiments, initial LCF cycles, up to 25% of estimated LCF life, had no effect on subsequent HCF fatigue strength for R = 0.1. Work is being continued to evaluate the amount of initial fractions of LCF life that do not influence subsequent HCF life for R = 0.5 and 0.8.

Extended fatigue life of engine components is one of the beneficial effects of surface treatments. This enhanced life is mostly attributed to a residual compressive stress field that is created in the vicinity of the component surface. An investigation in the Engine Rotor Life Extension (ERLE) program has been started to understand and quantify the influence of this phenomenon. An initial part of the investigation involves the determination of the effects of thermal exposure of surface treated samples. Models will be developed to characterize the formation and relaxation of the residual stresses. Data from compressive tests of cylindrical specimens have indicated that the inelastic compressive stress-strain behavior differs from the inelastic tensile

stress-strain behavior. The inelastic strain behavior of bend specimens will be compared to numerical predictions to verify the constitutive material models.

Fractographic assessments of crack growth on fracture surfaces created in various structural alloys have revealed some unexpected results. Fatigue and crack-growth specimens have been tested under specially designed load sequences that mark the failure process. Seminal work on an aluminum alloy has revealed early, unexpected fatigue damage and attributed the influence of stress ratio on crack growth rates to be primarily the result of environmental interaction with the crack growth rate. This experimental technique is being applied to powder metallurgy (PM) nickel-base superalloys and titanium alloys as part of the ERLE program to develop improved crack growth and fatigue initiation models. Load sequences are being evaluated to determine the combinations that are effective in marking the fracture surface. Crack growth rates for PM nickel-base superalloys that are lower than previously obtained for near threshold growth rates under dwell conditions have been produced with load sequencing. Some load sequences have been successful in marking fracture surfaces in a Ti-6V-4Al alloy.

In the early stages of the ERLE program, a review of the literature on PM nickel-base superalloys was conducted. Some results of this review lead to the evaluations of possible changes in material defects, microstructure, and mechanical behavior that could occur as a result of service conditions. While the PM nickel-base superalloys material characterizations in the virgin state are well known, the influence of service conditions could be better understood. Work has begun on characterizations of defect number and size distributions of material taken from various locations in engine components that have been removed from service. Also, the influence of load history on the qualification properties and the tensile, fatigue, and crack growth behaviors is being determined.

1.4 DEVELOPMENT OF EXPERIMENTAL PROCEDURES, METHODOLOGIES, AND LABORATORY ENHANCEMENTS

State-of-the-art experimental capability is critical for sophisticated studies of fundamental material properties and behavior. Providing cutting-edge capability within a reasonable budget requires the ability to efficiently maintain existing assets, to identify new technologies and realistically evaluate their potential, and to integrate both existing and new technologies with emerging techniques to obtain new types of data.

The University has attacked this challenge on two fronts. First, we have made a concerted effort to maintain and enhance the general laboratory infrastructure. Second, we have designed, fabricated, and tested a number of specific new technologies aimed at improving the tools available to AFRL/MLLMN laboratory researchers. Infrastructure improvements range from incorporation of commercial off-the-shelf (COTS) software for specific test automation tasks to an up-to-date standardized system layout and hardware implementation for all lab test stations. Specific new technologies include an improved data acquisition interface board with greatly enhanced signal-to-noise parameters, new algorithms and hardware for direct current potential difference (DCPD) measurements, and next-generation image processing algorithms and equipment to support the infrared damage detection system (IDDS). Details of the university's efforts in keeping the AFRL/MLLMN laboratories at the forefront of material characterization research are contained in Section 6.

2.0 INTRODUCTION

2.1 BACKGROUND

The U.S. Air Force (USAF) has various programs in place directed toward the advancement of new gas turbine engines and aerospace vehicle technology and the support of current gas turbine engines. These programs include Integrated High-Performance Turbine Engine Technology (IHPTET), National Turbine Engine Durability (NTED), Engine Rotor Life Extension (ERLE), etc. The primary goals are (1) improved performance, i.e., maintain properties at higher service temperatures, and (2) reduction in weight, i.e., use of lightweight materials with high-temperature capability. Advanced materials such as gamma titanium aluminide (γ-TiAl) alloys, high-temperature intermetallics, and CMC are leading candidates to satisfy these needs for various engine components. In addition, the need to extend the life of a wide range of current aerospace components has resulted in programs such as the HCF initiative, Aging Aircraft, and Propulsion Life Extension. These programs are directed toward conventional materials, such as aluminum alloys, Ni-base superalloys and titanium (Ti) alloys (near α and $\alpha+\beta$). To apply the advanced materials effectively or to consider further applications of conventional materials that have experienced service conditions, a thorough understanding of the material behavior must be obtained and a methodology of life prediction for these materials must be developed or refined.

2.2 PROGRAM OBJECTIVES

The primary objectives of this program are to:

(a) evaluate the performance of advanced and conventional materials under simulated service conditions

(b) develop and/or adapt experimental techniques for characterization of deformation, damage evolution, and failure of advanced and conventional materials under typical service conditions

(c) develop an understanding of the mechanisms leading to deformation, damage accumulation, and failure of advanced and conventional materials under a variety of test conditions, including simulated mission cycles

(d) develop physically based deformation and life prediction models necessary to ensure in-service reliability and maintainability of advanced and conventional materials subjected to aerospace usage loading conditions

(e) transition the new technology to USAF suppliers and customers

(f) use and update the data for various aerospace materials in the current archival system and enhance the materials data archival procedure.

2.3 REPORT ORGANIZATION

This third interim report presents the research conducted on the material behavior and modeling of aerospace materials within the Behavior/Life Prediction Section (MLLMN) of the Metals Branch (MLLM) in the Metals, Ceramics & Nondestructive Evaluation Division of the Materials and Manufacturing Directorate at Wright-Patterson Air Force Base, OH. This effort was conducted over the period from 25 May 2000 to 24 May 2001. The investigations that have been completed and were in progress during the second year of the contract will be discussed in this report.

In Sections 3, 4, and 5, the material properties and damage assessment for γ-TiAl, CMC, and other engine materials, respectively, are discussed. The development of experimental procedures and test techniques,

methodologies, and laboratory enhancements are presented in Section 6. Extended discussions of the work-in-progress are presented to provide as much information as possible about the current investigations. Copies of the manuscripts, which have been written on the completed efforts, are provided in the Compilation in the Appendix for the convenience of readers who wish to have more detailed information of the investigations readily available.

3.0 DAMAGE TOLERANCE STUDIES OF *g*-TiAl-BASE TITANIUM ALUMINIDES

3.1 MECHANISMS OF FATIGUE CRACK INITIATION IN TiAl INTERMETALLIC ALLOYS

3.1.1 Elastic Behavior of Fully Lamellar Gamma Titanium Aluminides [C1]

Gamma titanium aluminide (γ-TiAl) alloys are being researched for use in rotating components for gas turbine engines. Detailed three-dimensional (3-D) colony-level finite element (FE) models are simultaneously being developed at the U.S. Air Force Research Laboratory to predict damage initiation and accumulation in γ-TiAl during service loading. These models require knowledge of the orthotropic nature of the deformation and fracture behavior of individual colonies. While the elastic properties of gamma and alpha-2 single-phase materials have been extensively studied, the elastic response of fully lamellar two-phase materials has not received the same degree of attention. Our efforts are attempting to build an integrated experimental and analytical approach to deduce the colony properties in a γ-TiAl. Samples with gage sections composed of specifically oriented individual lamellar grains are being tested in tension to determine the elastic behavior of this two-phase structure. Preliminary 3-D FE analysis, using the constituent properties available in the open literature, shows general agreement between the model results and the experimental measurements.

3.1.2 Effects of Microstructural Anisotropy on Fatigue Behavior of *g*-TiAl Alloys

γ-TiAl alloys have received considerable attention as candidate materials for elevated temperature aerospace applications [4]. The lamellar microstructure consisting of alternating γ (L1$_0$, a = 0.397 nm, c = 0.405 nm) and α_2 (DO$_{19}$, a = 0.579 nm, c = 0.467 nm) laths in a colony shows better creep resistance and higher toughness, as well as improved fatigue crack growth resistance, than the duplex structure. However, the lamellar microstructure also shows significant crystallographic texture that results in anisotropic mechanical properties at the colony level [1,3,4,6]. The Orientation Imaging Microscopy (OIM) technique, based on the acquisition and analysis of Electron Back-scattered Diffraction Patterns (EBSP), or Kikuchi patterns, from a bulk sample, currently is able to image only one phase (γ) at a time. However, since γ and α_2 phases in a lamellar colony share a strict orientation relationship of (111)γ//(0001)α, γ// α, the colony orientation can be described based on the knowledge of the γ lath orientation alone. Due to the modest tetragonality of γ-TiAl (c/a = 1.02) and sensitivity limitations of the equipment, a face-centered cubic (FCC, a = 0.400 nm) unit cell was assumed for the γ phase and employed by the OIM software. The γ lath (or lamellar colony) orientation is being determined using the intensity pole figures (IPF) and the point group symmetry of the assumed FCC unit cell of the γ phase.

3.1.3 Defects in 3-95M

As gamma titanium aluminides mature into industrially accepted structural materials, increased demand for manufacturing defect-free product is required. While gamma alloys can be processed using techniques and equipment currently used for conventional titanium alloys, large-scale melting of these alloys has not been fully implemented. In a program aimed at addressing large-scale production of a gamma titanium-aluminide alloy, a number of issues pertaining to initial ingot quality were discovered and are being investigated. Among these are centerline porosity and/or piping, grain-size disparities, and high- and low-density regions related to insufficient melt homogenization. Our efforts are aimed at describing the assorted material quality issues and suggesting solutions for their eradication.

3.2 MODELING EFFORTS OF STRESS STATES LEADING TO CRACK INITIATION

3.2.1 Modeling of Elastic Behavior of Fully Lamellar Gamma Titanium Aluminides

An integrated experimental and analytical approach has been taken to deduce the colony properties in γ-TiAl. Three-dimensional finite element models of dogbone specimens used for experimental testing have been created. The individual grains in the specimen are modeled and are given properties based upon the metallographically determined orientation of the grain in the sample. Initial properties for the γ-TiAl material have been calculated using the constituent (γ and α_2) properties and a laminate model. Preliminary results indicate that the orthotropic properties determined using the constituent properties give a reasonable estimate of the longitudinal modulus as a function of lath orientation. On-going experimental and analytical efforts should allow a complete set of orthotropic properties for the material to be deduced.

3.2.2 Numerical Models of Orthotropic and Lamellar Grain Structures [C2]

To better understand the influence of anisotropy and relative orientation of neighboring grains on crack initiation, a method for numerically estimating localized stress concentrations that arise in materials with anisotropic crystalline grains has been developed. The method is based on comparisons of the volumetric distributions of specific components of stress. The method has been applied in the elastic regime within polycrystals of γ-TiAl. Effective elastic properties for the lamellar colonies are calculated from the constituent properties using a procedure developed for laminated orthotropic materials. It is postulated that the local anisotropy and differing orientations of adjacent grains of material can lead to microyielding at stresses below the mean yield stress of the material, resulting in a reduction of fatigue life for the material.

The method has been applied using finite element representations of crystalline structures in two and three dimensions. The results indicate that three-dimensional models of only moderate size and refinement, for which analyses in the plastic regime may be performed in a reasonable time with the current generation of supercomputers, can sufficiently capture the stress distributions as well as models of much larger size or higher refinement. Two-dimensional models using a random size variation of the crystals show that size variation does not significantly affect the stress distribution within the material. Stress distributions predicted by two-dimensional models using various geometric representations for shape of the lamellar colony phase compare well with each other, but show less deviation from the distributions of an isotropic material than do the stress distributions generated by three-dimensional models.

3.2.3 Analysis of Elastic-Plastic Deformation in TiAl Polycrystals [C3]

To investigate the effects of anisotropic yielding and localized plastic flow, a crystal plasticity model suitable for small-deformation elastic-plastic analysis of localized stress variations in γ-TiAl polycrystals has been developed. The modeling of the lamellar colonies introduces a uniform-stress approximation that eliminates the need for modeling individual lamellae explicitly, while capturing the most important features of the early plastic flow within a colony. The model incorporates both interlamellar (soft mode) and translamellar (hard mode) deformation of the lamellar colonies. Interlamellar slip behavior is controlled by a separate collection of slip systems whose properties are derived from measurements on polysynthetically twinned (PST) specimens.

The crystal plasticity model has been implemented as a user material model subroutine (UMAT) for the ABAQUS finite element code. When used to represent several hundred randomly oriented material grains, the model provides distributions and statistical data about the local stress, strain, and plastic deformation resulting from a prescribed macroscopic loading. Three-dimensional stress analyses of γ-TiAl polycrystals have been performed and yield useful information concerning the local stress variations caused by elastic anisotropy, orientation differences among adjoining grains, and localized plastic deformation. Efforts are

underway to model multinotched TiAl specimens using the crystal plasticity model, to identify the role of localized stress concentrations in the process of crack initiation.

3.3 ACOUSTIC EMISSION SIGNALS FROM GAMMA g-TiAl

Acoustic emission (AE) signals were collected in a room temperature tension test of a γ-TiAl material, 3-95M. The 3-95M was heat treated to create a fully lamellar microstructure with the average grain size between 300 and 400 μm. The AE systems had originally been set up to detect damage evolution, primarily fiber breaks, in metal matrix composites. Two pairs of wide band frequency sensors were used. Sensors were located at each end of the specimen that would allow detection of bulk or longitudinal waves. Sensors were also located at the ends of two wave-guides that were in contact with the sides of the specimen. These sensors would be most sensitive to the presence of surface waves. With either pair of sensors, the location of emitted signals along the length of the specimen could be determined.

This first test was conducted to assess whether signals of significant magnitude could be detected. Subsequent analysis would be needed to determine if these signals were associated with microcracking in lamellar colonies and/or between colonies and grains. Seven signals were recorded during the test before the signal associated with the catastrophic failure of the specimen occurred. These signals were more consistent in appearance from the bulk wave sensors than from the surface wave sensors. The number of signals detected depended on the threshold level settings that had been associated with MMC tests. The first, second, and fourth of the signals occurred in the root radius portion of the flat dogbone specimen. The first signal happened at 75% of the ultimate stress. The remaining four signals occurred within ± 0.2% of the location of final failure. The earliest (the third) of these signals happened at 95% of the ultimate stress. Additional evaluation of these signals needs to be made before continuing further tests.

4.0 DAMAGE ACCUMULATION AND FAILURE OF CERAMIC MATRIX COMPOSITES (CMC)

4.1 CHARACTERIZATION OF OXIDE/OXIDE NEXTEL™720/AS CMC

4.1.1 Creep Rupture Behavior of Oxide/Oxide Nextel™720/AS Composite with Effusion Holes [C4]

The creep rupture behavior of Nextel™720/AS CMC at 1100°C with 0.5 mm diameter effusion holes is under investigation. Dogbone specimens with 1, 2, 5, and 17 effusion holes were tested under sustained load (creep) conditions of σ_{net} = 100 MPa. Extensometry and sectioned samples from interrupted tests were used to characterize the extent of the damage zone in the vicinity of the holes. The extensometry data shows that creep strain for the unnotched specimen and the effusion hole specimens exhibit similar creep behavior. Hence, the presence of the effusion holes does not contribute to an increase in macro deformation for the specified loading conditions. Sectioned samples from interrupted creep tests with effusion holes show that the matrix crack morphology is similar to samples in the as received condition. Also, there is no evidence of broken fibers in the vicinity of the effusion holes. These results are unexpected based on the stress concentration factor for the effusion holes, K_t = 3.3, and the ultimate strength of the Nextel™720/AS material, σ_{ult} = 180 MPa. The machining of the 0.5-mm-diameter effusion holes has not damaged a sufficient quantity of fibers in a given volume to produce an effective stress concentration. The material has effectively redistributed the load to the surrounding material.

4.1.2 Damage Progression from Sharp Notches in Oxide/Oxide Nextel™720/AS Composite [C5]

Damage progression from sharp edge notches in an oxide/oxide CMC is being investigated using destructive evaluation of failed and interrupted test specimens. The double edge notched specimens were tested at 1100°C under monotonic and sustained load conditions in lab air. Results of the study show that no damage is observed in the notch tip region after thermal exposure with zero applied stress or rapid loading followed by immediate unloading. After sustained loading, however, matrix cracking and fiber breakage are observed near the notch tip. The extent of the damage is ≈ 1 mm beyond the notch tip, which is roughly the width of an individual fiber tow. A comparison of the fracture surface profiles for creep rupture specimens show that the damage observed in the unnotched specimens compare closely to that in the notched specimen away from the notch tips. The observed damage progression in notched specimens indicates that the stress concentration ahead of the notch tip is effectively redistributed within the first fiber tow during initial loading. The nearly uniform stress profile away from the notches results in overall creep behavior similar to the unnotched composite.

4.1.3 Effect of Stress Concentration on Damage Progression in Oxide/Oxide Nextel™720/AS Composite

Damage progression from sharp edge notches and circular effusion holes at 1100°C is under investigation in Nextel™720/AS. Damage in the vicinity of the stress concentration was examined after rapid loading, thermal exposure under zero load, and sustained loading at 100 MPa net section stress. At 1100°C, rapid loading and thermal exposure under zero load produce no observable changes in the matrix crack morphology in the vicinity of either type of stress concentration. Specimens containing circular holes exhibit delamination and fiber breakage close to one surface of the specimen. However, this damage is due to inadequate support of the back surface of the specimen during the machining of the holes and not due to the applied test conditions. Damage progression under sustained loads was examined in creep test specimens interrupted at approximately 50 percent

9

of the notched creep life. Under sustained loading, crack growth from the sharp edge notches is characterized by a through-thickness matrix crack and longitudinal fiber breakage. Crack growth from the sharp edge notches is consistent with the reduction in notch strength under creep loading. Further details of the damage progression from sharp edge notches are discussed in Section 4.1.2. In contrast, the creep damage in specimens containing circular holes shows no longitudinal fiber breakage or changes in the matrix crack morphology away from the machining induced damage. Creep rupture results show that the presence of effusion holes does not result in a loss of creep strength. Similarly, the fracture surfaces of specimens containing effusion holes more closely resemble the unnotched creep rupture specimens, and do not clearly show any indications of crack growth from the hole edges. Thus, the observed damage progression from sharp edge notches and effusion holes is consistent with the notched creep strength results.

4.1.4   Measurement of Through-Thickness Elastic Modulus (E_{zz}) on Oxide/Oxide Nextel™720/AS Composite

Ultrasonic wave propagation is used to determine through-thickness elastic modulus (E_{zz}) on Nextel™720/AS CMC thin plate material. Through-transmission wave propagation with piezoelectric transducers that have a resonant frequency of ≈ 1 MHz and an 8-bit, 100 MHz digitizing board are used to measure the time of flight through the specimen. The wave propagation speed in the specimen is calculated using the time of flight and the specimen thickness, which is nominally 2.5 mm. The elastic modulus is calculated using the density, Poisson's ratio, the wave speed, and the wave propagation equation for an infinite media with homogeneous isotropic properties. The through-thickness modulus for the Nextel™720/AS composite is ≈ 50 GPa using the wave propagation equation with Poisson's ratio of 0.07, density of 2568 kg/m^3, and wavespeed of 4.42 mm/µs. Aluminum and steel samples with geometry similar to that of the oxide/oxide composite are used to verify the applicability of the ultrasonic measurements and calculated elastic modulus. The measured through-thickness moduli for the aluminum and steel samples are within 10 percent of handbook results of 70 and 210 GPa, respectively. Measurements of the longitudinal modulus using ultrasonic wave propagation and the plate equation show excellent agreement with measurements from tensile tests on Nextel™720/AS composite, $E_{xx} \approx 80$ GPa.

4.2 MODELING AND MECHANICAL DESIGN ANALYSIS OF OXIDE/OXIDE NEXTEL™720/AS CMC

4.2.1   Analysis of Notch Tip Strains from Sharp Notched Oxide/Oxide Nextel™720/AS Composite

A double-edged sharp notch geometry was tested under tensile loading at room temperature test conditions. The notches are ≈ 1.88 mm deep and have a notch tip radii of ≈ 0.1 mm. The specimen widths are 15 mm and the normalized notch length is $2a/W = 0.25$. Strain gages, 0.8 mm square, were placed at the notch tips and in the center of the specimen to measure the strain profile in the notch plane. The strain gage data show that at a net section stress of 145 MPa, which is ≈ 90 percent of net-section ultimate strength, the strain at the notch tips increase when compared to the strain in the center of the specimen. Full-field displacement maps of notched specimens under quasi-static loading conditions show a similar uniform deformation profile in the notch plane. Sectioned samples from a similarly notched specimen loaded to 100 MPa and then unloaded show no evidence of matrix or fiber damage at the notch tips. This evidence supports the strain gage data that show that damage occurs only at stress concentration sites with net-section stresses > 60 percent of the net-section ultimate strength. In contrast, the finite element model predicts higher strains at the notch tips compared to the strain in the center of the specimen. Also, the predicted notch tip strains are larger than the strain gage measurements for a given net section stress. The error between the measured and predicted notch tip strains is attributed to applying homogenous material property behavior at the notch tip. In this geometry, the notch tip is approximately one tenth the size of the fiber tow. Analysis of specimens with a notch tip radii

that are two times the size of a fiber tow are in excellent agreement with measured notch tip strains for the same CMC.

4.2.2 Heat Transfer and Stress Analysis of Oxide/Oxide Nextel™720/AS Composite Combustor Conceptual Design

As part of the Ultra-Compact Ceramic Combustor (UC^3) research effort, the University of Dayton Research Institute (UDRI) has performed finite element analyses of several design concepts for oxide/oxide combustor shells. The objectives of these studies are to identify critical materials-related issues in the combustor design, and to develop strategies for designing such a system to address or avoid these problems.

All of the analyses performed thus far involve simplified (axisymmetric) geometries, but do include the inlet, combustion chamber, and outflow regions of the combustor. Since the precise operating conditions can only be estimated at this point, a nominal radiation condition representing the primary combustion event has been adopted, which maintains a steady-state temperature of approximately 1300°C on the inner wall of the cavity that encloses the combustion process. This peak temperature of 1300°C is thought to be a reasonable value, provided that active cooling of the shell is performed. The calculations also include the effect of radiative exchange between the cavity walls and the centerbody on the interior surface and between the cavity and the engine case on the exterior surface. The ABAQUS finite element code has been used for these calculations, in a two-step process involving steady-state thermal analysis, followed by a nonlinear static stress solution.

Additional calculations are in progress to compare the current oxide/oxide composite with SiC/SiC composite material and a new material developed by Siemens-Westinghouse and Composite Optics, Inc. that includes a thermal barrier coating layer.

4.2.3 Combustor Testing of Oxide/Oxide Nextel™720/AS Composite Rings

Technical support was provided for combustor testing of the Nextel™720/AS composite. The support consisted of purchasing the CMC panels and developing mechanical drawings for 121mm diameter rings that fit into the combustor test fixture. After 10 hours of exposure to combustion gases from JP8 fuel the ring was removed from the combustor rig for study. Many areas of the ring have extensive carbon deposits, while others are very clean. The ring is permanently warped which suggests exposure to high temperatures. A single through crack now exists that extends from the inside diameter to one of the cooling holes. Temperature indicating paint of a second ring without cooling holes shows that temperatures as high as 1200°C have been reached on the surface of the CMC ring. Tensile specimens will be machined from the exposed rings to characterize the retained strength.

4.3 FRACTURE AND CREEP RUPTURE BEHAVIOR OF NOTCHED MI SiC/SiC COMPOSITE

Monotonic tensile and sustained load (creep) tests of melt infiltrated (MI) High-Nicalon-S/SiC CMC were performed at room temperature and 1200°C in laboratory air. Dogbone specimens and double-edge notched specimens with notches that are $\approx$ 1.88 mm deep and have a notch tip radii of $\approx$ 0.1 mm are used to characterize the effects of the notches on the mechanical behavior. There is a 34% drop in the ultimate tensile strength from room temperature to 1200°C, 325 and 214 MPa, respectively. In contrast, the notched specimens show only an 18% drop in net-section strength from room temperature to 1200°C, 271.7 and 222.1 MPa respectively. The creep rupture limit for MI High-Nicalon-S/SiC is $\approx$ 140 MPa at 1200°C, which is comparable to the creep rupture limit of 150 MPa at 1100°C for the oxide/oxide Nextel™720/AS CMC. For the notched geometry, the Nextel™720/AS has no apparent creep rupture limit at 1100°C, with rupture data at 90 MPa. In contrast, the MI High-Nicalon-S/SiC CMC does have creep rupture limit of $\approx$ 110 MPa at 1200°C.

4.4   HIGH CYCLE FATIGUE OF CVI C_f/SiC COMPOSITE

Experimental support was provided for high-frequency HCF testing of chemical vapor infiltrated (CVI) C_f/SiC CMC. Tests were completed at frequencies of 40, 400 and 2000 Hz at a stress ratio of 0.05. The support effort consisted of writing a software package to provide waveform generation and load feedback control of the large Unholtz-Dickie HCF test system. This interim software package was necessary because the existing software did not provide the required functionality and the next-generation LabView®-based software and hardware system was not yet ready for use. Additional hardware and software were included in the setup to allow synchronization of an infrared camera with the cycle count so that damage-induced thermal changes in the specimen could be monitored over the duration of the test.

5.0 ENGINE ROTOR MATERIALS IN CURRENT USE

5.1 FRETTING FATIGUE BEHAVIOR OF PRDA V Ti-6Al-4V

5.1.1 Effect of Cu-Ni Plasma Coating on Fretting Fatigue Characteristics of Ti-6Al-4V Under a Flat-on-Flat Contact [C6]

An experimental investigation was conducted to explore the fretting fatigue behavior of Ti-6Al-4V specimens in contact with Cu-Ni plasma coated and as-received (uncoated) pads. Two types of tests were conducted. One type in which the fretting fatigue limit stress for a 10^7 cycle fatigue life was evaluated for each contact condition using a step loading approach [5], and one type in which the Cu-Ni coating integrity was characterized by testing several specimens against a single set of pads. Tests were conducted at 300 Hz under ambient laboratory conditions. Characterization of the pad surfaces before and after testing was carried out to investigate the fretting fatigue damage mechanisms for the two contact conditions.

The presence of the Cu-Ni plasma coating produced a higher fatigue limit stress than the as-received pads prolonged. Over time, the coating effectiveness degraded, resulting in decreased fatigue life of the fretting specimens. In contrast, the fatigue lives of specimens tested against the as-received pads increased over time. The surfaces of Cu-Ni plasma coated pads were smoother after testing than before testing due to the plastic deformation. On the other hand, the surfaces of as-received pads were rougher after testing than before testing.

5.1.2 Effect of Various Surface Conditions on Fretting Fatigue Behavior of Ti-6Al-4V [C7]

Prompted by the results of the investigation discussed in Section 5.1.1, additional experiments were conducted with varying pad surface conditions to further investigate fretting fatigue damage mechanisms. Ti-6Al-4V with a ~1 µm polish and Ti-6Al-4V that was grit blasted and stress relieved to RMS #64 were selected in addition to the Ti-6Al-4V that was low-stress ground and polished to RMS #8 (designated as-received) and Cu-Ni plasma spay coated Ti-6Al-4V pad conditions used in the previous work. Behavior against the Cu-Ni coated and as-received pads was characterized through determination of a fretting fatigue limit for a 10^7 cycle fatigue life to verify earlier results. In addition, the behavior against all four pad conditions was evaluated with S-N fatigue testing, and the repeated testing used to evaluate the Cu-Ni coating integrity was conducted on the roughened and as-received conditions. Results from these tests indicated that the Cu-Ni coated pads improved the fretting fatigue behavior of the Ti-6Al-4V specimens because of the level of surface roughness produced by the plasma spray process rather than by the coating composition. Improved fretting fatigue behavior was also observed for very smooth contact surfaces. The coefficient of friction, µ, was evaluated for the Cu-Ni coated and as-received pads to help identify possible crack nucleation mechanisms. A µ value was obtained of ~0.3 for the Cu-Ni coated pads and of ~0.7 for the as-received pads.

5.1.3 Characterization of Fretting Fatigue Nucleated Cracks Using C-Shaped Specimens

At Purdue University, fretting test have been conducted using Ti-6Al-4V fretting pads, in which small fretting fatigue nucleated cracks have been observed. To characterize the damage accumulated on these pads, C-shaped specimens were machined and heat tinted to indicate the location of fretting cracks, which was along the back portion of the C. The C specimens were then compression tested in fatigue at 300 Hz to characterize the effect of the presence of the cracks. Most of the testing was conducted by Mr. Bence Bartha from Purdue University, who was trained in the operation of the C-10. When Mr. Bartha returned to school, the tests were continued with specimens obtained from Purdue. Support for hardware development, alignment and test setup was provided for these tests by the University of Dayton.

5.1.4   An Investigation of Fretting Fatigue Crack Nucleation Life Using Shear Wave NDI [C8]

A study was conducted to investigate fretting fatigue damage of Ti-6Al-4V against Ti-6Al-4V under flat-on-flat contact with blending radii at room temperature. Both the location of and the time required to nucleate fretting fatigue cracks were investigated for two static average clamping stress values that are representative of those estimated for turbine engine blade attachments. The axial fatigue limits for a 10^7 cycle life were determined at 300 Hz and R = 0.5 for average clamping stresses of 200 and 620 MPa. Then, feasibility of *in situ* fretting fatigue crack detection using a shear wave ultrasonic non-destructive inspection (NDI) technique was evaluated. Fractography was used to characterize the level of fretting damage.

Fretting fatigue limits for a 10^7 cycle life under the clamping stress conditions used were 330 MPa for the lower clamping stress and 250 MPa for the higher clamping stress, and are lower than the uniaxial fatigue limit for this material by 60 percent and 70 percent, respectively. Using the shear wave ultrasonic technique, cracks with a surface length of approximately 2.5 mm were detected on 10 mm wide specimens in tests conducted at the higher clamping stress. For the lower clamping stress, crack nucleation required over 95 percent of the total life; for the higher clamping stress, crack nucleation was much sooner. Nucleation sites were identified within 500 µm of the specimen edge. The step loading technique used to evaluate the fatigue limit stresses was validated based on the fatigue lives of specimens tested using shear wave NDI.

5.1.5   An Investigation of Fretting Fatigue Crack Nucleation Life of Ti-6Al-4V Under Flat-on-Flat Contact [C9]

Further investigation of the Ti-6Al-4V against Ti-6Al-4V under flat-on-flat contact was conducted to identify both the location of and the time required to nucleate fretting fatigue cracks. As with the investigation discussed in Section 5.1.4, two static average clamping stress values (200 MPa and 620 MPa) that are representative of those estimated for turbine engine blade attachments were investigated. The effect of fretting fatigue on uniaxial fatigue life was quantified by interrupting fretting fatigue tests, and conducting uniaxial residual fatigue life and residual fatigue strength tests. Metallography, scanning electron microscopy and spectral analysis were used to characterize the level of fretting damage.

Fretting fatigue tests interrupted at 10^6 cycles indicated little observable damage and no reduction in residual uniaxial fatigue life for the lower clamping stress. Significant fretting damage in the form of cracks and reduction in residual uniaxial fatigue life was identified for half of the specimens subjected to the higher clamping stress. Limited residual fatigue strength testing revealed no reduction in strength greater than thirty percent for either clamping stress condition in the absence of fretting fatigue nucleated cracks.

Characterization of the fretted regions generated with the higher clamping stress indicated the presence of many cracks, which nucleate at acute angles to the contact surface and turn to propagate perpendicular to the fatigue-loading axis within a very short distance. These cracks may nucleate in less than 10% of life. For the lower clamping stress condition, fatigue crack nucleation was not identified in the interrupted samples, but characterization of the fretting debris indicated the presence of oxides that could be responsible for eventual crack initiation through surface embrittlement. In all cases, the region toward the specimen edges was identified as the region of primary crack nucleation.

5.1.6   Characterization of Fretting Fatigue Behavior Between Dissimilar Metals

Investigation of the flat-on-flat contact geometry is also being conducted with metals that are either harder or softer than the Ti-6Al-4V used for the fretting specimens in the fretting fatigue investigations to date. The test conditions for this evaluation are listed in Table 1 (below) and were selected to allow comparison to results obtained for tests conducted against Ti-6Al-4V pads of the same microstructure as the specimens, from previous work. This year one test was conducted against IN100 pads (the harder material) the results of

which indicated no change in fretting fatigue behavior from the tests against Ti-6Al-4V pads. The softer material to be used in this study is 7075 T6 Aluminum.

Table 1: $\lambda = 300$ Hz, Ambient Laboratory Conditions
(R=0.5, fatigue limit for 10^7 cycle fatigue life)

	7075 T6 Aluminum pads	IN 100 pads
$\sigma_N = 200$ MPa	1 test	2 tests
$\sigma_N = 650$ MPa	1 test	2 tests

5.1.7 Effect of Sample Thickness on Local Contact Behavior in a Flat-on-Flat Fretting Fatigue Apparatus [C10]

Thin plate samples of Ti-6Al-4V contacted on both sides with pads of the same material were used to simulate contact conditions in real structures subjected to fretting fatigue. Laboratory tests on specimens of varying thicknesses were used to determine the stresses that correspond to a fatigue life of 10^7 cycles using a step-loading procedure. For the specific apparatus used in this study, changes in thickness produced changes in the ratio of shear load to clamping load for a specific fretting pad geometry. Specimen thicknesses of 1, 2, and 4 mm, and stress ratios of R = 0.1 and R = 0.5 were investigated for two different contact pad lengths. Fatigue limit stresses in the specimen were found to be relatively insensitive to the average clamping or shear stress. Finite element analyses of the test geometry were used to provide details of the stress distribution in the contact region for the flat-on-flat geometry with blending radius. Results show that stress and displacement fields for a variety of test conditions corresponding to a fatigue life of 10^7 cycles vary widely and do not provide any clear indication of the existence of a simple parameter equivalent to a uniaxial fatigue limit stress. The stress and displacement fields are also shown to be very sensitive to the coefficient of friction used in the analysis.

5.1.8 Effect of Normal to Shear Load Ratios on HCF Stress Limit Under Fretting Fatigue Conditions [C11, C12]

Fretting fatigue experiments were conducted to determine the fatigue limit stress at 10^7 cycles for Ti-6Al-4V. A step-loading procedure was used to determine the fatigue limit stress that, in turn, was applied to the test geometry in numerical simulations using finite elements. Several fretting pad geometries and specimen thicknesses were used to obtain a range of normal and shear forces that produced the stress and displacement fields in the specimen. An evaluation was made of the conditions near the edge of contact, where peak stresses occur, to deduce parameters that lead to fretting fatigue failures at 10^7 cycles. However, no simple combination of stresses and slip displacements could be used to correlate all of the experimental data. A fracture mechanics methodology was also employed in order to determine the conditions for propagation or non-propagation of cracks that initiate in the edge of contact region. While no parameters were found which could uniquely predict the fretting fatigue failure, adjustment of the coefficient of friction based on computed slip displacements was shown to have a substantial effect on the stress and stress intensity factors. A correlation of friction coefficient with slip displacement is proposed as a possible method for consolidating data from fretting fatigue experiments conducted under different conditions.

5.2 FOREIGN OBJECT DAMAGE IN PRDA V Ti-6Al-4V

The characterization of foreign object impact sites on simulated airfoil specimens was continued from last year. Previously, the damage produced by glass bead ballistic impact was documented. Based on last year's

test results, 25 additional specimens were impacted using steel beads to produce the foreign object damage (FOD). Three different bead sizes (0.5, 1.33, and 2.03 mm diameter) were impacted against airfoils with two different leading edge radii (0.381 mm (0.015 in) and 0.127 mm (0.005 in)) at 305 m/s (1000 ft/s) using either 0 or 30-degree angles of incidence to the leading edge. Each impact site was characterized in the SEM prior to fatigue testing. The impact damage was quantified by measuring crater depth, length and depth, by estimating material loss and was qualitatively analyzed by identifying material shear, cracks and extrusions. Four crater types were identified for a given impact condition, as typified by material loss on the entrance and exit sides of the crater and by the mode of impact:

- Ahead of the leading edge crest
- Directly on the crest
- Beyond the crest
- A miss (of the leading edge) resulting in a dent.

After damage characterization, the specimens' residual fatigue strengths for a 10^7 fatigue life were evaluated by fatigue testing using a step loading approach at 350 Hz under ambient lab conditions for stress ratios of 0.1 and 0.5. Post test characterization in the SEM was conducted and included inspection of crack nucleation sites on the fracture surface as well as comparison of the impact sites to pretest characterization to correlate the previously identified damage modes with the fatigue strength results from mechanical testing.

5.3   MEAN STRESS EFFECTS ON THE HIGH CYCLE FATIGUE LIMIT STRESS IN Ti-6Al-4V

An investigation was undertaken to evaluate the effects of mean stress on the HCF limit stress under uniaxial loading. Tests were conducted at frequencies from 20 to 70 Hz up to 10^7 cycles using a step-loading technique. Data were presented in the form of a Haigh (Modified Goodman) diagram as alternating stress against mean stress. Tests in the regime R < -1 were conducted to determine the effect of negative mean stresses on the material behavior. The lowest mean stress corresponded to R = -4, below which the compressive yield stress of the material would be exceeded. While numerous models could provide approximate fits to the data in the constant life Haigh diagram for positive mean stresses, none of them captured the trends of the data over the entire mean stress range including R < -1. The Jasper equation, based on a constant range of stored energy density, was found to represent the positive mean stress data quite well. The equation was modified to account for stored energy density at negative mean stresses. The best fit to the data implies that compressive strain energy density contributes less than 30 percent to the fatigue process as energy under tensile stresses. Further, initiation to a fixed crack length beyond which crack propagation occurs does not explain the shape of the Haigh diagram. It is concluded that HCF crack initiation, which represents a majority of life, and crack growth threshold are independent quantities and represent entirely different mechanisms.

5.4   HCF TESTING OF Ti-6Al-4V USING ROUND DOGBONE SPECIMENS

A series of high cycle fatigue tests using Ti-6Al-4V round dogbone specimens were conducted on the C-10 test frame. First, a series of constant maximum load tests were conducted in order to confirm earlier results and to establish a baseline curve for failure under low-cycle fatigue in the 10^5 cycle regime. Subsequent tests used these high initial max. loads to subject specimens to 25 % of life before starting a step-loading procedure to determine the HCF limit stress corresponding to 10^7 cycles to failure. The effect of the prior LCF loading was found to have little or no effect on the subsequent HCF limit stress. After these tests were completed, a second series of tests were conducted where an initial lower max. load was incrementally increased every 10^7 cycles until failure. These step-load tests were used to establish the fatigue limit for stress ratios of 0.5 and 0.8. Constant max. load tests were conducted for stress ratios from 0.5 to 0.8 in order to obtain S-N data in the 10^7 life regime, to establish baseline fatigue limit stresses, and to compare with existing data. A comparison of the constant max load tests to the step loaded tests conducted so far shows a consistent max. load to failure whether the specimen is step-loaded or not.

5.5   CRACK GROWTH DETERMINATION FROM FRACTOGRAPHY IN Ti-6Al-4V

The effect of stress ratio (R) on crack growth rates in Ti-6Al-4V has been investigated. A spectrum with three stress ratios, R= 0.73, 0.69, and 0.64, is being used to determine the effect of various closure-free stress ratios on crack growth rates. The number of cycles per R-block are carefully chosen to allow for a complete iteration of the loading spectrum while the crack is growing within a single grain of the approximately 10 µm grain size Ti-6Al-4V material. This is done to facilitate the measuring of crack growth within each particular R-block. Past work has shown that the crack fronts tend not to be continuous as they travel from grain to grain in Ti-6Al-4V, thus making accurate crack growth rate measurements difficult. Results of this work have shown the existence of a non-closure-induced R-effect in Ti-6Al-4V, similar to that seen in Al-Cu alloys and Ni-base superalloys. The next phase of this program will be to assess the role of environment on crack growth rates as a function of applied stress ratio.

5.6   ENGINE ROTOR LIFE EXTENSION

5.6.1 Bending, Fatigue, and Thermo-Mechanical Fatigue (TMF) Residual Stress Relaxation for PM IN100

A study has been initiated to characterize the thermal residual stress relaxation in IN100 nickel-base powder metal. The purpose of this study is to develop an understanding of the relaxation of residual stresses, induced by shot peening, under isothermal loading. The shot peening specifications and test temperatures for this study were chosen to simulate applied surface treatments and engine operating conditions of aircraft turbine disks. The test specimens were shot peened by the Metals Improvement Co. of Cincinnati, OH. Future work will consist of Lambda Research Inc. performing the heat treatments and residual stress measurements. Residual stress measurements will be made at the surface and at selected depths from the surface. One specimen will be used to characterize the stress profile prior to heat treatment. Similar residual stress measurements will be performed on eight specimens after reaching selected exposure times at a single elevated temperature. Based on the thermal relaxation behavior of the first selected temperature a duplicate series of tests will be performed at two additional temperatures.

A second study to quantify the accuracy of the measured residual stress profile using X-ray diffraction is in progress. Rectangular specimens with dimensions of height = 7 mm, width = 6 mm and length = 100 mm were machined from IN100 powder metal alloy for four-point bend testing. In a four-point bend fixture, the applied bending moment will produce a linear distribution of stress and strain in the specimen for elastic loading. For inelastic loading, the top surface will yield in compression and the bottom surface will yield in tension. Removal of the applied moment will produce a state of tensile residual stress on the top surface, and a compressive residual stress on the bottom surface. The residual stress profile from plastic deformation in four-point bending has been calculated using finite element analysis at several load levels. Future work will include conducting the four-point bend test with strain gages on the top and bottom surfaces and measuring the residual stress profile using X-ray diffraction. Measured axial strains during loading and unloading in the four-point fixture and final deformed shape measurements of the specimen will provide data to support the finite element predictions.   Finally, the residual stress profile into the depth of the specimen can be measured using X-ray diffraction and compared to the finite element predictions.

5.6.2 Material Studies of Nickel-Base Superalloys

Literature survey of Ni-base superalloys
A significant amount of research work on Ni-base superalloys has been conducted for the past four decades. The ultimate purpose of the work was to increase the performance and reduce the weight of gas turbine engines and to predict accurately the engine life. To reach this purpose a computer simulation technique called probabilistic life analysis technique (PLAT) was employed and applied to all the engine materials in 1980s. This technique integrated information on initial material quality, fatigue and fracture mechanics,

component stress analysis and nondestructive evaluation (NDE) variability. The simulator evaluates each feature of a component and then computes occurrence rates for significant events such as parts removals, initiated cracks, inspection results, failures, etc., for a fleet of components. Hence the extensive data base on materials, mechanical testing and NDE, the life assessment methodology development and component testing, will assist the ERLE project to identify the key research areas.

Processing
Ni-base superalloys play a vital role in gas turbine engines. The IN100 alloy, employed in F-100 engine, and manufactured by powder metallurgy (PM, patented as Gatorzed), is the strongest among other superalloys. However, the information regarding the thermal mechanical processing and heat treatment was considered to be proprietary. Through literature and patent survey, detailed information has been obtained to gain deep understanding of the resultant microstructure and defects.

Defect
Previous systematic research work on IN100 (P/M) confirmed that two out of three fatigue crack initiation sites originated from defects, including voids and inclusions. Thus, it is crucial to study the defect identification, size, shape, volume fraction, and distribution. Optical quantitative microscopy is going to be performed on the polished samples from the bore, rim and central part of the disk cross section. The fatigue crack initiation sites of fatigued specimens will be identified by SEM and characterized by SEM dot mapping. The correlation between the crack location and stress level will be studied.

Microstructure
The Ni-base superalloys currently employed in F100 gas turbine engines are IN100, Waspoloy, and Astroloy. The mechanical properties of each material are significantly dependent on the microstructure, particularly the γ grain size and the volume fraction of γ'. For example PWA 1106, a creep resistant version of IN100, has much larger grain size than PWA 1074, a high yield strength version of IN100, owing to different heat treatment. The quantitative microscopy will be performed to determine the γ grain size and the volume fraction of γ' of each microstructure. The sizes of different γ', resulting from different stages of heat treatment, will be studied by SEM.

5.6.3 Fractography Assessments of Crack Growth and Load Interaction

Preliminary tests have been conducted to determine if load sequences can effectively mark the fracture surfaces of IN100 at elevated temperatures. The SEM is used to identify features on the fracture surfaces that are associated with the various portions of the loading sequence. Load sequencing has produced some surprising and interesting results (see discussion in Section 5.7) for fatigue crack growth behavior and the influence of load interactions in aluminum alloys.

Tests were conducted at 482 and 650°C on C(T) specimens with various combinations of low amplitude fatigue blocks with a large number of cycles and different stress ratios, R; high amplitude fatigue blocks with a small number of cycles with a stress ratio near zero; and dwell times at different stress levels. A test at 482°C produced crack growth rate data from below 10^{-9} to near 10^{-4} m/cycle, no crack growth at max load with a 400 s dwell, and a stress ratio effect that is not attributable to crack closure. The stress ratio effect persisted from a near threshold value of about 7 MPa$\sqrt{}$m for ΔK at R=0.73 to ΔK$\approx$30MPa$\sqrt{}$m, where the crack growth rates for R=0.73 and 0.64 coalesced.

A test at 650°C produced near threshold dwell crack growth rates below 10^{-8} m/s for 1000 s dwell time at 46 MPa$\sqrt{}$m. The crack front that was continuous in appearance during a fatigue block became irregular while transitioning from transgranular to intergranular crack growth during the start of a dwell period. Another test at 650°C revealed a pronounced, non-closure-related stress ratio effect in the threshold region. The stress ratio effect quickly diminished and disappeared as ΔK increased.

5.6.4 Basic Mechanical Properties - Baseline/Qualification and Usage

The ERLE initiative is a program designed to increase engine rotor life and reduce maintenance costs. This section of the ERLE program involves testing material from engine rotor disks with various degrees of real life usage. The current material being tested is IN100, and this material has not seen any real life usage. The test matrix that will be used for most of the rotor disks is as follows:

Tensile properties
- 3 specimens at R.T. 23°C
- 3 specimens at 427°C
- 3 specimens at 704°C

Fatigue (S-N) properties
- 6 specimens at 538°C with approximately 1000 MPa maximum stress, R = 0.05 at 0.5 Hz.

Creep Rupture properties
- 3 specimens at 732°C at 741 MPa

Creep properties
- 3 specimens at 704°C at 565 MPa

The tensile tests for the current material IN100 are complete and the results are as follows:

	23°C	427°C	704°C
UTS	1445-1483 MPa	1367-1408 MPa	1160-1188 MPa
Yield Strength	931-960 MPa	877-944 MPa	886-939 MPa
Modulus	218-219 GPa	195-201 GPa	163-172 GPa
Strain	19-36 %	25-34 %	26-36 %

The fatigue and creep tests are in process and there are no results to report.

5.6.5 Compression Testing of IN100 at 23°C

The compressive material behavior of two nickel-base powder metal IN100 alloys with nominal grain sizes of 10 μm and 25 μm were studied at 23°C. The test specimens were uniform diameter cylinders with nominal dimensions of 5.5 mm diameter by 8.3 mm long and 7.80 mm diameter by 15.60 mm long for the 10 μm and 25 μm grain size alloys, respectively. Specimens were instrumented with 1.6 mm square strain gages oriented in the loading direction (longitudinal) and perpendicular to the loading direction (transverse). All tests were performed in displacement rate control at 0.02 mm/s. The smaller specimens were used to refine the experimental test procedure. Specimen alignment in the load train and strain gage data collection proved to be difficult with the small samples; therefore, the larger specimens were used for the remaining tests.

The measured elastic properties in compression, Young's modulus (E) and Poisson's ratio (ν), show excellent agreement with measured tensile properties. However, post-yield true stress versus true strain behavior differs between tensile and compressive loading as shown in figure 1. The post-yield compressive true stress versus true strain curve has a 16% higher tangent modulus, E_T in figure 1, than the tensile curve when measured over the 7 to 10% true strain range. Finite element (FE) analysis with true stress-true strain tensile material data was used to calculate the compressive axial strain on the surface of the specimen at the mid-height location. The FE model included the steel loading platens and contact friction between the specimen and platens. Analyses were performed with three sets of friction conditions between the specimen and the

platens: completely fixed with nodes equivalenced between the specimen and platens, frictionless contact, and friction with a coefficient of friction (COF) between the specimen and platens, COF = 0.6.

The FE results from all three cases show that the amount of prescribed friction between the specimen ends and the platens does have an influence on the axial strain at the mid-height of the specimen. The FE predicted stress versus strain at the mid-height of the specimen is similar to the true stress-true strain input data. However, the FE predictions do not agree with the measured true stress-true strain compressive behavior as shown in Figure 1. Therefore, there is a difference between the tensile and compressive post-yield behavior. Characterizing the differences between the tensile and compressive post-yield behavior is necessary for the development of models to simulate material response to surface treatments and for predicting the retained residual stress profile.
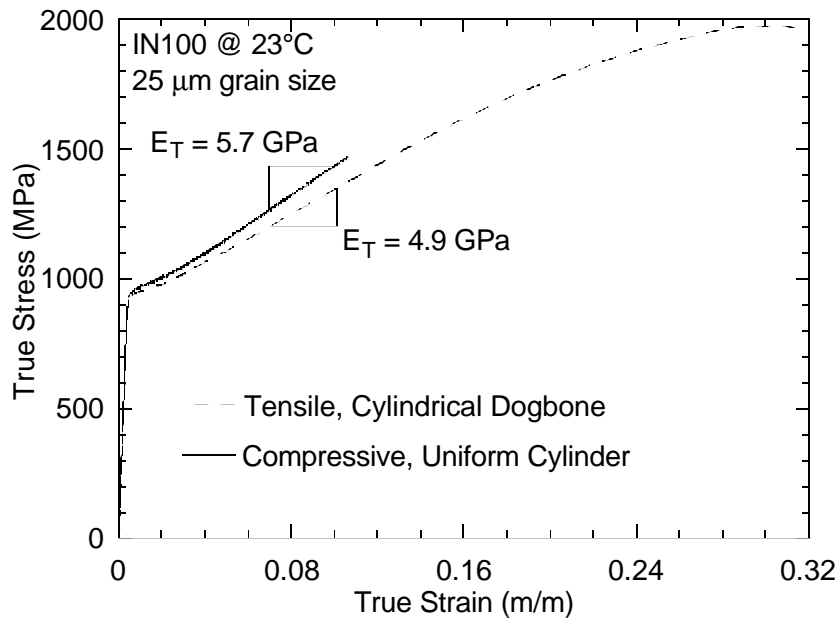

Figure 1.   True Stress Versus True Stain Tensile and Compressive Response for IN100 Powder Metal Superalloy at 23°C

5.7   FRACTOGRAPHY ASSESSMENT OF CRACK GROWTH IN TWO ALUMINUM ALLOYS

5.7.1 Fatigue Voids and Their Significance [C13]

Fatigue voids form in Al-alloys as a consequence of the separation of non-coherent secondary particulates from the matrix in early fatigue. The process of their formation is through the initiation, growth, and coalescence of multiple interfacial cracks around the particulate. Such voids become visible on the fatigue fracture surface if and when the crack front advances through them. In the event that the dominant crack forms and grows slowly, as in vacuum, each fatigue void is the potential source of an embedded penny-shaped crack. In air, the dominant crack forms and grows faster, giving less opportunity for multiple internal cracks to spawn off from the innumerable voids in the fatigue process zone. In vacuum, fatigue voids appear to be the potentia l origins of the dominant crack. In air, fatigue voids do not appear to affect the fatigue process at low and intermediate growth rates. At high crack growth rates involving considerable crack tip shear, angular planes of particulate concentration offer the path of least resistance. This explains the increasing density of fatigue voids with growth rate. Very high growth rates signal the onset of a quasi-static

crack growth component that manifests itself through growing clusters of micro-void coalescence associated with static fracture. Micro-voids have nothing in common with fatigue voids.

5.7.2 Microscopic Markers Reveal Root of the Fatigue Process in Al-Alloys [C14]

Specially programmed fatigue load sequences were designed to identify the progress of the fatigue crack growth. The idea was to build a zoom-in capability by inserting a small number of marker cycles between blocks containing a large number of baseline cycles. The baseline cycles grow the crack while the marker cycles highlight the crack front location by enforcing an instantaneous microscopic switch in crack extension mode that leaves a high contrast, striation-like mark on the fracture surface. The notch root fatigue tests under this type of loading sequence revealed that interfacial fatigue cracking was occurring early in the fatigue process around non-coherent second phase particles.

5.8   OTHER MATERIAL BEHAVIOR

5.8.1 Tension, Fatigue, and KIC Tests on Laser-Melted PM Ti-6Al-4V

Cylindrical and compact tension specimens were extracted from laser melted Ti-6Al-4V PM billets in both the hipped and unhipped condition. Tensile and fatigue specimens were tested in each of the three orientations using cylindrical specimens. Fracture toughness was determined in each of the three orientations using the compact tension specimens.

5.8.2 Tension and Fatigue Testing of Ti-6Al-4V/20% Vol. TiB

The tensile, compression and fracture toughness properties of Ti-6Al-4V/20% Vol. TiB were determined at room temperature. The processing of the material inclu ded extruded, extruded and annealed, and blind-die compacted. In the extrusion process the TiB whiskers were oriented parallel to the extrusion direction, whereas the blind die compaction allowed a random orientation of the whiskers. The tension specimens from the extruded material were oriented so that the applied load was parallel to extrusion direction but the compression and fracture toughness specimens were oriented so that the applied load was normal to the extrusion direction.

6.0 DEVELOPMENT OF EXPERIMENTAL PROCEDURES, METHODOLOGIES, AND LABORATORY ENHANCEMENTS

A number of new capabilities were added to the AFRL/MLLMN laboratories during FY01. These new capabilities generally fall into one of two categories:

- Infrastructure improvements related to overall laboratory test control and data management
- Specific types of apparatus or instrumentation that have been developed or enhanced.

The capabilities added in these two categories are discussed in the paragraphs below. As one might expect, some crossovers exist between the categories, and appropriate discussion is included to address these crossovers where they are important.

6.1 LABORATORY TEST CONTROL AND DATA MANAGEMENT

The AFRL/MLLMN laboratories are of sufficient size that a coordinated system of implementing new test technologies and methodology enhancements as well as managing the data collected from tests is required. The following paragraphs describe work performed to improve, extend, and/or replace this infrastructure.

6.1.1 WinMATE Development Support

As noted in the previous annual report, the UDRI is working with AFRL/MLLMN to implement the WinMATE test automation software and hardware system throughout the laboratory. The bulk of this effort is being conducted as part of a Small Business Innovation Research (SBIR) program; however, certain supporting analyses and evaluations are being conducted as part of the on-site contract to ensure that the new system will meet the needs of AFRL/MLLMN.

One significant WinMATE supporting effort on the on-site contract is the development of additional DCPD versus crack length solutions for various geometries. To ensure that these solutions are accurate, we have adopted a procedure whereby each geometry is analyzed using both finite element and finite difference techniques. Comparison of the results from the two techniques provides confirmation of the results as well as better estimates of the accuracy of the DCPD versus crack length solutions. The solutions that have been developed are being integrated into the WinMATE Analytical and Numerical Solution (WANS) Library. This library will be used to support all test automation control and data analysis in the WinMATE system.

Compliance Analysis of a Cracked Four-Point Bend Specimen
In an earlier study, a crack-length expression as a function of crack-mouth-opening compliance had been obtained for a four-point bend specimen containing a crack. This expression had restricted applicability because the numerical results in the literature [2] were only available for crack lengths, a, between 20 and 70% of the specimen width, W. This previous effort has been extended to develop a crack-length expression for the full range crack lengths, $0 \leq a/W \leq 1$.

For consistency in the development of the crack-length expression, compliance values were obtained from a finite element analysis for $0.1 \leq a/W \leq 0.9$. These numerical results were in excellent agreement with those values for $0.2 \leq a/W \leq 0.7$ in the referenced paper [2]. Analytical results were obtained for compliance behavior as the crack length approaches zero and the specimen width. The crack length can be conveniently given to within 1% accuracy for $0 \leq a/W \leq 1$ by the following expression:

$$\frac{a}{W} = 1 - \frac{1 + m_1 \sqrt{C'} + m_2 C' + m_3 C'^{(3/2)}}{\left(1 + m_1 \dfrac{\sqrt{C'}}{2} + C'\right)^2} , \tag{1}$$

where m_1, m_2, and m_3 are coefficients with values 1.682125, 2.541845, and 1.90981, respectively, that were determined by fitting the compliance results in a least square error sense. The nondimensional compliance, C', equals $\left[\dfrac{W}{S_j - S_n} E' B \dfrac{\Delta}{P}\right]$, where S_j and S_n are the major and minor spans of the specimen, E' is an effective modulus, B is specimen thickness, Δ is the crack-mouth-opening displacement, and P is the total force on the specimen. The effective modulus for a plane stress condition (B/W<<1) has the value of Young's modulus, E. For a fully constrained condition (B/W>>1), the effective modulus equals $\dfrac{E}{1 - \nu^2}$ where ν is Poisson's ratio. For laboratory test conditions, the value of E' should be between E and $\dfrac{E}{1 - \nu^2}$.

6.1.2   HCF Laboratory LabView® Software and Hardware Implementation

A standard LabView® software application is currently being developed to control and acquire data from all the test systems in the HCF laboratory. Development of this software is being performed in conjunction with implementation of a new, standardized hardware configuration to create a uniform system interface across the laboratory. The standardization of these two systems will greatly reduce the time needed to locate and fix potential problems. It will also reduce the time required to train staff members in the use of the systems.

6.1.3   Improvement in Load Frame Alignment Equipment and Procedures

Although load frame alignment has been studied both analytically and experimentally by a large number of laboratories (including AFRL/MLLMN), there continues to be a lack of understanding of the relationship between fundamental mechanics concepts and practical procedures needed to align a given test system. In addition, certain aspects, such as torsion bending, have not been addressed to any significant extent in current standards or in the literature.

Engineers and technical staff from the UDRI and AFRL/MLLMN have taken a systematic approach to developing the required understanding and incorporating torsion and other issues in the alignment process. This work has resulted in practical guidelines for both technical staff and project engineers, including tradeoffs that may be necessary to obtain the desired test results. The following discussion provides one illustration of these practical guidelines.

It is often possible to align a load frame such that there are very small bending strains in the center of the reduced section of an axial test coupon. Analyses and experiments show, however, that it is extremely difficult to obtain similar results for the regions near the ends of the reduced section. Thus, the test engineer may decide that the higher bending strains near the ends of the reduced section are not of concern for the following reasons.

1. The region where the extensometer will be placed (the center of the reduced section) will see low bending strains, and therefore, the measurements made will not contain significant bending errors.
2. The material being tested is fairly ductile, and the higher bending strains near the ends of the reduced section are unlikely to cause premature failure in those regions.

Obviously this is just one possible way of applying the guidelines that are being developed. These guidelines are currently being organized and will be used to produce a comprehensive load frame alignment procedure as well as a guide to understanding which aspects of load frame alignment are important for a given type of test on a given material.

6.1.4 Upgrade of Laboratory Test Automation Hardware and Instrumentation

The long-term process of upgrading AFRL/MLLMN laboratory hardware and instrumentation has continued throughout the past year. Specifically, two additional automation systems have been upgraded for use with WinMATE and a standard physical format for a typical test station has been adopted. A standard oscilloscope and interface hardware have been selected and a number of units have been purchased and installed. UDRI engineers also worked with a commercial interface board manufacturer to develop a highly stable, low-noise analog-to-digital (A/D) converter board that reduces the electronic noise threshold to less than four bits. This is compared with a threshold of almost 12 bits for the previous board. The new boards are now in production and six have been installed in laboratory systems.

6.1.5 Data Archival System

The Data Archive is a central computer on which test data generated by RG 2.3 is stored and indexed. Its purpose is to prevent the loss of valuable test data and provide independent user access within RG 2.3. During the past year a plan to upgrade the server hardware and relocate it to government computer support (MLOC) was implemented. The new configuration was selected to improve server reliability and MLOC response time by incorporating the hardware into MLOC's existing server structure. Transfer of computer software and hardware administration responsibilities took place during FY00. UDRI still supports local administration of file access privileges and works with MLOC on global system administration. In addition to the hardware upgrades, a large volume of test data for coupons was added to the archive, and the documentation provided to the users was updated.

Changes in the policies regarding computer software and hardware support from MLOC over the past year have made the Keyserver® system, which was put in place in 1996 to provide hands-off control of commercial software licenses for RG 2.3, obsolete. As a result, the Keyserver® was phased out at the end of this year.

6.2 APPARATUS AND INSTRUMENTATION

The AFRL/MLLMN laboratories have a long tradition of developing state-of-the-art instrumentation designed to provide critical information on material behavior under various test conditions. The following paragraphs describe work performed in FY00 by the University of Dayton to continue in this tradition of innovation and creativity.

6.2.1 Infrared Damage Detection System (IDDS) Enhancements

The IDDS described in the previous annual report has been enhanced with a microscope attachment to provide high-resolution images of cracks and crack precursor damage. Using this microscope and specialized techniques images have been obtained that appear to show lamellar structures in gamma titanium-aluminide materials. This is significant in that, if the images do show these features, we will be able to dynamically monitor them *in situ* during a test. Further study will be required to confirm that the images can reliably reveal lamellar or other microstructures.

In the process of conducting tests we have also identified a necessary hardware upgrade that will allow us to continue technique development. A new frame grabber board is needed so that the existing software can be

migrated to the Windows 2000 operating system. This migration will allow the IDDS software to be compatible with all of the other WinMATE modules.

6.2.2 High-Speed, High-Stability Direct Current Potential Difference (DCPD) Crack Detection System

A new, multichannel DCPD hardware system for both crack detection and propagation measurements has been evaluated in the laboratory. The system is based on recently developed technology for high-speed switching of the DCPD current. This technology has been coupled with an innovative method of maintaining a constant load on the DCPD power supply so that current and voltage transients are suppressed during the switching operation. The new system has the following advantages over any of the previous DCPD systems:

- Cost per channel is reduced by approximately 50%.
- The new system can acquire DCPD readings near maximum load without reducing the applied loading frequency.
- The new system is stable to better than 0.01% over long time periods. The exact stability and crack detection threshold is currently being studied.

The new DCPD hardware will be integrated with existing software and will be used as the standard DCPD system for both crack detection and crack propagation testing.

6.2.3 2kHz System Repairs and Validation Testing

The 2kHz magnetostrictive actuator in place at the start of this reporting period was over-reliant on silicone adhesives to seal critical components and prevent loss of coolant. This design issue eventually rendered the system inoperable due to large coolant leaks. The following steps were taken to rectify this situation:

- A new base plate was machined to eliminate unused cooling channels and ports and to accommodate hermetically sealed feed-throughs for power and temperature sensors.
- The end plate was remachined to accept a cylindrical insert sleeve for an O-ring seal, and unused holes previously filled with silicone were welded closed and ground flush.
- The magnesium end-cap (the coupler between the Terfenol and the aluminum output plate) was remachined with an O-ring groove and with proper clearance to the cylindrical insert sleeve.
- Modifications were implemented in the internal coolant path to reduce flow restrictions and backpressure.

On initial checkout after reassembly there was slight leakage past the O-ring, but this has since subsided. We speculate that this is due to completion of a break in period for the new O-ring and sleeve. Both Terfenol and coil temperatures are substantially reduced due to the coolant path improvements. New safety interlocks have been installed, and the system has run reliably during testing over nights and weekends since the rebuild.

6.2.4 20kHz System

A resonant fatigue system operating at ultrasonic frequencies near 20kHz was developed and delivered to the AFRL/MLLMN laboratory. The system produces tensile mean loads in addition to an alternating load by gripping the resonating portion of the system at nodes of zero displacement. The system is designed to provide data for any positive stress ratio fatigue test. The 20kHz system builds upon previous work, adding improved provisions for alignment and automation using a personal computer with a LabView® operator interface. Mean loads are produced with a rolling diaphragm pneumatic cylinder, while the high-frequency resonant loading is produced through a commercially available resonant ultrasonic oscillator and modified standard tooling. Mean load measurement is obtained through a conventional load cell, while alternating load

measurement is obtained through measuring the end displacement of the resonating section with an eddy current displacement gage.

The 20kHz system will to be used to dramatically reduce the test time required for HCF tests requiring $>10^7$ fatigue cycles for specimen failure. The reduced test time will allow researchers to gather data on material fatigue behavior within a reasonable time frame. Efforts are currently underway to upgrade the operator interface to be compatible with the other test systems in the High Cycle Fatigue Laboratory and to verify proper system operation.

6.2.5　C-20 Fretting Frame, Alignment, and Resonance

The C-20 shaker system has been in service for several years but testing was restricted to frequency bands between system resonances. Various other performance shortfalls have also been noted. During the past year the following tasks have been performed to eliminate, or minimize, the unwanted resonances and address the other performance issues:

- The unit was disassembled and cleaned.
- A number of worn or broken components were replaced.
- Various adjustments were made to bring the unit within manufacturer's specifications.
- A new fixturing system is being designed to improve load frame alignment.
- A fretting fatigue fixture was fitted to the system to allow rapid evaluation of materials under various fretting conditions.
- New amplifiers were purchased and installed to reduce the electronic noise produced by the older SCR-based amplifiers.
- A new direct current field supply with better current control was purchased and installed.
- Several channels of strain conditioning were added.

On completion of this work the C-20 unit exhibits significantly improved performance in all areas.

6.2.6　Technical Support for Displacement Mapping System Development

A camera mount was added to a servo-hydraulic test system and the grips were modified to facilitate imaging of small specimens. Technical support including specimen setup, software operation, and design of special step loaded tests was provided to the test engineer. The test engineer used the images obtained from this test setup to develop high-resolution, two-dimensional maps of in-plane displacements near crack tips.

7.0 REFERENCES

1. Davidson, D.L. and Campbell, J.B., *Metall. Trans.*, 1993, Vol. 24A, pp. 1555-1574.

2. Gross, B., Roberts E., Jr., and Srawley, J.E., "Elastic Displacements for Various Edge-Cracked Plate Specimens," *NASA Technical Note*, NASA TN D-4232, National Aeronautics and Space Administration, November 1967.

3. Hirohisa, S., Keiro, T., and Yasuhito, O. *Mater. Sci. & Eng*., 1998, Vol. A243, pp. 169-175.

4. Kim, Y-W. and Dimiduk, D.M., *JOM*, 1991, Vol. 34 (8), pp. 40-47.

5. Maxwell, D.C. and Nicholas, T., "A Rapid Method for Generation of a Haigh Diagram for High Cycle Fatigue," *Fatigue and Fracture Mechanics: 29th Volume*, ASTM STP 1321, T.L. Panontin and S.D. Sheppard, Eds., American Society for Testing and Materials, 1998, submitted for publication.

6. Yamaguchi, M. and Inui, H. *Ordered Intermetallics-Physical Metallurgy and Mechanical Behavior*, C. T. Liu, et al. Eds. Kluwer Academic Publisher, Netherlands, 1992, pp.217-235.

This page intentionally left blank.

APPENDIX
COMPILATION OF MANUSCRIPTS

LIST OF MANUSCRIPTS

W. John Porter, III[*], Reji John[†], Steve Olson[*], and Kezhong Li[*]

[†]Air Force Research Laboratory, Materials and Manufacturing Directorate,
AFRL/MLLMN, Wright-Patterson Air Force Base, OH 45433-7817
[*]Advanced Materials Characterization Group, Structural Integrity Division
University of Dayton Research Institute, Dayton, OH 45469-0128

Abstract

Gamma titanium aluminide (TiAl) alloys are being considered for application in rotating components of gas turbine engines. While the elastic properties of gamma and alpha-2 single-phase materials have been thoroughly investigated, the elastic response of fully lamellar, two-phase materials have not received the same amount of attention. Detailed reports on the elastic property information of two-phase gamma alloys are scarce. Also, colony-level properties are required for development of accurate models in these material systems. In an effort to determine colony-level properties, samples with gage sections composed of specifically-oriented individual lamellar grains were tested in tension to determine the elastic behavior of this two-phase structure. Preliminary attempts at modeling the elastic behavior of this material observed during testing will also be reported. The results of these tests and their implications to the design and use of gamma titanium components are discussed.

Keywords: gamma titanium aluminide; lamellar microstructure; elastic modulus; finite element modeling

Introduction

Gamma titanium aluminide (TiAl) alloys are being developed for application in rotating components for gas turbine engines. Based on the intermetallic gamma (face-centered tetragonal) and alpha-2 ($D0_{19}$-modified hexagonal close-packed) phases, TiAl and Ti_3Al, respectively, these alloys are noted for their high temperature strength retention, light weight, good oxidation resistance and stiffness [1-3]. While the elastic properties of gamma [4-8] and alpha-2 [5,9,10] single-phase materials have been thoroughly investigated, the elastic response of fully lamellar two-phase materials has not received the same amount of attention. Reports on the elastic property information of various gamma TiAl alloys are inconsistent [11,12]. The relative lack of information on the elastic behavior of two-phase, lamellar titanium aluminides is contrasted by the excellent work reporting the deformation and fracture behavior of this material system [13-16]. In order to accurately model the mechanical behavior of fully lamellar gamma TiAl, samples with gage sections composed of single lamellar grains were tested in tension to determine the elastic behavior of this two phase structure. Preliminary modeling results of the colony-level elastic behavior are presented and approaches for improving the model are discussed. The role of adjacent grains and their effect on the behavior of the gage section grain is also addressed.

Material and Test Parameters

The alloy used in this study, nominally Ti-46.5Al-3Nb-2Cr-0.2W (at%), was developed by Kim [3] and designated as K5. To obtain the large grain microstructure required for this testing, the forged material (approximately 10x20x2cm) was heat treated in air at 1400°C for 24 hours and homogenized at 900°C for 24 hours and then air cooled. The heat treatment temperature is in the single-phase alpha field for the composition. The resulting microstructure was near-fully lamellar with an average grain size of approximately 7 millimeters in diameter and lamellar spacing in the 1-3 micron range. A

photomicrograph of the microstructure is shown in Figure 1. This image was obtained using a scanning electron microscope (SEM) in the backscattered-electron (BSE) mode. In this photo, the dark contrast phase is gamma and the light contrast phase is alpha-2. The material's chemistry was analyzed before and after heat treatment and the results are shown in Table 1. Not surprisingly, the oxygen level was found to be significantly higher following heat treatment in air.

Thin sections (3mm thick) were sliced from the forged material using an electro-discharge machine (EDM) and then polished. Dogbone samples were then EDM'd from the thin sections such that the majority of the gage section of a specimen consisted of a single large grain with a specific surface orientation. A machining blank highlighting the microstructure is shown in Figure 2. The specimen and the specimen drawing are shown in Figure 3. Due to the significant anisotropy of fully lamellar material, the surface and edge orientations of the gage section grain were carefully determined through metallography.   The orientation information allows for determination of in-plane properties.   A schematic of the gage section lamellar orientation, as well as the grains outside the gage section of the specimen used in this study, is shown in Figure 4. The photomicrograph of the microstructure (Fig. 1) shows the gage section grain on the right side.   The low angle orientation (12°) of this grain is exemplified by the coarse lamellar spacing of this grain. The grain to the left represents a better view of the relatively fine lamellar spacing of the material.

Material response during testing was measured using strain gages located on the top and bottom faces of the sample. The grid size of the strain gages was 0.381mm (top to bottom) x 0.508mm (side to side). The gages were located as close to the mid-face or mid-thickness of the centerline of colony #2 (Fig. 4) as possible. Since all testing was done in the elastic regime of the material, a two-step approach for monitoring strain parallel and perpendicular to the lamellar orientation was undertaken. First, strain gages were applied on the top and bottom faces of the sample parallel to the orientation of the lamellae and then tested. The sample was then removed from the test machine and new gages were applied to monitor strain perpendicular to the lamellae.

The tests were done at room temperature on a servohydraulic machine in load control mode. A loading rate of 5MPa/sec was employed. To insure that the samples were loaded in the elastic regime, the tests were run to a maximum load of only 50 MPa.

Analysis

Using the initial elastic information from Table 2, a 3-dimensional finite element (FE) model of the sample was constructed (Fig. 5). The initial elastic properties (Table 2) were derived using elastic constant data from the literature for gamma- and alpha-2-phase material [17] and plate-based models that took into consideration the relative phase volume percentages seen in the material. The different shades of gray correspond to the grains making up the sample. Each grain represented in the FE model was assigned properties based upon the metallographically determined orientation of the grain in the sample (Fig. 4). Details of the finite element approach are also shown in Table 2.

Results and Discussion

The stress-strain data are shown in Figure 6a and 6b. The top and bottom longitudinal moduli values were measured to be 171 and 176 GPa, respectively and the negative slopes of the transverse cases were -654 GPa for the top and -685 GPa for the bottom. The average Poisson's ratio for top and bottom measurements is 0.260, lower than the value used in the FE analysis of 0.3326. While the orientation of grains adjacent to the gage section and the interaction at the grain boundaries will have a limited effect on the gage section grain properties, the extent of this effect is still being determined. Efforts are underway to monitor tests of samples with grain boundaries in the gage section to determine their effects on neighboring grain properties.   Strain will be monitored using full-field displacement techniques

allowing for simultaneous strain measurement at the grain boundary region and the grains within the gage and shoulder region of the samples.

Preliminary 3D finite element analysis results for each case are shown as lines in Figure 6a and 6b. General agreement between the modeling and the trends of the experimental data is shown. In order to improve the model, additional experiments aimed at understanding the role of neighboring grains and more detailed finite element analyses are required.

Summary and Conclusions

In an effort to understand the elastic behavior of gamma titanium aluminides with lamellar microstructures, tensile samples with a single lamellar grain in the gage section were loaded in the elastic regime to determine colony-level response. Strain was monitored by placement of strain gages in the transverse and longitudinal orientations on the top and bottom sides of the sample. Preliminary finite element analysis was able to capture the general trends of the anistropic behavior, however, more work is needed to understand and deduce the effects of constraint from neighboring grains.

Acknowledgements

References

[1] Y.W. Kim, J. Met. 41 (1989) 24.
[2] Y.W. Kim, D.M Dimiduk, J. Met. 43 (1991) 40.
[3] Y.W. Kim, J. Met. 46 (1994) 30.
[4] H. A. Lipsitt, D. Schechtman, R. E. Schafrik, Metall. Trans. A6 (1975) 1991.
[5] R. E. Schrafik, Metall. Trans. A8 (1977) 1003.
[6] Y. He, R. B. Schwarz, A. Migliori, S. H. Whang, J. Mater. Res. 10 (1995) 1187.
[7] K. Tanaka, T. Ichitsubo, H. Inui, M. Yamaguchi, M. Koiwa, Phil. Mag. Lett. 73 (2) (1996) 71.
[8] M. H. Yoo, J. Zou, C. L. Fu, Mater. Sci. Eng. A192-193 (1995) 14.
[9] H. A. Lipsitt, D. Schechtman, R. E. Schafrik, Metall. Trans. A11 (1980) 1369.
[10] K. Tanaka, K. Okamoto, H. Inui, Y. Minonishi, M. Yamaguchi, M. Koiwa, Phil. Mag. A 73 (5) (1996) 1475.
[11] C.J. Boehlert, M. Zupan, D.M. Dimiduk, K.J. Hemker, Microsample tension and tension-creep testing of fully-lamellar TiAl single crystals, in: Y-W. Kim, D.M. Dimiduk, M.H. Loretto (Eds.), Gamma Titanium Aluminides 1999, TMS, Warrendale, PA, 1999, pp. 669-77.
[12] T.A. Parthasarthy and P. Karpur, Air Force Research Laboratory (1997) unpublished research.
[13] H. Inui, M.H. Oh, A. Nakamura, M. Yamaguchi, Acta Metall. Mater. 40 (1992) 3095.
[14] S. Yokoshima, M. Yamaguchi, Acta Mater. 44 (1996) 873.
[15] M. Yamaguchi, H. Inui, S. Yokoshima, K. Kishida, D.R. Johnson, Mater. Sci. Eng. A213 (1996) 25.
[16] T.A Parthasarathy, M.G. Mendiratta, D.M. Dimiduk, Acta Mater. 46 (1998) 4005.
[17] M.H. Yoo, C.L. Fu, Met. Trans A 29A (1998) 49.

Table 1: Pre- (as-cast) and post-heat treatment chemistries of Ti-46.5Al-3Nb-2Cr-0.2W (a%) used in this study.

Element	pre-HT (a%) as-cast	post-HT (a%) forged+HT
Al	46.38	46.46
Nb	3.00	2.98
Cr	2.17	2.05
W	0.20	0.21
N	0.10	0.12
C	0.05	0.05
Fe	0.05	0.05
O*	1112*	3050*
Ti	(bal)	(bal)

*wppm

Table 2: Initial elastic assumptions and FEA information.

Elastic Assumptions	FEA Information
Model assumes 90% gamma/ 10% alpha-2	42,629 nodes and 38,390 elements
$E_1 = E_2 = 1.660E5$ MPa	Primarily 8-node brick elements with 6-node wedge elements used in certain areas
$E_3 = 1.428E5$ MPa	No wedge elements in gage section
$\nu_{12} = 0.3326$	Typical mesh spacing ~ 0.15 mm
$\nu_{13} = \nu_{23} = 0.1606$	Individual grains modeled
$G_{12} = 7.167E4$ MPa	Grain boundaries and orientations from SEM
$G_{13} = G_{23} = 8.626E4$ MPa	Only last 2.5 mm of grip section modeled
	One end of specimen fixed; other end forced to remain planar with axial displacements only
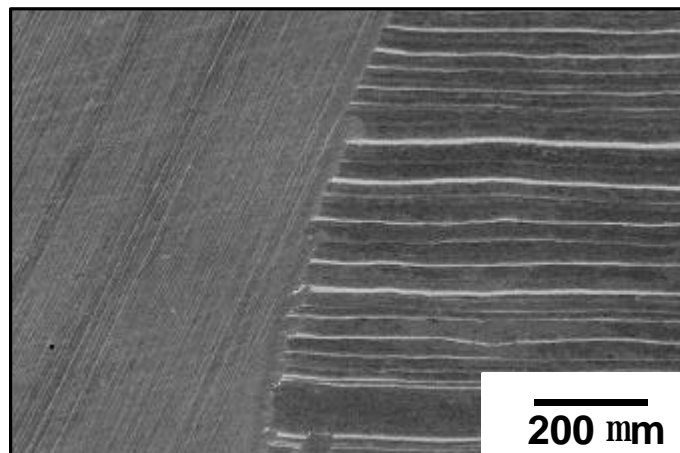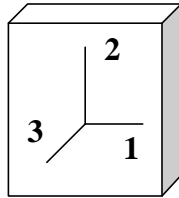
Figure 1: Microstructure of Ti-46.5Al-3Nb-2Cr-0.2W (a%) after 1400C/24hr heat treatment. (SEM BSE image).

Figure 2: Machining blank. Note the large grain size of material used in specimen manufacturing.
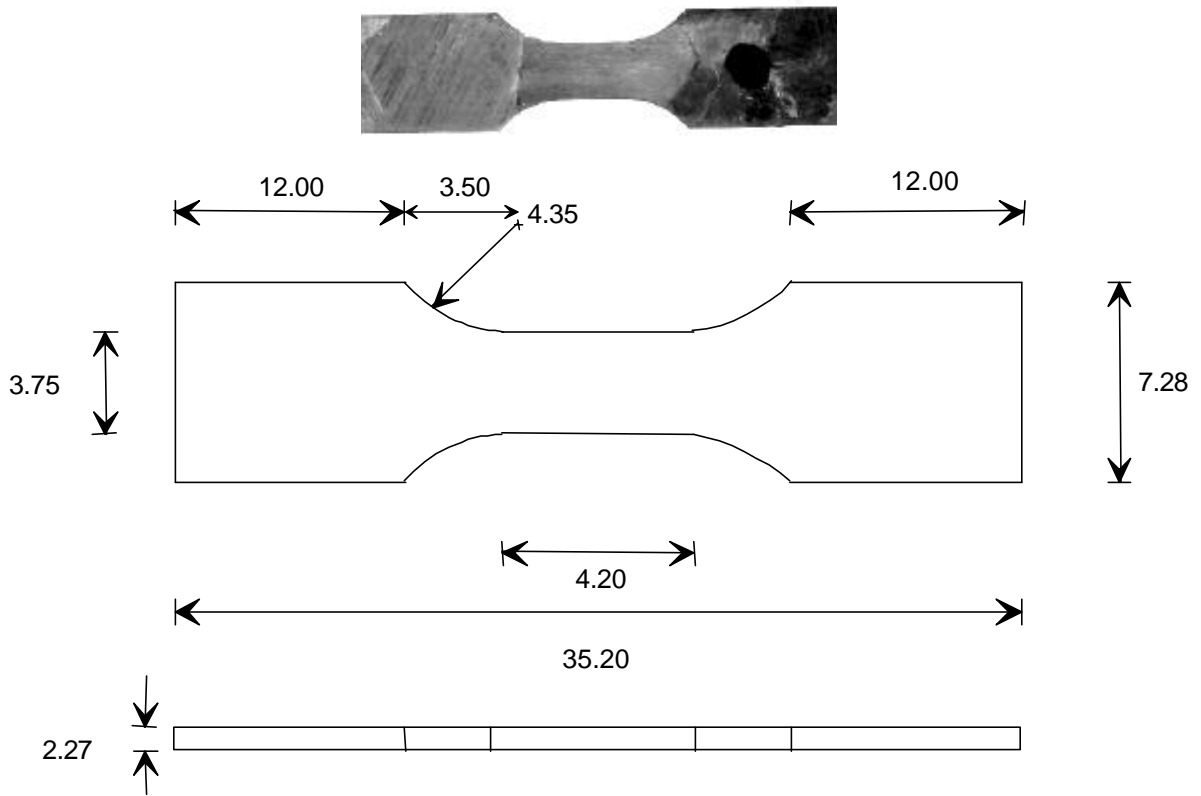
Figure 3: Photograph of specimen and specimen drawing. (note: all dimensions in millimeters)
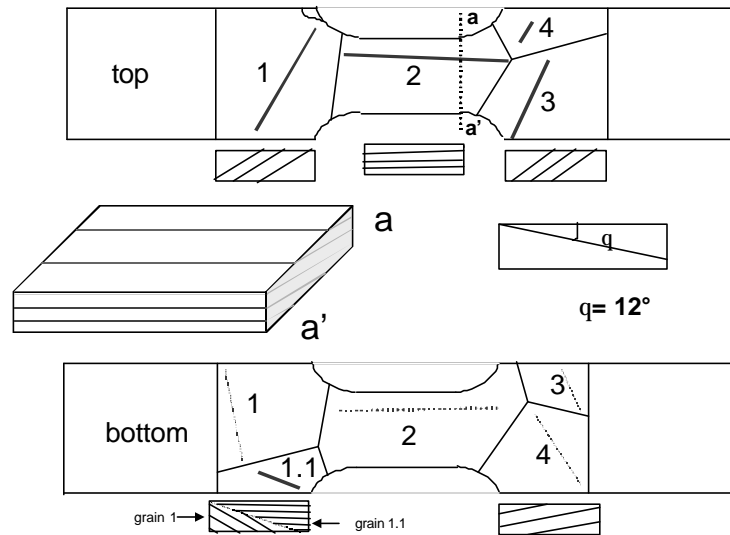
Figure 4: Schematic of lamellar orientations. Low angle boundary of gage section grain ($\theta=12°$) results in wide lamellar spacing seen in Fig. 1.
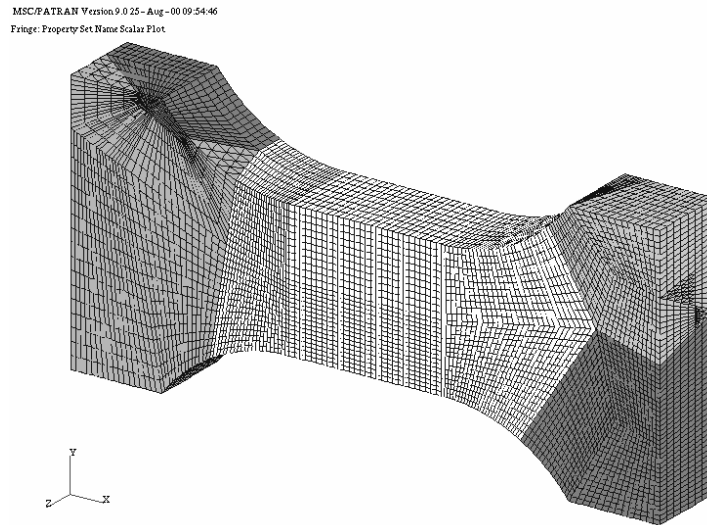
Figure 5: Finite element (FE) model of sample used in testing. The different shades of gray represent the grains in the sample. Specific properties were assigned to each grain based upon metallographically determined orientation.
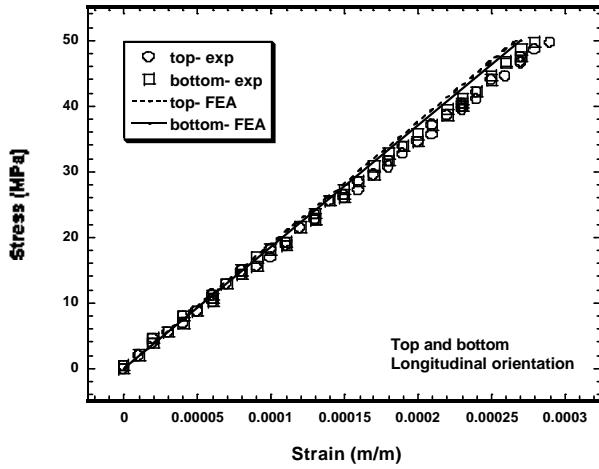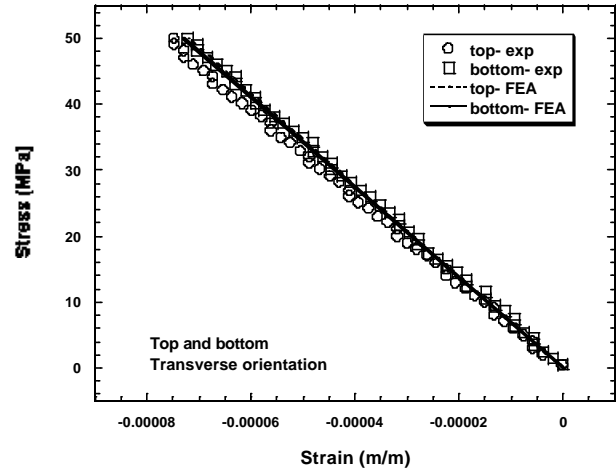
Figure 6 (a, b): Experimental and preliminary FEA results (symbols and lines, respectively): a) longitudinal top and bottom surfaces and b) transverse top and bottom surfaces.

This page intentionally left blank.

Numerical Models of Orthotropic and Lamellar Grain Structures **C2**

G.J. Frank, S.E. Olson*, R.A. Brockman

University of Dayton Research Institute, 300 College Park, Dayton, OH 45469-0110 USA

Abstract

In this paper, a method for numerically estimating localized stress concentrations that arise in materials with anisotropic crystalline grains is described. This method is used to quantify stress variations within polycrystals of γ–TiAl, a material system composed of two phases of orthotropic material - lamellar colonies of TiAl/Ti$_3$Al interspersed with small grains of pure TiAl. Effective elastic properties for the lamellar colonies are calculated from the constituent properties using a procedure developed for laminated orthotropic materials. It is postulated that the local anisotropy and differing orientations of adjacent grains of material can lead to microyielding at stresses below the mean yield strength of the material, resulting in a reduction in fatigue life for the material. The effects of local elastic anisotropy on stresses are presented as statistical variations in the stress distributions under simple states of loading. Three-dimensional and two-dimensional models are investigated.

Keywords: A. titanium aluminides based on TiAl, B. anisotropy, C. elastic properties, D. mechanical properties at ambient temperature, E. mechanical properties theory

1. Introduction

Considerable interest exists in the development of titanium aluminide (TiAl) alloys for use in high-temperature structural applications, due to their low density, strength retention at high temperature, and potential for excellent fatigue resistance. The best combination of mechanical properties is obtained with a duplex or small-grained nearly lamellar microstructure, in which a large fraction of the material exists in the form of lamellar colonies consisting of thin parallel layers of the γ (TiAl) and α_2 (Ti$_3$Al) phases. The lamellar microstructure exhibits some distinctive and complicated mechanical behavior. The survey by Appel and Wagner [1] is recommended for a thorough presentation of microstructural details, processing issues, and microstructural behavior.

Our interest in the current investigation is to quantify the stress variations within polycrystals of γ–TiAl to better understand the influence of anisotropy and relative orientation of neighboring grains on crack initiation. The length scale represented in a typical model is a millimeter or more in each direction. As such, it is impractical to model the lamellae explicitly since their thickness, which is controlled by the cooling rate during processing, is between ten nanometers and a few micrometers. However, a representation of the localized response within individual lamellar colonies is needed to obtain a meaningful picture of the variations in stress throughout the polycrystal.

Much of the detailed numerical modeling of γ–TiAl that has been performed to date focuses on the individual phases (particularly the γ phase, which represents most of the material volume), or on the study of localized response within a single lamellar colony. Fischer, Schlögl, and co-workers have developed finite element-based micromechanical models of unit cells within a lamellar colony in both two [2] and three dimensions [3-5]. These and similar models use crystal plasticity models that represent the relevant slip systems explicitly, to capture anisotropic yielding, flow, and hardening characteristics accurately. Lebensohn, et al. [6] have developed a simple model of a two-lamellae structure which represents the most important deformation mechanisms of a γ–TiAl polysynthetically twinned crystal.

Polycrystals of materials with a simpler structure at the grain level have been analyzed in two and three dimensions by numerous researchers. Early investigations such as the classical work of Taylor [7] and Bishop and Hill [8] used relatively simple kinematic constraints between adjacent grains. Most recent developments employ finite element-based models, in which fewer kinematic assumptions are required. γ–TiAl polycrystals have been analyzed in two dimensions by Dao, Kad, Asaro and co-workers in a series of pioneering papers [9-12]. Planar projections of the three-dimensional crystallography are used in these works to investigate characteristics of the localized stress field while controlling the size of the numerical system to be solved. Even in two dimensions, analyzing the individual lamellae is impractical, and the authors employ effective properties which define the plastic flow behavior of a lamellar colony as a homogeneous entity.

All of the finite element-based models of polycrystals cited above focus on the effects of plastic anisotropy. These works predict the orientation sensitivity of yielding in individual lamellar colonies, predict the overall macroscopic response at deformation states well above yield, or predict the stress state at large plastic deformation. However, γ–TiAl materials also have elastic anisotropy that induces stress variations at the grain level under elastic loading. Analytical studies by Kozaczek, et al. [13] on a random polycrystalline material have shown that grain size, shape, and orientation can create stress

concentration factors high enough to cause localized plastic microdeformation even when the polycrystalline aggregate is in the macroscopic elastic regime.

Finite element modeling of lamellar γ–TiAl grain structures utilizes continuum models in which there are abrupt changes in the properties of the continuum at the grain boundaries. Thus, the models include singularities at intersections between the grains. In all of the finite element models that simulate polycrystalline response, these singularities are neglected. In this work, we attempt to minimize the impact of the singularities by presenting our results as volume-weighted distributions of stress, rather than as stress at specific locations. Convergence studies confirm that this method of presentation provides reliable data that is unaffected by the presence of singularities at the material interfaces.

In what follows, effective elastic properties for the lamellar colonies are calculated from the constituent properties using a procedure developed for laminated orthotropic materials. Localized stress concentrations arising within polycrystals of γ–TiAl due to grain size, shape, and orientation are investigated using finite element models comprised of several hundred grains. The effects of local elastic anisotropy on stresses are presented as statistical distributions of stress data throughout the sample for a given nominal strain or applied stress. Three-dimensional and two-dimensional models are investigated.

2. Elastic Properties Identification

Our modeling approach represents individual γ grains and lamellar γ+α_2 colonies, and their orientations, explicitly. However, our main interest lies in characterizing the stress variations among grains, and the stress or strain concentrations caused by changes in stiffness and orientation from grain to grain. Models with a sufficient number of grains to eliminate boundary effects typically consist of several hundred two-dimensional or three-dimensional grains or lamellar colonies. In this setting it is impractical to model discrete lamellae, and we resort to the use of effective properties and strengths for the lamellar γ–TiAl microstructure.

Elastic properties for the γ phase are based upon measurements reported by Yoo and Fu [14] for a composition of roughly Ti-56Al. Values of the room temperature orthotropic elastic constants are listed in Table 1, in which directions (1,2,3) correspond to the [100], [010], and [001] crystal directions, respectively.

Table 1. Elastic Constants for g(TiAl)

E_1 = 140 GPa	ν_{12} = 0.284	G_{12} = 78 GPa
E_2 = 140 GPa	ν_{13} = 0.298	G_{13} = 105 GPa
E_3 = 135 GPa	ν_{23} = 0.298	G_{23} = 105 GPa

For the α_2 phase, the elastic constants again are based on measurements reported by Yoo and Fu [14]. Values of the orthotropic elastic constants are listed in Table 2. The α_2 crystal structure is hexagonal (DO_{19}); the '3' axis of the model is aligned with the 'c' crystal axis [0001], and the '1' axis is parallel to $[11\bar{2}0]$.

Table 2. Elastic Constants for a$_2$ (Ti$_3$Al)

E_1 = 125 GPa	ν_{12} = 0.454	G_{12} = 43 GPa
E_2 = 125 GPa	ν_{13} = 0.154	G_{13} = 62 GPa
E_3 = 191 GPa	ν_{23} = 0.154	G_{23} = 62 GPa

Effective room temperature elastic constants for lamellar γ–TiAl have been computed using the preceding elastic constants for each of the constituent materials. Constants for the lamellar material have been computed using a method developed for laminated orthotropic materials by Pagano [15]. A summary of effective orthotropic constants (in GPa) calculated for various proportions of α_2 and γ phases appears in Table 3. Orientation definitions for the elastic constants in Table 3 are aligned with the α_2 crystal structure.

40

Table 3. Effective Elastic Properties of Lamellar Colonies

Property	α_2:γ Ratio					
	1:1	**1:2**	**1:4**	**1:5**	**1:10**	**1:20**
E_1	160.2	171.4	179.7	182.0	187.0	189.6
E_2	160.2	171.4	179.7	182.0	187.0	189.6
E_3	206.4	211.5	215.5	216.6	218.9	220.2
G_{23}	64.6	65.5	66.3	66.5	66.9	67.1
G_{13}	64.6	65.5	66.3	66.5	66.9	67.1
G_{12}	59.4	64.7	69.3	70.3	72.6	74.1
ν_{23}	0.155	0.152	0.149	0.148	0.146	0.144
ν_{13}	0.155	0.152	0.149	0.148	0.146	0.144
ν_{12}	0.351	0.322	0.303	0.297	0.284	0.279

For the two-phase lamellar γ–TiAl, the crystallographic alignment at the γ-α_2 interfaces are $(111)_{\gamma}\| (0001)_{\alpha2}$ and $[1\bar{1}0]_{\gamma}\| [11\bar{2}0]_{\alpha2}$. To utilize the method described by Pagano, lamellar configurations have been simulated using alternating layers of α_2 and γ. Although actual lamellar γ–TiAl has multiple layers of γ phase for each layer of α_2 [16], numeric simulations show that models with single alternating layers provide results that are statistically indistinguishable from models with multiple layers of γ phase for each layer of α_2. Within each configuration, orientations for individual layers are assigned randomly from the range of possible orientations, and the elastic constants of the constituent materials are transformed into the appropriate orientations.

Values listed in Table 3 for each proportion of α_2:γ are the averages of results from three lamellar configurations containing 500 layers per configuration. Even with this large number of layers, computed values among the three configurations for any given α_2:γ ratio deviate by up to 2.2% from the average for that α_2:γ ratio. Comparisons with tensile tests on dogbone specimens dominated by a single lamellar colony (having an α_2:γ ratio of 1:9) in the gage section indicate that the elastic constants in Table 3 are a good approximation to the measured elastic constants for lamellar TiAl [17].

3. Modeling

The primary purpose of this paper is to examine stress distributions that can occur in polycrystalline structures and to investigate the capability of models, utilizing different degrees of refinement or using a two-dimensional representation for the microstructure, to accurately predict the stress variations. The structures considered here consist of both lamellar colonies and equiaxed γ (TiAl) grains, with an assumed volume fraction of lamellar γ–TiAl of 0.96. All of the analyses are confined to the elastic regime. Results for some three-dimensional models in which plasticity is considered are reported in a paper by Brockman [18].

For all of the models described here, elastic constants for the γ grains are those listed in Table 1. The constants selected for the lamellar colonies are listed in Table 4. Although our estimates for the effective properties include data from several sources and involve some level of approximation, these values are thought to be representative of the level of anisotropy present in the lamellar colonies. The results, presented as a deviation from the volumetric distribution of stress that would occur for an isotropic material, can be considered representative of the level of stress variation that occurs for material composed of mostly lamellar γ–TiAl.

Table 4. Elastic Constants Used for Lamellar Colonies in Finite Element Models

$E_1 = 164$ GPa	$\nu_{12} = 0.19$	$G_{12} = 82$ GPa
$E_2 = 164$ GPa	$\nu_{13} = 0.31$	$G_{13} = 82$ GPa
$E_3 = 148$ GPa	$\nu_{23} = 0.31$	$G_{23} = 68$ GPa

Three-dimensional models

Filling three-dimensional space with a regular pattern of two grain types significantly restricts the number of possible geometric configurations available. The selected geometric configuration consists of cubes, which represent the γ grains, alternating with truncated rhombic dodecahedra, which represent the lamellar colonies. Fig. 1 shows a finite element model of a polycrystal composed of an equal number of lamellar colonies and equiaxed γ grains. The model contains 256 colonies

and 256 grains, with the orientation of each grain being randomly generated. Fringe values in Fig. 1 depict the orientation of each grain with respect to the loading direction, which is parallel to the global 'x' axis for the case shown. Symmetry conditions are applied on the three rearward facing surfaces of the model. The remaining three faces are constrained to remain planar, but may expand or contract in response to a tensile loading on any one of the faces.
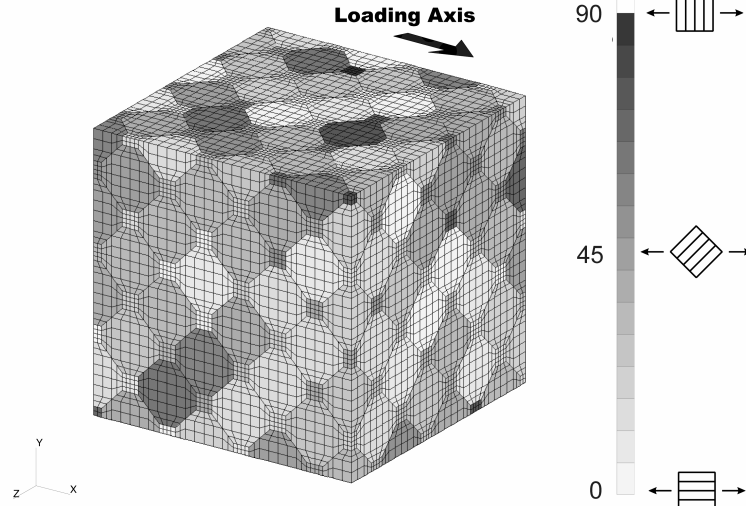

Fig. 1. Baseline 3D model using cubic packing scheme for the lamellae.

For the purpose of evaluating the effects of variations in model refinement, stress distributions have been computed for the various stresses of interest. The stress distributions indicate the volume of material above a specific fraction of the applied tensile stress, $s_{applied}$. For comparing models, we look at three stress components: s_{axial}, which is the global stress in the direction of the applied tensile loading; s_{norm}, which is the stress normal to the lamellae within each colony; and, t_{rs}, which is the resolved shear on lamellar planes.

In the limit, as the elastic constants of the material approach those of an isotropic material, the volume of material V for which the stress ratio is above a specific value f can be specified by explicit relations. For the uniaxial loading state defined above, these relations are:

$$V\bigg|_{\frac{s_{axial}}{s_{applied}}>f} = \begin{cases} 1 \text{ if } f < 1 \\ 0 \text{ if } f > 1 \end{cases} \tag{1}$$

$$V\bigg|_{\frac{s_{norm}}{s_{applied}}>f} = 1 - \cos\left[\frac{1}{2}\cos^{-1}(2f-1)\right] \tag{2}$$

$$V\bigg|_{\frac{t_{rs}}{s_{applied}}>f} = \cos\left[\frac{1}{2}\sin^{-1}(2f)\right] - \sin\left[\frac{1}{2}\sin^{-1}(2f)\right] \tag{3}$$

In all of the following comparisons, stress distributions computed using the preceding relations are overlaid on the results from the polycrystal models, thus allowing the stress variation that is due to the orthotropy of the material to be discerned from the distribution that is simply due to the orientation of the grain relative to the direction of loading.

Finite element analyses of the three-dimensional (3D) models have been performed with the ABAQUS code using 8-node hexahedral elements. The "baseline 3D model" shown in Fig. 1 has approximately 181,000 degrees of freedom (DOFs) and is of a size for which plastic deformation simulations can be analyzed in a practical time using the current generation of computers. To determine the effects of boundary conditions on the stress distributions, a model using more than five times as many colonies as that of the baseline 3D model has been developed, as shown in Fig. 2. Also, for evaluating the effects of mesh refinement, a model with eight times as many elements but the same number of colonies as the baseline 3D model has been developed, as shown in Fig. 3. The number of DOFs in these models (1.1 and 1.4 million DOFs for Figs. 2 and 3, respectively) and the lack of sparsity in the matrices make the models shown in Figs. 2 and 3 rather impractical for plasticity calculations at the present time.
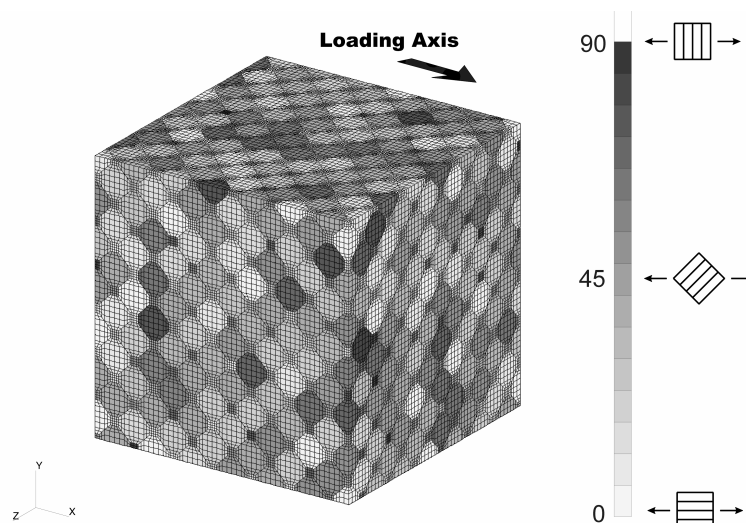
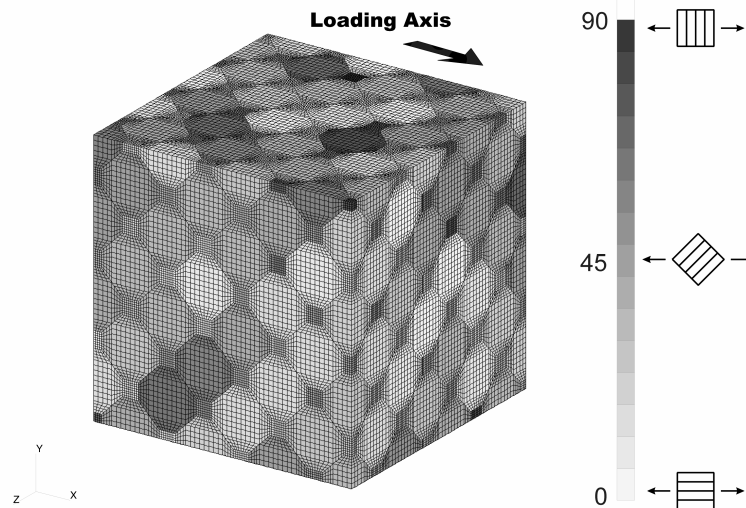Fig. 2. 3D model with significantly larger number of grains.

Fig. 3. 3D model with significant mesh refinement.

The response to axial loading has been used to determine effective elastic constants for the material. For all of the models shown in Figs. 1 through 3, the elastic constants are: E=178 GPa, G=72 GPa, and ν=0.23. These values have been repeatably computed within 1.5% by all of the cases evaluated.

Distributions of axial stress for the baseline 3D model are shown in Fig. 4, where the curves are average distributions from nine cases. The nine cases have been generated using three models with randomly defined crystal orientation, with each of the three models loaded in each of three orthogonal directions. The γ grains show a larger variation from the mean stress, and also have net mean stress that is higher than the average axial stress (as indicated by the fact that more than 50% of the γ grain volume is above an axial stress ratio of 1.0). The larger variation occurs for the γ grains because their moduli deviate more from the average values of the polycrystalline system than do those of the lamellar colonies.

To assess the impact of boundary conditions on the stress distributions, analyses have been run on a model with over five times as many grains as were used in the baseline 3D model. Fig. 5 compares the distribution of stress normal to the lamellae in the lamellar colonies for the baseline 3D model with the distribution for the model with more than five times as many grains (shown in Fig. 2). The two stress distribution curves generated from the finite element results represent the average of the analyses for multiple cases. Error bars, which show ±1 standard deviation from the mean, indicate the variation between cases at discrete locations on the curves. Applying a two-sample student's t-test with unequal variances to the two distributions indicates that the distributions from the models are statistically similar. Comparison with the isotropic material curve shows that the orthotropic lamellar colonies have a much smaller volume of material with a high stress normal to the lamellae than would occur for a material with more nearly isotropic properties.
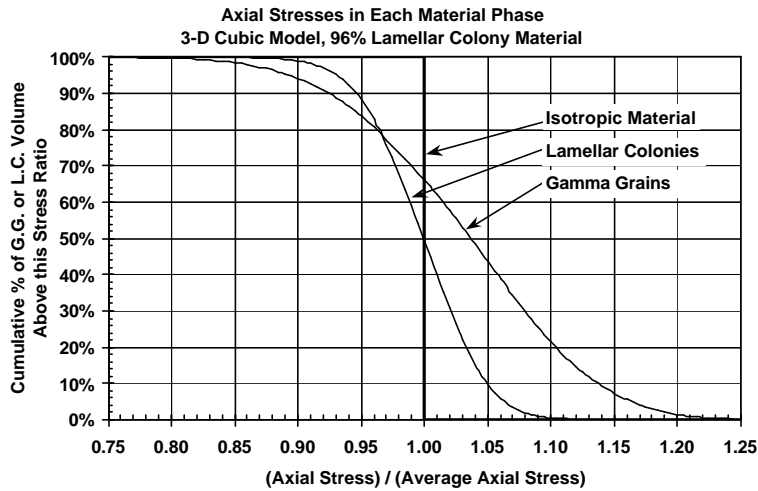
Axial Stresses in Each Material Phase
3-D Cubic Model, 96% Lamellar Colony Material

Fig. 4. Representative distribution of the stresses, aligned with the loading axis, as predicted by all three dimensional models.

Stress Normal to Lamella in Lamellar Colonies
3-D Model, 96% Lamellar Colony Material

Fig. 5. Distribution of the stresses, normal to the lamellae, in the lamellar colonies for the baseline 3D model and model with a significantly larger number of grains.

Fig. 6 shows data similar to that for Fig. 5, except that the distributions are for maximum transverse shear on the lamella. Applying a t-test to the two distributions shows that the distributions are statistically dissimilar at a 95% confidence level over the range $0.39 < \left(t_{rs} / s_{applied} \right) < 0.54$. However, simple observation of the distributions from the models shows that they are far more similar to each other than they are to the isotropic material curve. The distributions for the lamellar colonies show that at least 25% of the material volume has $t_{rs} / s_{applied} > 0.5$, which is above the maximum possible for an isotropic material.

44
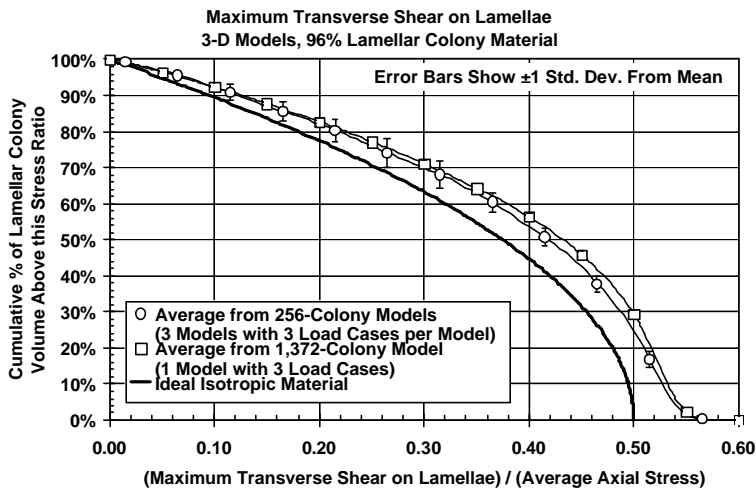
Fig. 6. Distribution of the resolved shear stresses in the lamellar colonies for the baseline 3D model and model with a significantly larger number of grains.

To assess the impact of element refinement on the stress distributions, analyses have been run on a model with eight times as many elements as were used in the baseline 3D model. For this comparison, the grain sizes and orientations are the same between the models, and only the element refinement is changed. Figs. 7 and 8 show data similar to that shown in Figs. 5 and 6, except that the comparison is for the baseline 3D model with the highly refined model shown in Fig. 3. High variability, as signified by relatively broad error bars, is due to the limited number of cases analyzed. Based on a student's t-test at a 95% confidence level, the stress distributions for the two models are statistically similar.

The key point demonstrated by these three-dimensional models is that averaging the results from relatively coarse finite element models with limited numbers of grains results in stress distributions that are very similar to those developed by models with far more grains or element refinement. Further studies are necessary to determine if similar coarse models can be used for analyses of problems in which plastic deformation is to be considered.
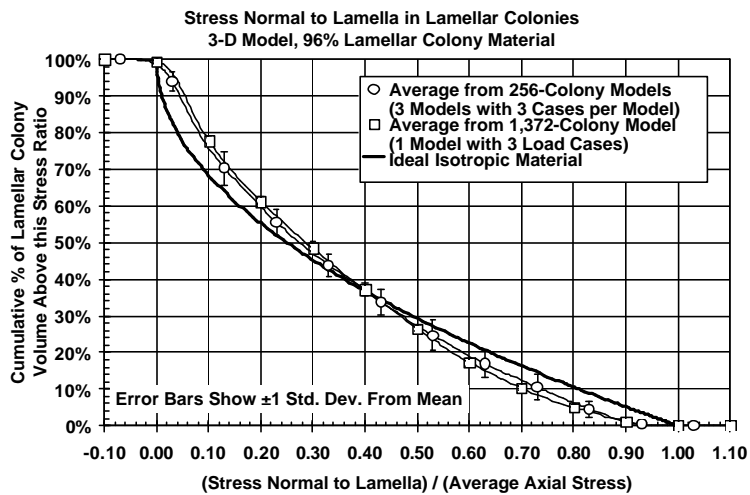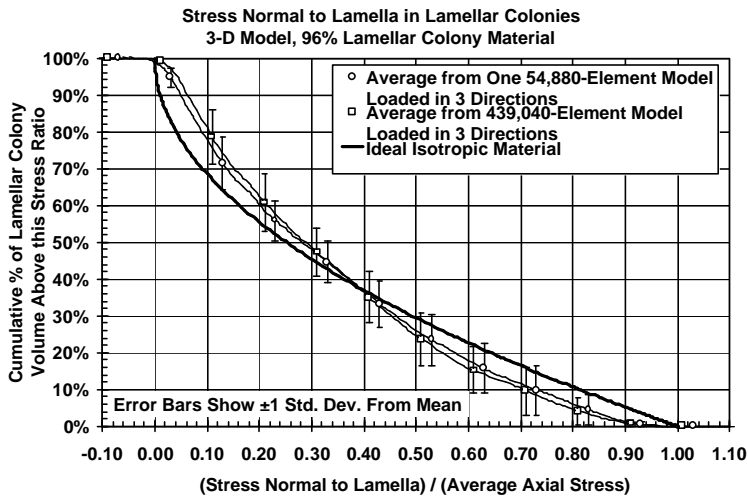

Fig. 7. Distribution of the stresses, normal to the lamellae, in the lamellar colonies for the baseline 3D model and model with significant mesh refinement.

Maximum Transverse Shear on Lamellae
3-D Models, 96% Lamellar Colony Material

Error Bars Show ±1 Std. Dev. From Mean

Cumulative % of Lamellar Colony Volume Above this Stress Ratio (y-axis)

○ Average from One 54,880-Element Model Loaded in 3 Directions
□ Average from One 439,040-Element Model Loaded in 3 Directions
— Ideal Isotropic Material

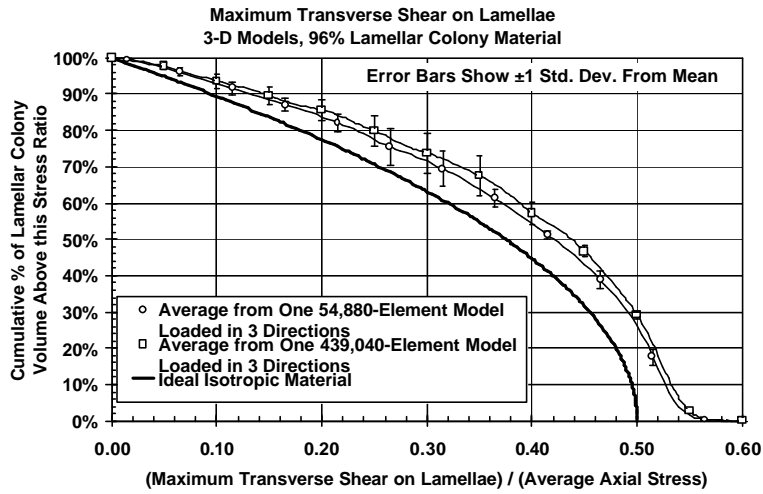**(Maximum Transverse Shear on Lamellae) / (Average Axial Stress)** (x-axis)

Fig. 8. Distribution of the resolved shear stresses in the lamellar colonies for the baseline 3D model and model with significant mesh refinement.

Two-dimensional models

Two-dimensional models have been analyzed to determine if simpler models can accurately capture the stress variation effects seen in the 3D models and to evaluate the effects of variations in grain size and shape. Filling two-dimensional space with a regular pattern of two grain types offers additional geometric configurations not possible in the 3D models. One possible geometric configuration represents the lamellar colonies with squares and uses smaller squares, inset and rotated by 45°, to represent the γ grains. This configuration is illustrated in Fig. 9. Another configuration represents the lamellar colonies with hexagons, with small inset triangles representing the γ grains. This latter configuration, illustrated in Fig. 10, is similar to that used by Kad, Dao, and Asaro [9], albeit with triangles used here in place of their squares and diamonds. Fringe values in Figs. 9 and 10 depict the orientation of each grain with respect to the loading direction, which is parallel to the global 'x' axis for the cases shown. Symmetry conditions are applied on two adjacent edges of the model. The remaining two edges are constrained to remain planar, but may expand or contract in response to a tensile loading on either of the faces. Plane strain conditions are assumed for the direction normal to the plane of the model.
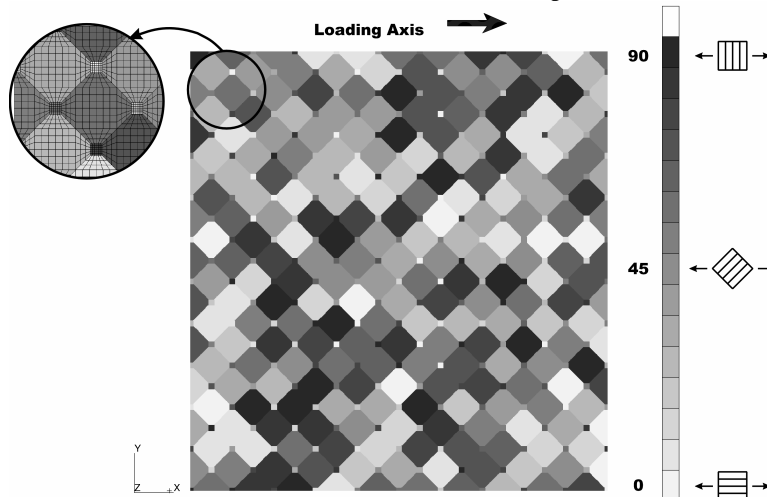

Fig. 9. Two dimensional finite element model using cubic packing scheme for the lamellae.
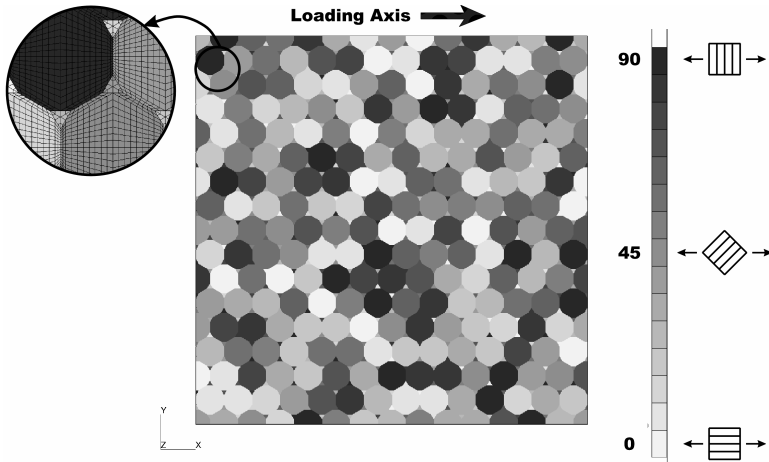
Fig. 10. Two dimensional finite element model using hexagonal packing scheme for the lamellae.

As was done for the three-dimensional models, the stress distributions are compared with the corresponding distributions for an isotropic material. In the limit, as the elastic constants of the material approach those of an isotropic material, the volume of material V for which the stress ratio is above a specific value f can be specified by explicit relations. For an isotropic material with the plane strain loading condition defined above, these relations are:

$$V\Big|_{\frac{s_{axial}}{s_{applied}}>f} = \begin{cases} 1 \text{ if } f < 1 \\ 0 \text{ if } f > 1 \end{cases} \tag{4}$$

$$V\Big|_{\frac{s_{norm}}{s_{applied}}>f} = \frac{1}{p}\cos^{-1}(2f-1) \tag{5}$$

$$V\Big|_{\frac{t_{rs}}{s_{applied}}>f} = 1 - \frac{2}{p}\sin^{-1}(2f) \tag{6}$$

To evaluate the effects of variability in colony size, finite element models have been developed that reproduce some of the size variability observed in nearly-lamellar γ–TiAl structures. Figs. 11 and 12 show two such models. Fig. 11 shows a model with no variation in grain size, while Fig. 12 shows a model in which the variation in grain size is specified as a random value with a standard deviation of 50% of the mean grain radius. These models are initially gridded with a uniform mesh of quadrilateral elements. Specific locations of lamellar colony region centroids are prescribed along with a radius value for each lamellar colony region. A sorting algorithm is used to assign elements to the region for which the distance between the element centroid and the region's centroid, normalized by the region's radius, is a minimum. γ grains, with varying radii, are seeded at the boundaries of the lamellar colony regions and the sorting algorithm is applied a second time to assign elements to the lamellar colonies or the γ grains. Quadrilateral elements are split into triangles in selected areas to minimize the jaggedness of the mesh. Although this scheme for model generation does not mimic the process by which grains are formed, it does result in a model that simulates two phases of material with randomly distributed crystalline size and shape.

Analyses of the two-dimensional (2D) models have been performed with the ABAQUS code using four-node quadrilateral elements, assuming plain strain conditions. Three-node triangular elements are also used in the γ phase for the model based on hexagonal-shaped lamellar colony regions (Fig. 10) and along some grain boundaries in the random grain size meshes (Figs. 11 and 12). The properties are specified such that the '3' direction of the grains lay in the X-Y plane of Figs. 9 through 12, with a random angular rotation assigned for each grain's orientation. For each of the 2D models, six cases have been analyzed. The six cases use three models with randomly defined crystal orientation (and possibly size), with each of the three models loaded in each of two orthogonal directions.

47
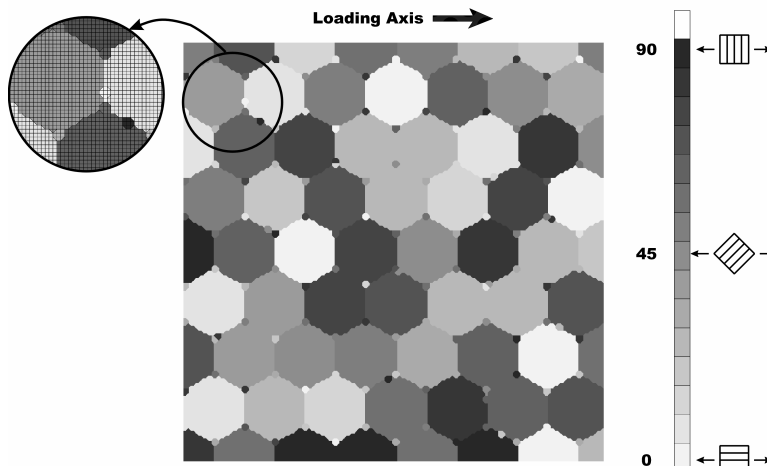
Fig. 11. Two dimensional finite element model using random grain generation with no variation in grain size.
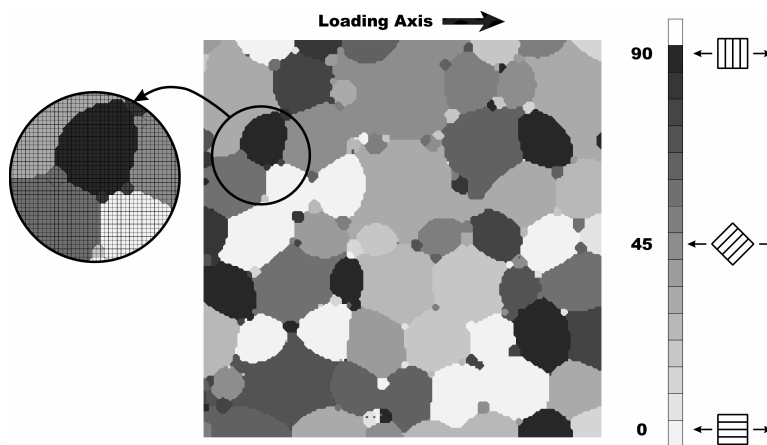
Fig. 12. Two dimensional finite element model using random grain generation with a 50% standard deviation in grain size.

Distributions of axial stress for the cubic 2D model are shown in Fig. 13. Nearly identical axial stress distributions are computed for all of the models shown in Figs. 9 through 12. The γ grains show a larger variation from the mean stress than do the lamellar colony regions. The larger variation occurs for the γ grains because their moduli deviate more from the average values of the polycrystalline system than do those of the lamellar colonies. Unlike the results for the 3D models, the γ grains have a net mean stress that is very close to the average axial stress. This difference between two and three-dimensional models is most likely due to the fact that the local '3' direction for all of the crystals is constrained to lie in the X-Y plane for the 2D models.

Axial Stress Distribution
2-D Cubic Model, 96% Lamellar Colony Material

Fig. 13. Representative distribution of the stresses, aligned with the loading axis, as predicted by all two dimensional models.

       The effect of variations in grain geometry has been assessed by comparing stress distributions from the cubic 2D model wit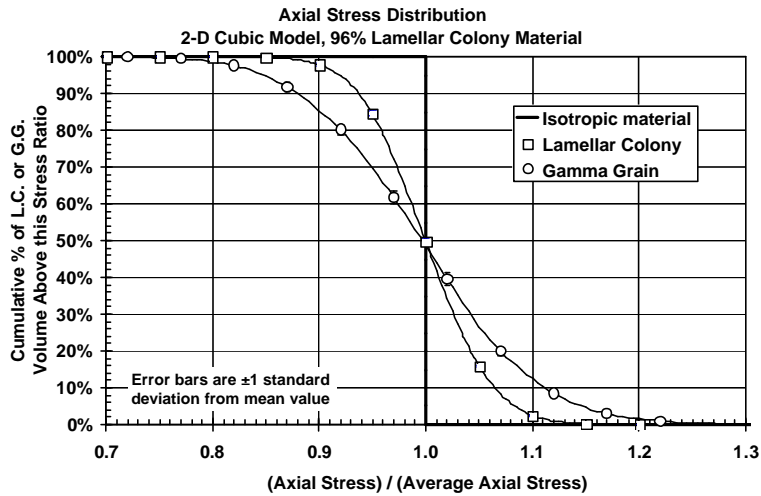h results from the hexagonal 2D model. Fig. 14 compares the distribution of stress normal to the lamellae in the lamellar colonies for these two cases. The two stress distribution curves generated from the finite element results represent the average of the analyses for six cases. Error bars, which show ±1 standard deviation from the mean stress, indicate the variation between cases at discrete locations on the curves. Applying a two-sample student's t-test with unequal variances to the two distributions indicates that the distributions from the models are statistically similar. Fig. 15 shows the distributions for maximum transverse shear on the lamella. Applying a t-test to the two distributions shows that they are statistically dissimilar at a 95% confidence level over the range $0.20 < \left(t_{rs}/s_{applied} \right) < 0.40$. However, the two models agree closely

for high stress levels, with both models indicating that approximately 20% of the material volume has $t_{rs}/s_{applied} > 0.5$.
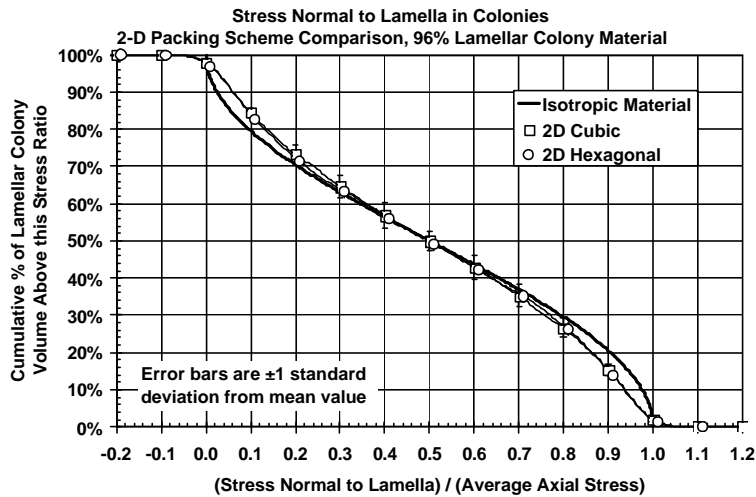
49

Stress Normal to Lamella in Colonies
2-D Packing Scheme Comparison, 96% Lamellar Colony Material

Fig. 14. Distribution of stresses, normal to the lamellae, in the lamellar colonies for 2D models with cubic and hexagonal packing schemes for the lamellae.

Maximum Transverse Shear on Lamellar Colonies
2-D Model Comparison, 96% Lamellar Colony Material

Fig. 15. Distribution of resolved shear stresses in the lamellar colonies for 2D models with cubic and hexagonal packing schemes for the lamellae.

The differences between the hexagonal and cubic modeling schemes indicate that grain shape does affect the distribution of stress in the grains. However, the difference may possibly be influenced by the use of triangular elements in the mesh. Fig. 16 compares distributions for maximum transverse shear computed using the 2D hexagonal mesh with 91,392 elements (shown in Fig. 10) with data from a coarser mesh of 21,313 elements (not shown). The coarser mesh has only triangular elements in regions representing γ grains. The triangular elements exhibit some degree of shear locking, resulting in differences in stress distributions observed with increasing mesh refinement.
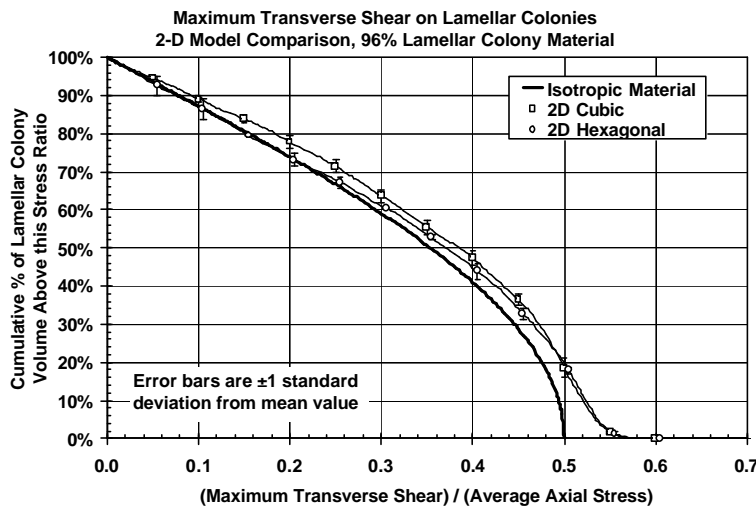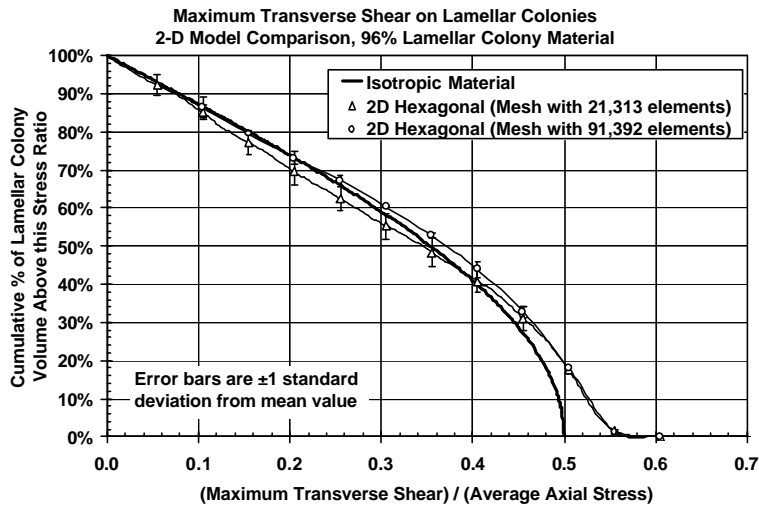
Fig. 16. Distribution of resolved shear stresses in the lamellar colonies for 2D models with hexagonal packing schemes for the lamellae and varying levels of mesh refinement.

The effect of variations in grain size on stress levels has been assessed by comparing stress distributions from random models (shown in Figs. 11 and 12) having size distributions with standard deviations of 0% and 50% of the mean size. Fig. 17 compares the distribution of stress normal to the lamellae in the lamellar colonies for these two cases, while Fig. 18 compares the distribution of maximum transverse shear on the lamella. Applying a two-sample student's t-test to the data shown in Figs. 17 and 18 indicates the distributions from the models are statistically similar. This result suggests that variations in stress due to size variability alone are not the principal cause for inducing γ–TiAl material with high variability in grain size to fail at low strains.

Generally speaking, the deviations of the stress distributions for the 2D models from the variation in stress caused purely by orientation (as shown by the distribution for an isotropic material) are smaller than the deviations shown for the 3D models. This result may be primarily attributed to the 2D restriction that one of principal axes of the crystalline system must be parallel to the direction of the plain strain axis. While the degree of variability for the elastic analyses is not large, this factor may become very important for plasticity analyses, where the stress distributions for the orthotropic crystals deviate far more significantly from the stress distributions for an isotropic material.
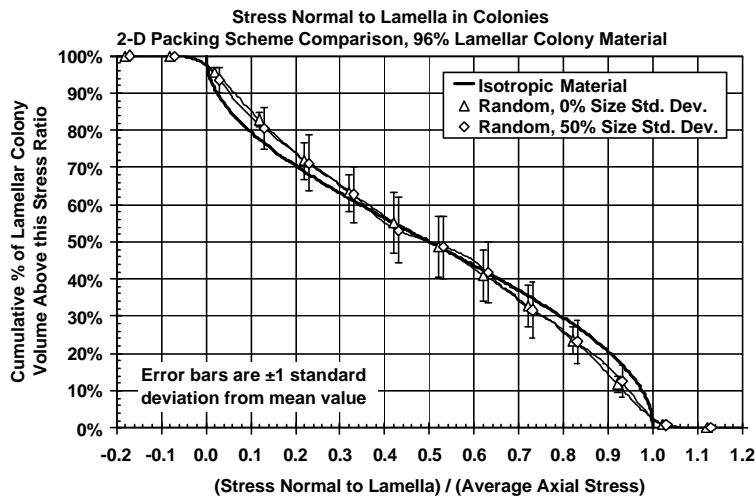

Fig. 17. Distribution of stresses, normal to the lamellae, in the lamellar colonies for 2D models with no variation in grain size and 50% standard deviation variation in grain size.

51

Maximum Transverse Shear on Lamellar Colonies
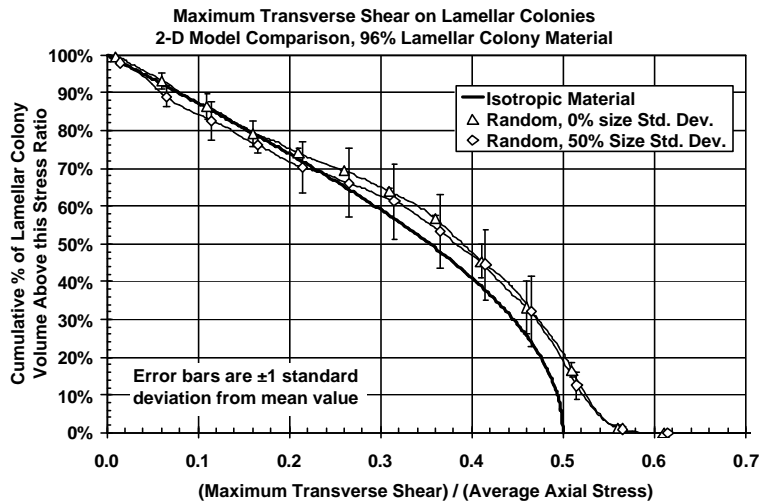**2-D Model Comparison, 96% Lamellar Colony Material**

Fig. 18. Distribution of resolved shear stresses in the lamellar colonies for 2D models with no variation in grain size and with 50% standard deviation variation in grain size.

4. Conclusions

A method for evaluating the effects of stress concentrations that occur at the grain level in polycrystalline materials composed of anisotropic crystals has been presented. The method is based on comparisons of the volumetric distributions of specific components of stress. The method has been applied in the elastic regime for a γ–TiAl material system composed of two phases of orthotropic material, lamellar colonies of TiAl/Ti$_3$Al interspersed with small grains of pure TiAl. Requirements on model size and refinement necessary to produce reasonable statistical information have been investigated. The method has been applied using finite element representations of crystalline structures in two and three dimensions. The results indicate that three-dimensional models of only moderate size and refinement, for which analyses in the plastic regime may be performed in a reasonable time with the current generation of supercomputers, can sufficiently capture the stress distributions as well as models of much larger size or higher refinement. Two-dimensional models using a random size variation of the crystals show that size variation does not significantly affect the stress distribution within the material. Stress distributions predicted by two-dimensional models using various geometric representations for shape of the lamellar colony phase compare well with each other, but show less deviation from the distributions of an isotropic material than do the stress distributions generated by the three-dimensional models.

Acknowledgements

References

[1] Appel F Wagner R. Mat Sci Eng 1998;R22:187.
[2] Parteder E Siegmund T Fischer FD Schlögl S. Mat Sci Eng 1996;A192-193:149.
[3] Schlögl SM Fischer FD. Comp Mat Sci 1996;7:34.
[4] Schlögl SM Fischer FD. Phil Mag A 1997;75:621.
[5] Schlögl SM Fischer FD. Mat Sci Eng 1997;239-240:790.
[6] Lebensohn R Uhlenhut H Hartig C Mecking H. Acta Mater 1998;46:4701.
[7] Taylor GI. J Inst Metals 1938;62:307.
[8] Bishop JFW Hill R. Phil Mag 1951;42:1298.
[9] Kad BK Dao M Asaro RJ. Phil Mag A 1995;71:567.
[10] Kad BK Dao M Asaro RJ. Mat Sci Eng 1995;192-193:97.

[11] Kad BK Asaro RJ. Phil Mag A 1997;75:87.
[12] Dao M Kad BK Asaro RJ. Phil Mag A 1996;74:569.

[13] Kozaczek KJ Petrovic BG Ruud CO McIlree AR. Modeling of stress distributions on the microstructural level in Alloy 600. In: PVP-Vol. 306, Fatigue and Crack Growth: Environmental Effects, Modeling Studies, and Design Considerations, ASME, 1995;223.

[14] Yoo MH Fu CL. Met Mat Trans 1998;29A:49.

[15] Pagano NJ. Exact moduli of anisotropic laminates. In: G. P. Sendeckyj, editor. Mechanics of Composite Materials, Academic Press, New York, 1974.

[16] Parthasarathy TA Mendiratta MG Dimiduk DM. Acta Mater 1998;46:4005.

[17] Porter WJ. Private Communication. University of Dayton Research Institute, 2000.

[18] Brockman RA. Submitted to Int J Plasticity, 2000.

This page intentionally left blank.

Analysis of elastic-plastic deformation in TiAl polycrystals C3

Robert A. Brockman

University of Dayton Research Institute, Dayton, OH 45469-0110 USA

Abstract

A computational model is described for analyzing stress variations within polycrystals of γ-TiAl, including the effect of anisotropic yielding and small-scale plastic flow. Interlamellar (soft mode) slip behavior is controlled by a separate collection of slip systems whose properties are derived from measurements on polysynthetically twinned (PST) specimens. When used to represent several hundred randomly oriented material grains, the model provides distributions and statistical data about the local stress, strain, and plastic deformation resulting from a prescribed macroscopic loading.

Keywords: Constitutive models; Crystal plasticity; Polycrystals; Intermetallics

1. Introduction

Considerable interest exists in the development of titanium aluminide (TiAl) alloys for use in high-temperature structural applications, due to their low density, strength retention at high temperature, and potential for excellent fatigue resistance. The best combination of mechanical properties for many purposes is achieved with a small-grained lamellar microstructure, in which the material is arranged in lamellar colonies consisting of thin parallel layers of the γ (TiAl) and α_2 (Ti$_3$Al) phases. A related nearly lamellar microstructure containing a small fraction of equiaxed gamma grains provides improved ductility. The lamellar microstructure exhibits some distinctive and complicated mechanical behavior, which we discuss in more detail below. The survey by Appel and Wagner (1998) is recommended for a thorough presentation of microstructural details, processing issues, and microstructural behavior.

Our interest in the current investigation is to quantify the stress variations within polycrystals of γ-TiAl, to better understand the influence of factors such as anisotropy, localized plastic flow, and relative orientation of neighboring grains on crack initiation. The length scale represented in a typical stress model is a millimeter or more in each direction. As such, it is impractical to model the lamellae explicitly: their thickness, which is controlled by the cooling rate during processing, is between ten nanometers and a few micrometers. However, a representation of the localized response within individual lamellar colonies is needed to obtain a meaningful picture of the variations in stress throughout the polycrystal.

Much of the detailed numerical modeling of γ-TiAl that has been performed to date focuses on the individual phases (particularly the γ phase, which represents most of the material volume), or on the study of localized response within a single lamellar colony. Fischer, Schlögl, and co-workers have developed finite element-based micromechanical models of unit cells within a lamellar colony in both two (Parteder, 1995) and three dimensions (Schlögl, 1996, 1997a,b). These and similar models use crystal plasticity models that represent the relevant slip systems explicitly, to capture anisotropic yielding, flow, and hardening characteristics accurately. Lebensohn, et al. (1998) have developed a simple model of a two-lamellae structure which represents the most important deformation mechanisms of a γ-TiAl PST crystal, and which may be extended to analyze polycrystal behavior through a mean-field approach.

Polycrystals of materials with a simpler structure at the grain level have been analyzed in two and three dimensions by numerous researchers. Early investigations such as the classical work of Taylor (1938) and Bishop and Hill (1951) used relatively simple kinematic constraints between adjacent grains. Most recent developments employ finite element-based models, in which fewer kinematic assumptions are required, although the correct representation of interactions at the grain boundaries remains a challenging problem (Harder, 1999). Marketz et al. (1999) have performed finite element analyses of near-γ TiAl polycrystals with a small number of grains, and suggest that an effective property model based on Hill's criterion might be used to represent the fully lamellar microstructure.

TiAl polycrystals have been analyzed in two dimensions by Dao, Kad, Asaro and co-workers in a series of pioneering papers (Kad, 1995a,b, 1997; Dao, 1996). Planar projections of the three-dimensional crystallography are used in these works to investigate characteristics of the localized stress field while controlling the size of the numerical system to be solved. Even in two dimensions, analyzing the individual lamellae is impractical, and the authors employ effective properties which define the plastic flow behavior of a lamellar colony as a homogeneous entity. Similar calculations in three dimensions, which have not been reported to date, are the focus of this paper.

The interlamellar (soft mode) and translamellar (hard mode) deformation of lamellar colonies has been studied most extensively by experiments using PST (polysynthetically twinned) single crystals. While it seems clear that scale-related constraints are important in determining the yield strength in various orientations, the relative importance of lamellar spacing, lamellar colony size, and domain size within individual lamellae as scale parameters remains an open question. Appel and Wagner (1998) summarize much of the work directed toward defining Hall-Petch relationships for the strength of PST crystals.

It is interesting that a complete and definitive explanation of the mechanisms at work in the distinctive soft-mode yielding behavior has not emerged. Over a broad range of intermediate orientations, slip appears to occur almost exclusively on the (111) planes of the γ lamellae; that is, parallel to the interlamellar boundaries. However, the strengths associated with this mode of deformation are significantly lower than one expects based on the measured properties of the individual material phases (Figure 1).
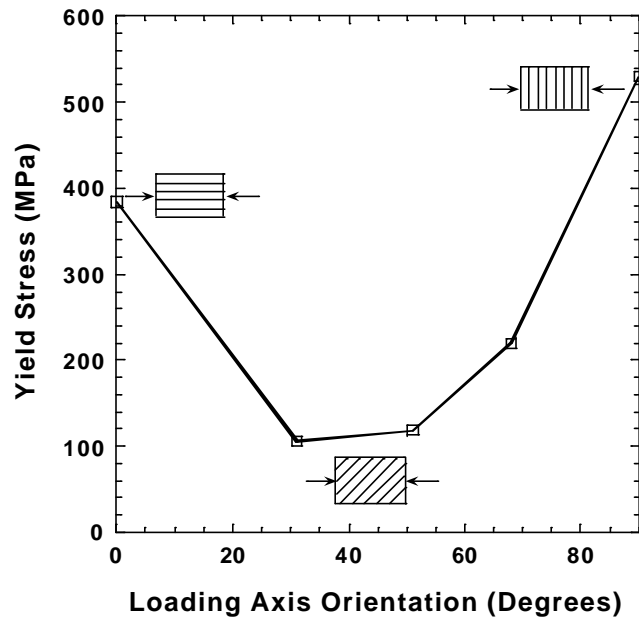

Figure 1. Dependence of yield strength on lamellar orientation;
PST data in compression taken from Inui, et. al. (1992).

One complicating factor is the wide variety of material variants for which data are reported in the materials science literature. Apparent disparities between the strengths reported for individual material phases and the soft-mode behavior of PST specimens may be the result of complicated microscale deformation mechanisms, or of actual variations in material properties related to processing and other sources. It is difficult, for example, to produce material samples of pure γ-TiAl with composition similar to that which occurs in the lamellar form.

Hazzledine and Kad (1995) offer a detailed discussion of the yield anisotropy of the lamellar microstructure, noting that dislocation pileups occur at domain boundaries in the soft mode and at lamellar boundaries in the hard mode. However, as noted by Hazzledine, it has not been possible experimentally to demonstrate whether the soft mode deformation is distributed throughout the lamellae or concentrated in the lamellar interfaces. Numerical studies with two-dimensional models by Kad, Dao and Asaro (1995, 1996) exhibit very high concentrations of hydrostatic stress at grain boundaries between lamellar colonies with dissimilar orientations, leading them to suggest that constraints imposed by neighboring

crystals are a dominant factor in determining the yield stress. Their conjecture is that the high degree of constraint present in a polycrystal is missing in the single-crystal PST specimens that exhibit a strong soft-mode effect.

This uncertainty about the nature of the soft mode deformation, which dominates the inelastic behavior of lamellar γ-TiAl in a wide range of intermediate orientations, has important implications in the construction of continuum models for this class of materials. While it is possible, given accurate data, to construct accurate crystal plasticity models of the individual phases of the material, it may well be impossible at present to extend these models directly to reproduce the anisotropic yield behavior of the lamellar microstructure.

Recently, Kim et al. (1999) presented an interesting discussion of the hard-mode behavior of lamellar TiAl; in the process, they provided a possible description of the interlamellar slip mode of deformation in terms of a combination of slip and twinning confined to the neighborhood of the interlamellar boundaries. These two deformation modes generate equal but opposite displacements normal to the interlamellar boundary plane, and the net slip occurs parallel to the boundaries provided these systems cooperate. When the slip is required to cross the lamellar boundaries, much higher stress is required to initiate slip on the pyramidal planes of the α_2 phase. This interpretation suggests that the soft-mode plastic flow behavior of fully lamellar γ-TiAl is linked to interlamellar boundary characteristics that will not be predicted adequately by continuum mechanical models of the individual material phases.

In the modeling technique discussed herein, we introduce the interlamellar slip behavior explicitly in the form of additional systems having slip planes coincident with the interlamellar boundaries. Strength and hardening properties associated with the soft-mode response are derived from experimental PST specimen data. While this approach is adequate for our immediate objective of modeling the stress variations in γ-TiAl polycrystals, the need for such an empirical device underscores the need for clarifying the nature of the interlamellar slip behavior. Methods for simulating this complicated response on a finer length scale than that adopted in the present model are needed, both to improve our understanding of the physical processes and to minimize the need for difficult and expensive laboratory tests in characterizing new materials.

Despite the amount of discussion devoted to materials science issues in this section, the focus of this paper is on mechanics, and on the construction of a workable model for stress estimation on a length scale somewhat smaller than the grain size. The unanswered questions associated with the materials science of TiAl are of interest in the present discussion because of their effect on one's approach to the mechanics problem at hand. Is it reasonable to assume that published data for strengths of the individual material phases are generally high compared with the corresponding strengths within a lamellar colony? If so, how can one define (or measure) a reasonable collection of the material properties, strengths, and hardening models required for elastic-plastic analysis? Alternatively, is it reasonable to assume that highly localized deformation mechanisms produce the soft-mode response? The analysis presented here subscribes to the latter view, if only by virtue of the properties assumed in the material descriptions, but is readily adapted to the former viewpoint as well. Resolution of these questions is not addressed in this paper, and will require a combination of novel experiments and new techniques for detailed microstructural modeling.

In what follows, we outline the generic crystal plasticity model and associated numerical solution, followed by the definition of model parameters and assumptions for the γ phase (TiAl), α_2 phase (Ti$_3$Al), and the fully lamellar γ+α_2 microstructure. Initial yielding and stress-strain curve predictions are made for PST specimens at various orientations and compared with experimental data. Finally, we present calculations based on a three-dimensional polycrystal model composed of fully lamellar γ-TiAl and a small volume percentage of equiaxed γ grains. This model comprises several hundred grains, and provides interesting data about the variation in stress and plastic strain throughout the sample for a given nominal strain or applied stress.

2. Crystal Plasticity Model

The anisotropic crystal plasticity model employed here is a rate-independent form similar to that described by Steinmann, et. al. (1998). We assume a pointwise elasticity relationship of the form

$$\dot{\sigma}_{ij} = C_{ijmn}\left(\dot{\varepsilon}_{mn} - \dot{\varepsilon}_{mn}^{p}\right)$$

(1)

In our implementation, which works with the ABAQUS finite element code, material calculations are performed in terms of the material axis system, using the Cauchy stress and rate of deformation. Net rotations of the material are removed by transforming the stress and strain prior to applying the constitutive model, and restored afterward. Therefore, the coordinate

system used is corotational in nature, and aligned with the (initial) principal material directions. It should be mentioned that our interest lies primarily in relatively small plastic deformation, so the discussion is limited to small deformations.

The yield function for each slip system (which we designate by upper-case indices) is expressed in terms of the stress components referred to the slip plane normal $\hat{\mathbf{n}}^{(I)}$, the preferred slip direction $\hat{\mathbf{s}}^{(I)}$, and the co-shear direction $\hat{\mathbf{c}}^{(I)} = \hat{\mathbf{n}}^{(I)} \times \hat{\mathbf{s}}^{(I)}$,

$$
\begin{aligned}
\tau^{sn(I)} &= \sigma_{ij} s_i^{(I)} n_j^{(I)} \\
\tau^{cn(I)} &= \sigma_{ij} c_i^{(I)} n_j^{(I)} \\
\tau^{nn(I)} &= \sigma_{ij} n_i^{(I)} n_j^{(I)}
\end{aligned}
\tag{2}
$$

Here $\tau^{sn(I)}$ is the Schmid resolved shear stress. The remaining (non-Schmid) stresses on the slip plane may have an effect on yielding and post-yield behavior, although this effect may be difficult to measure. We will retain the non-Schmid terms in the theoretical formulation, but the calculations that follow are limited to yield conditions based on $\tau^{sn(I)}$ alone.

Plastic flow is assumed to be restricted to the slip plane in all cases. Therefore, when the co-shear and normal stress are included in the yield function, a non-associated plastic flow behavior results. The use of a non-associated flow rule leads to an unsymmetric tangent material stiffness, a property which is inherited by the system model equations.

The yield condition for a specific slip system $(\hat{\mathbf{n}}^{(I)}, \hat{\mathbf{s}}^{(I)})$ is

$$
F^{(I)}(\boldsymbol{\sigma}) - Y^{(I)}(\boldsymbol{\gamma}) = \alpha^{sn(I)} \left| \tau^{sn(I)} \right| + \alpha^{cn(I)} \left| \tau^{cn(I)} \right| + \alpha^{nn(I)} \left| \tau^{nn(I)} \right| - Y^{(I)}(\boldsymbol{\gamma}) = 0
\tag{3}
$$

Here $\alpha^{sn(I)}$, $\alpha^{cn(I)}$, and $\alpha^{nn(I)}$ are weighting factors for the stress components. In classical single-crystal plasticity, with yielding determined by the resolved shear stress, $\alpha^{sn(I)} = 1$, $\alpha^{cn(I)} = 0$, and $\alpha^{nn(I)} = 0$. The slip magnitudes $\gamma^{(I)}$ are the primary variables in the final constitutive equation system. The corresponding yield surface normal vectors may be written as

$$
v_{ij}^{(I)} = \frac{\partial F^{(I)}}{\partial \sigma_{ij}} = \alpha^{sn(I)} \operatorname{sgn}\left(\tau^{sn(I)}\right) s_i^{(I)} n_j^{(I)} + \alpha^{cn(I)} \operatorname{sgn}\left(\tau^{cn(I)}\right) c_i^{(I)} n_j^{(I)} + \alpha^{nn(I)} \operatorname{sgn}\left(\tau^{nn(I)}\right) n_i^{(I)} n_j^{(I)}
\tag{4}
$$

The plastic flow rule assumes that slip occurs in the slip plane with normal $\hat{\mathbf{n}}^{(I)}$ along the preferred slip direction $\hat{\mathbf{s}}^{(I)}$. Summing the contributions from the set of all active slip systems, which we denote by A, gives

$$
\dot{\varepsilon}_{ij}^p = \sum_{I \in A} \dot{\gamma}^{(I)} \mu_{ij}^{(I)}
\tag{5}
$$

in which

$$
\mu_{ij}^{(I)} = \frac{1}{2}\left(s_i^{(I)} n_j^{(I)} + n_i^{(I)} s_j^{(I)} \right) \operatorname{sgn}\left(\tau^{sn(I)}\right)
\tag{6}
$$

defines the direction of the plastic strain rate for system I, and $\dot{\gamma}^{(I)}$ is its magnitude. Because the flow directions $\mu_{ij}^{(I)}$ reflect the sign of the shear stress, the slip rates $\dot{\gamma}^{(I)}$ are expected to be non-negative.

The strain hardening characteristics are assumed to be controlled by the accumulated plastic strain magnitudes, and may include interaction between slip systems. The hardening characteristics do not include local constraint effects that may lead to varying hardening behavior within a material grain, although it is possible to introduce this effect through property variations. Defining the hardening moduli $H_{IJ} = \partial Y^{(I)} / \partial \gamma^{(J)}$,

58

$$\dot{Y}^{(I)} = \sum_{J \in A} H_{IJ} \dot{\gamma}^{(J)} \tag{7}$$

The consistency condition requires that the plastic flow rates be related to the stress rates via

$$\dot{\gamma}^{(I)} = \pi_{ij}^{(I)} \dot{\sigma}_{ij} \tag{8}$$

with

$$\pi_{ij}^{(I)} = \sum_{J \in A} H_{IJ}^{-1} v_{ij}^{(J)} \tag{9}$$

In the solution of finite element systems which employ the plasticity model, it is necessary also to define an instantaneous relationship between rates (or increments) of stress and strain at a point, i.e.,

$$D_{ijmn} = \frac{\partial \left(\Delta \sigma_{ij} \right)}{\partial \left(\Delta \varepsilon_{mn} \right)} \tag{10}$$

This calculation can be accomplished most conveniently in terms of the compliance tensor (the inverse of **D**), which we denote by **S**. Combining the elasticity relation (1) and the plastic strain relation (5) yields

$$\dot{\sigma}_{ij} + \sum_{I \in A} \dot{\gamma}^{(I)} C_{ijmn} \mu_{mn}^{(I)} = C_{ijmn} \dot{\varepsilon}_{mn} \tag{11}$$

and next using the consistency condition (8),

$$\dot{\sigma}_{ij} + \sum_{I \in A} C_{ijmn} \mu_{mn}^{(I)} \pi_{kl}^{(I)} \dot{\sigma}_{kl} = C_{ijmn} \dot{\varepsilon}_{mn} \tag{12}$$

Multiplying by the elastic compliance tensor results in

$$\dot{\varepsilon}_{ij} = \left(S_{ijmn} + \sum_{I \in A} \mu_{ij}^{(I)} \pi_{mn}^{(I)} \right) \dot{\sigma}_{mn} = S_{ijmn}^{(tan)} \dot{\sigma}_{mn} \tag{13}$$

If non-Schmid stresses are omitted ($\alpha^{cn(I)} = \alpha^{nn(I)} = 0$), and the matrix of derivatives H_{IJ} is symmetric, then $\mathbf{S}^{(tan)}$ and the corresponding tangent stiffness **D** are symmetric.

3. Solution Procedure

In most finite element computations, the initial value problem to be solved at a material point is *strain-driven*; that is, the increments or rates of strain are assumed known, and the updated values of stress and the state variables at the end of this increment must be computed. For a typical time (or load) step, the computational problem is:

Given: σ_{ij}, { $\gamma^{(I)}$; I=1,2,...,N} at time t

$\dot{\varepsilon}_{ij}$ for the time interval (t, t+Δt)

Determine: σ_{ij}, { $\gamma^{(I)}$; I=1,2,...,N} at time $t + \Delta t$.

The first step in the solution procedure is the computation of a trial elastic stress state, based on the assumption of elastic behavior during the step. This is consistent with the conditions $\dot{\gamma}^{(I)} = 0$;I=1,2,...,N. Based on the trial solution, one can examine the yield condition for each slip system to estimate which systems are active during the step.

At any stage of the solution, which we identify by the iteration counter (n), an estimate of the stresses $\sigma_{ij}^{(n)}$ and plastic flow increments $\Delta\gamma_{(n)}^{(I)} = \dot{\gamma}_{(n)}^{(I)}\Delta t$ are available, and we wish to determine improved estimates $\sigma_{ij}^{(n+1)} = \sigma_{ij}^{(n)} + \delta\sigma_{ij}$ and $\Delta\gamma_{(n+1)}^{(I)} = \Delta\gamma_{(n)}^{(I)} + \delta\gamma^{(I)}$. The consistency condition at the end of the step requires

$$F^{(I)}\left(\sigma^{(n+1)}\right) - Y^{(I)}\left(\gamma_{(n+1)}\right) = v_{ij}^{(I)}\left(\sigma_{ij}^{(n)} + \delta\sigma_{ij}\right) - \left[Y^{(I)}\left(\gamma_{(n)}\right) + \sum_{J\in A}H_{IJ}\delta\gamma^{(J)}\right] = 0 \tag{14}$$

or

$$F^{(I)}\left(\sigma^{(n)}\right) - Y^{(I)}\left(\gamma_{(n)}\right) + v_{ij}^{(I)}\delta\sigma_{ij} - \sum_{J\in A}H_{IJ}\delta\gamma^{(J)} = 0 \tag{15}$$

The first two terms represent the residual, the amount by which the consistency condition is violated, at iteration (n). The remaining terms are proportional to $\delta\gamma^{(I)}$ by virtue of the elasticity and plastic flow relationships:

$$R_{(n)}^{(I)} = F^{(I)}\left(\sigma^{(n)}\right) - Y^{(I)}\left(\gamma_{(n)}\right) = -\sum_{J\in A}\left(v_{ij}^{(I)}C_{ijmn}\mu_{mn}^{(J)} + H_{IJ}\right)\delta\gamma^{(J)} \tag{16}$$

or

$$\sum_{J\in A}Q_{IJ}\delta\gamma^{(J)} = -R_{(n)}^{(I)} \tag{17}$$

Notice that (17) requires that $\mu_{ij}^{(I)}$ be defined such that $\gamma^{(I)}$ is positive. If the derivatives H_{IJ} are constant (linear hardening), the system above is linear and a solution is obtained in a single step. However, the set of active slip systems must be reviewed at each iteration. The iterative solution is therefore a two-level process, in which a Newton iteration is performed under the assumption of a known set A of active slip systems, and interrupted and restarted whenever the active set appears to change.

Numerical singularities or near-singularities in the Jacobian matrix Q_{IJ} are common. This problem is a numerical manifestation of the problem that the deformation fields generated by various slip systems are not linearly independent; in many situations, more than one combination of slip system magnitudes can be found which satisfies the stress-strain, plastic flow, and consistency conditions. Hence, the solution for $\delta\gamma^{(I)}$ may not be unique. To obtain a solution, we employ a singular value decomposition as suggested by Anand and Kothari (1996). The singular value decomposition of $\mathbf{Q}$ is

$$\mathbf{Q} = \mathbf{USV^T} \tag{18}$$

Here $\mathbf{U}$ is a matrix whose columns are the normalized eigenvectors of $\mathbf{QQ^T}$, called the left singular vectors. $\mathbf{V}$ contains the eigenvectors of $\mathbf{Q^TQ}$, the right singular vectors. $\mathbf{S}$ is a diagonal matrix containing the square roots of the eigenvalues of $\mathbf{Q^TQ}$ and $\mathbf{QQ^T}$, called the singular values of $\mathbf{Q}$. The matrix

$$\mathbf{Q^+} = \mathbf{VS^+U^T} \tag{19}$$

in which

$$S_{ii}^+ = \left\{\begin{matrix} 1/S_{ii} & S_{ii} > 0 \\ 0 & S_{ii} = 0 \end{matrix}\right\} \tag{20}$$

is the pseudoinverse of $\mathbf{Q}$. The solution $\mathbf{dg} = -\mathbf{Q}^{+}\mathbf{R}$ is identical to the solution $\mathbf{dg} = -\mathbf{Q}^{-1}\mathbf{R}$ when $\mathbf{Q}$ is non-singular. If $\mathbf{Q}$ is singular the solution obtained using the pseudoinverse has the property that $\|\mathbf{dg}\| = \sqrt{\mathbf{dg}^{\mathrm{T}}\mathbf{dg}}$ is minimized.

In practice, the iteration strategy may become complicated due to the need to modify the set A of active systems, especially when relatively large strain increments are attempted. One unambiguous way to resolve this problem is to adopt a subincremental approach, in which the solution is performed in a series of steps defined by the times at which individual slip systems become active or inactive during the solution. At the beginning of a subincrement, one can determine the current set of active systems based on the yield functions $F^{(I)}$ and their rates of change $\dot{F}^{(I)}$. The first (or next) subincrement then consists of a Newton iteration with the set of active slip systems fixed, and with the endpoint corresponding either to the end of the specified time increment, or to the time at which any one of the slip systems changes status. This event-driven strategy is effective in practice, since the number of subincrements required is generally quite small.

4. Model Parameters for TiAl Intermetallics

In this section we define specific constitutive model parameters for titanium aluminides in the form of pure γ (Ti-Al) and α_2 (Ti$_3$Al) phases, and for the lamellar microstructure formed from both phases arranged in a series of lamellar plates. Elastic properties for both pure phases have been published by several authors, and are in reasonable agreement with one another. Yield strengths have been reported in several publications, exhibiting somewhat less agreement.

The most serious difficulties in defining suitable model parameters arise in connection with the lamellar TiAl microstructure. Nearly all of the available data for lamellar TiAl is derived from experiments on polysynthetically twinned (PST) specimens consisting of single crystals exhibiting the fully lamellar microstructure. Typically, the microstructure of PST specimens differs from that of lamellar TiAl in polycrystalline form, and the differences in yield strength and hardening behavior are not particularly well-defined. A great deal of scatter is present in the reported values of yield strength as obtained from PST data (Inui, et al., 1992; Parthasarathy, et al., 1998; Kim, et al., 1999), although most of this effect is almost certainly due to variations in material composition and microstructure.

Below we outline a collection of model parameters for the TiAl materials of interest, derived from a variety of sources. It should be noted that inconsistencies in the data are unavoidable because of differences in material composition, processing, and experimental techniques. Considerable work remains to define consistent and reliable properties for this class of materials, and to understand the relationship between key properties of the individual phases and that of the material in lamellar form.

4.1. Model Properties for $\mathbf{g}$(Ti-Al)

Elastic properties for the γ phase are based upon measurements reported by Yoo and Fu (1998) for a composition of roughly Ti-56Al. In particular, we take

$E_1 = 140$ GPa	$\nu_{12} = 0.2840$	$G_{12} = 78$ GPa
$E_2 = 140$ GPa	$\nu_{13} = 0.2977$	$G_{13} = 105$ GPa
$E_3 = 135.4$ GPa	$\nu_{23} = 0.2977$	$G_{23} = 105$ GPa

in which directions (1,2,3) correspond to the [100], [010], and [001] crystal directions, respectively. Yielding and hardening properties of the γ phase are similar to those used by Parteder, et al. (1995). The crystalline structure is face-centered tetragonal (Ll$_0$) with aspect ratio 1.02. Here we employ the slip systems of an FCC lattice as a first approximation, with the preferred slip planes {111} and directions [110]. Parteder et al. further classify these systems as either pure (ordinary dislocations, involving Al atoms only) or mixed (superdislocations), noting that the mixed systems are more difficult to activate than the pure systems. The pure Al slip systems are: $(111)[\bar{1}10]$, $(\bar{1}11)[110]$, $(1\bar{1}1)[110]$, and $(11\bar{1})[\bar{1}10]$.

Figure 2 shows initial yield point predictions along various loading axis directions, for two values of critical resolved shear stress (CRSS). In the first case, a CRSS of 90 MPa is assumed for all slip systems; in the second calculation, an initial CRSS of 120 MPa is assigned to the mixed slip systems. Only resolved shear stresses are included in the yield condition for both calculations (i.e., non-Schmid effects are neglected). The cusps in the upper curve are due to a change in the active slip system; near the $0°$ and $90°$ orientations, the pure Al modes with lower critical stress are active, while the mixed modes dominate for intermediate orientations. The initial yielding plots correspond to the lower bound obtained by plotting the inverse of the Schmid factor divided by the CRSS for all slip systems.
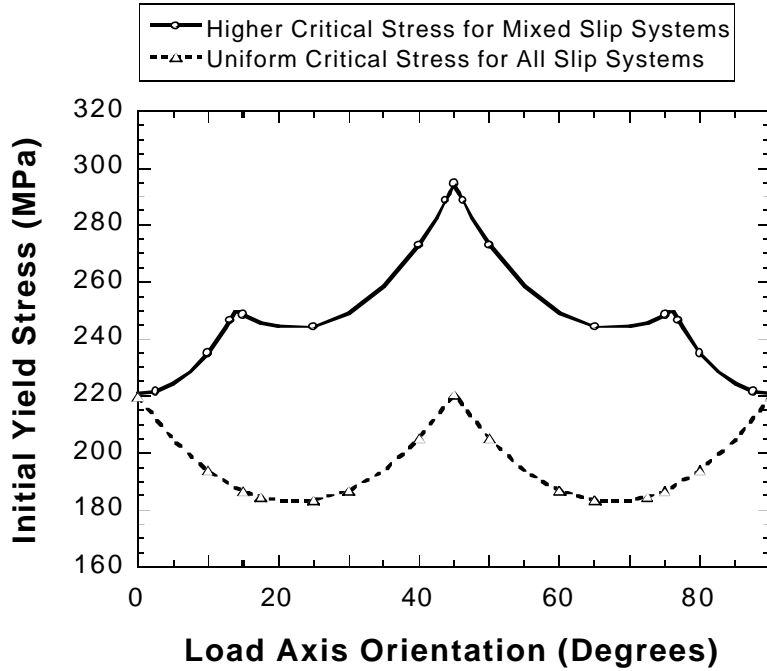

Figure 2. Initial yield predictions for gamma grains.

The assumed values of the hardening moduli are 800 MPa for the self-hardening terms (H_{II}) and for the latent hardening terms (H_{IJ}) for coplanar systems; for non-coplanar systems, $H_{IJ} = 1120$ MPa ($q = 1.4$; Parteder, 1995). It should be noted that our treatment of the hardening behavior is quite rudimentary, since our interest lies mainly in the very small strain regime. Refinement of the hardening models is an important area for future investigation.

4.2. Model Properties for $\boldsymbol{a}_2$ (Ti$_3$Al)

For the α_2 phase, the elastic constants again are based on measurements by Yoo and Fu (1998). Values of the orthotropic elastic constants are as follows:

$E_1 = 125$ GPa $\quad$ $\nu_{12} = 0.4541$ $\quad$ $G_{12} = 43$ GPa
$E_2 = 125$ GPa $\quad$ $\nu_{13} = 0.1539$ $\quad$ $G_{13} = 62$ GPa
$E_3 = 190.9$ GPa $\quad$ $\nu_{23} = 0.1539$ $\quad$ $G_{23} = 62$ GPa

The α_2 crystal structure is hexagonal (DO$_{19}$); the '3' axis of the model is aligned with the 'c' crystal axis [0001], and the '1' axis is parallel to [11$\overline{2}$0].

The inelastic properties for α_2 are based on data collected by Yamaguchi and Inui (1993) for a Ti$_3$Al compound having approximately 36.5 at% aluminum. Data for the individual slip systems appear in Table 1. Details of the strain hardening characteristics of α_2 are not well-defined at present. Assumed values of the latent hardening coefficients used in the present model are listed in Table 2. All hardening values are expressed in MPa.

Table 1. Slip system geometry and strengths for a_2-TiAl.

Slip System Description	Planes and Directions	Yield Strength	Self Hardening Modulus
Prism	$\{1\bar{1}00\} <11\bar{2}0>$	100 MPa	500 MPa
Basal	$(0001) <11\bar{2}0>$	329 MPa	500 MPa
Pyramidal	$\{11\bar{2}1\} <\bar{1}\bar{1}26>$	911 MPa	1500 MPa

Table 2. Hardening coefficients for a_2-TiAl.

	Prism	Basal	Pyramidal
Prism	800	1000	1000
Basal	1000	800	1000
Pyramidal	1000	1000	2000

Initial yield stress predictions for α_2 grains in various loading orientations are shown in Figure 3; in all cases the loading direction is the 'x' (horizontal) axis. Rotation in the basal plane causes only slight variations in the yield strength since the relevant slip systems all possess similar strengths, and each slip direction is only 30 degrees removed from the next. Rotation of the 'c' (hexagonal) axis toward the loading direction produces a very pronounced effect, as the higher-strength pyramidal systems eventually control the initial yielding behavior.
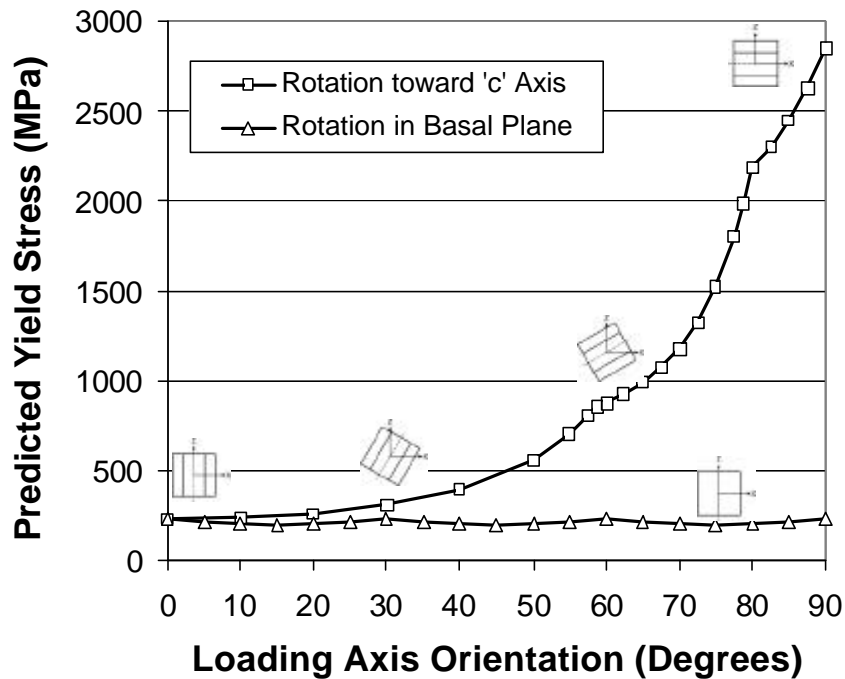

Figure 3. Initial yield predictions for α_2 grains.

4.3. Effective Model Properties for Lamellar g+a_2 TiAl

Our modeling approach represents individual γ grains and lamellar γ+α_2 colonies, and their orientations, explicitly. However, our main interest lies in characterizing the stress variations among grains, and the stress or strain concentrations

caused by changes in stiffness and orientation from grain to grain. Models with a sufficient number of grains to eliminate boundary effects typically consist of several hundred three-dimensional grains or lamellar colonies. In this setting it is impractical to model discrete lamellae, and we must resort to the use of effective properties and strengths for the lamellar TiAl microstructure.

Effective room temperature elastic properties for lamellar TiAl have been computed by Frank (1999), based on laminate calculations using the method described by Pagano (1974). A summary of effective orthotropic constants for various proportions of α_2 and γ phases appears in Table 3. All moduli are given in GPa.

Table 3. Effective elastic properties of lamellar TiAl.

Property	α_2:γ Ratio			
	1:1	**1:2**	**1:5**	**1:10**
E_{11}	160.3	171.3	182.1	186.8
E_{22}	160.1	171.5	181.9	187.2
E_{33}	206.4	211.5	216.6	218.9
ν_{12}	0.351	0.322	0.297	0.284
ν_{13}	0.155	0.153	0.147	0.147
ν_{23}	0.156	0.152	0.148	0.145
G_{12}	59.4	64.7	70.3	72.6
G_{13}	64.6	65.6	66.4	66.9
G_{23}	64.6	65.5	66.5	66.8

The potential slip systems of interest within a lamellar colony include those of both the γ and α_2 layers, as well as interlamellar slip modes. The coordinate system adopted for the α_2 phase is used also for the lamellar material, since the direction $(0001)_{\alpha_2}$ is aligned with the stacking direction of the lamellar planes. The slip geometry for the γ phase is transformed to a common coordinate system using the orientation relationships (Inui, et al., 1992):

$$(111)_\gamma \| (0001)_{\alpha_2} \quad \text{and} \quad \langle 1\bar{1}0 \rangle_\gamma \| \langle 11\bar{2}0 \rangle_{\alpha_2} \tag{21}$$

Considering the slip modes which may occur in the individual material phases, the mean free path of dislocation movement in the lamellar structure, for systems having components normal to the lamellar interfaces, is on the order of the lamellar thickness, which can be much less than 1 μm (Parthasarathy, 1998). Therefore, the strengths and hardening parameters associated with selected systems in the individual phases must be adjusted to reflect the differing constraint situation in the lamellar colony. As a first approximation, we introduce a correction for the critical stress of each system,

$$\tau_C = \tau_0 + \frac{k}{\sqrt{d_L}} \tag{22}$$

in which d_L is the lamellar spacing. The slope of this correction is relatively small ($k = 0.02 - 0.08$ MPa-m$^{1/2}$), and depends upon the particular set of initial yield data selected for use. Although (22) has the form of a Hall-Petch correction, we hesitate to describe it as anything so systematic. The variety of material data used in defining the model constants is great, and the primary function of the correction (22) has been to correct for variations between material strengths measured at different laboratories, using different variants of the material. The proper means of applying such a correction, even for a consistent body of material data, remains unresolved, since the controlling dimension for a given system may be related to lamellar spacing, domain size, colony size, or some combination of these lengths, depending on the geometry of the system.

As was mentioned earlier, the nature of the interlamellar slip behavior of γ-TiAl is not completely understood. Computation of appropriate properties and deformation characteristics in the neighborhood of the lamellar interfaces from first principles currently is infeasible. At the same time, experimental evaluation of meaningful continuum-level properties

of the interface may not be possible because of the extremely small length scale at which the interface deformation mechanisms operate. Therefore, we employ the expediency of an independently defined interlamellar slip system, whose properties are derived from analyses of PST single crystal experiments. The alternative to this approach is to assume, for the lamellar microstructure, lower strengths than those indicated by experiments on the constituent material phases. Although we have chosen the former approach, the plasticity model described here can be applied using either set of assumptions.

The slip systems included in the lamellar material description are given in Table 4. The slip systems from the individual constituents are retained, and three additional interlamellar systems are introduced. The α_2 basal slip systems have been eliminated, since the slip planes coincide with the interlamellar slip planes; due to the much lower strength of the interlamellar modes, the basal slip systems in the α_2 phase would never be activated in practice.

Table 4. Slip system geometry and strengths for lamellar $\gamma+\alpha_2$ TiAl.

Slip System Description	Planes and Directions	Yield Strength
γ	$\{111\}$ $[110]$	90 MPa
α_2 Prism	$\{1\bar{1}00\} <11\bar{2}0>$	100 MPa
α_2 Pyramidal	$\{11\bar{2}1\} <\bar{1}\bar{1}26>$	911 MPa
Interlamellar	$(0001) <11\bar{2}0>$	56 MPa

The use of both sets of constituent slip systems in the lamellar model corresponds to the assumption of an isostress condition in the lamellar microstructure in the neighborhood of a stress point; that is, both material phases experience the same stress components, while their strains may differ. While more sophisticated constraint conditions between the phases can be imposed, the isostress assumption predicts the onset of macroscopic plastic flow with reasonable accuracy. This is possible because the elastic moduli of the phases are approximately equal, and because the yield behavior in virtually all material orientations is controlled by a limited subset of the slip systems.

For loading which is nearly aligned with the lamellar planes, yielding is controlled by the γ systems and the α_2 prism modes, which are activated at virtually the same time. Loading perpendicular to the lamellae involves the γ phase, followed by the α_2 pyramidal slip modes. Translamellar slip is controlled by the pyramidal slip system in the α_2 phase. In practice, the pyramidal modes are likely to be activated only as a result of dislocation pileup because of their high strength. In a wide range of intermediate orientations, the interlamellar behavior is the prevailing feature of the plastic flow behavior. Furthermore, within a polycrystal composed of lamellar colonies with random orientations, interlamellar slip in favorably oriented colonies dominates the initial stages of inelastic response.

Figure 4 shows a comparison of initial yield strength as predicted by the lamellar model, compared with two sets of experimental data (Parthasarathy, et al, 1998; Inui, et al., 1992). A strength constant k = 0.02 MPa-m$^{1/2}$ (eq. 22) provides the closest agreement with the measurements of Parthasarathy (1998) and coworkers for the initial yield points, while a value of 0.07 MPa-m$^{1/2}$ better matches the 0.2 percent offset data obtained by Inui, et al. (1992). The predicted curves are identical at intermediate orientations, since the strength associated with interlamellar slip is a property of the lamellar microstructure, and is not subjected to the same correction as the constituent strengths.
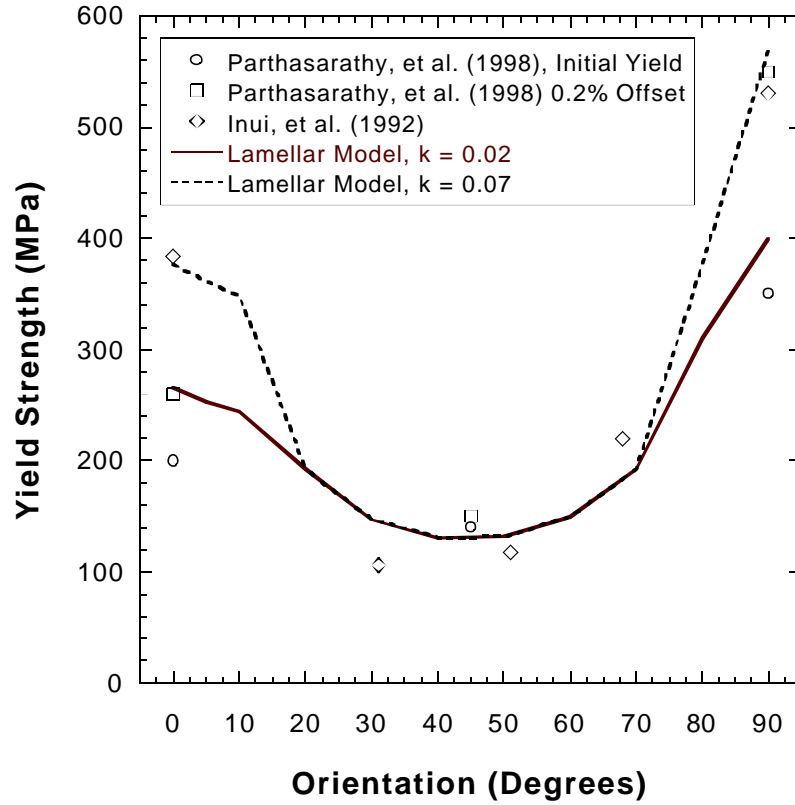
Figure 4. Predicted yield strength of lamellar colony at various orientations.

Predictions of stress-strain curves for k = 0.02 MPa-m^{½} are shown in Figure 5, and compared with the microstrain measurements of Parthasarathy and coworkers. The strain scale is rather highly magnified, since the experimental conditions were limited to strains on the order of 0.5 percent; in this regime, a more sophisticated representation of the strain-hardening behavior would be desirable for improved accuracy.
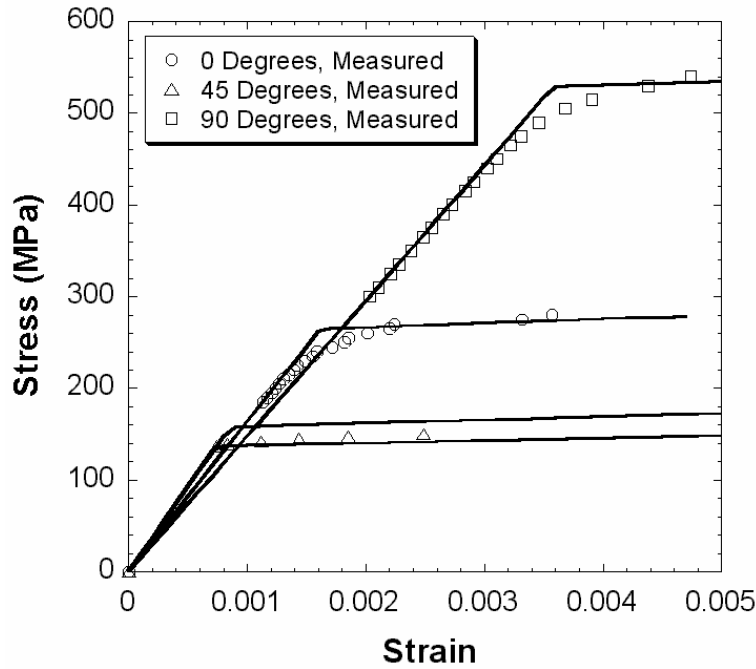
Figure 5. Predicted stress-strain curves for lamellar TiAl.

5. *Polycrystal Analysis*

The crystal plasticity model described above has been implemented in the form of a user-supplied material model (UMAT) for the ABAQUS finite element code. For each TiAl material variant, appropriate properties, including the relevant slip system geometry, are defined separately and used in the same solution algorithm.

Figure 6 shows a finite element model of a polycrystal composed of an equal number of lamellar colonies and equiaxed γ-TiAl grains. The volume fraction of lamellar TiAl is 0.96, with an assumed α_2: γ ratio of 1:5 within the lamellar colonies. Because of the relatively small fraction of γ grains present, filling the three-dimensional space with a regular pattern of both grain types is difficult. Here we use a geometry generation procedure develop by Frank (1999), in which cubic γ grains alternate with truncated rhombic dodecahedra representing the lamellar colonies. The width of the lamellar colonies is approximately 145 μm, and the overall length of the model in each direction is about 0.77 mm. The model contains a total of 512 grains, with the orientation of each grain being randomly generated. Fringe values in Figure 6 depict the orientation of each grain with respect to the loading direction, which is parallel to the global 'x' axis. Symmetry conditions are applied on the three rearward facing surfaces of the model. The remaining three faces are constrained to remain planar, but may expand or contract in response to the loading.
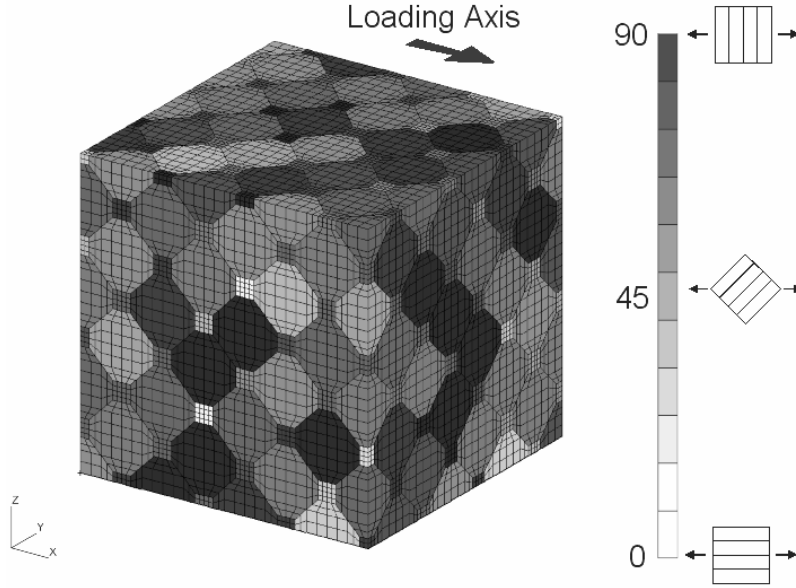
Figure 6. Polycrystal finite element model with randomly oriented grains.

In Figure 7, we compare a trace of macroscopic stress and strain under uniaxial compression loading with the measurements reported by Parthasarathy, et al. (1998). The macroscopic response is quite reasonable. However, it is not clear why the prediction using $k = 0.07$ MPa-m$^{1/2}$ provides closer agreement with the experiment than $k = 0.02$. According to Parthasarathy, the polycrystals used in the experiment exhibited a more refined microstructure than the PST crystals from which properties were measured, but are otherwise similar.

Figures 8 and 9 represent an attempt to separate the effect of local stress variations caused by anisotropy and differing orientations in adjacent grains from that due purely to crystal orientation. The Schmid resolved shear stress (SRSS) on the interlamellar planes,

$$\tau^{sn(IL)} = \overline{\sigma}_{ij} n_i^{(IL)} s_j^{(IL)} = \overline{\sigma}_{11} n_1^{(IL)} s_1^{(IL)} \tag{23}$$

is used to normalize the resolved shear stresses obtained from the finite element prediction. In the absence of localized stress concentrations, this normalized shear stress should equal one. Figure 8 depicts the ratio of the predicted shear stress to the SRSS for a nominal strain of 0.1 percent, where the response is predominantly elastic. The most variation in the shear stress occurs in lamellar colonies for which the SRSS is small (and in fact the stress ratios for some colonies are much larger than the range shown in the figure). However, the magnitude of the interlamellar shear stress for these extreme cases is quite small. A noticeable variation in the resolved shear stress from the SRSS is evident even in colonies that are favorably oriented for interlamellar slip (i.e., near 45 degrees to the loading axis). This fluctuation in the stresses is caused by local changes in the stress path resulting from elastic anisotropy, orientation differences in neighboring grains, and localized yielding.
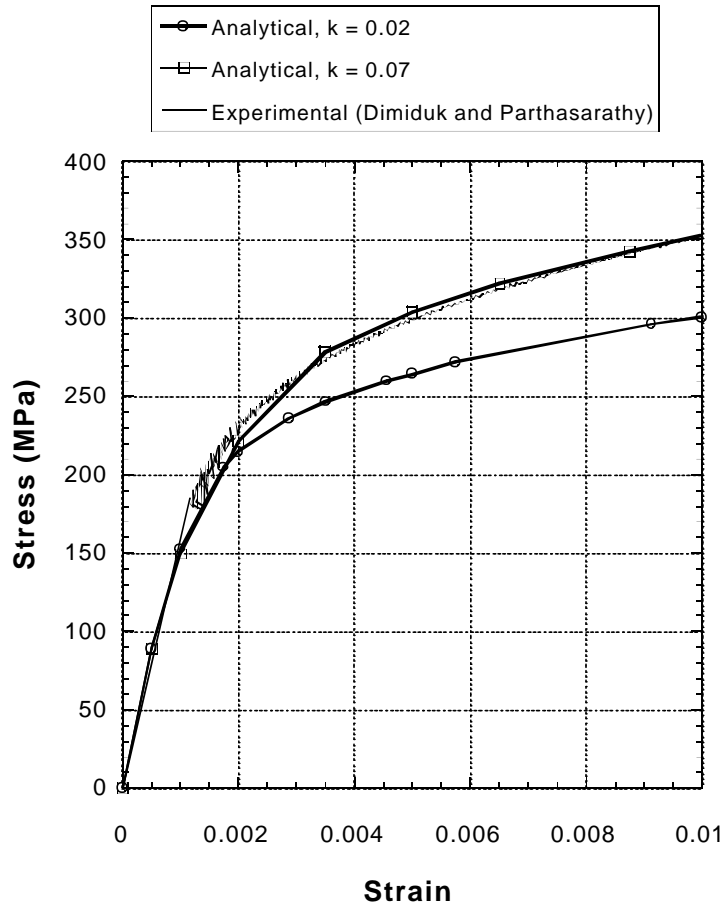
68

Figure 7. Predicted and measured stress-strain curves for TiAl polycrystal.

Figure 9 is a histogram relating the level of interlamellar shear stress (normalized by SRSS) to the cumulative fraction of material volume experiencing that shear stress or less. Only lamellar colonies are included in this data. The interlamellar stress is less than the SRSS only in about 20 percent of the material volume, while the interlamellar shear stress exceeds 2×SRSS only in about ten percent of the material. As was mentioned above, this latter population contains mostly material grains for which the absolute stresses are quite low compared with the interlamellar CRSS. Half of the material is subjected to interlamellar shear stress which is less than about 1.3×SRSS.
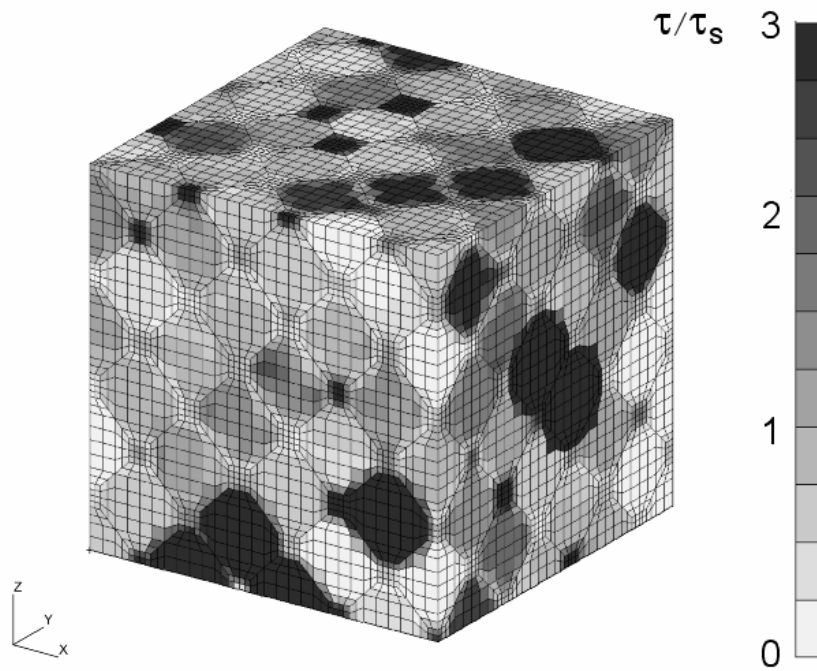
Figure 8. Predicted ratio of interlamellar resolved shear stress to Schmid stress in polycrystal finite element model. Ratios different from one reflect the influence of localized stress variations and orientation mismatch between adjacent grains.
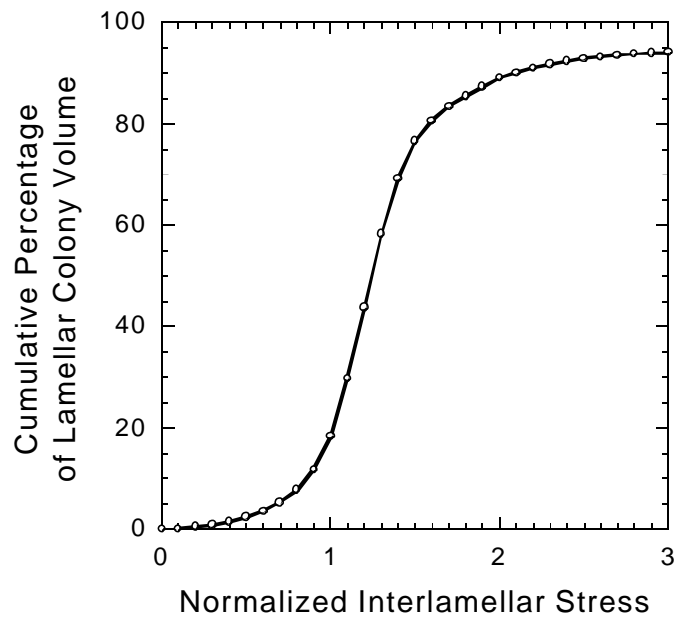

Figure 9. Distribution of interlamellar shear stresses in γ-TiAl polycrystal. Shear stresses within each grain are normalized with respect to the Schmid stress in that grain.

In Figures 10 and 11, the distribution of effective plastic strain,

70

$$\varepsilon_p = \int_0^t \frac{2}{3} \dot{\varepsilon}_{ij}^p \dot{\varepsilon}_{ij}^p \, dt$$

$$(24)$$

is shown at nominal strain levels of 0.2 and one percent, respectively. At a strain of 0.002, much of the polycrystal remains elastic; however, localized plastic strains exist which are 50 percent greater than the nominal strain. At one percent macroscopic strain, nearly all of the sample has yielded. Those grains containing unyielded material are oriented such that the loading is nearly perpendicular to the lamellar planes. Localized effective plastic strains exist which are nearly four times as large as the nominal strain. Figure 12 contains the same data in the form of a histogram plot.
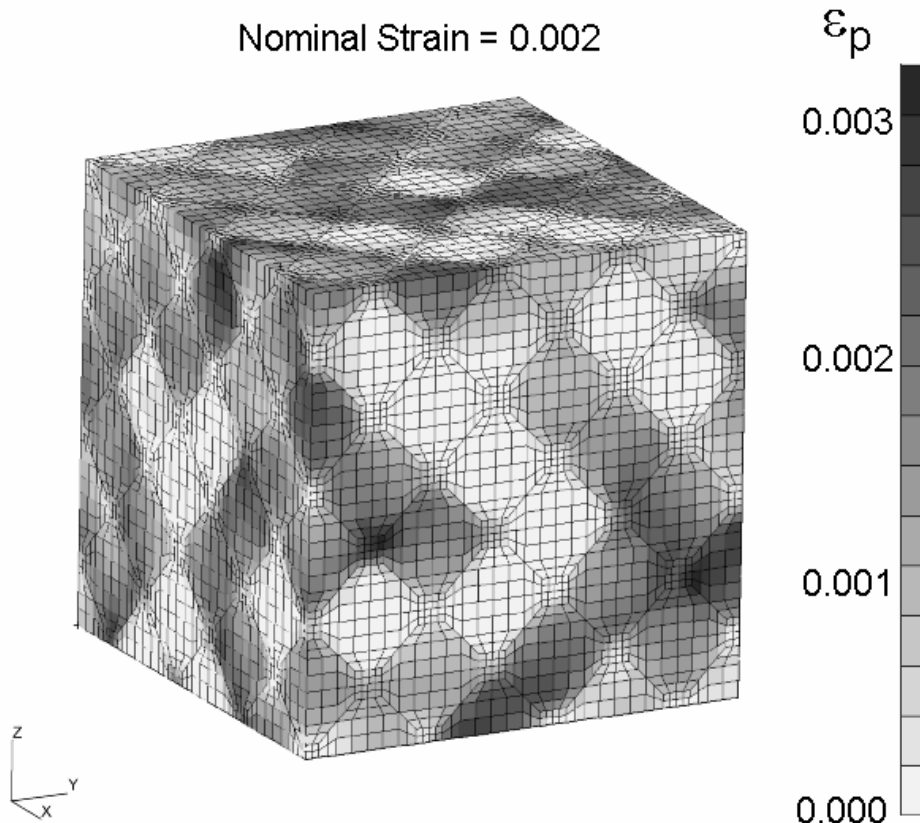

Figure 10. Effective plastic strains in TiAl polycrystal corresponding to a macroscopic strain of 0.2 percent.
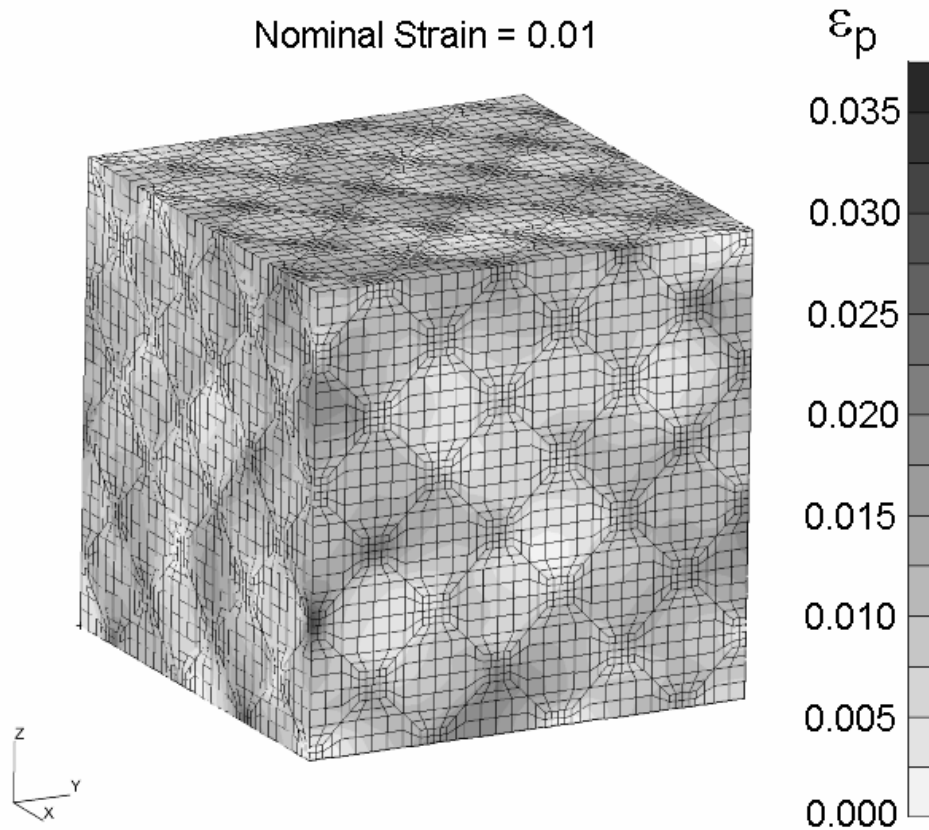
Figure 11. Effective plastic strains in TiAl polycrystal corresponding to a macroscopic strain of one percent.

6. Summary

A crystal plasticity model suitable for small-deformation elastic-plastic analysis of localized stress variations in polycrystals of lamellar $\gamma+\alpha_2$ TiAl, as well as the individual phases of the material, has been presented. The modeling of the lamellar colonies introduces a uniform-stress approximation that eliminates the need for modeling individual lamellae explicitly, while capturing the most important features of the early plastic flow within a colony. The model has been implemented as a user material model subroutine (UMAT) for the ABAQUS finite element code. Three-dimensional stress analyses of polycrystals containing several hundred grains have been performed, and yield useful information concerning the local stress variations caused by elastic anisotropy, orientation differences among adjoining grains, and localized plastic deformation.
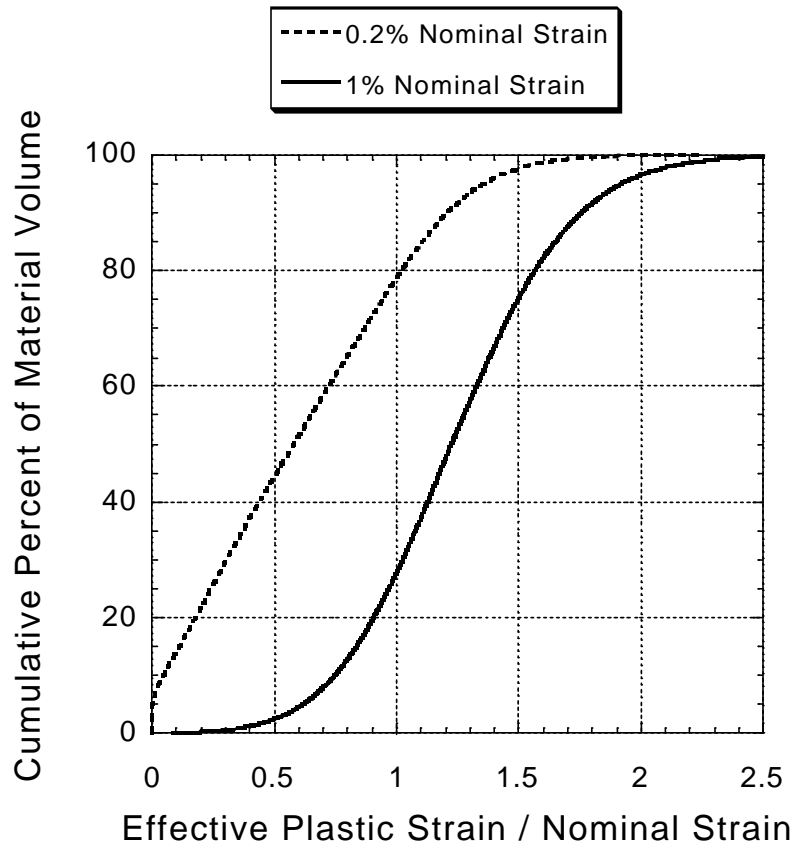
Figure 12. Effective plastic strain variation in polycrystal model. At 0.2 percent elongation, five percent of the volume remains elastic, and 20 percent experiences plastic strains larger than the nominal strain. At one percent elongation, most of the material volume sees plastic strains in excess of the nominal value due to local strain variations.

Acknowledgements

References

Anand, L., Kothari, M., 1996. A computational procedure for rate-independent plasticity. J. Mech. Phys. Solids 44(4) 525-558.

Appel, F., Wagner, R. 1998. Microstructure and deformation of two-phase γ-titanium aluminides. Mat. Sci. Eng. R22 187-268.

Bishop, J. F. W., Hill, R., 1951. A theoretical derivation of the plastic properties of a polycrystalline face-centered metal. Phil. Mag. 42 1298-1307.

Dao, M., Kad, B.K., Asaro, R.J., 1996. Deformation and fracture under compressive loading in lamellar TiAl microstructures. Phil. Mag A 74(3) 569-591.

Frank, G.J., 1999. University of Dayton Research Institute, Private Communication.

Harder, J., 1999. A crystallographic model for the study of local deformation processes in polycrystals. Int. J. Plasticity 15 605-624.

Hazzledine, P.M., Kad, B.K., 1995. Yield and fracture of lamellar γ/α_2 TiAl alloys, Mat. Sci. Eng. A 192 340-346.

Inui, H., Oh, M.H., Nakamura, A., Yamaguchi, M., 1992. Room-temperature tensile deformation of polysynthetically twinned (PST) crystals of TiAl. Acta Metall. Mater. 40(11) 3095-3104.

Kad, B.K., Dao, M., Asaro, R.J., 1995a. Numerical simulations of plastic deformation and fracture effects in two phase γ-TiAl and α_2-Ti$_3$Al lamellar microstructures. Phil. Mag. A 71(3) 567-604.

Kad, B.K., Dao, M., Asaro, R.J., 1995b. Numerical simulations of stress-strain behavior in two phase $\alpha_2+\gamma$ lamellar TiAl alloys. Mat. Sci. Engng. A 192-193 97-103.

Kad, B.K., Asaro, R.J., 1997. Apparent Hall-Petch effects in polycrystalline lamellar TiAl. Phil.Mag. A 75(1) 87-104.

Kim M-C., Nomura, M., Vitek, V., Pope, D.P., 1999. Deformation of polysynthetically twinned TiAl single crystals with near-hard orientation. Mat. Res. Soc. Symp. Proc. 552 KK3.1.1-6.

Marketz, W.T., Fischer, F.D., Clemens, H. 1999. Deformation behavior of gamma titanium aluminides – micromechanical modeling of single PST crystals and polycrystalline materials. In Kim, Y-K., Dimiduk, D.M., Loretto, M.H. (eds) Gamma Titanium Aluminides 1999. The Minerals, Metals, and Materials Society 579-586.

Pagano, N.J. 1974. Exact moduli of anisotropic laminates. In Sendeckyj, G.P. (ed.) Mechanics of Composite Materials. Academic Press, New York.

Parteder, E., Siegmund, T., Fischer, F.D., Schlögl, S., 1995. Numerical simulation of the plastic behavior of polysynthetically twinned Ti-Al crystals. Mat. Sci. Engng. A 192-193 149-154.

Parthasarathy, T.A., Mendiratta, M.G., Dimiduk, D.M., 1998. Flow behavior of PST and fully lamellar polycrystals of Ti-48Al in the microstrain regime. Acta Mater. 46(11) 4005-4016.

Schlögl, S.M., Fischer, F.D., 1996. Micromechanical modelling of TiAl intermetallics. Comp. Mat. Sci. 7 34-39.

Schlögl, S.M., Fischer, F.D., 1997a. The role of slip and twinning in the deformation behaviour of polysynthetically twinned crystals of TiAl: a micromechanical model. Phil. Mag. A 75(3) 621-636.

Schlögl, S.M., Fischer, F.D., 1997b. Numerical simulation of yield loci for PST crystals of TiAl. Mat. Sci. Engng. A 239-240 790-803.

Steinmann, P., Kuhl, E., Stein, E., 1998. Aspects of non-associated single crystal plasticity: influence of non-Schmid effects and localization analysis. Int. J. Sol. Struct. 35(33). 4437-4456.

Taylor, G.I., 1938. Plastic strain in metals. J. Inst. Metals 62 307-324.

Yamaguchi, M., Inui, H., 1993. TiAl compounds for structural applications. In Dariola, R., Lewandowski, J.J., Liu, C.T., Martin, P.L., Miracle, D.B., Nathal, M.V. (eds) Structural Intermetallics. The Minerals, Metals, and Materials Society 127-142.

Yoo, M.H., Fu, C.L., 1998. Physical constants, deformation twinning, and microcracking of titanium aluminide. Metallurgical and Material Trans. 29A 49-62.

EFFECT OF SMALL EFFUSION HOLES ON CREEP RUPTURE BEHAVIOR OF OXIDE/OXIDE NEXTEL™720/AS COMPOSITE

Dennis J. Buchanan*, Victoria A. Kramb*, Reji John and Larry P. Zawada
Materials and Manufacturing Directorate, Air Force Research Laboratory (AFRL/MLLN), Wright-Patterson Air Force Base, OH 45433-7817
* University of Dayton Research Institute, Dayton, OH 45419

Abstract

Oxide/Oxide Ceramic Matrix Composites (CMC) are currently being evaluated for high-temperature aerospace applications where their beneficial resistance to oxidation is critical for retaining mechanical properties under long-life conditions. Many of these component applications require holes for cooling and attachment points. An investigation on the effects of 0.5 mm diameter effusion holes on the creep rupture behavior was initiated. The Oxide/Oxide CMC studied during this investigation was Nextel™720/AS. The matrix was Alumina-Silica reinforced with an eight-harness satin weave (8HSW) mat of Nextel™720 fibers. Multiple effusion hole patterns were evaluated at elevated temperature (1100°C) under sustained-load (creep) conditions. Extensometry and sectioned samples from interrupted tests were used to characterize the damage zone in the vicinity of the holes. The presence of 0.5 mm diameter effusion holes in specimens subjected to sustained load conditions showed no detrimental effects to the creep behavior or to the fiber and matrix in the vicinity of the holes.

Introduction

Damage tolerant ceramic matrix composites (CMC) that exhibit relatively little degradation in mechanical properties at elevated temperature are being evaluated for high temperature aerospace applications. Many existing CMC materials suffer from oxidation problems at service temperature conditions. Oxide/oxide CMC have an inherent resistance to oxidation and therefore exhibit little or no degradation in mechanical properties at expected service temperatures. Many studies [1-8] have shown that oxide/oxide CMC exhibit excellent tensile and fatigue properties at room and elevated temperatures. Several studies [5,9,10] have shown that CMC with Nextel610 fibers suffer from excessive creep deformation at temperatures ≤ 1000°C. However, Nextel720 fibers exhibit significant creep resistance up to 1100°C [9,10]. Hence, the US Air Force is considering the use of oxide/oxide CMC with Nextel720 fibers for applications with temperature requirements in the range of 1000-1100°C.

Material

The Nextel[TM]720/AS CMC used in this investigation was manufactured by COI Ceramics, Inc, of San Diego, CA. The Nextel[TM]720 fibers, which are produced by the 3M Company of St. Paul, MN [15], are ≈ 12 μm in diameter. Approximately 400 fibers are bundled together in tows and woven into a balanced eight-harness-satin weave (8HSW) cloth. The matrix consists of a porous alumina-silica (AS) that is weakly bonded to the fibers without an engineered interphase. The panels used in this study contained 12 plies. Section samples of panels used in this study showed that the fiber volume fraction range was 42 - 50%. Figure 1 shows microcracks distributed throughout the matrix rich regions of the composite as a result of panel shrinkage that occurred during processing. Additional details about the manufacture of the CMC can be found in Ref. [12].
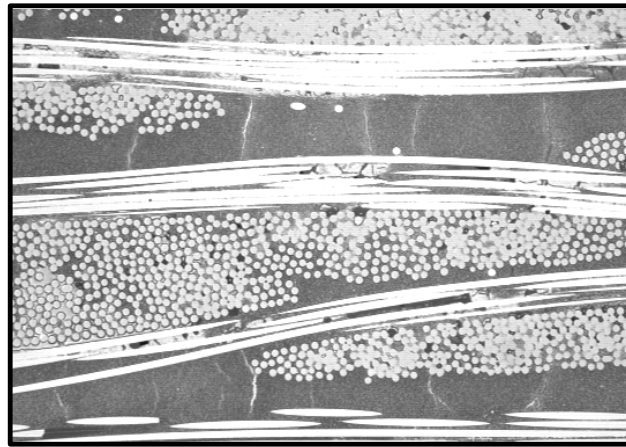
200 μm

Figure 1. *Microstructure of (0°/90°) 8HSW Nextel^{TM}720/AS microstructure highlighting the matrix cracks due to processing.*

Experimental Procedure

Figure 2 represents examples of the effusion hole patterns that were used for this study. The top figure shows a possible array configuration of effusion holes for a component that requires cooling air. The three figures below show sub-elements of that pattern that were used for the creep tests. The nominal dimensions of the specimens were, width (W) = 10.0 mm in gage section, thickness (B) ≈ 2.5 mm and length ≈ 140 mm. All effusion holes were 0.5 mm in diameter with the hole-axis perpendicular to the loading axis. Geometries tested include a one, two and five hole pattern shown in Fig 2.
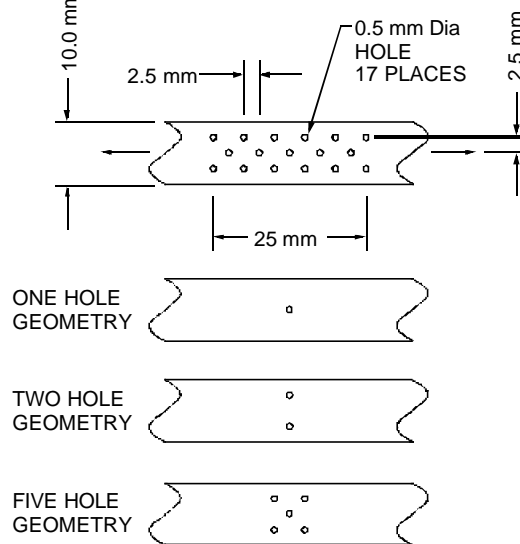

Figure 2. Schematic of effusion hole geometries.

The specimens were measured and photographed to document the condition of the effusion holes prior to testing. The specimen ends were tabbed with fiberglass tabs to provide a flat uniform surface for the smooth grip surfaces and to minimize the possibility of grip failure. The specimens were mounted in a precisely aligned, rigid grip system [16] that minimized specimen bending and rotation. A clamshell furnace with silicon-carbide heating elements and four-zone control were used for the elevated temperature creep tests. Thermal profile maps on the

specimen showed that the specimen was uniformly heated, ± 0.6%, over the entire gage section of the specimen. All creep tests were loaded to 100 MPa net section stress at a loading rate of 20 MPa/s. Applied load, temperature and extensometry data were collected during the test.

The cross-sectional area used to calculate the net-section stress was based on the minimum cross-section of a plane perpendicular to the loading axis. The net-section stresses were based on cross-sectional area only and did not include the effects of stress risers due to the stress concentration factor of the geometry. Since the holes were small and were spaced several diameters apart the elastic stress concentration for these effusion hole geometries was $K_t = \sigma_{tip}/\sigma_{net} \approx 2.9$, which assumed isotropic and homogeneous material properties. Consequently, the load on the one, two and five effusion hole specimens were -5%, -10% and -10% less, respectively, than the uniform gage sample.

Experimental Results

The creep notch mouth opening displacement (NMOD)/ gage length or creep strain versus time for the effusion hole specimens and the unnotched specimen are shown in Fig. 3. All specimens were tested at 1100°C at a net section stress of $\sigma_{net} = 100$ MPa. The arrows in Fig. 3 signify that all the specimens were interrupted prior to failure. The creep data in Fig. 3 shows that creep strain for the unnotched specimen and the effusion hole specimens exhibited similar creep behavior.
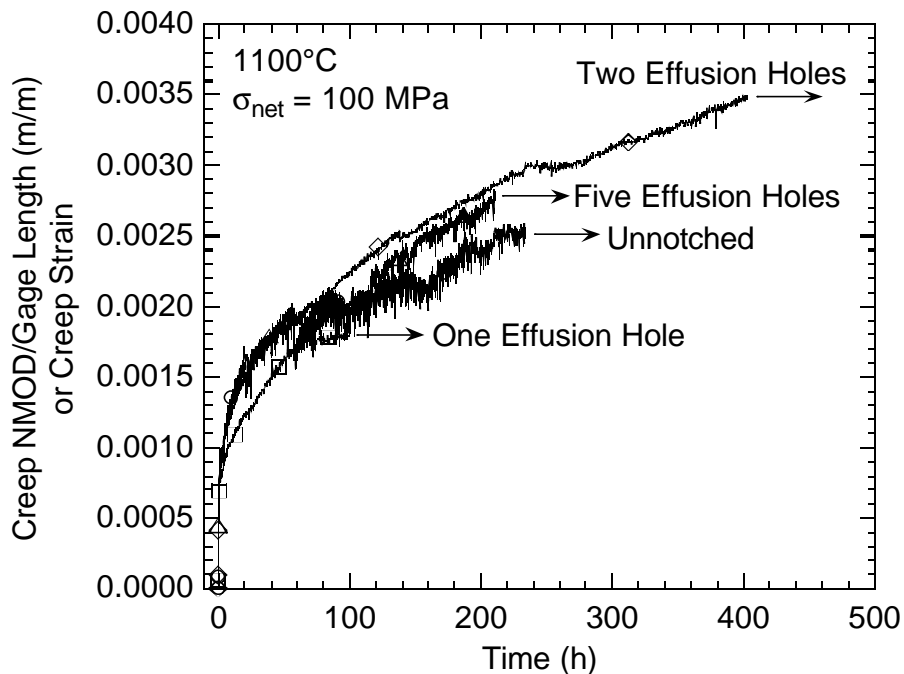

Figure 3. Creep strain or NMOD/Gage Length versus time for different effusion hole patterns.

Figure 4 shows the net-section stress versus NMOD divided by extensometer gage length or strain. The tensile tests were conducted at room temperature after the prior elevated temperature exposure. The heat treated dogbone sample was used as a baseline comparison for the retained strength tests of the crept effusion hole specimens. The heat treated dogbone specimen showed a ≈ 50% loss in room temperature retained strength after heat treatment at 1100°C for 100 hours. The one effusion hole specimen was subjected to the same time at temperature as the heat treated dogbone, however it was also subjected to a sustained load of 100 MPa over the 100 hours at temperature. The one effusion hole specimen showed a ≈14% decrease in room temperature retained strength compared to the heat treated specimen. The five effusion hole sample which was crept at 1100°C and

100 MPa for approximately 212 hours showed a 35% decrease in room temperature retained strength compared to the heat treated specimen. The one effusion hole specimen had similar strength to the heat treated dogbone, the reduction in retained strength of the five hole sample was due to the longer exposure time at temperature.
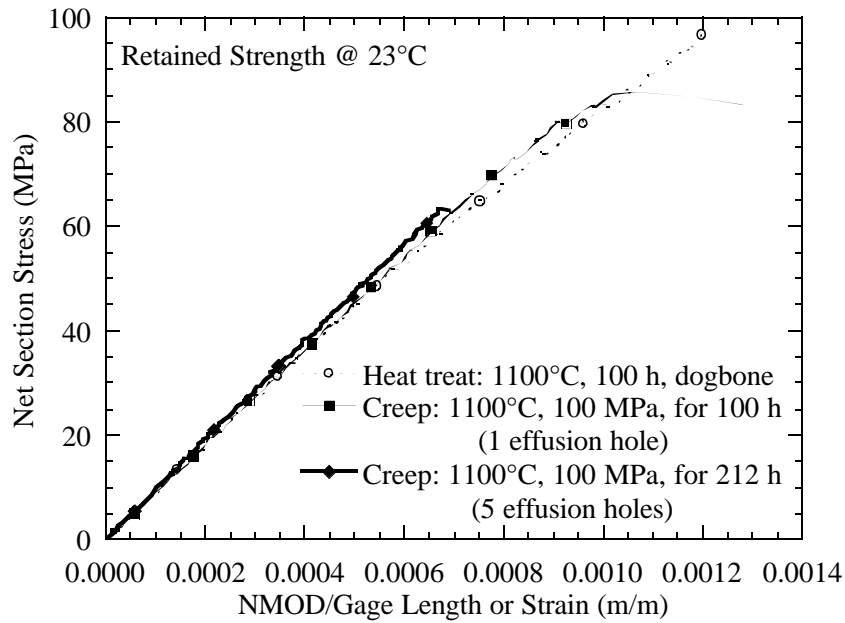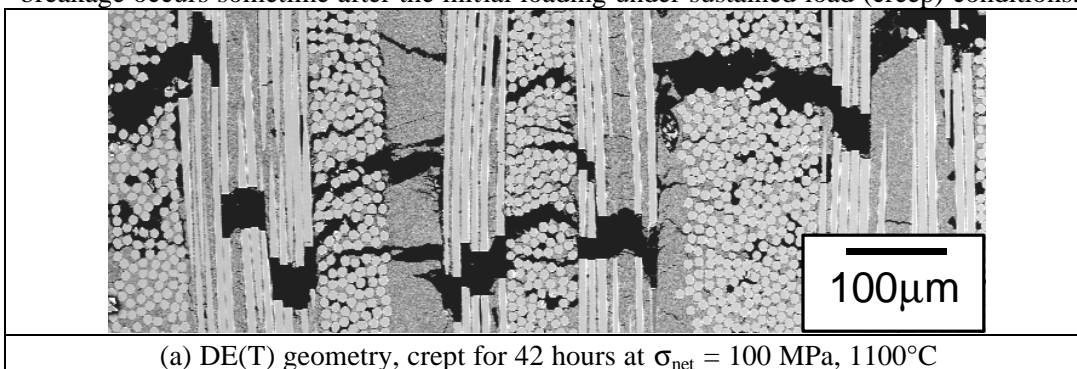

Figure 4. Retained tensile strength for different effusion hole patterns.

Figures 5a and 5b are backscatter scanning electron microscope (SEM) images of polished sections at the notch tips of a DE(T) geometry [17] and the two hole effusion specimen, respectively. In Figs. 5a and 5b the horizontal direction was ≈1mm or half the thickness of the specimen and the vertical direction was ≈ 0.4 mm and coincides with the specimen loading axis. The DE(T) geometry had two edge notches, each of length, a ≈ 1.88 mm, with a normalized notch length of 2a/W ≈ 0.25 and a notch tip radius, r ≈ 0.1 mm. The effusion hole geometry, as shown in Fig. 2, had two effusion holes with radius of r ≈ 0.25 mm. These SEM images were taken at the notch tip. The black areas of the images are mounting epoxy that was used to reinforce the cracks and porosity in the matrix regions during the polishing. Both images show the distributed matrix cracks that were shown in the as received material of Fig. 1. The DE(T) geometry in Fig. 5a shows broken fibers and large matrix cracks at the notch tip for a specimen that was interrupted after 42 hours, approximately 50% of the creep rupture life. In contrast, the two hole effusion geometry in Fig. 5b, which was interrupted after 400 hours, shows no evidence of broken fibers and matrix crack distribution similar to the as received condition. Kramb et al. [17] characterized the damage progression under creep loading for the DE(T) geometry and has shown that fiber breakage occurs sometime after the initial loading under sustained load (creep) conditions.
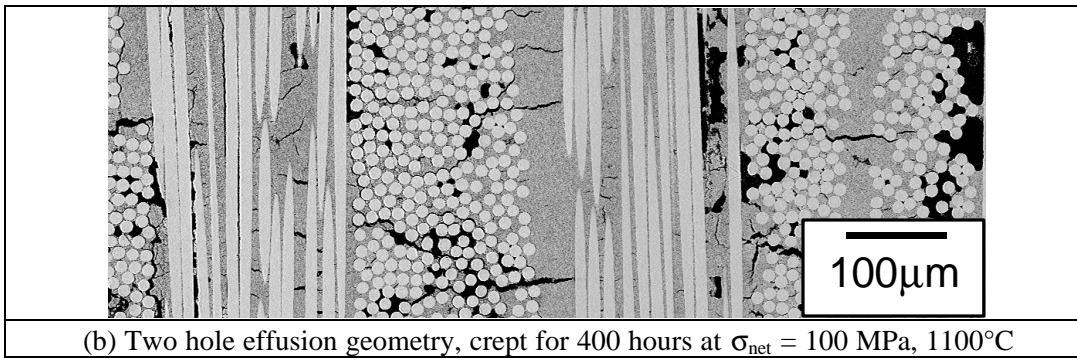

(a) DE(T) geometry, crept for 42 hours at σ_{net} = 100 MPa, 1100°C

(b) Two hole effusion geometry, crept for 400 hours at $\sigma_{net} = 100$ MPa, 1100°C

Figure 5. Fiber and matrix damage at notch tip for DE(T) and effusion hole geometries.
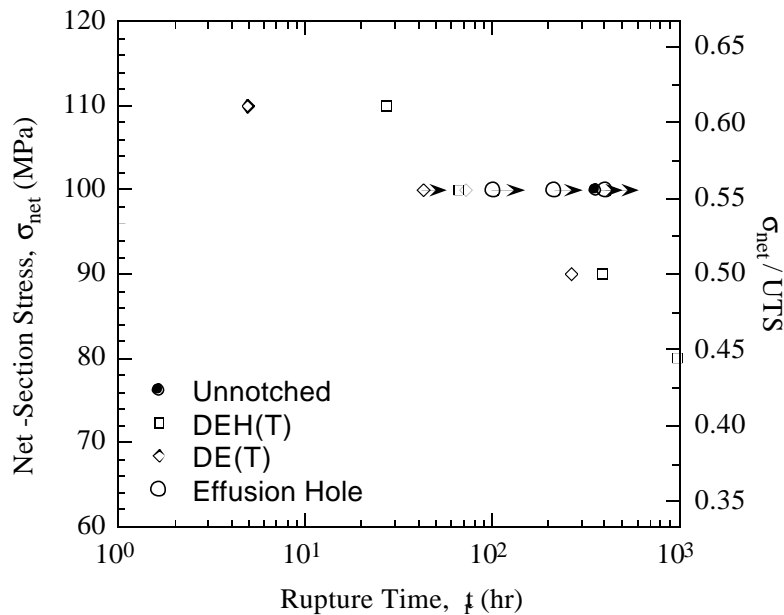

Figure 6. Creep rupture behavior of double notched and effusion hole geometries.

Figure 6 shows the applied net section stress versus creep rupture time for double edge notch and effusion hole geometries at 1100°C. All effusion hole geometries were conducted at net section stress of $\sigma_{net} = 100$ MPa, with all tests interrupted prior to failure. The DE(T) and DEH(T) double edge notched geometries both exhibited rupture lives < 100 hours for $\sigma_{net} = 100$ MPa. The effusion holes specimens show no degradation in creep behavior from the unnotched geometry while the double notched geometries show a reduction in creep rupture life when compared to the unnotched geometry [12,14].

<u>Summary</u>

The creep rupture behavior of oxide/oxide CMC Nextel[TM]720/AS with effusion holes was investigated. Specimens with one, two and five effusion holes were tested under sustained-load (creep) conditions at $\sigma_{net} = 100$ MPa, 1100°C. The creep behavior of the effusion hole geometries and unnotched geometry were similar. SEM images taken at the notch tip of the two-hole effusion specimen showed no evidence of fiber breaks or matrix damage beyond the as received condition. In contrast, the DE(T) geometry showed evidence of extensive fiber breaks and matrix damage when interrupted after only 42 hours.

References

[1] Zawada, L. P. and Lee, S. S., "Mechanical Behavior of CMCs For Flaps and Seals," *Proceedings of Advanced Research Projects Agency (ARPA) Advanced Ceramics Technology Insertion Program (ACTIP) Annual Review*, W.S. Coblenz, Ed., Washington, DC, August 1995.

[2] Zawada, L. P. and Lee, S. S., "Evaluation of Four CMCs For Aerospace Turbine Engine Divergent Flaps and Seals," *Ceramic Engineering and Science Proceedings*, Vol. 16, No. 4, 1995, pp. 337-339.

[3] Mouchon, E. and Colomban, Ph., "Oxide Ceramic Matrix/Oxide Fiber Woven Fabric Composites Exhibiting Dissipative Fracture Behavior," *Composites*, Vol. 26, 1995, pp. 175-182.

[4] Lange, F. F., Tu, W. C, and Evans, A. G., "Processing of Damage-Tolerant, Oxidation- Resistant Ceramic Matrix Composites by a Precursor Infiltration and Pyrolysis Method," *Materials Science and Engineering*, Vol. A195, 1995, pp. 145-150.

[5] Zawada, L. P., Hay, R. S., Lee, S. S., and Staehler, J., "Characterization and High Temperature Mechanical Behavior of an Oxide/Oxide Composite," *Journal of the American Ceramic Society*, Submitted for publication, January 2001.

[6] Zawada, L. P., "Longitudinal and Transverse Tensile Behavior of Several Oxide/Oxide Composites," *Ceramic Engineering and Science Proceedings*, Vol. 19, No. 3, 1998, pp. 327-340.

[7] Levi, C. G., Yang, J. Y., Dalgleish, B. J., Zok, F. W. and Evans, A. G., "Processing and Performance of an All-Oxide Ceramic Composite," *Journal of the American Ceramic Society*, Vol 81, No. 8, 1998, pp. 2077-2086.

[8] Heathcote, J. A, Gong, X. -Y, Yang, J., Ramamurty, U., and Zok, F. W., "In-Plane Mechanical Properties of an All-Oxide Ceramic Composite," *Journal of the American Ceramic Society*, Submitted for publication, 1998.

[9] Wilson, D. M., Lieder, S. L., and Lueneburg, D.C., "Microstructure and High Temperature Properties of Nextel 720 Fibers," *Ceramic Engineering Science Proceedings*, Vol. 16, No. 5, 1995, pp. 1005-1014.

[10] Yun, H. M. and DiCarlo, J. A., "Time/Temperature Dependent Tensile Strength of SiC and Al_2O_3-Based Fibers," *NASA Technical Memorandum 107370*, NASA Glenn Research Center, Cleveland, OH, USA, 1996.

[11] Kramb, V. A., John, R., and Zawada, L. P., "Notched Fracture Behavior of an Oxide/Oxide Ceramic Matrix Composite," *Journal of the American Ceramic Society*, Vol. 82, No. 11, 1999, pp. 3087-3096.

[12] John, R., Buchanan, D. J. and Zawada, L. P., "Notch-Sensitivity of a Woven Oxide/Oxide Ceramic Matrix Composite," *Environmental, Mechanical, and Thermal Properties and Performance of Continuous Fiber Ceramic Composite (CFCC) Materials and Components, ASTM STP 1392*, Michael G. Jenkins, Ed., ASTM, West Conshohocken, PA, Submitted for publication, July 1999.

[13] Buchanan, D. J., John, R., and Zawada, L. P., "Notched Fracture Behavior of Oxide/Oxide Nextel™720/AS Composite," The 24th Annual Cocoa Beach Conference and Exposition, The American Ceramic Society, January 2000.

[14] John, R., Buchanan, D. J. and Zawada, L. P., "Creep Deformation and Rupture Behavior of a Notched Oxide/Oxide Nextel™720/AS Composite," The 24th Annual Cocoa Beach Conference and Exposition, The American Ceramic Society, January 2000.

[15] 3M Company Product Data Sheet, 3M Ceramic Fiber Products, 3M Center-Building 207-1W-11, St. Paul, MN 55144-1000.

[16] Hartman, G. A. and Buchanan, D. J., "Methodologies for Thermal and Mechanical Testing of TMC Materials," *Characterisation of Fibre Reinforced Titanium Matrix Composites*, 77th Meeting of the AGARD Structures and Materials Panel, AGARD Report 796, Bordeaux, France, 27-28 September 1993.

[17] Kramb, V. A., Buchanan, D. J., and John, R., "Damage Progression from Notches in an Oxide/Oxide Ceramic Matrix Composite under Sustained Loads," *Submitted to the Journal of Material Science*, December, 2000.

This page intentionally left blank.

Damage Progression from Notches in an Oxide/Oxide Ceramic Matrix Composite under Sustained Loads

Victoria A. Kramb[1],*, Dennis Buchanan[1] and Reji John

Materials and Manufacturing Directorate (AFRL/MLLN)
Air Force Research Laboratory
Wright-Patterson Air Force Base
OH 45433-7817
USA

[1] University of Dayton Research Institute, 300 College Park, Dayton, OH 45469-0128, USA.
* Corresponding author

Abstract

Damage progression from sharp edge notches in an oxide/oxide ceramic matrix composite was investigated using destructive evaluation of failed and interrupted test specimens. The double edge notched specimens were tested at 1100°C under monotonic and sustained load conditions, in lab air. Results of the study showed that thermal exposure at 1100°C, with zero applied stress produced no significant observable changes in the matrix crack morphology of the composite from the as received condition.   Similarly, rapid loading followed by immediate unloading at 1100°C produced no observable damage in the notch tip region. Under sustained load conditions however, matrix cracking and fiber breakage were observed near the notch tip. The extent of the damage was ≈ 1 mm beyond the notch tip, which roughly the width of an individual fiber tow. A comparison of the fracture surface profiles for creep rupture specimens showed that the damage observed in the unnotched specimens compared closely to that in the notched specimen away from the notch tips. The observed damage progression in notched specimens, indicated that damage within the first fiber tow effectively redistributed the notch tip stress concentration during the initial loading. Under sustained loading, the nearly uniform stress condition away from the notches resulted in overall creep behavior similar to the unnotched composite.

Keywords: ceramic matrix composites, damage progression, creep, notched creep, oxide/oxide, elevated temperature

Introduction

Oxide/oxide ceramic matrix composites (CMC) are currently under consideration for high temperature aerospace applications due to their inherent resistance to oxidation. The oxide/oxide CMC systems produced with Nextel610 or Nextel720 fibers and alumina-silica (AS) matrices utilize no fiber matrix interphase. In these CMC systems, the weak, friable matrix offers a low energy crack path through the composite, allowing cracks to be readily deflected by the fibers [1-3]. This crack deflection mechanism imparts a high degree of damage tolerance to several different oxide/oxide CMC systems at room temperature [4-7]. In particular, the Nextel720/AS system produced by Engineered Ceramics, Inc., exhibited notch insensitive behavior at low temperatures ($\leq$ 1000°C) [6]. However at temperatures $\geq$ 1100°C notch sensitive behavior was observed under tensile loading. Under sustained loads notch sensitivity increased significantly [6]. A change in the notch sensitivity with temperature indicated a change in the damage mechanisms. Kramb et al. [4,5] showed that when temperature was increased from 23 to 950°C a reduction in distributed matrix cracking resulted in a 50% reduction in notch strength in a Nextel610/AS composite produced by General Electric Aircraft Engines Co. Similarly, in this paper, the damage progression from sharp edge notches in Nextel720/AS at 1100°C will be examined and correlated with the change in notch sensitivity under sustained loads.

Experimental Procedure

Material

The Nextel720/AS CMC used in this investigation was produced by Engineered Ceramics, Inc. The Nextel720 fibers, produced by the 3M Company [8], consisted of 85% fine grained (0.05µm) polycrystalline alpha alumina and 15% mullite (SiO_2). The average fiber diameter was approximately 12µm. The individual fibers were bundled into tows containing approximately 400 individual fibers, and woven into an eight harness satin weave (8HSW) cloth. The composite panel used in this study contained 12 plies. Sections of the Nextel720 cloth were prepregged with alumina powder and a silica forming polymer before stacking. No coating was applied to the fibers before prepregging. The green tile was sintered in air at 1000°C. The resulting sintered matrix consisted of porous alumina-silica (AS) that is bonded to the fibers with no naturally occurring or engineered interphase. Extensive microcracking present throughout the matrix is a result of the shrinkage that occurred during processing (Fig. 1). These microcracks are distributed throughout the interior matrix as well as on the specimen surface. Image analysis of polished cross sections showed that the fiber volume fraction was 45%. Further details of the composite processing and microstructure are discussed in [6,9].

Test Procedure

All mechanical testing was conducted in lab air using the double edge notched specimen geometry shown in Fig. 2(a). The specimen ends were rigidly clamped using friction grips, resulting in

rotationally constrained end conditions. The fiber orientation relative to the loading axis was [0°/90°] for all specimens. The edge notches were cut using a diamond saw, which produced a notch height of 0.22 mm. The notch length to specimen width ratio (2a/W) was approximately 0.25.

Monotonic and sustained load tests were conducted using a servo-controlled, hydraulic, horizontal test system [10] under load control, at a rate of 20 MPa/s. Applied load and crack mouth opening displacement (CMOD) were recorded continuously during initial loading and periodically during sustained loads. A high temperature extensometer, with alumina rods, was used to measure CMOD on the edge of the specimen, as shown in Fig. 2(a). Normalized CMOD was calculated by dividing the measured CMOD by the gage length of the extensometer, $\approx$ 9.6 mm.

Elevated Temperature Testing

Heating of the test specimen was achieved using a closed-loop controlled, two-zone oven. Uniform heating ($\pm$1.2% of average) was achieved across 15 mm in length centered on the specimen notch. Temperature was monitored using Platinum-10% Rhodium, S-type, beaded thermocouples that were bonded to the specimen surface using a small drop of Zircar^{TM} (Zircar Products, Inc., 110 North Main Street, Florida, NY 10921) ceramic adhesive. The adhesive was cured for 15 minutes at room temperature and 15 minutes at 100°C. The adhesive was white in color, matching the color of the Nextel720/AS specimen, which eliminated temperature errors due to differential radiant heat absorption. The Zircar^{TM} was also easily removed from the specimen surface after testing. Further details of the test equipment have been described elsewhere [10].

The effect of temperature alone on the Nextel720/AS composite was evaluated by examining as received, untested specimens after varying times at 1100°C. These specimens were sectioned and polished using the same procedures as for the notched test specimens.

Destructive evaluation of interrupted test specimens was performed on specimens that were unloaded and removed from the test frame before fracture. Subsurface damage was identified by sectioning and polishing the specimen in the notch plane region as illustrated in Fig. 2(b). Specimens were vacuum impregnated with Caldofix^{TM} mounting epoxy before polishing to reinforce the matrix cracks and open porosity in the matrix. Polishing using light pressure and water lubricant on a diamond impregnated lapping film successfully polished the surface without causing additional damage to underlying plies. Diamond grit size was decreased from 30 µm for the initial rough polish to 0.5 µm for final polishing. Sectioned and polished specimens were inspected optically and with scanning electron microscopy (SEM). Before SEM imaging, specimens were sputter coated with gold-palladium. Backscatter electron imaging was used to minimize charging effects and to highlight microcracks.

Results and Discussion

<u>Sustained Load Tests at 1100°C</u>

The CMOD versus time behavior for sharp edge notched specimens under sustained loading at 1100°C is shown in Fig. 3(a). The notched deformation behavior can be compared to the unnotched creep strain-time behavior shown in Fig. 3(b). For both specimen geometries, the initial rapid primary creep deformation quickly slows to a secondary steady state creep rate. The secondary creep behavior continues to failure with little or no tertiary creep behavior. However, the unnotched tensile stress-strain behavior shown in Figure 4 shows that without time dependent deformation, the behavior is nearly linear. Nonlinear deformation under sustained loading indicated a change in the damage mechanism had occurred from the monotonic loading. Therefore, destructive evaluation of specimens subjected to sustained loads was conducted to identify the operative damage mechanisms.

The maximum loads chosen for the specimens that underwent destructive evaluation were based on the deformation behavior shown in Fig. 3(a). The maximum stress chosen for the interrupted sustained load tests was σ_n = 100 MPa. An initial assessment of the damage progression was conducted for three loading conditions: (1) notched but untested, (2) notched, monotonically loaded to 100 MPa and immediately unloaded, (3) notched and subjected to a sustained load of 100 MPa for approximately 50% of the creep rupture life. Damage in the notch tip region was evaluated by destructive evaluation of the specimens using the sectioning procedure shown schematically in Fig. 2(b). After removing the specimen from the test system, excess material far from the damage zone was removed above and below the notch plane. The specimen was then sectioned perpendicular to the notch in the loading direction, just behind the notch tip. The sectioned specimens were then polished along this through-thickness cross-section to obtain a view of the damage in the notch tip region. The top surface matrix was removed on the faces of some sections, so that the 0° fibers within the top surface ply could be observed. All polished specimen cross sections were imaged using SEM as previously discussed.

The effect of thermal exposure on the matrix crack morphology of the Nextel720/AS composite was assessed by comparing polished cross sections in the as received condition and after 62 hours at 1100°C. A comparison of the micrographs in Fig. 5 show that the large matrix cracks within the matrix rich regions in the as received composite showed no differences after the thermal exposure. The small (<50μm) matrix cracks between fibers within the tows showed some evidence of coarsening, however this effect was very slight. Overall the observed differences between matrix crack morphology in the as received and thermally exposed conditions were minimal. Results of tension tests conducted on specimens that were subjected to thermal exposure at 1100°C showed a reduction in tensile strength. However, the reduction in composite tensile strength due to thermal exposure was not reflected by an observable change in the pre-existing processing cracks.

Damage that may have occurred while cutting the notch was examined in a specimen that was notched but untested. The polished cross-section shown in Fig. 6(a), revealed no longitudinal fiber breaks immediately behind the notch tip region. A comparison with the matrix cracking in the as received composite (Fig. 5(a)) shows that the matrix crack morphology in both specimens is similar. Thus, the extent of damage ahead of the notch due to the saw cut was also minimal.

The effect of initial loading was examined by comparing the notch tip region of the as saw-cut specimen to that of the specimen loaded to 100MPa and immediately unloaded (at 1100°C). Figure 6(b) shows that no longitudinal fiber breaks were observed due to loading the specimen. Similarly, the matrix crack pattern was similar to that of the unnotched thermal exposure specimen. Thus, the observable damage in the notch tip region due to the rapid loading was very limited. Minimal damage during the initial loading is consistent with the nearly linear deformation behavior for monotonic tension tests. Thus, the observed lack of additional matrix cracking or fiber breakage in the notch tip region indicates that the effects of rapid initial loading and temperature exposure on damage progression are minimal.

The effect of sustained loads on the damage progression was examined through destructive evaluation of an interrupted notched creep test specimen. This specimen was subjected to 43 hours at 100 MPa, which corresponds to approximately 50% of the creep rupture life at that stress level. The damage progression from both notch tips was examined and compared. As shown in Figure 6(c), immediately behind both the notch tips matrix cracks became interconnected and traversed several plies of the composite. In addition, longitudinal fiber breaks occurred along the matrix crack. Further polishing behind one notch tip showed that the interconnected matrix cracking and longitudinal fiber breaks were no longer observed at a depth of 0.5 mm (Fig. 7a). The crack growing from the opposite notch however, exhibited longitudinal fiber breaks up to 1.3 mm from the notch tip (Fig. 7b). The presence of a crack at each notch tip indicates that crack formation occurred early in the creep test. Under continued sustained loads, the growth of a dominant crack from one of the notch tips would result in a longer crack length. Nevertheless, the average extent of fiber breakage and matrix crack growth ahead of the notch tip was $\approx$ 1 mm after 43 hours at 100 MPa. A typical fiber tow is approximately 0.9 mm in width, therefore, a damage zone $\approx$ 1 mm in length indicated that the stress concentration produced by the saw-cut notch tip was effectively redistributed within the first fiber tow ahead of the notch tip. The matrix cracks observed farther away from the notch tip (> 1.5 mm) were nearly the same as that observed for the as received and thermal exposure specimens. Thus, > 1.5 mm away from the notch tip no effect of sustained loading on the composite was observed.

The fracture surface profiles of creep rupture specimens were also examined to identify damage mechanisms that occur during final failure. The fracture surface profile for the DE(T) specimen that failed after 72 hours at σ_n = 100 MPa is shown in Figure 8(a). Near the left notch tip, individual fibers extend 1-2 mm from the notch plane. Extensive matrix cracking between fibers and tows allowed plies to fail on different planes, thus no single crack can be defined extending from the notch tip. Away from the notch tip matrix cracking between fibers is reduced, resulting in failure of the longitudinal fibers as bundles or entire tows. The fracture behavior away from the notches compares closely to that of the unnotched creep rupture specimen shown in Fig. 8(b). The similarity between the fracture profiles of the unnotched creep specimen and the central portion of the DE(T) specimen indicates that the matrix cracking and fiber breakage observed near the notch tip occurred very rapidly during the primary creep. This distributed damage zone effectively redistributed the stress concentration ahead of the notch during the primary creep. The stress redistribution resulted in a nearly uniform stress condition across the remaining undamaged ligament of the DE(T) specimen. As a result of the nearly uniform stress condition in both specimens, the secondary creep behavior of the DE(T) specimen was similar to that of the unnotched creep specimen.

Summary and Conclusion

The results of the destructive evaluation showed that the damage mechanisms and fracture behavior in Nextel 720/AS CMC are time and stress dependent at 1100°C. A comparison of the matrix crack morphology in the as received composite with that in a specimen exposed for 62 hours at 1100°C resulted in no significant observable differences. Similarly, observations of damage progression from sharp edge notches showed that rapid loading followed by immediate unloading resulted in no observable changes in the fiber or matrix crack morphology from the as saw-cut condition. Under sustained load conditions however, distributed matrix cracking and longitudinal fiber breakage were observed. After 43 hours at $\sigma_n = 100$ MPa, matrix cracking and longitudinal fiber breakage were observed over a region ≈ 1 mm ahead of the notch tip. Fracture surface profiles for the edge notched creep rupture specimens showed that immediately ahead of the notch tip, longitudinal fibers extended far from the fracture plane. In contrast, away from the notches in the middle ligament of the specimen, the fracture profile was relatively flat with very little fiber extension. A comparison between the fracture surface profiles of edge notched and unnotched creep rupture specimens showed that the flat fracture morphology exhibited by the edge notched specimen was very similar to that observed in the unnotched creep rupture specimen. Thus, in edge notched specimens under sustained loads, damage occurred rapidly during the primary creep near the notch tip. Secondary creep behavior for the undamaged ligament in the edge notched specimen was similar to that of the unnotched creep specimen.

References

1. T. J. Lu, *J. Am. Ceram. Soc.* **1** (1996) 266.

2. W. C. Tu, F. F. Lange and A. G. Evans, *J. Am. Ceram. Soc.* **2** (1996) 417.

3. C. G. Levi, J. Y. Yang, B. J. Dalgleish, F. W. Zok and A. G. Evans, *J. Am. Ceram. Soc.* **8** (1998) 2077.

4. V. A. Kramb, R. John, L. P. Zawada, *J. Am. Ceram. Soc.* **11** (1999) 3087.

5. V. A. Kramb, Ph.D. Thesis, University of Dayton, Department of Materials Engineering, 1999.

6. R. John, D. J. Buchanan and L. P. Zawada, in "Environmental, Mechanical, and Thermal Properties and Performance of Continuous Fiber Ceramic Composite (CFCC) Materials and Components, ASTM STP 1392", (American Society for Testing and Materials, West Conshohocken, PA, 2000).

7. J. A. Heathcote, X. Y. Gong, J. Y. Yang, U. Ramamurty and F. W. Zok, *J. Am. Ceram. Soc.* **10** (1999) 2721.

8. 3M Company Product Data Sheet, 3M Ceramic Fibers Products, 3M Center-Building 207-1W-11, St. Paul, MN 55144-1000.

9. L. P. Zawada, Ceram. Eng. Sci. Proc. **3** (1998) 327.

10. G. A. Hartman and S. M. Russ, in "Metal matrix composites: testing, analysis, and failure modes, ASTM STP 1032", (American Society for Testing and Materials, Philadelphia, PA, 1989).

Figure Captions

Figure 1.   Nextel720/AS composite polished cross section optical micrographs (a) microstructure of the [0/90] composite (b) higher magnification micrograph exhibiting matrix cracks due to processing.

Figure 2.   Schematic of (a) double edge notched DE(T) specimen geometry, W = 15.0 mm, B = 2.6 mm and 2a/W = 0.25. (b) notch region sectioned for damage assessment.

Figure 3.   Effect of applied stress level on sustained load behavior at 1100°C (a) DE(T) geometry (b) unnotched specimen.

Figure 4.   Tensile stress-strain behavior of Nextel720/AS (a) DE(T) geometry (b) unnotched composite.

Figure 5.   SEM micrographs of polished sections (a) as received composite (b) as received composite after 62 hour thermal exposure at 1100°C. White arrows indicate matrix cracks due to processing.

Figure 6.   SEM micrographs of the notch tip region for (a) an untested, as saw-cut, specimen, (b) after loading to $\sigma_n = 100$ MPa with immediate unloading (c) interrupted after 43 hours at $\sigma_n = 100$ MPa. The white arrow in (c) indicates broken longitudinal (0°) fibers.

Figure 7.   SEM micrographs of the region approximately 0.5 mm ahead of the notch tip, DE(T) creep specimen interrupted after 43 hours at $\sigma_n = 100$ MPa.

Figure 8.   Fracture surface profiles of creep test specimens at 1100°C (a) DE(T) $\sigma_n = 100$ MPa (b) unnotched specimen, $\sigma = 150$ MPa
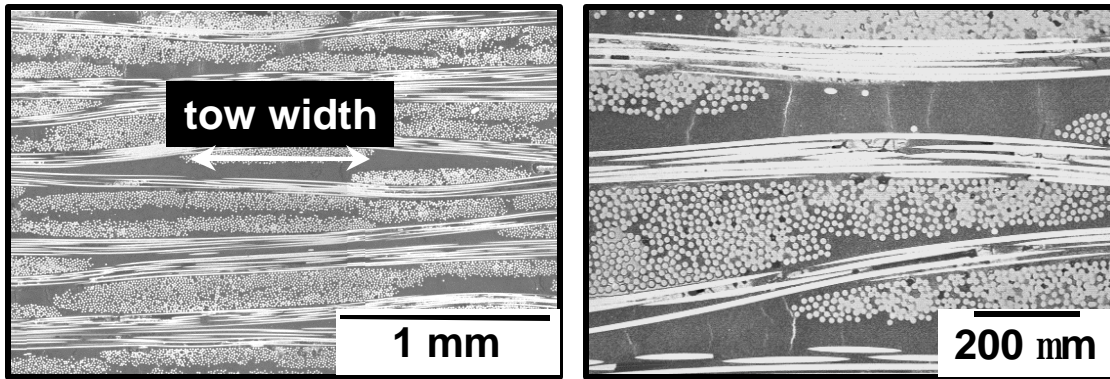
Figure 1. Nextel720/AS composite polished cross section optical micrographs: (a) microstructure of the [0/90] composite (b) higher magnification micrograph exhibiting matrix cracks due to processing.
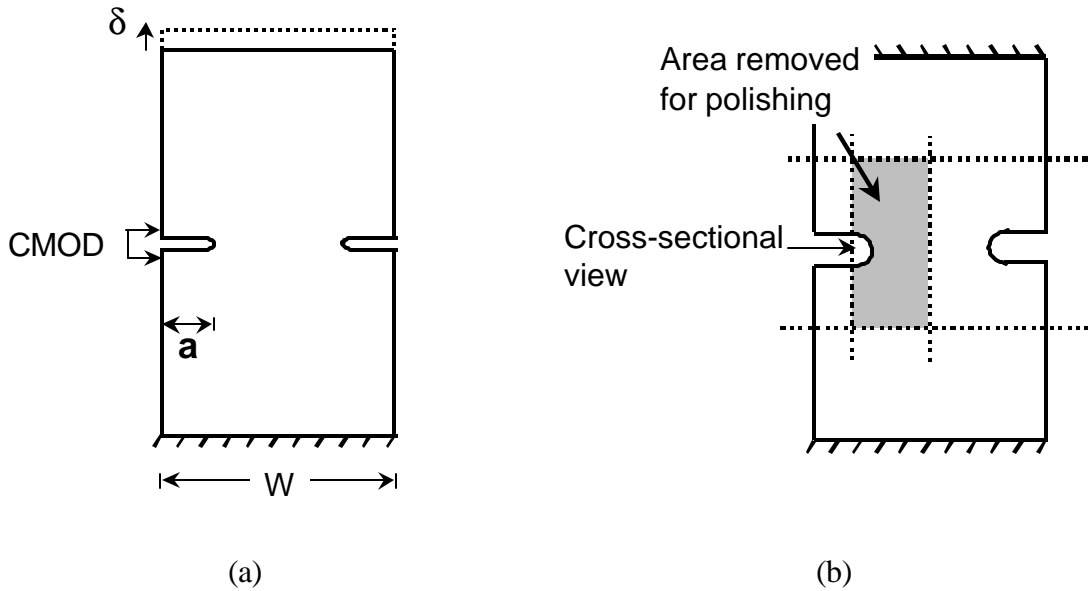

(a)   (b)

Figure 2. Schematic of (a) double edge notched DE(T) specimen geometry, W = 15.0 mm, B = 2.6 mm and 2a/W = 0.25. (b) notch region sectioned for damage assessment.
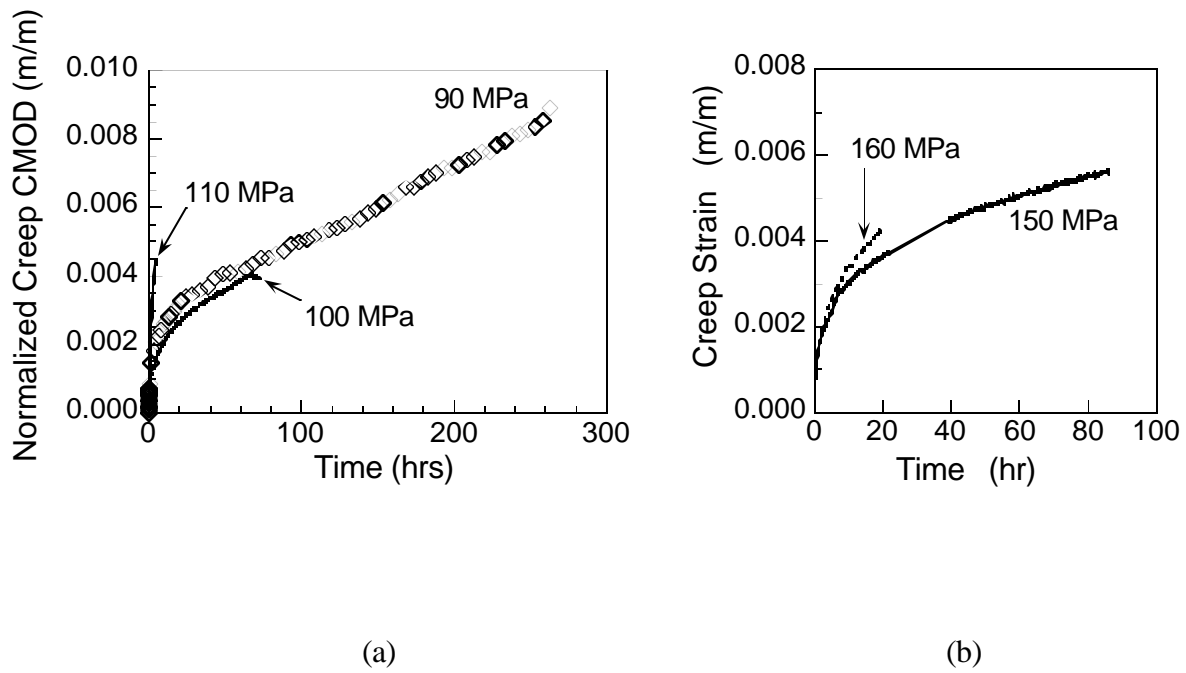
(a)   (b)

Figure 3. Effect of applied stress level on sustained load behavior at 1100°C (a) DE(T) geometry (b) unnotched composite.

(a)   (b)
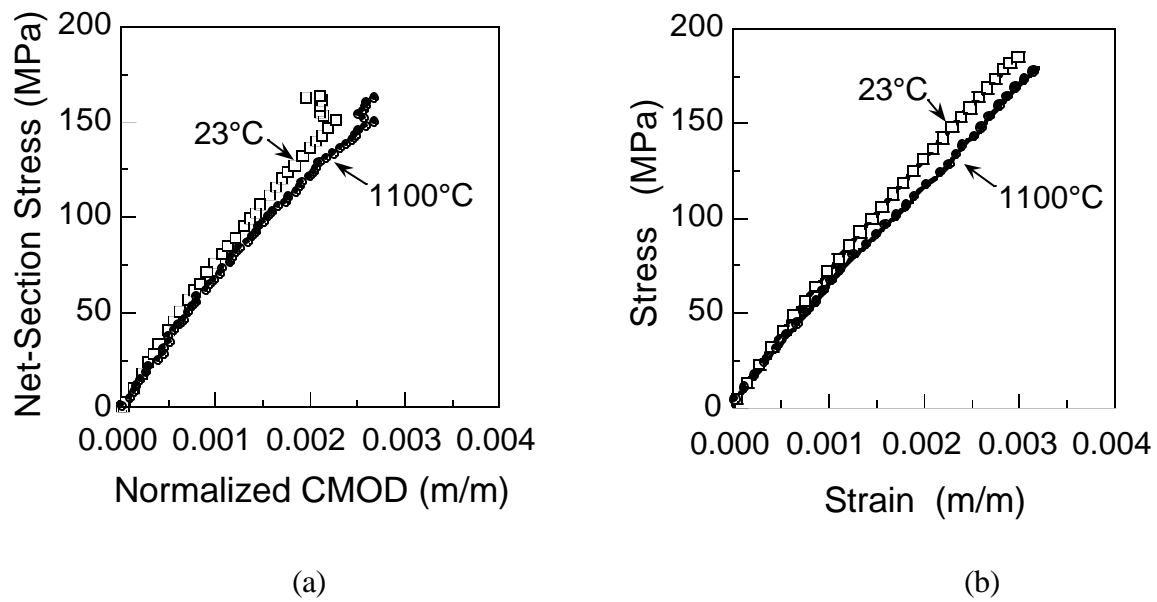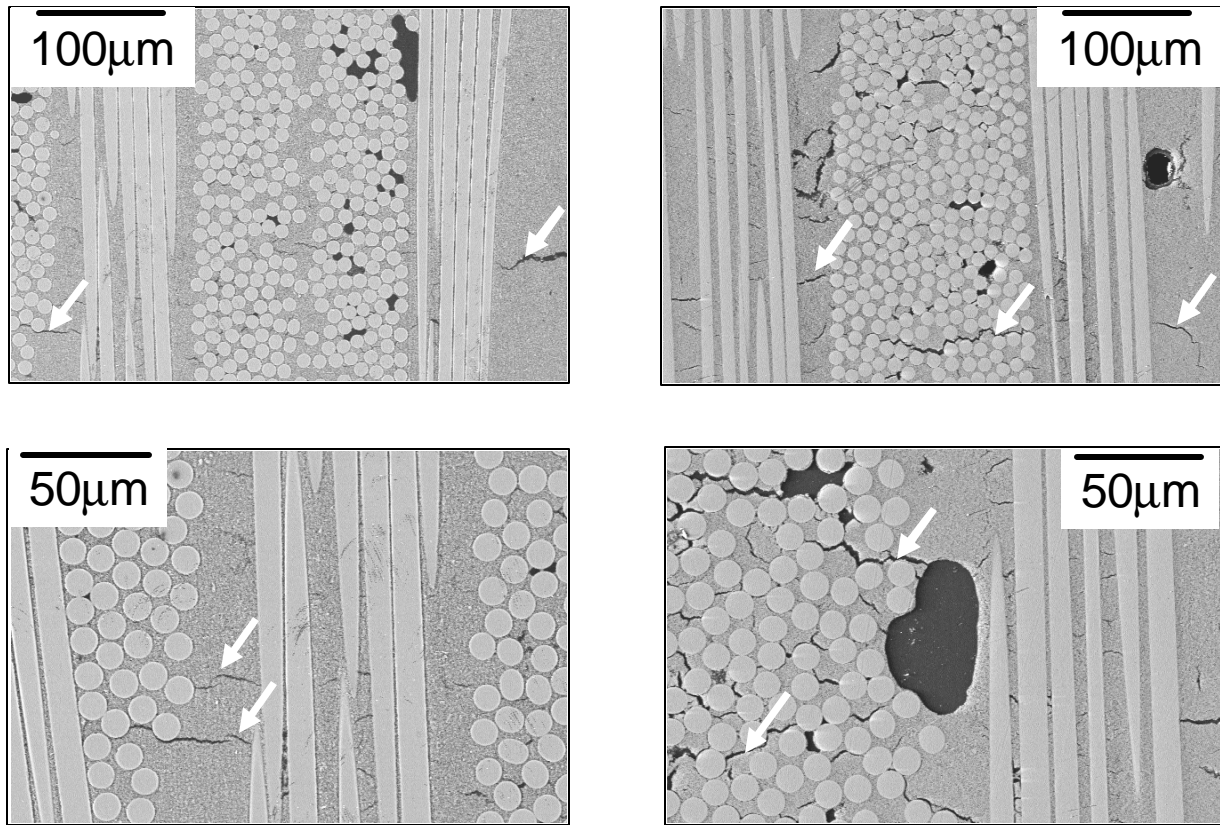
Figure 4.   Tensile stress-strain behavior of Nextel720/AS (a) DE(T) geometry (b) unnotched composite.

(a)   (b)

Figure 5.   SEM micrographs of polished sections (a) as received composite (b) as received composite after 62 hour thermal exposure at 1100°C. White arrows indicate matrix cracks due to processing.
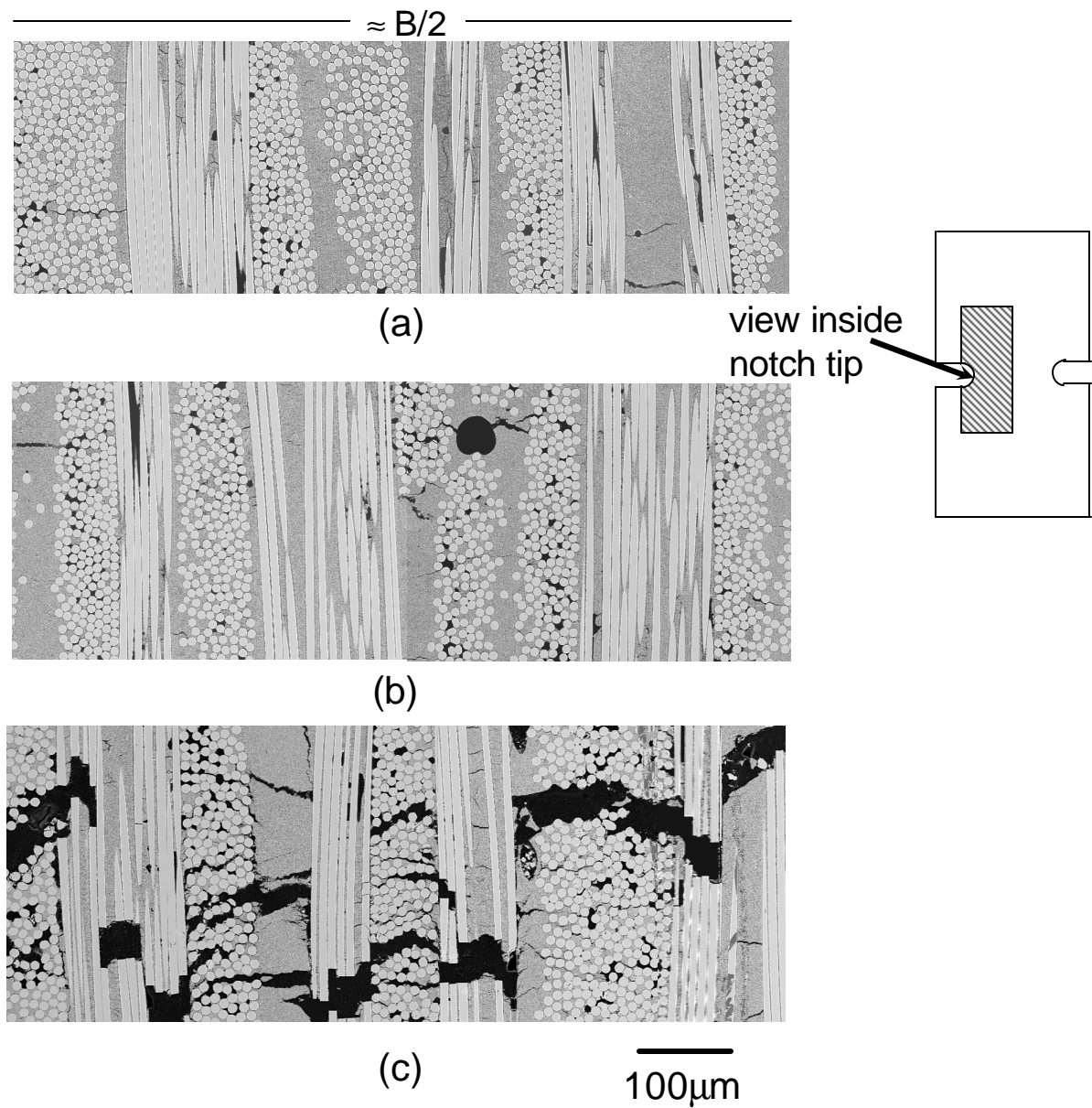
Figure 6. SEM micrographs immediately ahead of the notch tip in (a) an untested, as saw-cut, specimen, (b) after loading to $\sigma_n = 100$ MPa with immediate unloading (c) an interrupted creep test specimen after 43 hours at $\sigma_n = 100$ MPa.
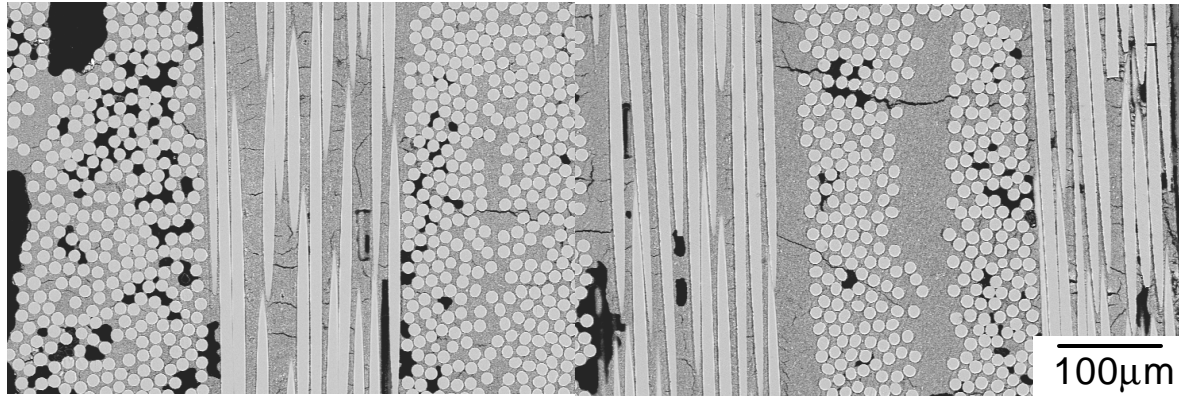
(a)
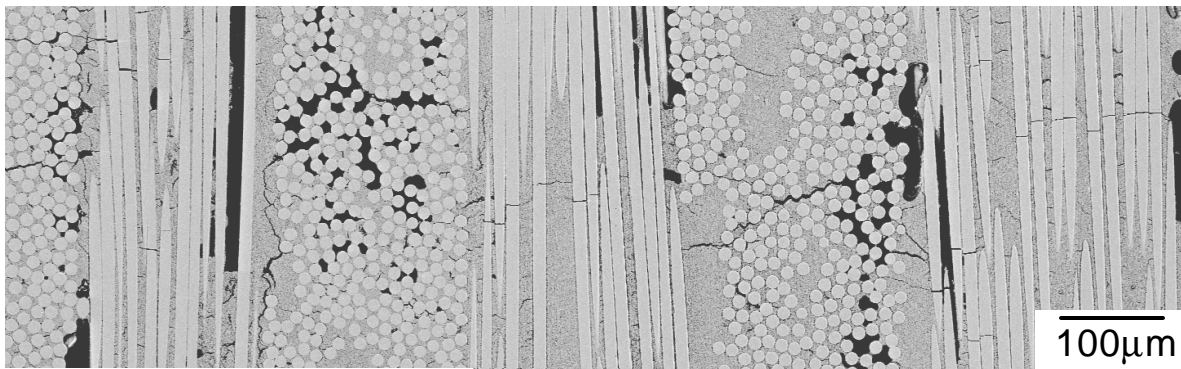
(b)

Figure 7.   SEM micrographs of the crack tip region ahead of both notch tips. (a) crack tip approximately 0.5 mm notch tip showing no further crack growth (b) crack tip region ahead of the opposite notch approximately 1.3 mm from the notch tip. DE(T) creep specimen interrupted after 43 hours at $\sigma_n = 100$ MPa.

notch tip   1.0 mm   notch tip

(a)

1.0 mm
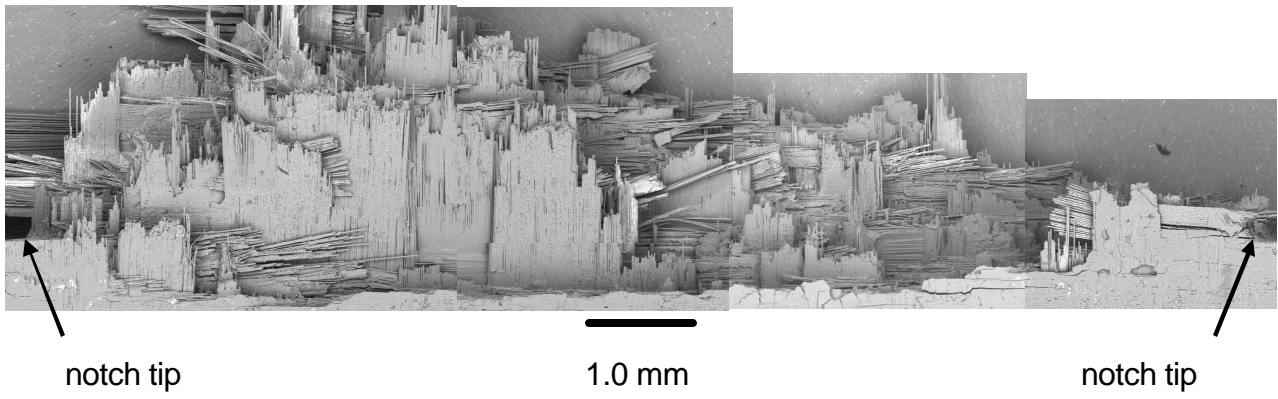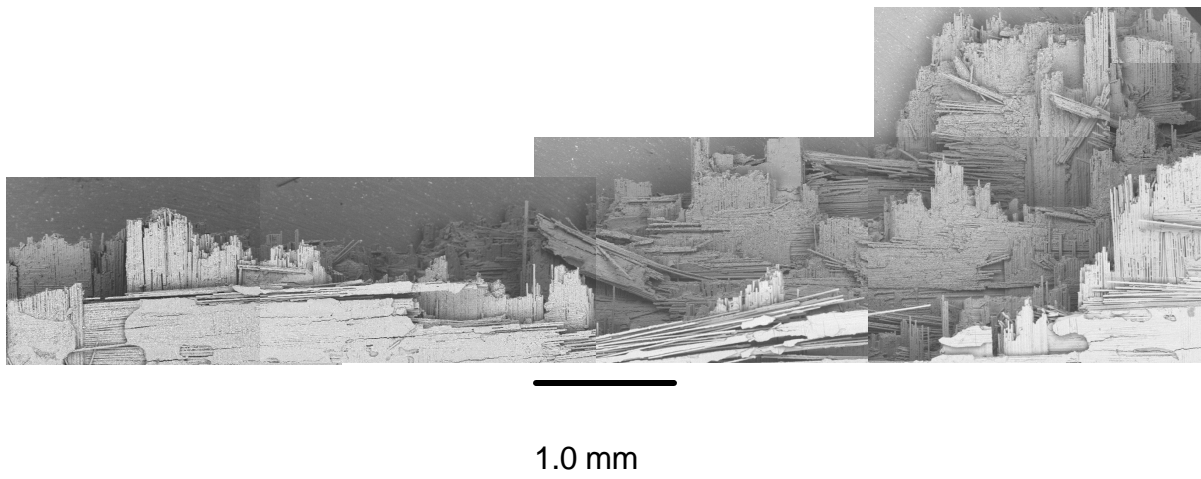
(b)

Figure 8.   Fracture surface profiles of creep test specimens at 1100°C (a) DE(T) σ_n = 100 MPa (b) unnotched specimen, σ = 150 MPa

This page intentionally left blank.

Alisha Hutson*
Advanced Materials Characterization Group, Structural Integrity Division
University of Dayton Research Institute, Dayton, OH 45469-0128, USA.

Mitsuo Niinomi
Department of Production Systems Engineering, Toyohashi University of Technology, 1-1,
Hibarigaoka, Tempaku-cho, Toyohashi 441-8580, Japan

Ted Nicholas
Air Force Research Laboratory, Materials & Manufacturing Directorate (AFRL/MLLMN),
Wright-Patterson Air Force Base, OH 45433-7817, USA.

Daniel Eylon
Graduate Materials Engineering, University of Dayton, Dayton OH 45469-0240, USA

ABSTRACT

An experimental investigation was conducted to explore the fretting fatigue behavior of Ti-6Al-4V specimens in contact with varying pad conditions. Four pad conditions were selected: bare Ti-6Al-4V with a ~1 μm finish, bare Ti-6Al-4V that was low-stress ground and polished to RMS #8 (designated as "as-received"), bare Ti-6Al-4V that was grit blasted and stress relieved to RMS #64, and Cu-Ni plasma spay coated Ti-6Al-4V. Behavior against the CuNi coated and as-received pads was characterized through determination of a fretting fatigue limit for a 10^7 cycle fatigue life. In addition, the behavior against all four pad conditions was evaluated with S-N fatigue testing, and the integrity of the Cu-Ni coating over repeated testing was assessed and compared with behavior of specimens tested against the as-received and roughened pads. The coefficient of friction, μ, was evaluated to help identify possible crack nucleation mechanisms, which are discussed. Characterization of the untested contact pad surfaces is presented.

INTRODUCTION

Fretting fatigue is a phenomenon that can occur wherever vibrating machinery comes in contact and at least one of the components is subjected to bulk loading. It often results in damage that may lead to premature component failure. The problem has been observed in many places, from the multi-strand steel cables used for ship rigging to the rotating components of aircraft engines. Because the problem is so widespread, it has been the focus of numerous investigations conducted world wide on a variety of test geometries and material systems [1-9]. Fretting fatigue often takes place in the presence of other types of damage, leading to confusion regarding the source of and micro-mechanisms responsible for premature failures. With the myriad of conditions influencing the fretting fatigue phenomenon, a comprehensive understanding of how fretting fatigue occurs and the follow-on of accurate life prediction modeling has been elusive.

The development of an all encompassing test apparatus to investigate fretting fatigue has been equally difficult. Most investigations to date have focused either on a specialized geometry specific to a few applications or on a geometry designed to investigate the fundamentals of fretting fatigue. In previous work by the authors, a test system was developed to simulate fretting fatigue as it occurs in turbine engine blade attachments while allowing investigation of fretting fatigue in a generalized geometry that can relate to many types of applications. Turbine engine blade roots, and the companion component region on the disks, experience fretting in a flat-on-flat contact with rather large radii at the edges of contact. The apparatus that was developed employs flat fretting pads, with

radii at the edges of contact, against a flat specimen. While this type of geometry does not lend itself to analysis as well as other geometries that have been the focus of the bulk of fretting fatigue research, a geometry that provides information at an intermediate level of complexity is required as the next step toward the development of an accurate life prediction model that bridges the gap between laboratory and service conditions.

Another step to bridging the gap between experimental investigations and the problems observed in service involves investigating the material systems, complete with fretting palliatives, currently in use. Previous investigations by the authors have addressed fretting fatigue behavior of the raw materials under the flat-on-flat with blending radii contact geometry [10, 11] and some preliminary work has been conducted to assess fretting fatigue behavior with a coating comparable to those used in turbine engines [12]. The purpose of the present investigation is to interrogate the effect of both composition and surface topography of a Cu-Ni plasma spray deposited coating on fretting fatigue behavior using the Ti-6Al-4V substrate investigated in earlier work and to identify mechanisms responsible for observed differences in behavior. Qualitative characterization of the contact surfaces using scanning electron microscopy (SEM) is included.

EXPERIMENTATION

2.1   Testing Apparatus

The fretting experiment used in this study was designed to closely simulate the primary loading conditions under which fretting fatigue damage occurs in turbine engine blade attachments. The test geometry employs flat fretting pads, with a radius at the edge of contact, against a flat specimen under axial fatigue, as in Figure 1. The static clamping load is imposed via instrumented bolts, whose internal strain gages allow quantification of the clamping load. An electromagnetic shaker system was used to apply the axial fatigue loads. Removable fretting pads facilitated control of the surface conditions. The test configuration, which employs identical gripping at both ends of the specimen, produced two nominally identical fretting fatigue tests for each specimen. Fretting damage in the form of wear scars and cracks occurred at both ends of the specimens at the edges of contact, shown in the magnified view in Figure 1. Additional details of the test apparatus can be found in [10].

2.2   Material

Two Ti-6Al-4V microstructures have been tested to date: bar stock, which refers to a vacuum annealed and stress relieved microstructure, and plate stock, which refers to a forged $\alpha+\beta$ duplex microstructure that has been used for the bulk of a U. S. Air Force sponsored high cycle fatigue program [13, 14]. Because the two microstructures have different material properties, the results are presented normalized with the appropriate parameter to allow a comparison independent of material properties. Where normalization of the data is deemed inappropriate, the necessary labels are included. All specimens and fretting pads were initially low stress ground to a # 8 surface finish. Some pad and specimen surface conditions were changed after manufacturing, as described in the next section.

2.3   Test Matrix

To achieve the objective of characterizing fretting fatigue behavior as a function of contact material and surface roughness, a test matrix was developed to incorporate bare Ti-6Al-4V, over a range of contact pad roughnesses, and Cu-Ni plasma spray coated pads. The Cu-Ni coating was deposited on as-received Ti-6Al-4V pads via a plasma spray process representative of that used in real hardware [12]. Some uncoated Ti-6Al-4V pads were modified from the as-received condition to achieve a smoother surface through metalographic mechanical polishing. Additional pads were modified to achieve a rougher surface through grit blasting and subsequent stress relief annealing. The rougher surface was intended to simulate the roughness of the Cu-Ni coated pads to determine if previously observed changes in fretting fatigue behavior were a result of the coating or of the rougher surface [12]. Representative photos of each pad type are shown in Figures 2a -d.

The test condition selected for this investigation was identified based on prior work [10, 11]. Baseline data for R=0.5 from the previous work using as-received pads are presented in Figure 3 for a broad range of test conditions produced with various combinations of pad geometry and clamping loads. The fatigue limit data in figure 3 are presented as normalized with the unfretted fatigue limit for the respective materials, plotted against the

100

average applied clamping stress. A clamping stress of 420 MPa (note solid vertical line in Figure 3) was identified as the highest clamping stress that a blade attachment region might experience in service, so it was selected as the focus of this investigation [15]. As with previous work, a blending radius of 3.175 mm and a nominal pad length of 12.7 mm were maintained, resulting in a contact length of 6.35 mm. To achieve the 420 MPa clamping stress on a 10 mm wide fretting specimen with the 6.35 mm contact length, a 26 kN clamping load was required. Note that actual clamping stresses (shown in Figure 3) are approximately 30% higher than was intended due to the manner in which the clamping load was controlled; however, the higher clamping stress condition was consistent throughout the testing for this study, so that the comparisons made below are still valid. For this investigation the actual clamping stress imposed was ~ 620 MPa. A stress ratio of 0.5 was selected as best representing service conditions of blade attachments from the stress ratio values incorporated in previous work.

All baseline tests [10, 11] were conducted using a step loading procedure to obtain the fretting fatigue limit for a 10^7 cycle fatigue life. The procedure involves applying blocks of cycles at increasing values of constant maximum stress for each block of cycles until the specimen fractures, and then calculating the fatigue limit from the final stress, number of cycles at the final stress, and the stress from the prior block, using linear interpolation [16]. The test matrix, given in Table 1, includs tests conducted using the step loading procedure to compare the behavior of specimens tested against as-received pads and Cu-Ni coated pads for a 10^7 cycle fatigue life. In each of these tests, the initial axial stress was selected based on the need to run at least 10^7 cycles at that stress.

Since coefficient of friction, μ, has been identified as an important parameter in fretting fatigue behavior, two gross sliding tests were conducted to quantify μ for the as-received and Cu-Ni coated pad conditions. For these tests, the specimen was clamped in the same configuration used for the fatigue tests, and was then subjected to a constant displacement of 0.02 mm/s over a total displacement of ~ 8 mm. Ambient laboratory conditions were maintained throughout each test. Coefficient of friction was calculated by dividing the axial load at the onset of gross sliding, identified by changes in the slope of the load versus stroke curve, by the clamping load.

Comparison of the Cu-Ni versus as-received behavior was also evaluated by conducting fretting fatigue tests using a typical S-N approach. The S-N tests were conducted against polished pads and roughened pads as well as the as-received and Cu-Ni coated pads to help identify damage mechanisms responsible for observed differences in the step test results. Each specimen was tested at a maximum axial stress of 300 MPa at a stress ratio of 0.5. The reason for the choice of 300 MPa as the maximum axial stress is given later.

Finally four sets of tests were conducted to quantify how the pads would wear under repeated use. (Some results are reported in [qf12].) These tests are identified as "Series of 5" tests in the tables and figures that follow. In each series, five specimens were tested in sequence against a single set of pads. As with the S-N tests, each specimen was subjected to 300 MPa at a stress ratio of 0.5. All fatigue tests were conducted under ambient laboratory conditions at constant frequency with values ranging from 300 to 400 Hz, depending on the value necessary to avoid resonance conditions.

RESULTS & DISCUSSION

The data presented below are given in both tabular and graphical forms, as appropriate. Data in tabular form are included to provide information on details of fracture location, applied clamping stress and % deviation, which refers to the amount the applied load varies across the contact as a percentage of the total applied load.

3.1   *As-received vs. Cu-Ni Coated Pads*

The initial comparison of fretting fatigue behavior with as-received and Cu-Ni coated pads was conducted through the step tests identified in Table 1, for which the results are given in Table 2 and Figure 3 [12]. A step test was successfully conducted with the as-received contact pads, resulting in a fatigue limit of ~ 265 MPa. This datum (normalized with the unfretted fatigue limit) is represented in Figure 3 by a solid, inverted triangle along with results at nominally identical conditions from [11], indicated by hollow circles. The average fatigue limit from the current test result and the data from [11] is ~ 250 MPa. The level of scatter in these tests was relatively low, producing a standard deviation of ~ 11.4 MPa, even though average clamping stresses differed by as much as 10%.

The first step test with the Cu-Ni coated pads was conducted with the initial stress selected assuming no improvement from the as-received pad condition. The result was a successful step test, shown by the solid circle in Figure 3, in which an appreciable increase in fatigue limit was noted (see 98-586 in Table 2 – initial stress = 240 MPa) [12]. Another step test was attempted. This time the initial stress of 300 MPa was selected to minimize the number of steps and dispel any question of coaxing due to the step loading process. However, the specimen (98-587

in Table 2) failed in the first loading block. Another step test with Cu-Ni pads was attempted using the same initial conditions as the first tests against Cu-Ni pads. A fatigue limit of over 300 MPa, for which the normalized value is noted by the solid square in Figure 3, was obtained (see 97-008 in Table 2).

Note that the two successful step tests against Cu-Ni coated pads were conducted at substantially different clamping stresses. By the time 97-008 was conducted, the system used to control the clamping loads had been improved, so the intended 420 MPa clamping stress could be achieved with greater accuracy. Also, 97-008 was conducted on Ti-6Al-4V bar stock while 98-586 was conducted on Ti-6Al-4V plate stock. When the fretting fatigue limits for these two tests are normalized with unfretted fatigue limits for their respective materials, the results are 0.38 and 0.50. 97-008 cannot be said to differ from the baseline bar stock results in any significant way; however, 98-586 indicated an improvement in fretting fatigue behavior compared to the baseline plate stock results. In short, the improvement allowed by the Cu-Ni coating is moderate.

Because of the time and expense involved in coating additional pads, fatigue lives were determined for the remaining tests, allowing the "early" failure of 98-587 to be evaluated against other S-N tests. Six S-N tests were conducted at 300 MPa at R = 0.5 (the conditions used for 98-587) against as-received pads. Multiple tests were conducted to evaluate statistical variability. The mean fatigue life for these tests was 1,450,000 cycles with lives ranging from 530,000 to 2,500,000 cycles.

Figure 4 shows the S-N data from these tests compared to the tests against Cu-Ni pads and the fatigue limit data presented above. Tests against Cu-Ni pads produced higher lives than the as-received pad, indicating an improvement in fretting fatigue behavior also noted in the fatigue limit data. However, these results taken alone, do not indicate the mechanisms responsible for the differences in mechanical behavior.

3.2 Coefficient of Friction Measurements

Coefficient of friction has been identified as a key parameter in understanding and modeling fretting fatigue behavior. Thus, measurements of coefficient of friction, μ, were made for the as-received and Cu-Ni coated pads against as-received specimens to identify the source of differences in both fatigue limits and fatigue lives observed in the results described in the previous section. The tests designed to quantify μ were stroke controlled tension tests in which the specimen, gripped in the same manner as in the fatigue tests, was allowed to slip in the grips while axial load as a function of time was acquired. A clamping load of 21 kN was used to minimize the possibility of plastic deformation due to the clamping load. The resulting clamping stress was 330 MPa. No attempt was made to evaluate μ locally along the contact. Rather, an average value of μ for the entire contact region was calculated from the clamping load and the axial load at the onset of gross slip, thereby allowing a comparison of μ and slip behavior characteristic of the contact conditions used throughout this investigation.

One test for each pad condition was conducted and the results are shown in Figure 5 and Table 3. For these tests, the clamping stresses were closely controlled to minimize % deviation while maintaining nominally identical clamping stresses between the tests. The curves do not reflect the general trend one expects for a transition from partial stick to gross sliding and so the identification of gross slip and thus, the selection of loads to calculate μ was difficult. The loads identified with gross sliding are shown in Figure 5. Details of clamping stress, % deviation, and resultant values of μ are shown in Table 3. For the Cu-Ni coated pads, the load did not level out to a constant value in the gross sliding portion of the test. The monotonically increasing load observed beyond 0.6 mm is most likely a result of contact asperities on the fretting pads gouging troughs in the specimen surface. Still, the transition from partial slip to gross sliding for the Cu-Ni pad contact is distinct compared to the behavior of the as-received contact.

The load vs. stroke curve produced with the as-received surface shows a bilinear behavior in the first portion of the curve where partial slip is occurring, followed by transition to a nominally constant load during the gross sliding portion of the test. Sliding of approximately the same magnitude was observed in both grips for this contact condition, whereas the Cu-Ni pad slipped only in the upper grip. The intersection of the two linear regions observed in the first portion of the curve may mark the point during the test where gross sliding began in one of the grips. This intersection occurs at a load that would result in a coefficient of friction of approximately 0.3, which is closer to what one would expect for relatively smooth Ti-6Al-4V than the value of 0.7 calculated from the 14.6 kN axial load. One possible explanation for the 14.6 kN load is that μ increased as the pad slipped along the specimen, thus requiring increasingly higher loads to overcome the resistance to motion. Values for μ on the order of 0.7 have been documented in similar types of contacts in regions undergoing sliding [17].

Overall, the Cu-Ni pads produced a much lower coefficient of friction than the as-received pads. However, if we take the knee in the first portion of the as-received pad test as the point at which gross sliding commenced, the resulting μ values are nominally the same. Thus, the expected fretting fatigue behavior should be nominally the

same, especially when considering the many possible sources by which experimental scatter may be increased.

3.3 Effect of Roughness

Experimental data from the S-N and step tests reflect an improvement in fretting fatigue behavior in the presence of the Cu-Ni pad coating. Results from gross sliding tests designed to quantify μ do not adequately explain the differences in behavior. Further, none of the results indicate whether the improved fretting fatigue behavior was caused by coating material or by surface roughness, which was observed to be greater for the coated pads than for the as-received pads. To address this issue three S-N tests were conducted with Ti-6Al-4V pads that had been roughened to approximate the Cu-Ni pad roughness (Figure 2c).

These tests produced a broad range of fatigue lives, from 250,000 to over 40 million cycle (Table 2), reflecting more experimental scatter than the smoother contacts. Note that the lowest fatigue life can be related to either the higher clamping stress or the higher % deviation. A higher average fatigue limit of ~ 20.4 million cycles was obtained using the roughened pads compared to the Cu-Ni pad results, indicating that the improvement in fatigue life observed between the Cu-Ni pad tests and the as-received pad tests is related more to surface roughness than to contact material. The mechanism responsible for the improved fretting fatigue behavior is not clear from these results, but it may be related to actual contact area, which was not quantified here, stress & displacement fields around asperity contacts, or the minimal test volume resulting from the localized contacts.

To further investigate the effect of surface roughness on fretting fatigue behavior, three specimens were tested: one polished specimen with polished pads (98-585), one as-received specimen with polished pads (99-610), and one polished specimen with as-received pads (98-600). In these three cases, the fatigue lives were not markedly different from the results obtained using as-received pads. The tests with polished pads produced slightly higher fatigue lives (approximately a factor of two), although the statistical significance of this difference is not clear in light of the large amount of experimental scatter observed throughout this investigation.

3.4 "Series-of-5" Results

The final fatigue tests conducted were the "series-of-5" tests. For these tests, fatigue life was the experimentally observed quantity. As mentioned earlier, these tests involved testing a specimen until failure, retaining the pads, and testing another specimen with the used pads [12]. This procedure was performed with five specimens for each set of pads. The purpose of these experiments was to quantify the integrity of the Cu-Ni coating, and compare the behavior against as-received and roughened pad types. The results for these tests are given in Figure 6, which shows the cycles to failure for each test as a function of the test position in the series, and in Table 2. Tabular results are included to allow the reader to identify exact cycle counts for each test, and to provide details of clamping condition, test frequency, and failure location, although the details are inconclusive. Note in Table 2 that the first test shown for each series is included as S-N data in the previous discussion. Four "series-of-5" tests were completed: one with Cu-Ni coated pads [12], one with roughened pads, and two with as-received pads [12].

Initially, the performance observed in Figures 4 for Cu-Ni coated and roughened pads was better than the as-received uncoated pads. The S-N data from Figure 4 is shown again in Figure 6 in position 1 in the series. For the S-N data obtained with as-received pads the resulting average and two standard deviation error bars are shown in Figure 6 to allow comparison of results from other pad surface conditions at all series positions. Over the series, the resulting fatigue lives for all of the pad types were scattered over a full decade and showed no trend with position in the series, applied clamping stress, or % deviation. The only conclusion from these results is that the behavior of specimens against the as-received fretting pads may be considered a worst case, since none of the other cases indicated lower fatigue lives either initially, or after subsequent tests against the same set of pads.

One detail of interest from the "series of 5" tests is related to the failure locations identified in Table 2. While all of the specimens tested against the rougher (Cu-Ni coated and roughened) pads failed in the upper grip, the failure locations in the specimens tested against as-received uncoated pads was less consistent (Figure 6). The region of the coated and roughened pads where failures occurred were inspected using Scanning Electron Microscopy (SEM), but nothing was noted that might cause preferential crack nucleation. In fact, fretting damage of pads was minimal (Figure 7a & b).

If the trends created initially by the varying surface roughnesses are examined, some inferences can be made about what is happening at different positions in the series. The rougher contacts resulted in failure in nearly the same location throughout the series, which implies that a feature on the pads is producing the fractures in this

region, even though the feature could not be observed with SEM characterization techniques. Since very little materia l removal has been noted for the contact conditions investigated here, the possibility that the roughness feature did not wear away is quite likely. In cases with as-received pads where a crack has propagated to failure, an increased roughness in the region of the crack nucleation site has been noted on the fretting pads. Increased roughness of this type may be the source of the statistically significant increases in fatigue lives observed for the tests at positions two and four in the As-received series #1. While this hypothesis does not hold for all of the cases here (position 2 in As-received series #2), the surface roughness produced by the crack mouth has not been characterized, and is likely to vary depending on the time required for crack propagation.

3.5 Closing Remarks

Several observations are made on the general behavior of the contact condition investigated here. First, the fracture location (upper vs. lower) for the fatigue tests, or slip location for the tension tests, is determined by statistical variability. This observation is significant because the test frame requires the specimens to be tested in a manner that would drop any debris escaping from the upper grip into the lower grip, possibly bringing the validity of the results into question. Since no bias in the failure location was observed, we can conclude both that the condition under investigation produces minimal amounts of fretting debris, and that the results are valid within our ability to control the contact and loading conditions. The notable exceptions to this trend are the cases with the Cu-Ni coated and roughened pads in the "Series of 5" tests. In these cases, the statistical sampling may be considered as biased, since only one statistical sample is represented.

Second, no trend was observed as a function of test frequency for the fatigue tests. The frequencies used for each test are included in the tabular results here, as they may be of interest to the reader. Since the values differ by less than 25% and no differences in behavior were noted, the different values used are considered to be the same. If the frequency values differed by an order of magnitude or more, strain rate effects may have influenced the observed behavior, but for the range of frequencies in this investigation, the difference in behavior should be negligible.

Finally, the fretting fatigue behavior appears to be insensitive to both applied clamping stress and % deviation, or how much the applied load varies across the contact as a percentage of the total applied load. This observation has been noted in our previous work [10, 11] and is also apparent when comparing the values of clamping stress and % deviation in the tabular results for this investigation. For this reason, we have included the three S-N tests where the actual clamping stress and % deviation could not be measured because of problems with the test equipment.

CONCLUSIONS

From the tests conducted in this investigation for the purpose of characterizing the fretting fatigue behavior of Cu-Ni plasma spray coated Ti-6Al-4V, the following conclusions may be drawn:
1. The fretting fatigue limit of Ti-6Al-4V tested against a Cu-Ni coated pad reflected a nominal improvement over the fretting fatigue limit of the alloy tested against itself.
2. The mechanism responsible for the improved fretting fatigue behavior is more related to the surface roughness resulting from the plasma spray process than from the contact material.
3. Fatigue results (both fatigue limit and S-N) are insensitive to the value of applied clamping stress or the non-uniformity of the clamping load across the contact.
4. S-N and "series of 5" tests reflected higher scatter for rough contacts, perhaps because of the expected variability of the stress fields around asperity contacts. Note that statistical variability of the rougher contacts was not evaluated because of the expense of generating fretting pads.
5. The "series of 5" test results did not indicate any degradation of the Cu-Ni coating; however, large amounts of experimental scatter obscured whatever trends might have been present. The results did indicate that the as-received pad surface produced the worst case fretting fatigue behavior of the conditions investigated.

Additional information regarding crack nucleation mechanisms may be obtained through rigorous characterization and post mortem examination of the fretted specimens and pads.

REFERENCES

1. Ruiz, C., Boddington, P. H. B., and Chen, K. C., "An Investigation of Fatigue and Fretting in a Dovetail Joint," *Experimental Mechanics*, vol. 24, 1984, pp. 208-217.

2. Bryggman, U. and Söderberg, S., "Contact Conditions and Surface Degradation Mechanisms in Low Amplitude Fretting", *Wear*, vol. 125, 1988, pp. 39-52.

3. Del Puglia, A., Pratesi, F., and Zonfrillo, G., "Experimental Procedure and Parameters Involved in Fretting Fatigue Tests," *Fretting Fatigue, ESIS 18*, R.B. Waterhouse and T.C. Lindley, Eds., Mechanical Engineering Publications, London, 1994, pp. 219-238.

4. Fellows, L. J., Nowell, D., and Hills, D. A., "On the Initiation of Fretting Fatigue Cracks," *Wear*, vol. 205, 1996, pp. 120-129

5. Fouvry, S., Kapsa, P., and Vincent, L., "Quantification of Fretting Damage," *Wear*, vol. 200, 1996, pp. 186-205.

6. Vingsbo, O. and Schon, J., "Gross Slip Criteria in Fretting," *Wear*, vol. 162-164, 1993, pp. 347-356.

7. Zhou, Z. R. and Vincent, L., "Mixed Fretting Regime," *Wear*, vol. 181-183, 1995, pp. 551-536.

8. Adibnazari, S. and Hoeppner, D.W., "The Role of Normal Pressure in Modeling Fretting Fatigue," *Fretting Fatigue, ESIS 18*, R.B. Waterhouse and T.C. Lindley, Eds., Mechanical Engineering Publications, London, 1994, pp. 125-133.

9. Waterhouse, R.B., "Effect of Material and Surface Conditions on Fretting Fatigue," *Fretting Fatigue, ESIS 18*, R.B. Waterhouse and T.C. Lindley, Eds., Mechanical Engineering Publications, London, 1994, pp. 339-349.

10. Hutson, A. and Nicholas, T., "Fretting Fatigue of Ti-6Al-4V Under Flat-on-Flat Contact", International Journal of Fatigue, Vol 21, No. 7, pp. 663-670, 1999.

11. Hutson, A.L., Nicholas, T., Olson, S.E. and Ashbaugh, N.E., "Effect of Sample Thickness on Local Contact Behavior in a Flat-on-Flat Fretting Fatigue Apparatus," submitted to International Journal of Fatigue, 2000.

12. Niinomi, M., Hutson, A.L., Shell, E.B., Eylon, D. and Nicholas, T., "Effect of Cu-Ni Plasma Coating on Fretting Fatigue Characteristics of Ti-6Al-4V Under Flat-on-Flat Contact," submitted for publication by ASTM in association with the 3rd International Symposium on Fretting Fatigue in Nagaoka, Japan, May 2001.

13. Peters, J.O. and Ritchie, R.O., "Foreign-Object Damage and High-Cycle Fatigue: Role of Microstructure in Ti-6Al-4V," submitted to International Journal of Fatigue, 2000

14. Moshier, M.A., Nicholas, T. and Hillberry, B.M., "Determining a True Material Fatigue Crack Growth Threshold," submitted to International Journal of Fatigue, 2000.

15. Van Stone, R., "Fretting and High Cycle Fatigue in Titanium," presented at the 3rd National Turbine Engine High Cycle Fatigue Conference, San Antonio, TX, 1998.

16. Maxwell, D.C. and Nicholas, T., "A Rapid Method for Generation of a Haigh Diagram for High Cycle Fatigue," Fatigue and Fracture Mechanics: 29th Volume, ASTM STP 1321, T.L. Panontin and S.D. Sheppard, Eds., American Society for Testing and Materials, 1998, submitted for publication.

17. Murthy, H. and Farris, T.N., "Fretting Fatigue of Ti-6Al-4V Subjected to Blade/Disk Contact Loading," Proceedings of Symposium Developments in Fracture Mechanics for the New Century, Japan Society for Materials Science, Osaka, May 2001, In-Press.

FIGURE CAPTIONS

Figure 1.   Schematic of the fretting fatigue gripping system and location of fretting damage.

Figure 2a.   Un-contacted as-received pad surface.

Figure 2b.   Un-contacted polished pad surface.

Figure 2c.   Un-contacted "roughened" pad surface.

Figure 2d.   Un-contacted Cu-Ni coated pad surface.

Figure 3.   Comparison of normalized fretting fatigue limit from baseline results [10, 11] to current test results with Cu-Ni coated and as-received pads.

Figure 4   Comparison of S-N behavior from baseline results [11] to current test results with Cu-Ni coated, roughened, polished and as-received pads. Fatigue limit data is included assuming a 10^7 cycle fatigue life for the fatigue limit stress.

Figure 5.   Load vs. Stroke data acquired to determine coefficient of friction.

Figure 6.   Comparison of fatigue lives from "series of 5" tests against Cu-Ni coated, as-received uncoated, and roughened uncoated pads.

Figure 7a.   Cu-Ni coated pad wear damage

Figure 7b.   Roughened pad wear damage

TABLES

Pad Type

		Polished	As-received	Cu-Ni coated	Roughened
		(~1μm finish)	(#8 finish)	(~#64 finish)	(~#64 finish)
Test Type	**Step Tested**	———————	1 test [12]	2 tests [12]	———————
	S-N	2 tests*	4 tests	1 test	2 tests
	"Series of 5" (S-N)	———————	2 series of 5 tests per series [12]	1 series of 5 tests [12]	1 series of 5 tests

Table 1. Test matrix for the Cu-Ni coating study.

Specimen Designation	Pad surface	Test Frequency (Hz)	Test Type	Fracture location	Applied Clamping Stress (MPa)	% deviation
98-586 [12]	Cu-Ni	400	Step	upper	726	4%
97-008	Cu-Ni	300	Step	upper	417	1%
98-584 [12]	as-received	400	Step	lower	680	6%
99-B71 [11]	as-received	300	Step	upper	635	-4%
99-B72 [11]	as-received	300	Step	lower	611	-2%
99-B73 [11]	as-received	300	Step	upper	620	7%
99-B77 [11]	as-received	300	Step	upper	652	14%
98-587 [12]	Cu-Ni	400	S-N	upper	729	-8%
99-605	Cu-Ni	300	S-N	lower	721	-14%
99-593	#64	300	S-N	upper	677	-6%
99-606	#64	300	S-N	upper	812	-15%
99-611	#64	300	S-N	upper	not measured	
98-592 [12]	as-received	400	S-N	upper	625	-8%
98-599	as-received	325	S-N	lower	659	-1%
99-600 [12]	as-received	300	S-N	upper	588	5%
99-607	as-received	300	S-N	upper	677	-5%
99-608	as-received	300	S-N	lower	not measured	
99-609	as-received	300	S-N	lower	782	0%
98-585	polished	300	S-N	lower	724	-2%
99-610*	polished	300	S-N	lower	not measured	
98-600*	as-received	300	S-N	lower	603	-1%
98-587 [12]	Cu-Ni	400	1 of 5	upper	729	-8%
98-588 [12]	Cu-Ni	400	2 of 5	upper	748	-7%
98-589 [12]	Cu-Ni	400	3 of 5	upper	716	-10%
98-590 [12]	Cu-Ni	400	4 of 5	upper	636	-6%
98-591 [12]	Cu-Ni	400	5 of 5	upper	683	1%
99-593	#64	300	1 of 5	upper	677	-6%
99-596	#64	325	2 of 5	upper	730	-6%
99-597	#64	325	3 of 5	upper	806	-9%
99-598	#64	325	4 of 5	upper	797	-10%
99-599	#64	325	5 of 5	upper	812	-3%
98-592 [12]	as-received	400	1 of 5	upper	625	-8%
98-593 [12]	as-received	400	2 of 5	upper	635	-8%
98-596 [12]	as-received	400	3 of 5	lower	752	-2%
98-597 [12]	as-received	400	4 of 5	lower	736	-3%
98-598 [12]	as-received	400	5 of 5	upper	750	-4%
99-600 [12]	as-received	300	1 of 5	upper	588	5%
99-601 [12]	as-received	300	2 of 5	lower	727	6%
99-602 [12]	as-received	300	3 of 5	lower	723	-4%
99-603 [12]	as-received	300	4 of 5	lower	682	-2%
99-604 [12]	as-received	300	5 of 5	lower	691	-9%

Table 2: Results from fatigue tests.

Specimen Designation	Pad surface	Slip location	m	Applied Clamping Stress (MPa)	% deviation
97-009	as-received	both	0.70	336	-1%
97-010	Cu-Ni	upper	0.33	339	-2%

Table 3: Sliding coefficient of friction test results.

Specimen

Fretting Pad

No Slip
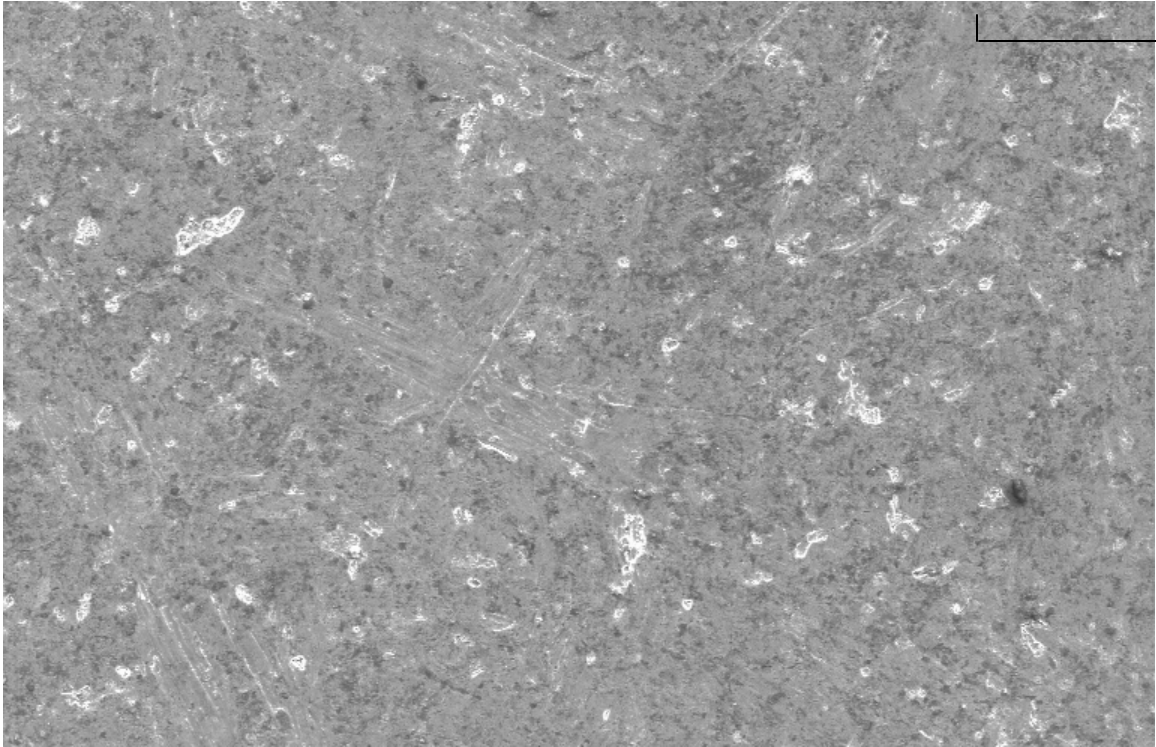
Fretting Region

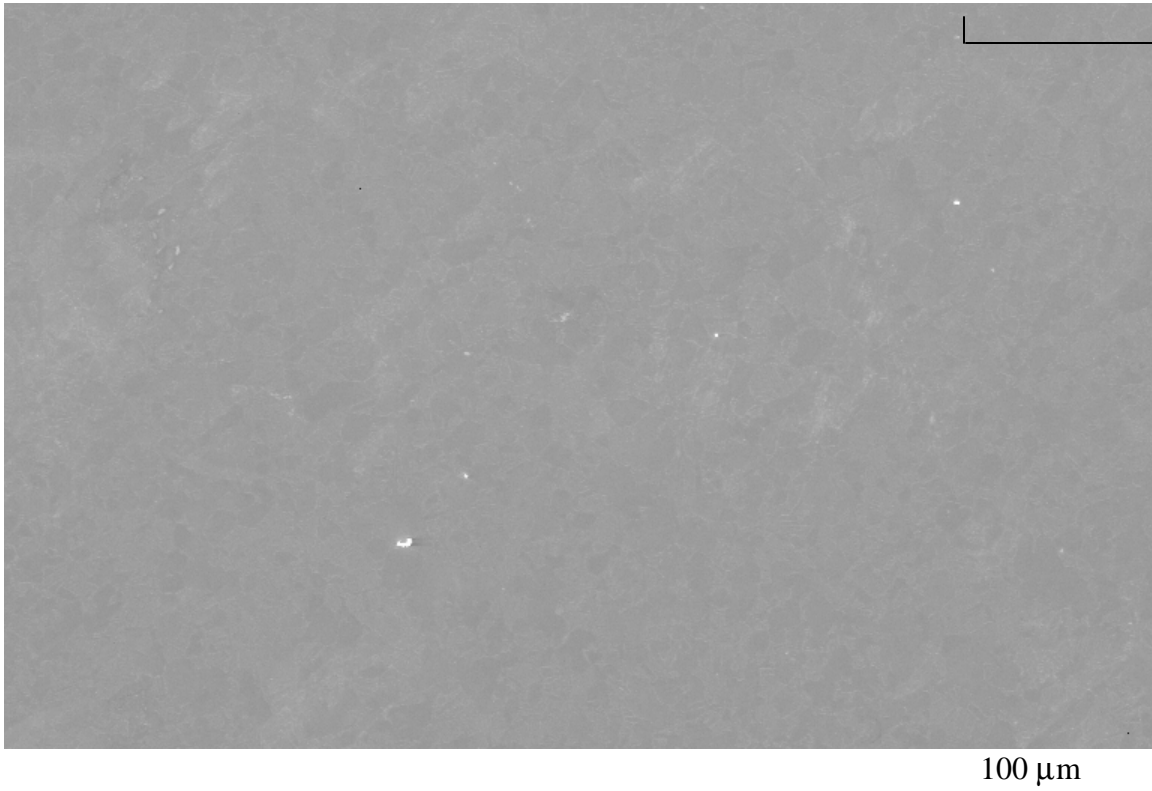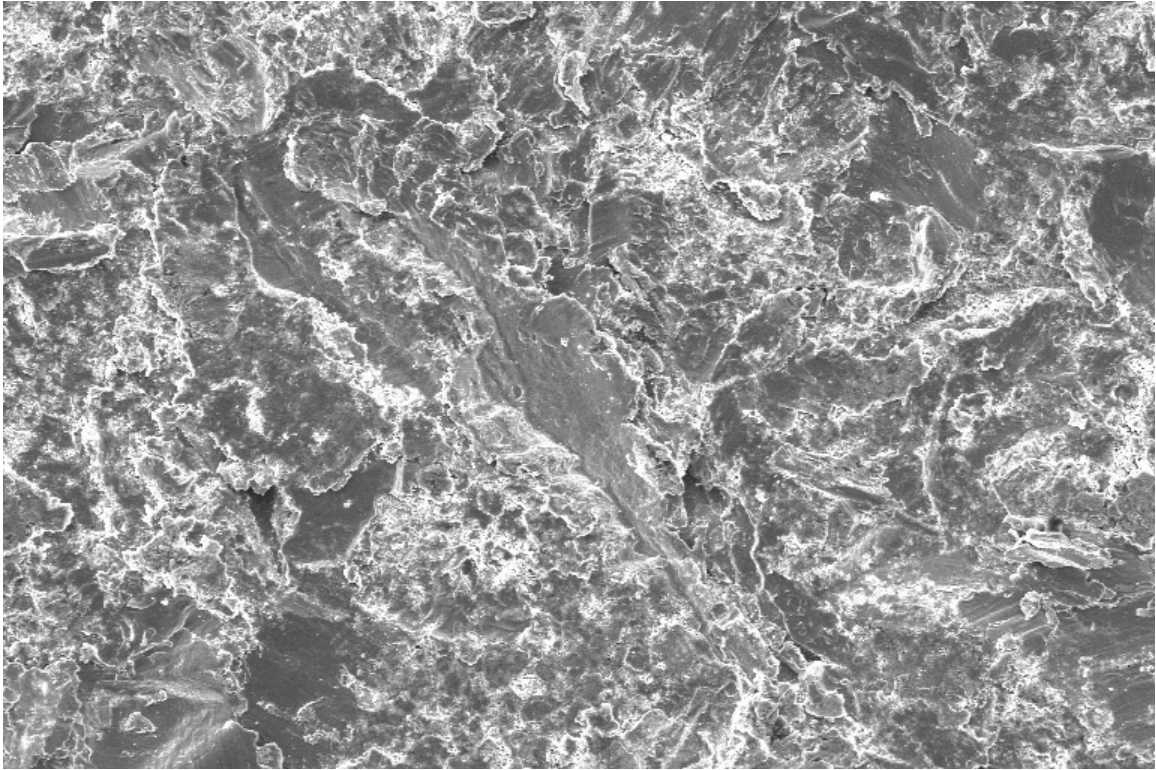No Contact

Instrumented Bolts
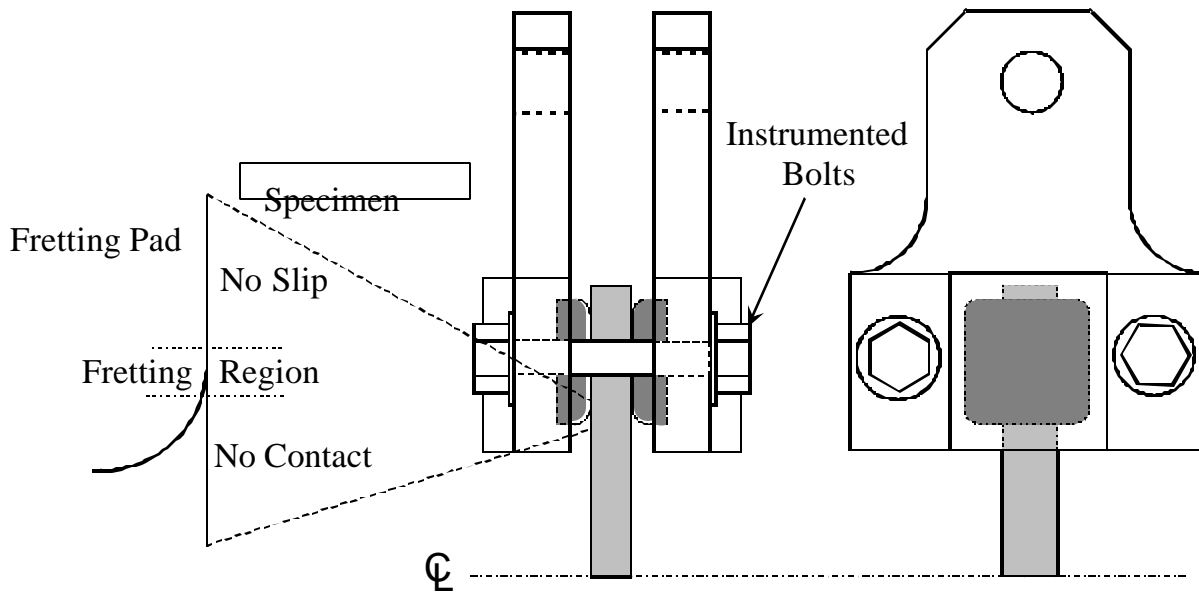
Figure 1.

100 mm

Figure 2a.

100 µm

Figure 2b.

Figure 2c.

100 μm
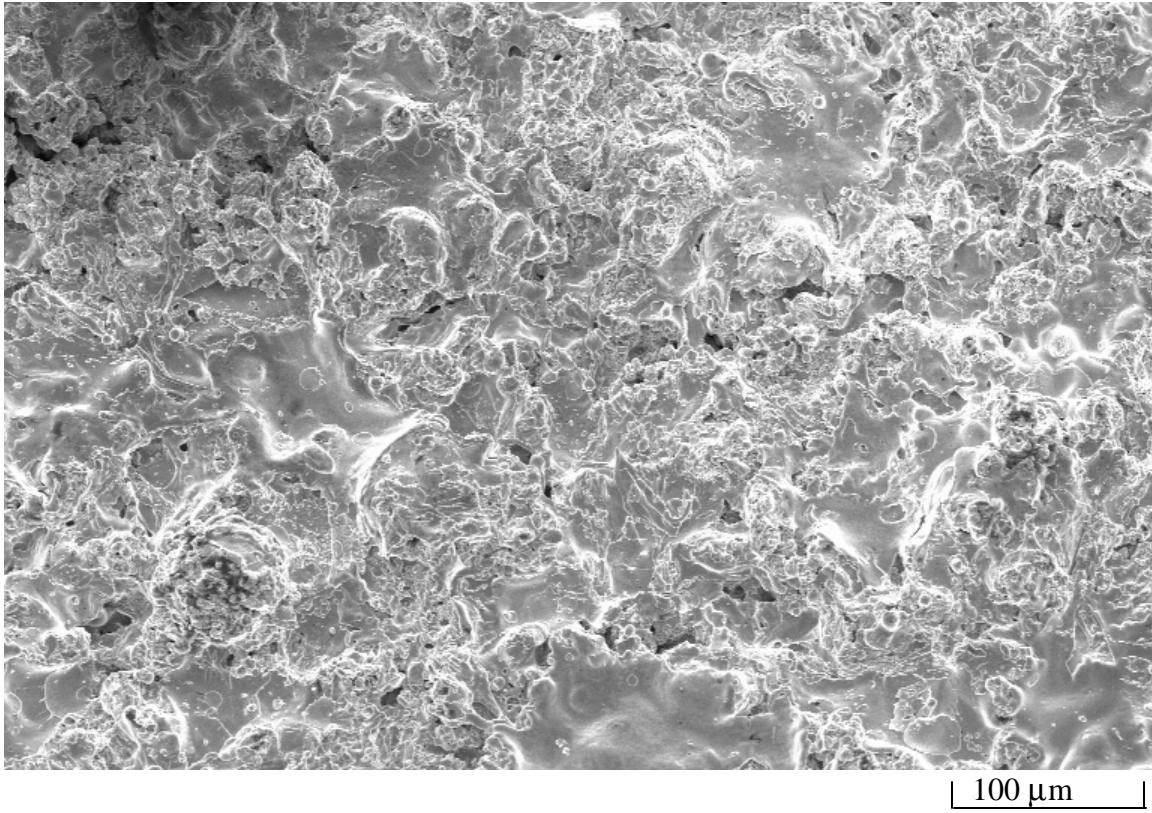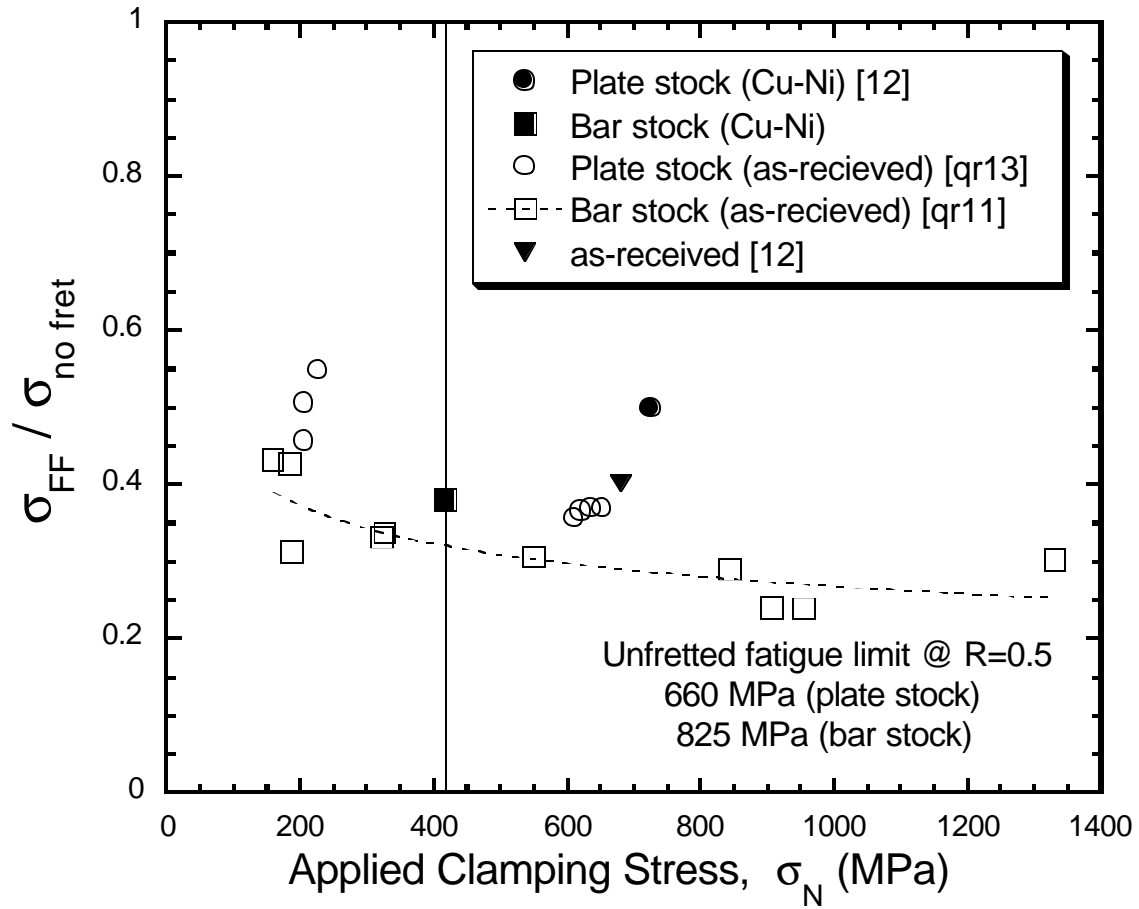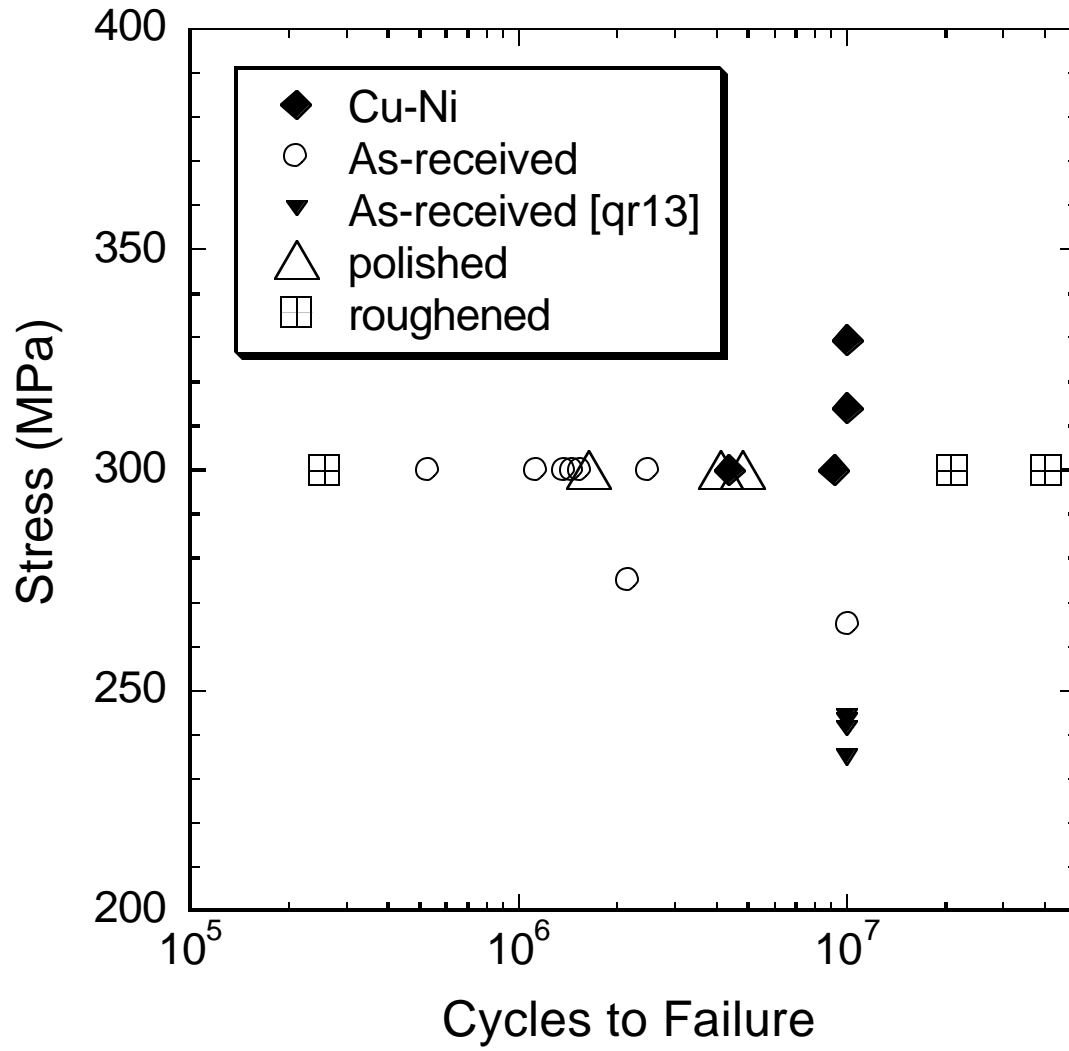
Figure 2d.

Figure 3.

Figure 4
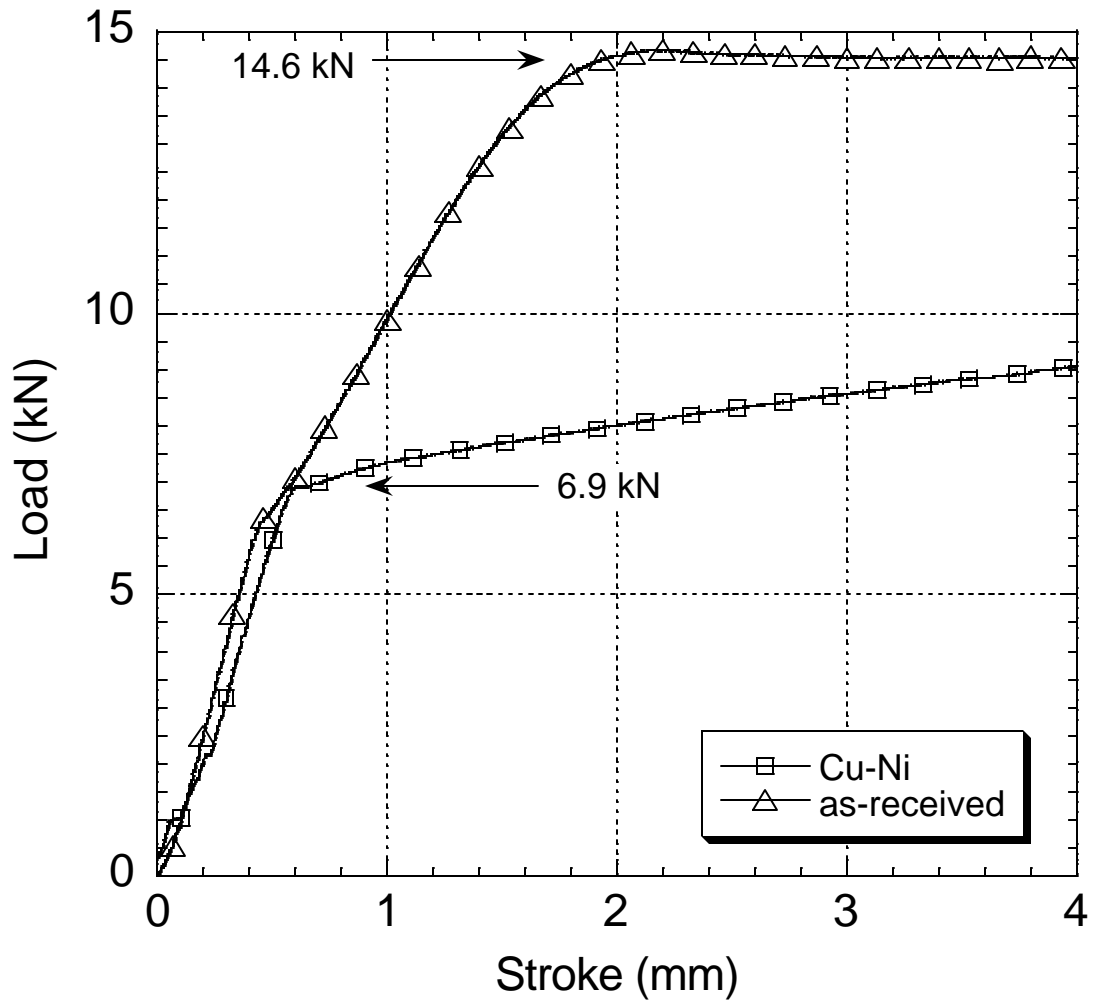
Figure 5.

Figure 6.

200 μm
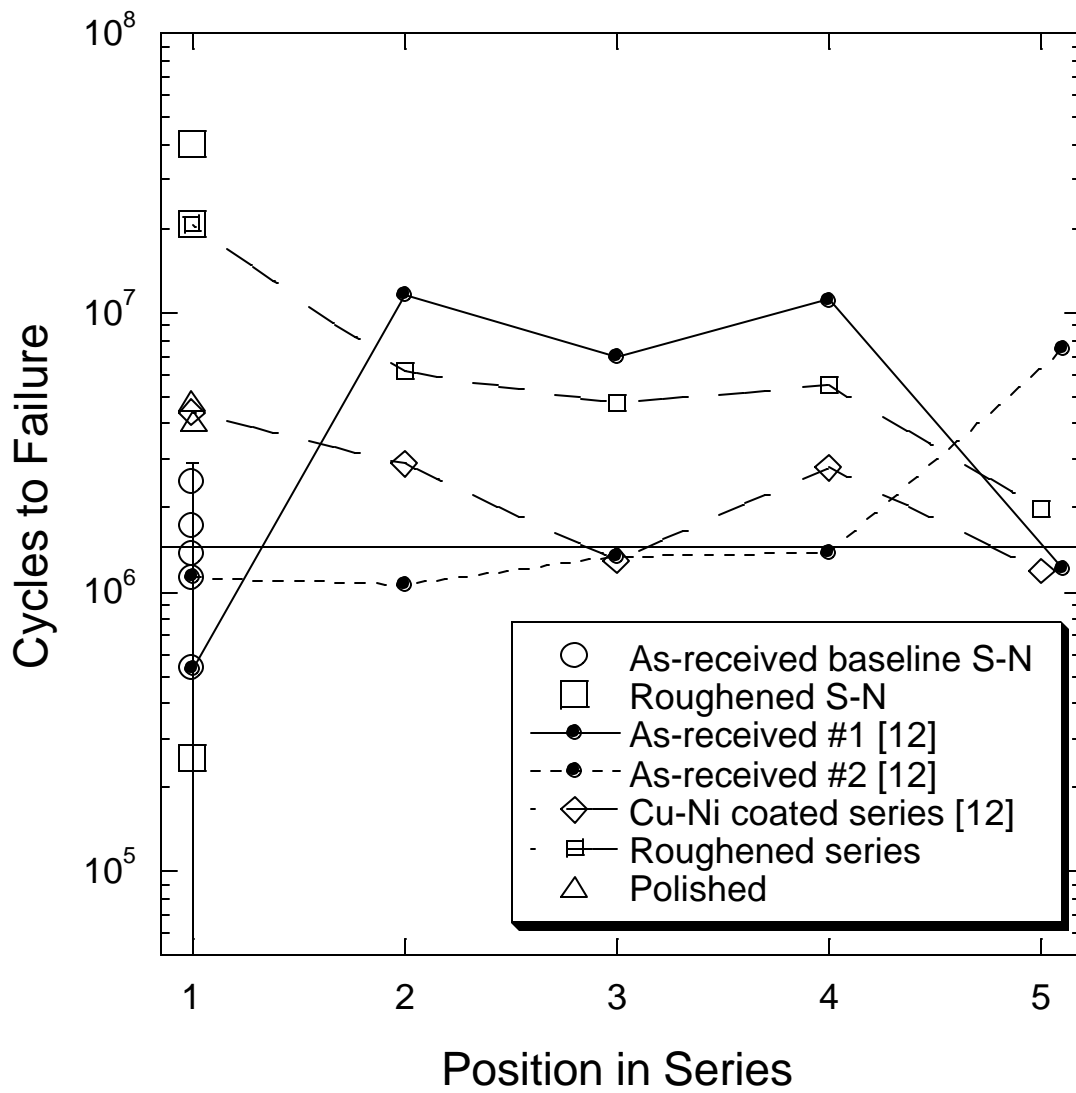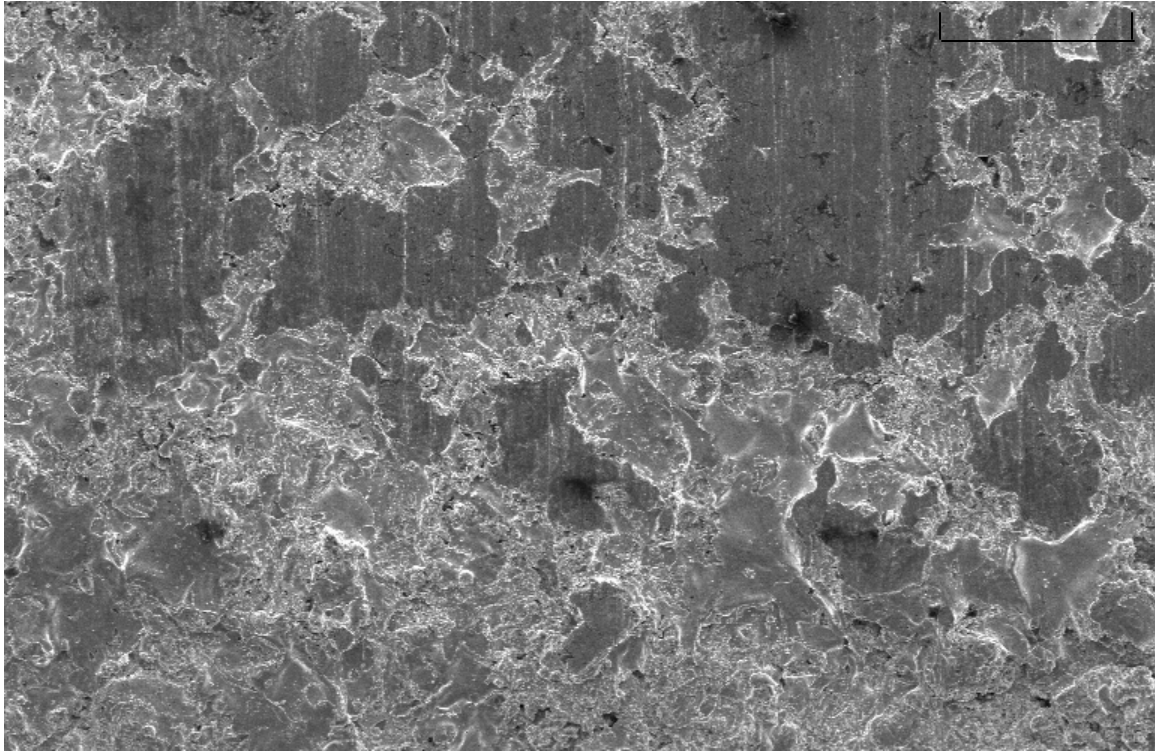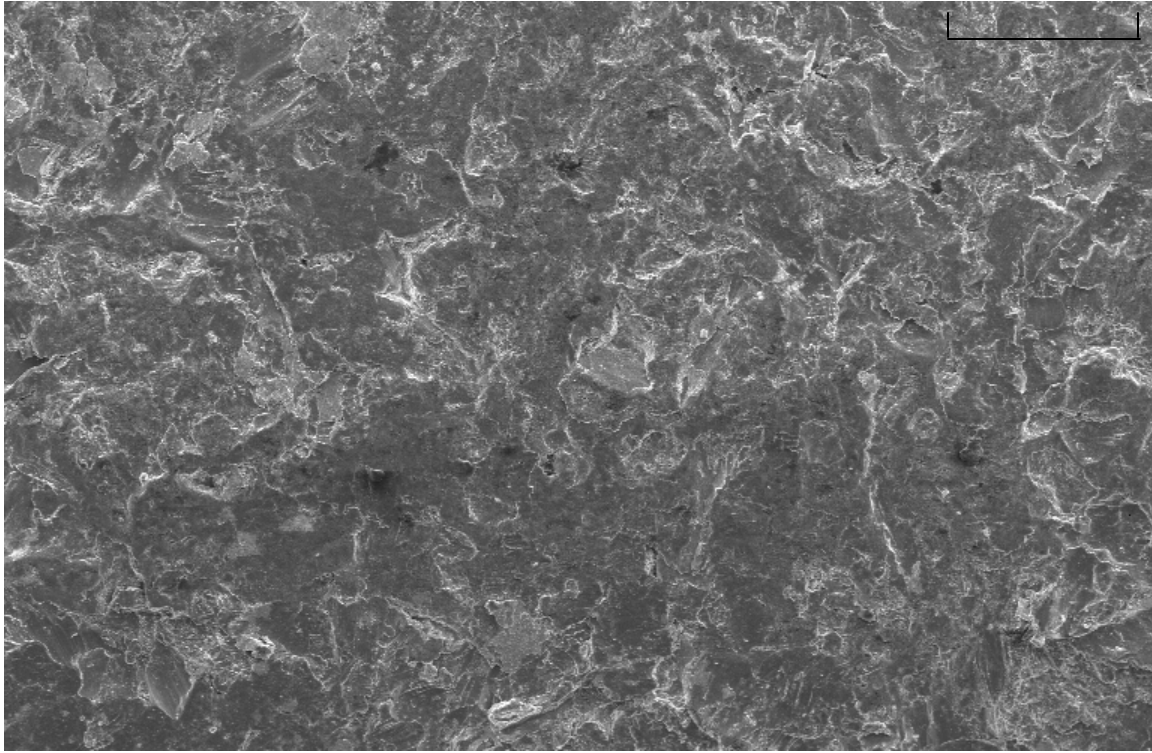
Figure 7a.

200 µm

Figure 7b.

This page intentionally left blank.

Effect of Cu-Ni Plasma Coating on Fretting Fatigue Characteristics

of Ti-6Al-4V Under Flat-on-Flat Contact

M. Niinomi[1], A. L. Hutson[2], E. B. Shell[3], D. Eylon[4],

and T. Nicholas[5]

[1] Department of Production Systems Engineering, Toyohashi University of Technology,

1-1, Hibarigaoka, Tempaku-cho, Toyohashi 441-8580, Japan

[2] Advanced Materials Characterization Group, Structural Integrity Division, University of

Dayton Research Institute, Dayton, 300 College Park, OH 45469-0121, U.S.A.

[3] Center for Materials Diagnostics, University of Dayton, 300 College park, Dayton, OH 45469-

0121, U. S. A.

[4] Graduate Materials Engineering, University of Dayton, 300 College Park, OH 45469-0240, U.S.A.

[5] Metals, Ceramics & NDE Division, Materials and Manufacturing Directorate,

Air Force Research Laboratory (AFRL/MLLN),

Wright-Patterson AFB, OH 45433-7817, U.S.A.

Abstract

The fretting fatigue tests of Ti-6Al-4V were carried out using Cu-Ni plasma coated and

as-received pads (un-coated pads). Fretting fatigue tests of Ti-6Al-4V, where Cu-Ni plasma

coated and as-received pads were used, repeatedly were also carried out. The characterization of

pads before and after testing were carried out in order to investigate the mechanism of fretting fatigue of Ti-6Al-4V in contact with the Cu-Ni plasma coated pad is used.

Cu-Ni plasma coating on the pads prolonged the fretting fatigue life of Ti-6Al-4V. The fretting fatigue life of Ti-6Al-4V decreased with repeated use of test when the Cu-Ni plasma coated pads. On the other hand, the opposite trend was observed when the as-received pads were repeatedly used. The surfaces of Cu-Ni plasma coated pads were smoother after testing than before testing due to the plastic deformation. On the other hand, the surface of as-received pads were rougher after testing than before testing.

I. Introduction

High cycle and low cycle fatigue, corrosion, and fretting fatigue are the main causes of failures in components of turbine engines for aircrafts. Among them, fretting fatigue is the most complex failure where the fatigue and fretting are overlapped. Fretting reduces the fatigue life of components remarkably. The components are failed much earlier under fretting fatigue conditions than expected under usual fatigue conditions.

Turbine engine blade root experiences fretting in flat-on-flat with rather large radii at the edges of contact. A fretting fatigue test method incorporating a flat-on-flat type of contact [1] has been successfully done on the Ti-6Al-4V, which is a representative $\alpha + \beta$ type titanium alloy for turbine engine blades.

Surface modification is done in order to enhance the fretting fatigue life of the turbine engine blade made of titanium alloys [2-5]. Some of them improve the fretting fatigue behavior of the titanium alloys. Further improvement of fretting fatigue life by surface coating is required;

however, the mechanism of improvement of fretting fatigue life by surface coating is unclear, as is the mechanism of pure fretting fatigue.

Cu-Ni plasma coating was, therefore, adopted in order to improve the fretting fatigue of Ti-6Al-4V in this study. Fretting fatigue tests were carried out on Ti-6Al-4V with Cu-Ni plasma coated Ti-6Al-4V fretting pads. The results were compared with those obtained when the un-coated pads were used. The fretting fatigue tests in which the pads were used repeatedly were also done in order to investigate the durability of Cu-Ni plasma coating. Characterization of fretted specimens, fracture surfaces and fretted pads were done mainly using an SEM and a profilometry. The mechanism of fretting fatigue in this study was, then, discussed.

II. Experimental procedures

The material used for axial specimens and fretting pads was a Ti-6Al-4V alloy, which was supplied in the form of a forged plate with duplex structure of $\alpha + \beta$. Axial specimens with a width of 10 mm, a thickness of 2 mm and a length of 100 mm, and fretting pads with a length of 25.4 mm, a width of 12.4 mm, a thickness of 6.2 mm and a contact radius of 3.2 mm were machined from the heat-treated material of Ti-6Al-4V alloy. All specimens and fretting pads were finally low stress ground.

The test machine used in this study is developed at AFRL for fatigue testing at frequency of up to 500 Hz. The fretting experimental setup was designed to simulate the loading conditions under which fretting fatigue damage occurs in turbine blade attachments. The test apparatus used to fret the samples simulates the blade root geometry by employing flat fretting pads, with a radius at the edge of contact, against a flat specimen as shown in Fig.1 [1].

123
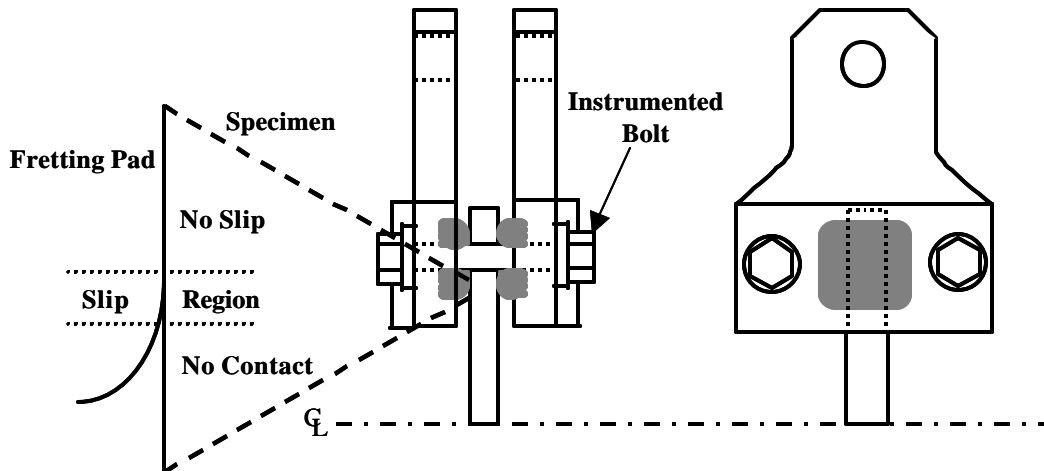
Fig. 1 Schematic drawing of fretting fatigue system

Testing was conducted using the stepped loading approach developed by Maxwell and Nicholas [1] when the specimen was not failed after first 10 million cycles at a set maximum axial stress. Haigh, or Goodman stress representing a fatigue limit off a 10^7 cycle fatigue life was calculated when the stepped loading approach was carried out.

Some of the as-received pads were plasma coated with Cu-Ni at Praxair Surface Technology Inc. according to the specification of Pratt & Whitney Co. Ltd. Some sets of the Cu-Ni plasma coated and un-coated pads ,or as-received pads, were reused 5 times in order to investigate the durability of the Cu-Ni Plasma coated layer. In the case of as-received pads, 2 sets fretting fatigue tests were carried out.

White Light Interference Profilometry [6] was used to measure the surface topography of the as-received and coated pads before and after the tests.. SEM observation was also carried out on the surface of pads. Hardness of the coated layer and matrix of the pad were measured on the cross-section of the coated pad using a Vickers hardness tester at a load of 10 g.

III. Experimental results and discussion

1. Effect of Cu-Ni plasma coating on fretting fatigue

The fretting fatigue results using as-received and coated pads are shown in Table 1. The testing conditions are also shown in the same table. The stepped loading approach was used to evaluate the fretting fatigue life of Ti-6Al-4V. The fatigue limit stress is around 23 % greater when the Cu-Ni plasma coated pads were used than when the as-received pads were used. The Cu-Ni plasma coating on the pads is, therefore, effective in improving the fretting fatigue life of Ti-6Al-4V.

Table 1 Fretting fatigue results using Cu-Ni plasma coated and as-received pads obtained from stepped loading approach

	Initial maximum axial stress, $s_{initial}$ (MPa)	Final maximum axial stress, s_{final} (MPa)	Goodman stress, $s_{Goodman}$ (MPa)	Number of cycles to failure at final maximun axial stress	Total number of cycles to failure, Nf
As-received pad	250	275	273.8	2,143,088	22,143,088
Cu-Ni plasma coated pad	240	336	335.4	4,584,528	84,584,528

Normal stress, s_{normal}, = 420 MPa; Testing frequemcy = 400 Hz; Stress ratio = 0.5

The Vickers hardness of Cu-Ni plasma coated layer is smaller than that of specimen as will be mentioned later. The wear damage of the specimen is considered to be lower when the coated pads are used than when the as-received pads are used. Lower wear damage associated with coated pads may prolong the fretting fatigue life of Ti-6Al-4V.

2. Repeated tests

The results for fretting fatigue tests, in which the pads were repeatedly used are shown in Fig. 2. This figure shows the relationships between the number of cycles to failure and the series position for as-received and Cu-Ni plasma coated pads, respectively. Two series of tests

were done in the case of as-received pads as stated above. Therefore, as-received 1 indicates the

data of one series, and as-received 2 indicate the data of another series. The description of step

loading in Fig.2 means that the data have been obtained by stepped loading approach.
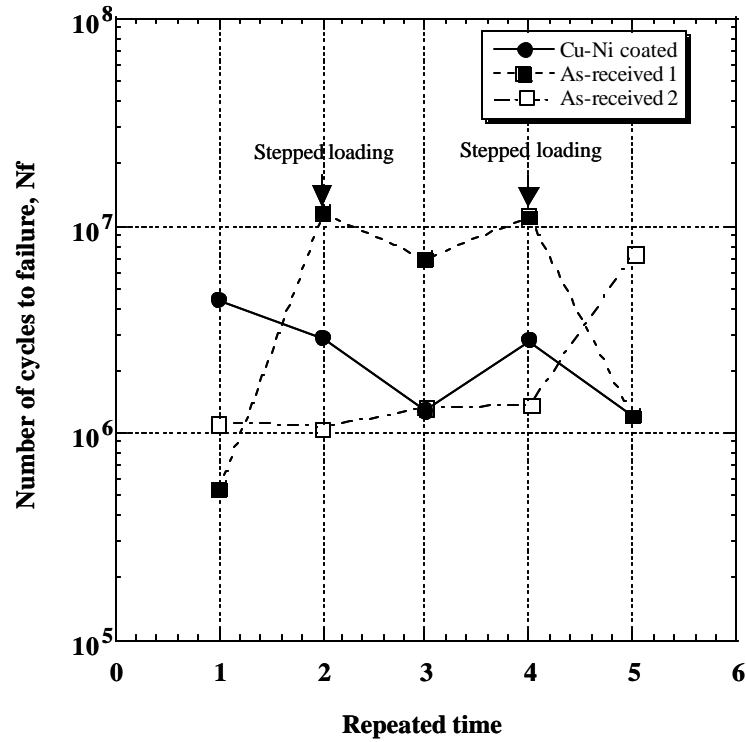
Fig. 2 Repeated fretting fatigue tests results Cu-Ni coated and as-received pads.

The fretting fatigue life of T-6Al-4V decreases with the repeated time when the Cu-Ni

plasma coated pads are used.

Initially, the fretting fatigue life when the as-received pads were used is shorter than

when the Cu-Ni plasma coated pads were used. However, the fretting fatigue lives using as-

received pads 1 increases to be greater than those obtained using Cu-Ni plasma coated pads for

the second, third and fourth times, and decreases to be smaller than that using Cu-Ni plasma

coated pads at the final time. When using as-received pads 2, the fretting fatigue life increases

with the repeated time, and at the final time the fretting fatigue life becomes to be greater than that using Cu-Ni plasma coated pads.

3. Vickers hardness of coated layer and matrix of pad

Vickers hardness values of Cu-Ni plasma coated layer and matrix of pad are shown in Table 2. Vickers hardness of plasma-coated layer is smaller than that of pad matrix, Ti-6Al-4V. The soft Cu-Ni layer is, therefore, fretted with the harder material, Ti-6Al-4V, when the Cu-Ni plasma coated pads are used. The softer layer improves the fretting fatigue life of Ti-6Al-4V.

Table 2 Vickers hardness of coating layer and pad matrix obtained from cross-section

	Vickers hardness
Coating layer	109.7
Pad matrix	383.9

Load : 10 g

4. SEM observation on the surface of coated pad

SEM micrographs on the surface of the coated pad before and after testing are shown in Figs.3 and 4, respectively. The surface of the Cu-Ni plasma coated pad before testing is relatively rougher while that after testing is relatively smoother due to the plastic deformation. Some cracking is also observed in the Cu-Ni plasma coated layer of pad after testing as also shown in Fig.4.
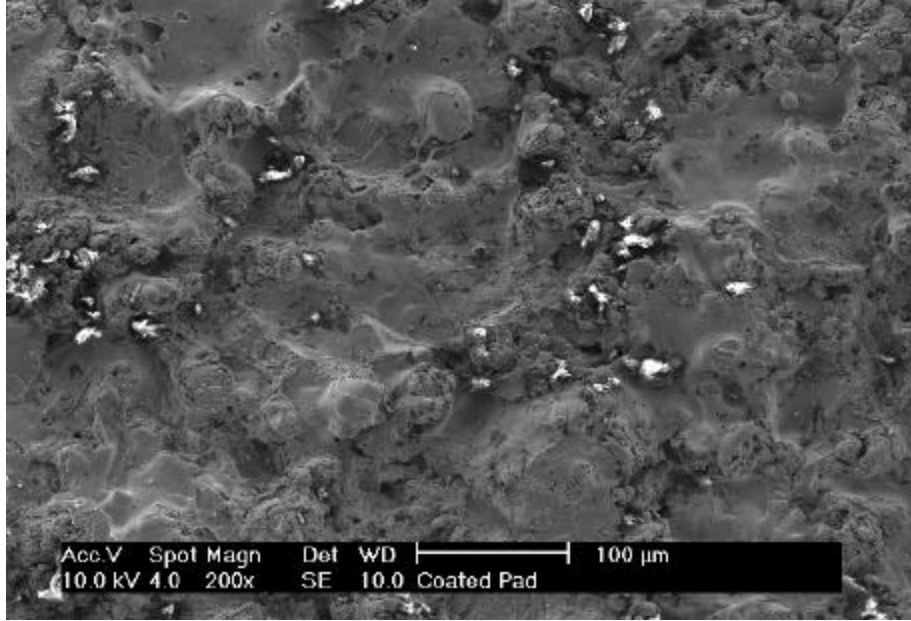
Fig. 3 SEM micrograph showing coating surface before testing.
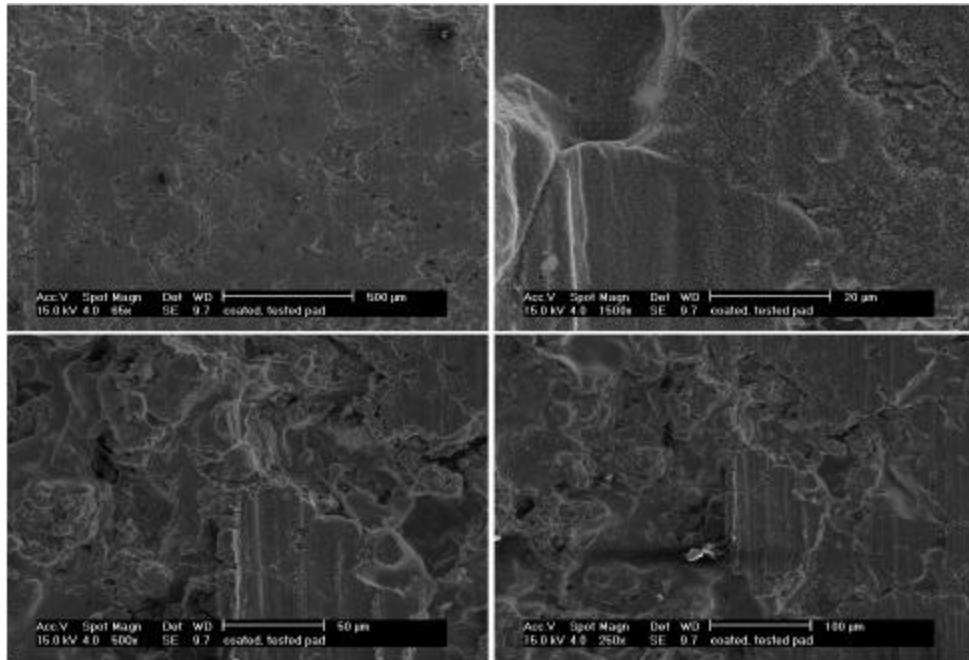
Fig. 4 SEM micrographs showing plastic deformation on coated pad.

5. Surface roughness of coated and as-received pad

The mean height, R_{AVE}, and the root mean square average of the measured height, R_{RMS}, on non-contacted and contacted area of the Cu-Ni plasma coated and as-received pads with

128

specimen after testing are shown in Table 3. The surface roughness of non-contacted coated pad

is greater than that of the non-contacted as-received pad. The surface roughness of the contacted

area is smoother than that of non-contacted area in the Cu-Ni plasma coated pad. However, in as-

received pad, the opposite trend is observed.

**Table 3 Roughness of contact and non-contacted area of
coated and as-received pads in μm**

	Coated pad		As-received pad	
	Non-contacted area	Contacted area	Non-contacted area	Contacted area
RAVE(μm)	10.58	4.14	1.29	1.42
RRMS(μm)	13.01	6.17	1.74	1.94

RAVE : the mean height at calculated over the entire measurement area
RRMS : the root mean square average of the measured height deviations taken
within the evaluation area

Therefore, considering the trend of the fretting fatigue life of the specimen obtained from

repeated tests, increasing surface roughness of pads may be one of the factors that increases the

fretting fatigue life of the specimen. In the case of repeated tests using as-received pads 1, at the

final time, the fretting fatigue life of the specimen was much smaller than that at the forth time.

In this case, the surface roughness may be greater enough to increase the stress concentration to

enhance the crack initiation.

The effect of surface roughness of pad on the fretting fatigue of Ti-6Al-4V should, therefore,

be investigated in further details.

IV. Conclusions

129

The fretting fatigue tests of Ti-6Al-4V were carried out using Cu-Ni plasma coated and as-received pads. The fretting fatigue tests of Ti-6Al-4V, where Cu-Ni plasma coated and as-received pads are used, repeatedly were also carried out. The characterization of pads before and after testing were carried out in order to investigate the mechanism of fretting fatigue of Ti-6Al-4V when the Cu-Ni plasma coated pad is used. The following results were obtained.

1. Cu-Ni plasma coating on the pads prolongs the fretting fatigue life of Ti-6Al-4V.

2. The fretting fatigue life of Ti-6Al-4V decreases with repeated time of test when the Cu-Ni plasma coated pads are repeatedly used. On the other hand opposite trend is observed when the as-received pads are repeatedly used.

3. The surface of Cu-Ni plasma coated pads is smoother after testing than before testing due to the plastic deformation. On the other hand, the surface of as-received pads is rougher after testing than before testing.

References

[1] A. L. Hutson, T. Nicholas and R. Goodman : Int. Journal of Fatigue, 21(1999), pp.663-669.

[2] M. K. Cabel and J. J. Bethke: Wear, 46(1978), pp.81-96.

[3] S. Chakravarty, R. G. Andrews, P. C. Patnaik and A. K. Koul : JOM, (1995), April,

  pp.31-35.

[4] T. C. Lindley: Int. J. Fatigue, 19(1997)1, pp. S39–S49.

[5] R. C. Bill: Wear, 106(1985), pp.283-301.

[6] P. D. Nicolaou, E. Shell, J. Woo and T. E. Matikas: Mat. Sci. Eng., A269(1999), pp.98-103.

This page intentionally left blank.

An Investigation of Fretting Fatigue Crack Nucleation Life Using Shear Wave NDT

Alisha Hutson*, David Stubbs*, and Ted Nicholas

Air Force Research Laboratory, Materials and Manufacturing Directorate, Wright-Patterson AFB, OH 45433.

*University of Dayton Research Institute, Dayton, OH 45469

ABSTRACT

A study was conducted to investigate fretting fatigue damage of Ti-6Al-4V against Ti-6Al-4V under flat-on-flat contact with blending radii at room temperature. Both the location of and the time required to nucleate fretting fatigue cracks were investigated for two static average clamping stress values that are representative of those estimated for turbine engine blade attachments. The axial fatigue limit for a 10^7 cycle life was determined at 300 Hz and R = 0.5 for average clamping stresses of 200 and 620 MPa. Then, feasibility of *in situ* fretting fatigue crack detection using a shear wave ultrasonic Non-Destructive Inspection (NDI) technique was evaluated. Fractography was used to characterize the level of fretting damage.

Fretting fatigue limits for a 10^7 cycle life under the clamping stress conditions used were 330 MPa for the lower clamping stress and 250 MPa for the higher clamping stress, and are lower than the uniaxial fatigue limit for this material by 60 percent and 70 percent, respectively. Using the shear wave ultrasonic technique, cracks with a surface length of approximately 2.5 mm were detected on 10 mm wide specimens in tests conducted at the higher clamping stress. For the lower clamping stress, crack nucleation required over 95% of the total life; for the higher clamping stress, crack nucleation was much sooner. Nucleation sites were identified within 500 μm of the specimen edge. The step loading technique used to evaluate the fatigue limit stresses was validated based on the fatigue lives of specimens tested using shear wave NDI.

INTRODUCTION

Fretting fatigue, which is a phenomenon caused by localized relative motion between contacting components under vibratory load, has been shown in numerous studies [1, 2, 3] to produce early component failure through premature crack initiation. While many test systems have been developed to elucidate the manner in which fretting fatigue damage propagates, employing both idealized contact geometries [2, 3] and geometries designed to simulate real components [1], the mechanisms responsible for such damage are not clear. Results from a test geometry at an intermediate level of complexity are required to bridge the gap between laboratory and service conditions, particularly in turbine engine blade attachments.

The authors have published work on a novel test geometry that simulates the essential features of turbine engine blade root attachments, while maintaining the simplicity of a more generalized geometry [4, 5]. The previously published work established the viability of the apparatus in investigating fretting fatigue behavior and documented initial results on the effect of several factors critical to the fretting problem.

The purpose of the present investigation was to extend the scope of previous work by answering questions regarding the mechanisms of fretting fatigue crack nucleation in the current test geometry. Of specific interest were the location of fretting fatigue crack nucleation and the

portion of life spent nucleating cracks. To aid in the research two experimental techniques were employed: *in situ* crack detection using current Non-Destructive Inspection (NDI) techniques, and fretting fatigue limit stress evaluation using a step loading approach developed to permit rapid generation of data. Identification of crack nucleation life and location has not been examined for the contact geometry under investigation. The application of the selected NDI technique has not, as far as the authors know, been attempted under any contact conditions. Validation of the step loading technique has been performed for uniaxial conditions [6], but not for the complex stress states under contact conditions found in fretting fatigue.

EXPERIMENTAL SETUP
Fretting Fatigue Apparatus
        The fretting fatigue testing was conducted on an electromagnetic shaker system, which was used to apply the high frequency axial fatigue loads. Static clamping loads were imposed via instrumented bolts, whose internal strain gages allowed quantification of the clamping load. The test geometry employed removable flat fretting pads, with a radius at the edge of contact, against a flat specimen, as in Figure 1. Fretting damage in the form of wear scars and cracks occurred at both ends of the specimen at the edges of contact, shown in the magnified view in Figure 1. The test apparatus imposed normal and internal shear loads and a bending moment that may be disregarded, as it has been shown to be small relative to other parameters [7]. The reported experimental data only include the applied normal load and shear load, which is equal to one half of the applied axial load. Four regions on the specimen surface (two on each end of the specimen) were subjected to nominally identical fretting fatigue conditions, so both fracture surfaces and non-failure fretting scars were available for post-mortem inspection from each test. Additional details can be found in [4].

Crack Detection Apparatus
        In situ detection of fretting fatigue cracks was facilitated with the use of Ultrasonic Shear Wave NDI, which is a common NDI technique in components with inaccessible surfaces, such as the contact region of the fretting fatigue specimens in this investigation. The technique works by propagating shear waves into the region where cracks may exist in the component and then detecting the shear wave energy that reflects from cracks. The propagated or "incident" shear waves are usually created by mode conversion of longitudinal waves (emitted by an ultrasonic transducer) through coupling wedges on the surface of the component (see Figure 2.) When directed at appropriate angles the incident shear waves propagate through the component through multiple internal reflections as shown in Figure qf05. In general, cracks with cross-sectional dimensions equal to or larger than the ultrasonic wavelength reflect and/or scatter enough ultrasonic energy to be detected. A portion of the reflected shear wave energy propagated back through the component is converted into longitudinal energy in the coupling wedge and detected by the transducer.
        For this work it was desired to detect fatigue cracks on the order of 0.25 mm in a Ti-6Al-4V alloy for which the shear wave velocity is 3.29 mm/µs [8]. The frequency needed to generate ultrasonic shear waves in Ti-6Al-4V with 0.25 mm wavelengths is ~ 13 MHz. Ultrasonic transducers[1] with a center frequency of 10 MHz and -6 dB bandwidths greater than ± 5 MHz were selected. The transducers screwed into polymer coupling wedges designed to produce 45°

_____

[1] Model V5020, Panametrics, Inc., 221 Crescent St., Waltham, MA 02154

shear waves in steel. The nearly identical shear wave velocities of Ti-6Al-4V and most steels assured that the coupling wedges would work well for the Ti-6Al-4V fretting fatigue specimens. Two commercial ultrasonic pulser-receivers[2] with variable excitation energies, adjustable gains, variable damping, and high/low pas filters were used to excite the ultrasonic transducers and receive signals from them. The received ultrasonic signals were digitized by a commercial analog-to-digital converter[3] with a 100 MHz sampling rate and 8-bits of amplitude resolution.

For these tests, the specimen and pad configuration was not changed. Two transducer-coupling wedge assemblies were attached to the fretting fatigue specimen using a fast curing epoxy according to the diagram in Figure qf06, after the specimen was installed into the test fixture. The transducers were attached on opposite sides of the specimens and directed the ultrasound in opposing directions (see Figure qf06). This configuration directed the shear waves into the region beneath the fretting pads where fatigue cracks were expected to occur.

Both transducers propagated ultrasonic energy into the specimen at a repetition rate of approximately 1 kHz during the mechanical fatigue testing. In the region where the fretting pads were in contract with the specimen, some of the shear wave energy was reflected back to the transducers (see Figure qf08). As the fretting induced cracks propagated the signature of the reflected ultrasonic energy in the time window preceding the pad reflections changed. Cracks were detected by comparing successive ultrasonic signals, which were acquired at 500,000 mechanical fatigue cycle intervals.

Throughout each test several peaks in the analog waveform were monitored for changes in height and overall shape. When changes in the waveform suggested crack nucleation, the specimen was removed to verify the presence of a crack optically. If no crack could be identified under 100X magnification, the specimen was replaced in the test frame in the original position and the test was continued. If a crack was found, the damage at all potential crack sites was documented in the SEM and the specimen was heat treated to mark the crack size on the fracture surface. Then, the sample was replaced against the same set of pads and cycled to fracture to provide data on fatigue crack propagation life for the complex loading condition.

After each test was completed, the data was processed to allow verification of observations made during the test. The data processing was conducted using an alignment procedure in which the signals were shifted forward or backward in time so that the arrival time of largest pad reflection was set to a selected value. This process was required because the mechanical strains induced during mechanical testing changed the time-of-arrival of the ultrasonic reflections between successive data acquisitions. Although the time changes were small, approximately 0.06 μs, alignment in time of all of the ultrasonic signals improved the analysis for crack detection. The temporal location of the fretting pad reflection signals remained nearly constant throughout the tests providing a convenient marker for the analysis of the reflected ultrasonic energy (Figure qf08).

The current test environment introduced some features not present in environments where ultrasonic crack detection is typically used. Interference from the surrounding high frequency environment was a primary concern. Also, cracks were expected to nucleate at the edges of the specimen while the crack detection hardware was to be focused on the center of the specimen.

---

[2] Model 5072, Panametrics, Inc., 221 Crescent St., Waltham, MA 02154

Model PR35, JSR Ultrasonics, Inc., 3800 Monroe Ave., Pittsford, NY 14534

[3]Model DASP100A, Signatec, Incl, 355 N. Sheridan Street, Corona, CA 91720

Further, the potential existed for the crack to propagate to failure at the selected test frequency before waveform changes could be identified and the test stopped. In previous work, one test had been conducted using the shear wave apparatus with the higher clamping stress condition. A crack was detected and the test stopped prior to failure, but the crack was relatively large with respect to the overall specimen cross-section.

Materials & Machining

Fretting fatigue specimens and fretting pads were machined from forged AMS4928 Ti-6Al-4V with an duplex annealed microstructure. Since no cracks were expected in the pads, orientation with respect to loading for the pads was not specified or identified. Fretting fatigue specimens were machined with the fatigue axis oriented in the longitudinal direction. The material yield strength is 930 MPa; the tensile strength is 980 MPa, and the modulus is 120 GPa. Microstructure details are can be found in reference [9]. All specimens and fretting pads were low stress ground to an RMS 8 μinch surface finish.

Test Conditions

To achieve the objectives described above, two series of tests were conducted: one in which the specimens were fatigued without interruption until fracture, and one in which the specimens were interrupted based on the results of *in situ* crack detection. Consistent with previous work [4], a 3.2 mm radius was selected for the contact radii. Finite element modeling of the blade root indicated operating stresses normal to the flat region of the blade that is in contact with the disk to range from 140 MPa to 420 MPa [10]. The clamping stresses used in this investigation were ~200 MPa and ~ 620 MPa and were selected to approximate the stress range determined for service components. The pad lengths selected were 12.7 mm and 25.4 mm and with the selected contact radius, resulted in contact lengths of 6.35 mm and 19.05 mm. Fretting fatigue samples were 10 mm x 2 mm x 150 mm. All fretting fatigue tests were conducted at room temperature in lab air at 300 Hz.

In the first series of tests each sample was tested to failure using a step loading procedure to obtain the fretting fatigue limit for a 10^7 cycle fatigue life. The procedure involved applying blocks of cycles at increasing values of constant maximum stress for each block of cycles until the specimen fractured. The fatigue limit was then calculated from the final stress, number of cycles at the final stress, and the stress from the prior block, using linear interpolation [11]. Six tests were conducted at the 620 MPa clamping stress condition, and three were conducted at the 200 MPa clamping stress condition. The purposes of these tests were to establish an average fatigue strength for a 10^7 cycle fatigue life with data on the repeatability of each condition, and to provide fretted surfaces at 100 percent of life. Fretting scars were characterized in the SEM for comparison to partial life damage characterization from subsequent tests.

In the second series of tests, each specimen was fatigued at a constant maximum stress nearly equal to the average fatigue strength determined in the first series of tests, until cracks were detected using the shear wave crack detection technique described above, or until the specimen fractured. Three tests for each clamping stress condition were conducted. The specimens subjected to the 200 MPa clamping stress were tested at 350 MPa axial stress; specimens subjected to the 620 MPa clamping stress were tested at 260 MPa axial stress. These tests will be referred to as N_{DET} tests. Both the step load fatigue limit and the applied fatigue stress for N_{DET} tests are referred to as σ_A. A stress ratio, R, of 0.5 was used throughout.

EXPERIMENTAL RESULTS
Step Load Test Results
    The results of the step load tests are shown in Figure qf07, which shows the estimated fatigue limit for 10^7 cycles versus average applied clamping stress. Note that these results are also documented in reference [12]. Some data in Figure qf07 are included from previous work and were generated with a contact radius of 3.2 mm at R = 0.5 [4]. At 200 MPa average clamping stress, the average fatigue strength is ~ 330 MPa; at 620 MPa, the average fatigue strength is ~ 250 MPa. Error bars representing two standard deviations are included. In previous work, experimental results revealed no effect of applied clamping stress on fatigue limit within the range of clamping stresses investigated [4, 5]. However, in this study, a subtle increase in fatigue limit was observed as a function of decreasing clamping stress, as seen in Figure qf07. The effect was not evident until repeated tests at the same condition indicated the level of statistical scatter.

N_{DET} Results
    Three tests were conducted at the 200 MPa clamping stress in which the intent was to interrupt the tests based on crack detection with the shear wave ultrasonic technique. Table 1 lists cycles to failure as well as the cycle count of the last shear wave data acquisition. Total lives ranged from 3.1 million to 14.6 million cycles and bracketed the estimated 10^7 cycle fatigue life, thereby validating the step loading technique for this test condition. Since two of the three lives actually exceeded 10^7 cycles, the difference between the average limit stress for the step load tests and the applied stress used in the N_{DET} tests was statistically insignificant.
    None of the attempts to detect cracks on samples subjected to the 200 MPa clamping stress were successful. Throughout each test, no shear wave signal changes indicative of crack nucleation could be verified over the life of the specimen. Before the data acquisition cycle following the one listed in the second column in Table 1 could be reached, the specimen failed.
    Figure 7 shows representative waveforms from 99-B56. Some changes were present at 21.85, 21.95, 22.75, and 22.85 μs that could have indicated the presence of a crack; however, the signal at these locations tended to fluctuate, even between shear wave data acquisitions. Without a reference to compare against, and with such fluctuations occurring throughout the test (note early waveform changes in Figure 8), identifying which increases represented crack nucleation was difficult.
    In the test on sample 99-B57 some changes in the waveform were observed that were thought to be indications of crack nucleation (Figure 9), but careful inspection in the SEM did not reveal any cracks. Since the sample had already been cycled beyond the estimated fatigue life, the specimen was kept intact for a future characterization study.
    The third test, conducted on 99-B59, also failed before cracks could be detected. The cracks on this specimen were missed, in part, because the life of the specimen was short relative to the other two specimens. Also, as with the previous two tests, the peak heights had a tendency to vary, leading to confusion regarding which changes in the signal indicated crack nucleation. Observations made on 99-B57 lead the authors to conclude that these changes were not representative of crack nucleation, but of another phenomenon.
    Oxidation accumulation from fretting fatigue is one possible source of these fluctuations. During fretting fatigue an oxide layer was built up along the contact region undergoing relative slip. Initially, this layer was not present, and the pad and specimen were acoustically coupled by virtue of the clamping load, resulting in peaks in the signal where waves reflected off the edge of

contact. Introduction of an oxide layer at the edge of contact would have reduced the coupling in that location. If the oxide layer were removed, the signal response from the edge of contact increased again. Also, little change would be observed if the specimen were removed from the test rig and then replaced in the same location and orientation, since the oxide would be adhered to either or both of the contacting surfaces. The presence of the hypothetical oxide layer was verified by SEM characterization, discussed below.

These results partially answer one of the stated objectives. Fretting fatigue tests under the 200 MPa clamping stress condition nucleated cracks late in life. Assuming no cracks were present at the last cycle count for which shear wave data were acquired leads to the conclusion that less than 4 percent of life was spent in crack propagation. This conclusion is a direct contradiction of the findings from earlier researchers [2, 3, 13] that indicate the presence of cracks very early in life.

Cracks were successfully detected in two of the three tests planned for the 620 MPa clamping stress. The cycles to failure for these tests are given in Table 2. As with the tests at 200 MPa clamping stress, the cycles to failure results recorded for these tests were within the expected level of scatter for such tests, although the results at the higher clamping stress were consistently lower than the 10^7 cycle life of the step tests. The lower cycles to failure was probably a result of the difference between the average fatigue limit, 253 MPa, and the actual applied axial stress, 260 MPa. However, these results can still be used to support the validity of the step loading technique for fretting fatigue as the lives for this test condition were still within the scatter expected for a 10^7 cycle life.

The cracks successfully detected on 99-B60 and 99-B61 were fairly large, even when considering that the cracks were shallow compared to the surface length. As with the tests at the lower clamping stress, fluctuations in the waveform occurred throughout the tests that did not represent crack nucleation (note regions between 32.8 and 32.9 μs, and at 33.0 and 33.9 μs in Figure 10). Cracks were identified in 99-B60 and 99-B61 by changes in peaks adjacent to the largest reflection from the edge of contact, such as those shown at 32.1, 32.25, 33.15, and 34.05 μs. Since four potential nucleation sites were being inspected simultaneously, the waveform fluctuations obscured crack signals until the cracks were quite large. The time to propagate the detected cracks to failure was very small compared to the total specimen life.

While these results do not provide adequate information on the crack nucleation life for the 620 MPa clamping stress condition, they do support the feasibility of the technique. Neither the noise nor the high frequency environment were enough to prevent detection of fretting cracks. Coupling of the pad and specimen introduced changes in the acoustic response, but since the peaks were relatively constant, changes in the waveform indicating the presence of a crack were still identifiable.

The third attempt made to locate a crack earlier in the propagation life, using sample 99-B62, was unsuccessful. As in the case of the 140 MPa test, the specimen failed before a crack could be detected. Again, the life of the third specimen was shorter than the previous two specimens, and shorter than the expected specimen life. The scatter in the lives for these tests is not unexpected. The lives for the 620 MPa clamping stress tests fall within a factor of two; the 200 MPa clamping stress tests fall within a factor of four. This level of scatter is more than acceptable for a phenomenon with so much potential variability, where an order of magnitude would be considered reasonable scatter.

CHARACTERIZATION RESULTS

All samples were characterized in the SEM to provide qualitative information on the level of damage generated in each test. Both faces of the unfailed end of fractured samples were inspected for secondary cracking and level of wear and fracture surfaces features were documented in the estimated region of initial crack nucleation.

Fretted surface characterization

Fretting scars from the unfailed ends of failed N_{DET} specimens are shown in Figures 11 and 12 for the 200 MPa and 620 MPa clamping stress conditions, respectively. Both photos were taken in the SEM using backscatter imaging to enhance wear features. The level of damage was roughly the same for both specimens, although wear products were present over a larger area on specimens tested at the 200 MPa clamping stress compared with the 620 MPa condition.

While the lower clamping stress samples were characterized exclusively by wear, the higher clamping stress samples were also characterized by the presence of cracks (Figures 13), which were found on the unfailed ends of the samples tested to failure. The surface length of these cracks ranged anywhere from 200 μm to 1.6 mm and all appeared to nucleate near the specimen edges during SEM characterization. By comparison, no cracks larger than 20 μm were observed on the samples subjected to 200 MPa clamping stress, and the cracks that were found were contained entirely within the fretting debris. Previous work [14] has shown that cracks such as those observed on the specimens subjected to lower clamping stress were either non-propagating, or propagate in a manner that leads to spalling of the wear products.

Fracture surface characterization

Representative fracture surfaces from step tested specimens for both clamping stresses are shown in Figures 14 and 15. The micrographs show the nucleation regions of the fracture surfaces for 200 MPa and 620 MPa clamping stresses, respectively, and include the entire thickness of the specimen. Figures 16 and 17 give closer views of initial nucleation sites, indicated by the boxes in Figures 14 and 15, for each test condition. All four images were taken in backscatter mode, where darker regions represent different alloy phases, different levels in the fracture topography, or cracking parallel to the fatigue axis.

Inspection of both fracture surfaces reveals that the cracks nucleated from roughly the same region with respect to the edge of the sample, and propagated into the specimen in the direction of the arrows (see Figures 14 and 15). The 200 MPa specimen fracture surface has a more planar appearance with no evidence that any cracks nucleated other than the initial one that fractured the specimen. The 620 MPa specimen shows evidence of multi-plane cracking and chipping (note damage to the right of the box in Figure 15) resulting from the propagation of multiple cracks. A crack front opposite of the initial crack nucleation site on the 620 MPa specimen is also apparent. The nucleation sites in Figures 14 and 15 are within 500 μm of the specimen edge. Flat crack propagation regions are present toward the center of the specimen, where cracks would not have been able to open early in the test because the material was constrained. Multi-branch cracks, such as the one shown in Figure 13, where two or more cracks lie perpendicular to the axis of fatigue loading, were observed, providing evidence of a locally complex stress state.

Closer inspection of the primary nucleation site of the 200 MPa specimen also reveals a very planar fracture with no cracks parallel to the fatigue loading axis, pointing to the dominance of axial loading on crack propagation for this contact configuration and loading condition. The magnified view of the 620 MPa specimen fracture surface shows evidence of a higher stress state

and the multi-axial nature of that stress state in the form of cracking parallel to the fatigue axis.

As stated above, no cracks were successfully detected using the shear wave ultrasonic crack detection technique for the specimens subjected to 200 MPa clamping stress. Thus, only fracture surfaces for the specimens subjected to 620 MPa clamping stress for the N_{DET} tests are presented. The image in Figure 18 documents the crack detected using the Shear Wave NDI technique. This crack measured ~2.3 mm long on the surface at the time of inspection and extended far beyond the left edge of the photo. The image in Figure 19 shows the corresponding fracture surface after the test was finished. The dark region of the fracture surface indicates the crack depth at the time the test was interrupted at 7,020,000 cycles. Final fracture occurred at 7,350,000 cycles. One feature to note on this specimen is depth of the crack, which is ~ 800 μm at it's maximum, compared to it's surface length of ~ 2.3 mm. Also, the primary crack nucleation site is ~ 500 μm from the sample edge.

The second test conducted under the 620 MPa clamping stress condition was stopped based on ultrasonic waveform changes at 6,125,000 cycles, at which time a crack 2.6 mm long was identified (Figure 20). The corresponding fracture surface after the test was finished is shown in Figure 21, where the dark region of the fracture surface indicates the crack depth at the time the test was interrupted. In this case, the crack propagated nearly to the other side of the specimen before it was identified. A smaller crack can be seen propagating from the opposite side of the fracture surface, and some multi-level cracking is apparent from the line of unoxidized fracture (light line within the dark region) existing within the region of the fracture surface exposed to heat tinting. Final failure occurred at 6,227,000 cycles.

In both tests more than one crack was identified upon inspection. The first specimen contained two additional cracks (approximately 900 μm and 350 μm) on the same end of the specimen as the dominant crack, but on the opposite side. The second contained three additional cracks (approximately 500, 340, and 250 μm), of which the largest was located in the opposite end of the specimen from the dominant crack. These results indicate that cracks nucleated earlier in the specimens subjected to the higher clamping stress. In specimens subjected to the lower clamping stress, no cracks of any size were observed up to 11 million cycles, while many cracks of appreciable size were identified in the specimens subjected the higher clamping stress.

The results of the of the step and N_{DET} tests, taken together, provide evidence of the location of crack nucleation. All nucleation sites for both contact conditions were identified near the corners. The number of nucleation sites was dependent on the clamping stress. The higher clamping stress produced multiple nucleation sites, of which one would eventually dominate. The secondary cracks provided better identification of the nucleation sites, which is between 50 μm and 500 μm of the specimen edge.

CONCLUSIONS AND RECOMMENDATIONS
From the research detailed above, the following conclusions can be drawn.
- Cracks nucleated at or near specimen corners regardless of the applied normal stress.
- The time required for nucleation of cracks differed for the two clamping stress conditions: the 200 MPa condition spent over 95% of life nucleating cracks, while the 620 MPa condition nucleated cracks much sooner.
- Shear wave crack detection is a viable experimental monitoring technique for high contact clamping forces.
- The step loading approach can be used to rapidly determine fatigue limits under fretting fatigue conditions.

REFERENCES

1. Ruiz, C., Boddington, P. H. B., and Chen, K. C., "An Investigation of Fatigue and Fretting in a Dovetail Joint," *Experimental Mechanics*, Vol. 24, 1984, pp. 208-217.
2. *Fretting Fatigue, ESIS 18*, R.B. Waterhouse and T.C. Lindley, Eds., Mechanical Engineering Publications, London, 1994.
3. *Standardization of Fretting Fatigue Test Methods and Equipment, ASTM STP 1159*, M. Helmi Attia, and R. B. Waterhouse, Eds., American Society for Testing and Materials, Philadelphia, 1992.
4. Hutson, A., Nicholas, T., and Goodman, R., "Fretting Fatigue of Ti-6Al-4V Under Flat-on-Flat Contact", *International Journal of Fatigue*, Vol. 21, No 7, 1999, pp. 663 – 670.
5. Hutson, A. and Nicholas, T., "Fretting Fatigue Behavior of Ti-6Al-4V against Ti-6Al-4V under Flat-on-Flat Contact with Blending Radii," *Fretting Fatigue: Current Technologies and Practices, ASTM STP 1367*, D.W. Hoeppner, V. Chandrasekaran, and C.B. Elliot, Eds., American Society for Testing and Materials, West Conshohocken, PA, 1999, pp. 308 - 321.
6. Bellows, R. S., Muju, S. and Nicholas, T., "Validation of the Step Test Method for Generating Goodman for Ti-6Al-4V," *International Journal of Fatigue*, Vol. 21, No 7, 1999, pp. 687 – 698.
7. Hutson, A.L., "Fretting Fatigue of Ti-6Al-4V Under Flat-on-Flat Contact with Blending Radii," M.S. Thesis, School of Engineering, University of Dayton, Dayton, OH, August, 2000.
8. U.S. Air Force Technical Report #AFML-TR-79-4214, Materials Engineering Materials Selector 1990, 1100 Superior Ave., Cleveland, Ohio 44114-2543.
9. Haritos, G.K., Nicholas, T. and Lanning, D., "Notch Size Effects in HCF Behavior of Ti-6Al-4V," *International Journal of Fatigue*, Vol. 21, No 7, 1999, pp. 643 – 652.
10. Van Stone, R., "Fretting and High Cycle Fatigue in Titanium," presented at the 3rd National Turbine Engine High Cycle Fatigue Conference, San Antonio, TX, 1998.
11. Maxwell, D.C. and Nicholas, T., "A Rapid Method for Generation of a Haigh Diagram for High Cycle Fatigue," *Fatigue and Fracture Mechanics: 29th Volume, ASTM STP 1321*, T.L. Panontin and S.D. Sheppard, Eds., American Society for Testing and Materials, 1999, pp. 626-641.
12. Hutson, A.L., Nicholas, T., Olson, S.E. and Ashbaugh, N.E., "Effect of Sample Thickness on Local Contact Behavior in a Flat-on-Flat Fretting Fatigue Apparatus," International Journal of Fatigue, in press.
13. Blanchard, P., Colombie, C., Pellerin, V., Fayeulle, S. and Vincent, L. "Material Effects in Fretting Wear - Application to Iron, Titanium, and Aluminum Alloys," *Metallurgical Transactions*, Vol. 22A, 1991, pp. 1535-1544.
14. Fayeulle, S., Blanchard, P., and Vincent, L., "Fretting Behavior of Titanium Alloys," *Tribology Transactions*, Vol. 36, No. 2, 1993, pp. 267-275.

FIGURES:
Figure 1. Fretting fatigue gripping system.
Figure 2. Coupling wedges were used to convert the ultrasonic energy from longitudinal to shear wave modes.

Figure 3. Ultrasonic crack detection using shear waves.   Internal reflections of the shear waves allowed ultrasonic energy to propagate through the specimen to the location underneath the fretting pads where fatigue crack initiated.

Figure 4. Ultrasonic transducer placement schematic.

Figure 5. Fatigue limit stress at R = 0.5 versus average clamping stress for a 10^7 cycle life.

Figure 6. Typical ultrasonic signal acquired before cracks were detected.

Figure 7. Waveform changes over the specimen life that may have represented crack nucleation (99-B56).

Figure 8. Waveform fluctuations that do not indicate a crack presence (99-B56 early in test).

Figure 9. Waveform fluctuations occurring in a sample that showed no cracks on inspection (99-B57).

Figure 10. Waveform changes over the specimen life that indicated the presence of a fretting nucleated crack (99-B61).

Figure 11. Damage for N_{DET} specimen at 140 MPa clamping stress. Fatigue loading axis is vertical. (N_f = 14,630,000 cycles)

Figure 12. Non-crack damage for N_{DET} specimen at 420 MPa. Fatigue loading axis is vertical. (N_f = 6,227,000 cycles).

Figure 13. Secondary fretting crack nucleated at 420 MPa clamping stress. Fatigue loading axis is vertical. (Nf ~ 4.1 million cycles)

Figure 14. 99-B74 (140 MPa clamping stress) – step load test fracture surface.

Figure 15. 99-B72 (420 MPa clamping stress) – step load test fracture surface.

Figure 16. Magnified view of estimated primary crack nucleation site in Figure 6.4.

Figure 17. Magnified view of estimated primary crack nucleation site in Figure 6.5.

Figure 18. Crack detected using shear waves for 420 MPa clamping stress. Fatigue loading axis is vertical. (N = 7,020,000 cycles – 99-B60)

Figure 19. Fracture surface of specimen with successful shear wave crack detection (99-B60). Arrows indicate crack tip position at time of crack detection.

Figure 20. Crack detected using shear waves for 420 MPa clamping stress. Fatigue loading axis is vertical. (N = 6,125,000 cycles – 99-B61).

Figure 21. Fracture surface of specimen with successful shear wave crack detection (99-B61).

TABLES:

Table 1: N_{DET} test results for 140 MPa clamping stress

Specimen	N (last SW signal)	Cycles to Failure
99-B56	14,110,000	14,628,924
99-B57	10,900,000	>11,000,000
99-B59	3,000,000	3,099,251

Clamping stress = 140 MPa, Axial stress = 350 MPa

Table 2: N_{DET} test results for 420 MPa clamping stress

Specimen	Cycles to N_{det}	Cycles to Failure	Crack length (mm)
99-B60	7,019,649	7,349,240	2.3*
			0.90
			0.35
99-B61	6,125,123	6,227,169	2.6*
			0.50
			0.34
			0.25
99-B62	na	4,126,650	na

Clamping stress = 420 MPa, Axial stress = 260 MPa; * indicates failure crack
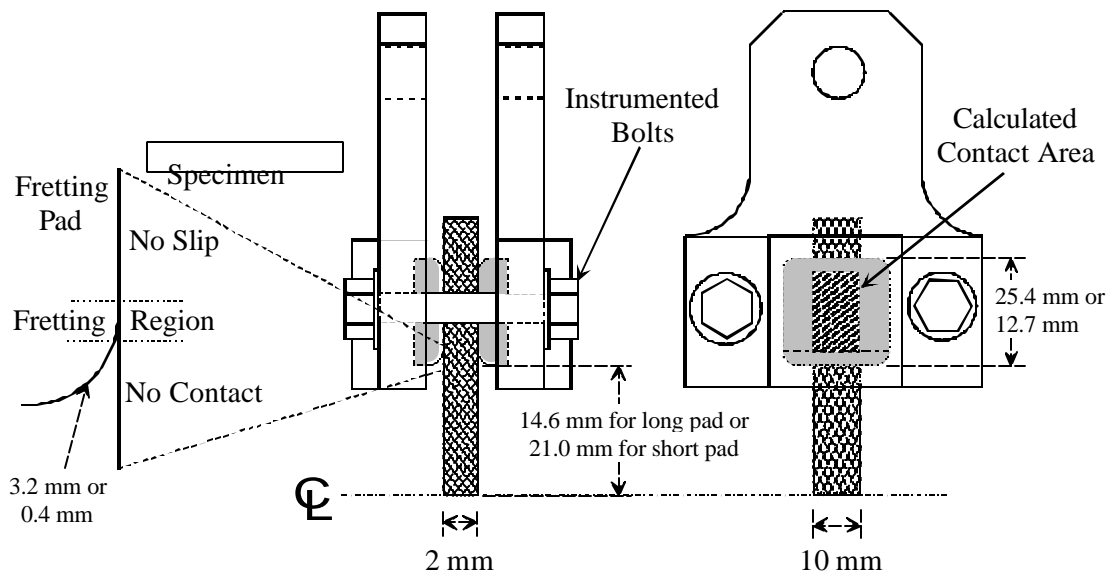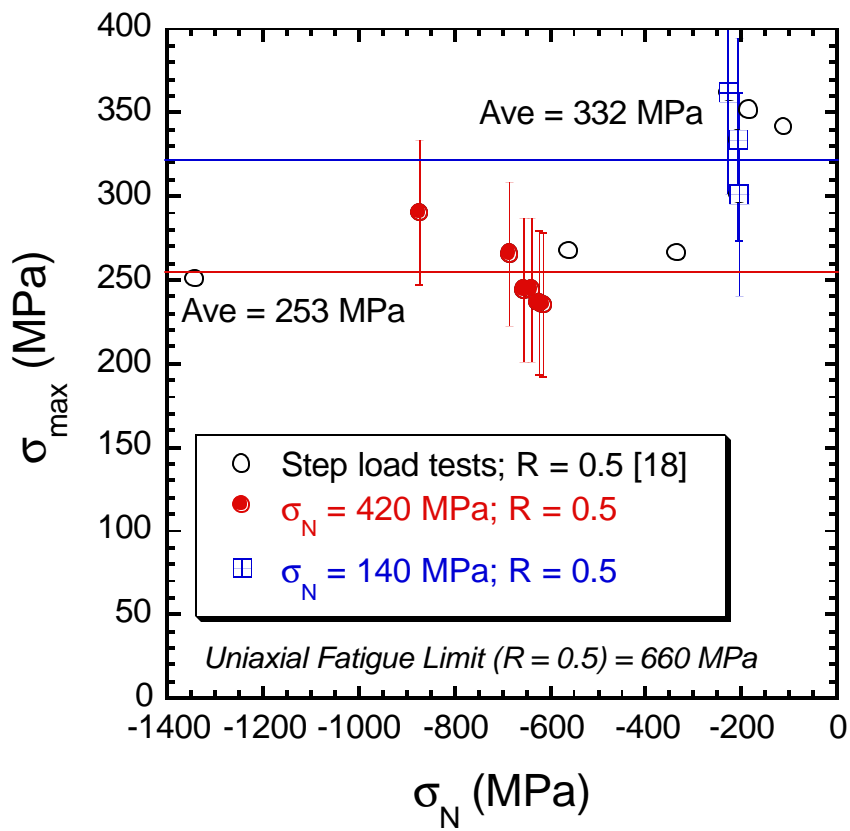
Figure 1.
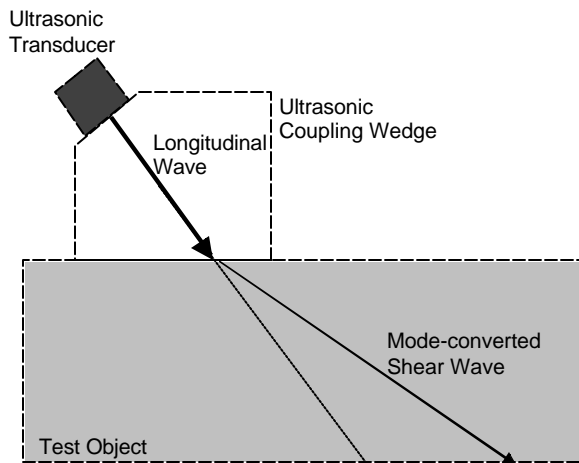
Figure 2.
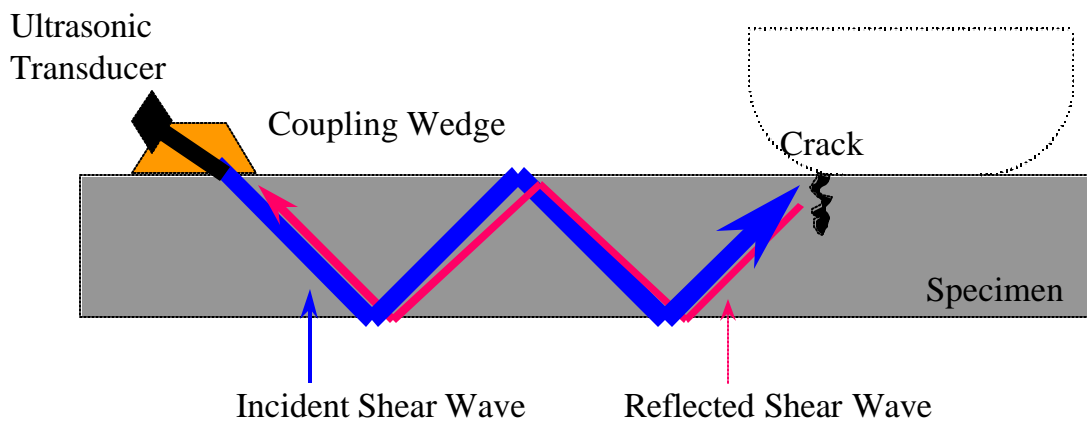
Figure 3.
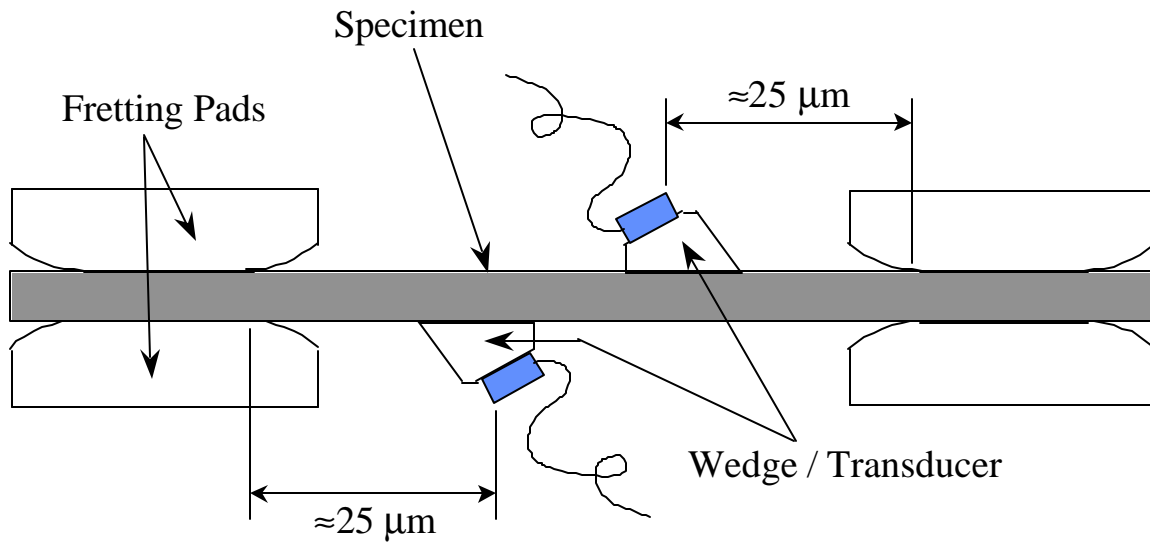
Figure 4.

Figure 5.

Typical Time Domain Results from Ultrasonic Shear Wave Propagation

Figure 6.

99-B56

Figure 7

99-B56

Figure 8

99-B57

Figure 9.

99-B61

Figure 10

200 μm
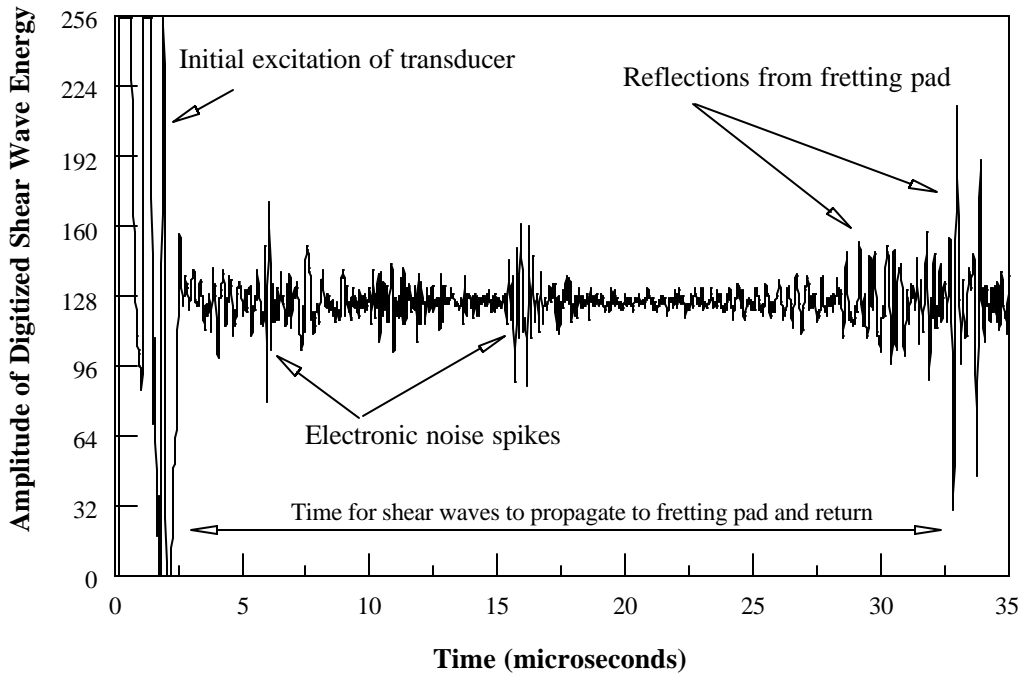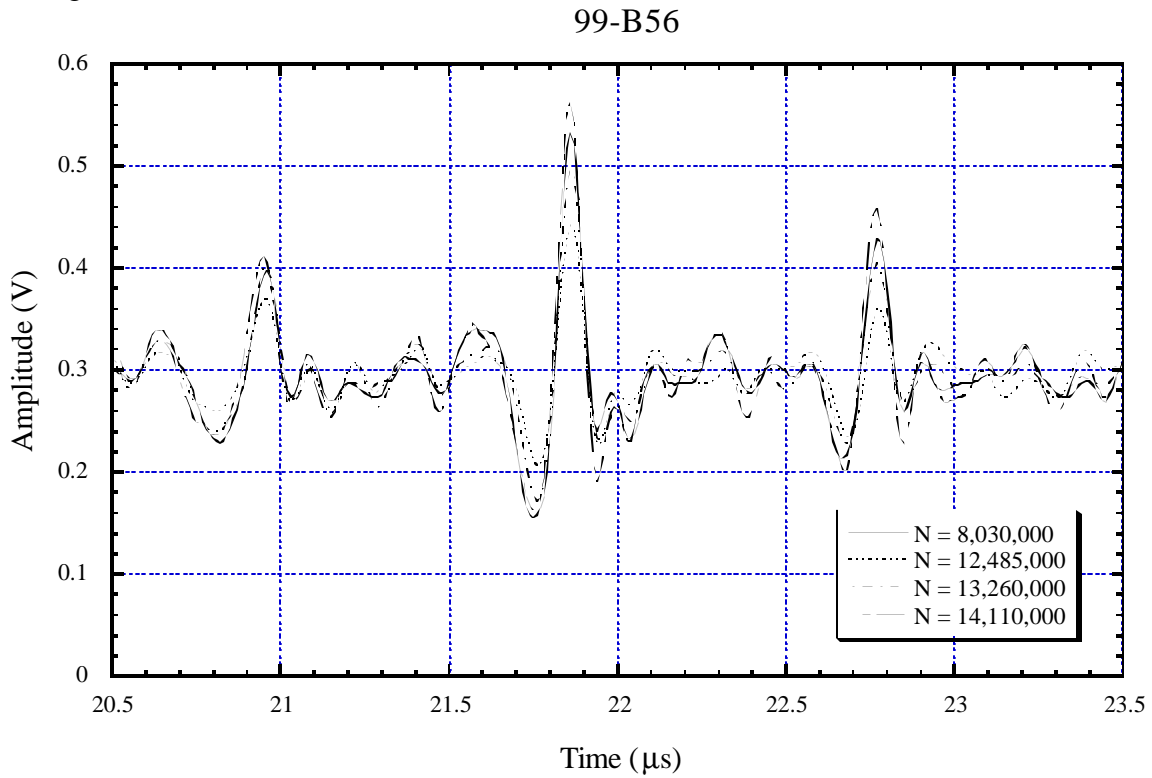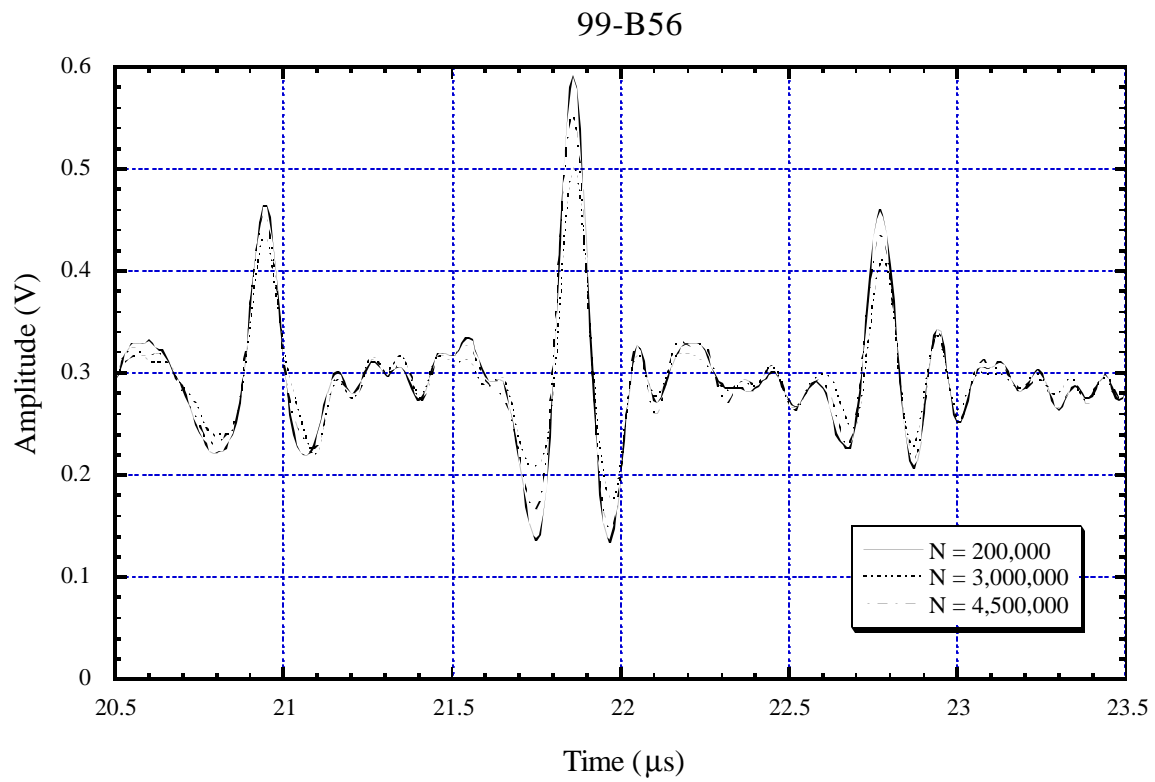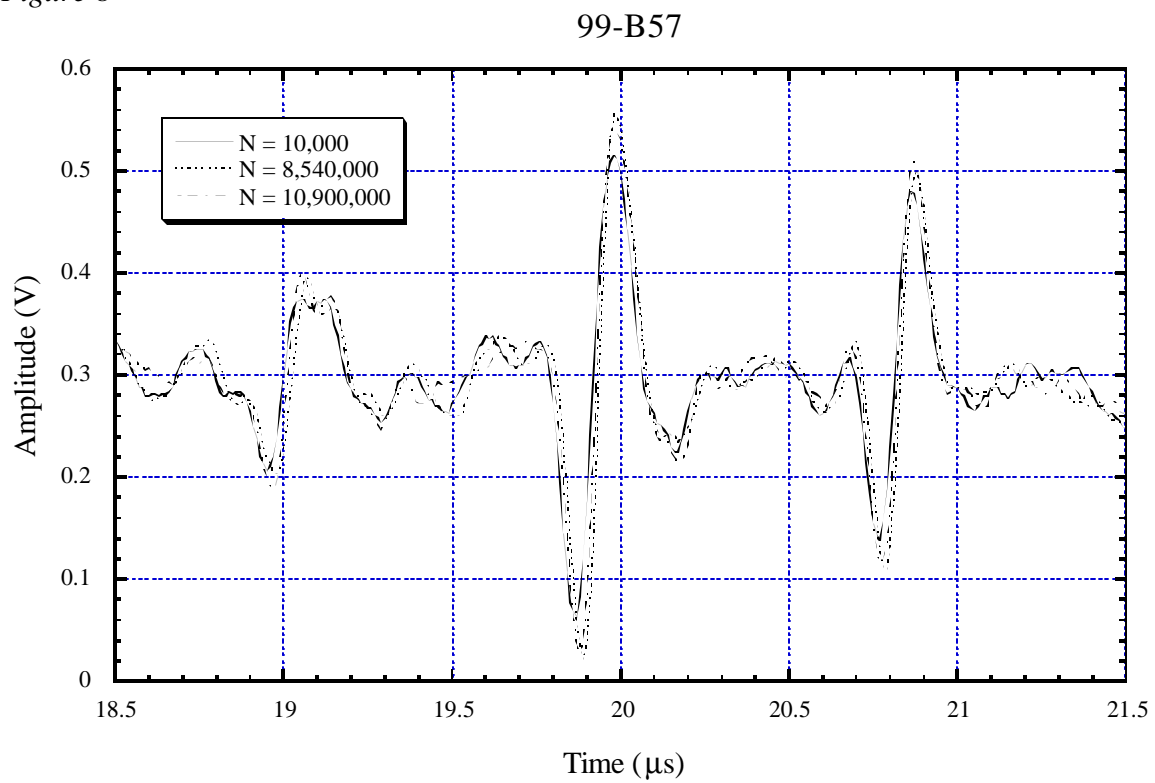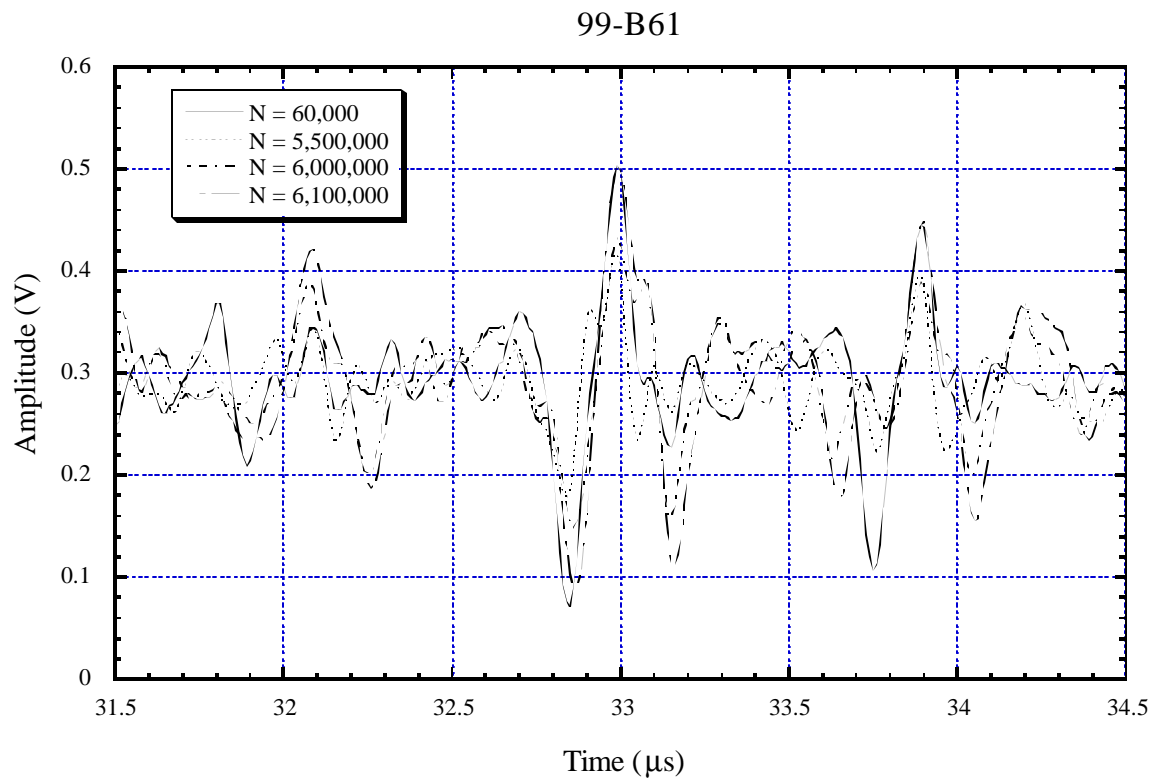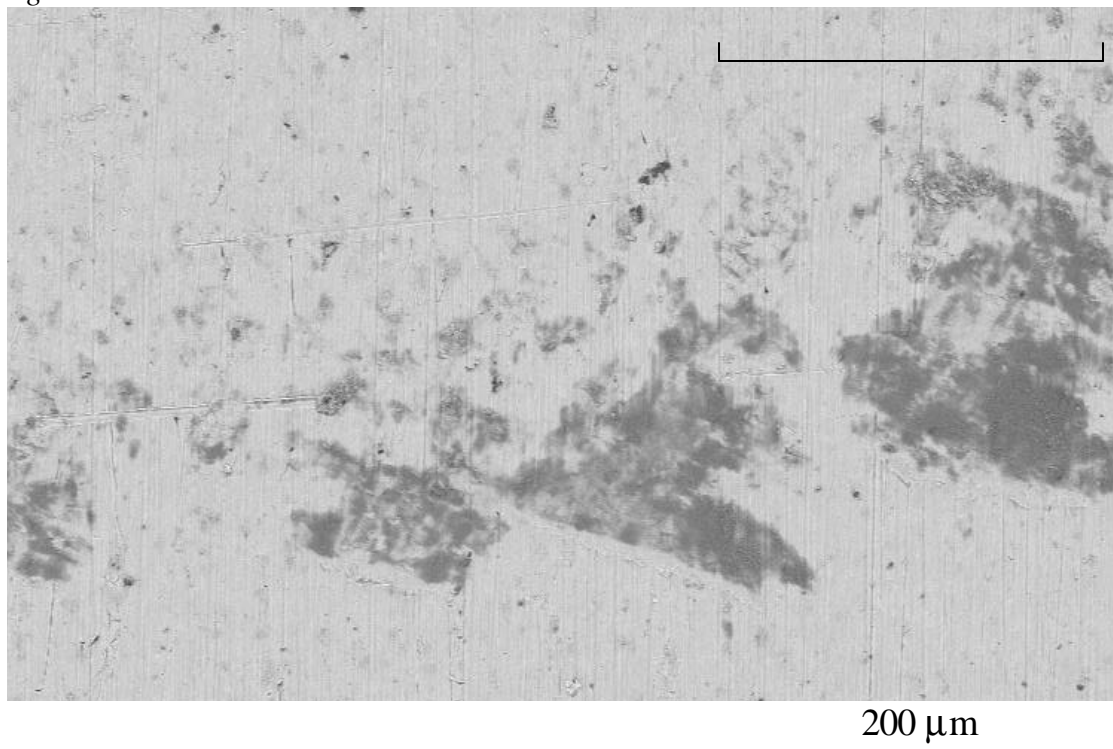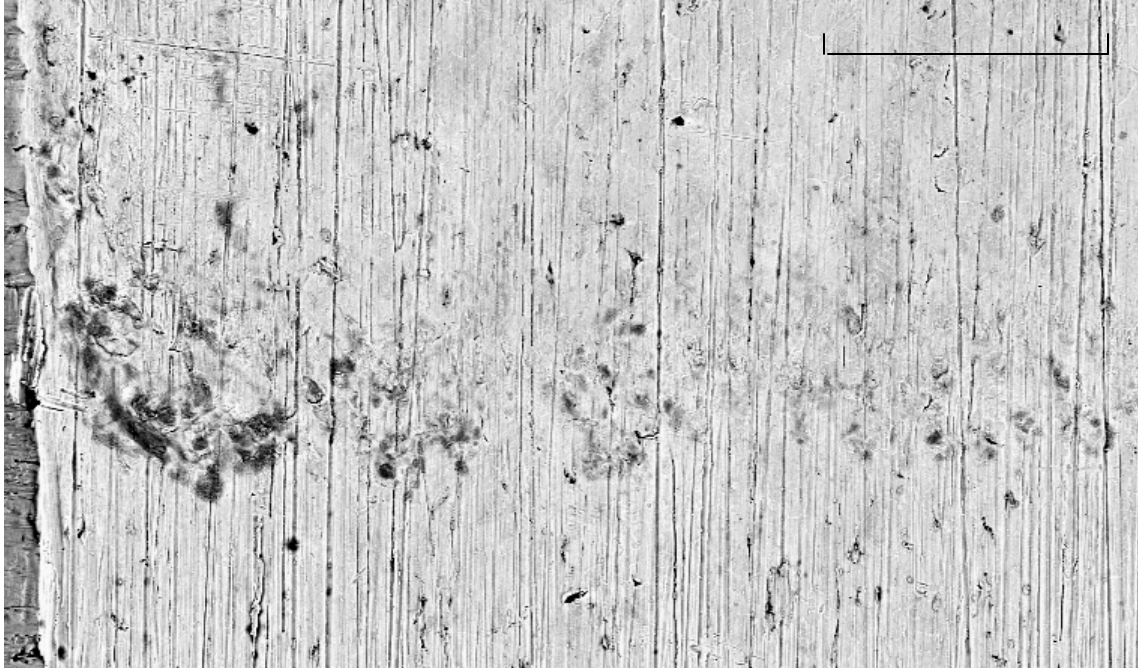
Figure 11

100 µm

Figure 12

secondary crack

100 µm
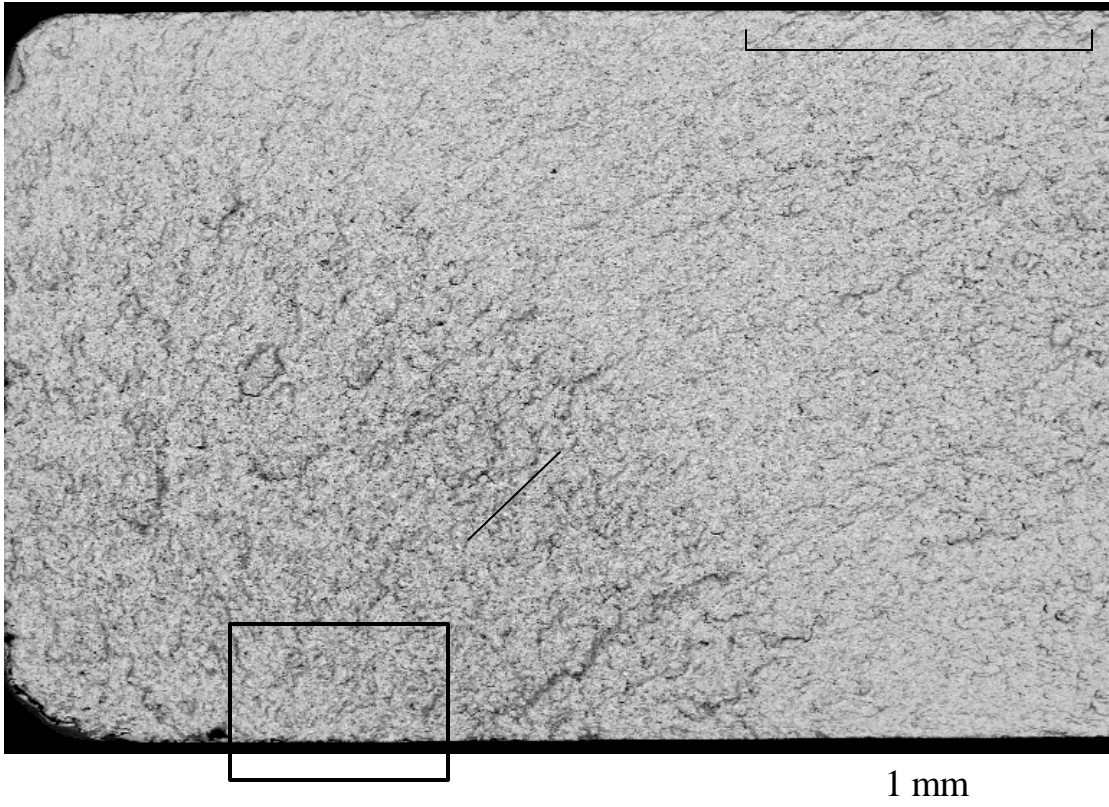
Figure 13

Figure 14.
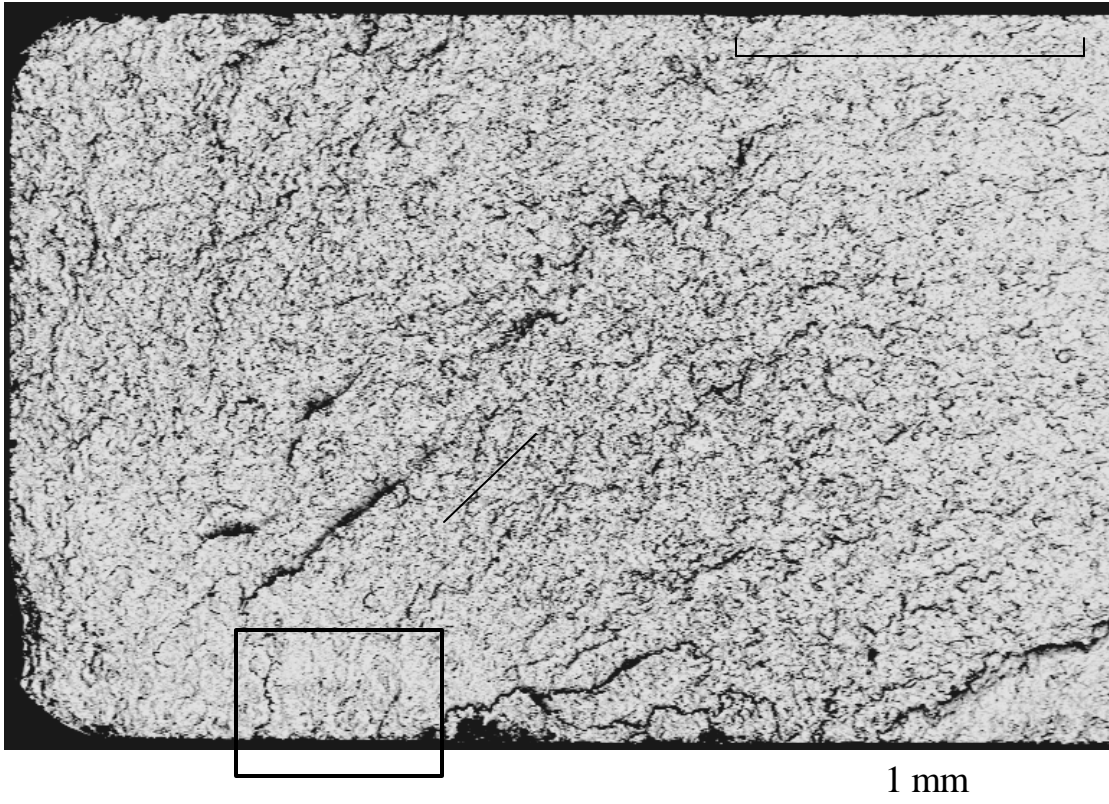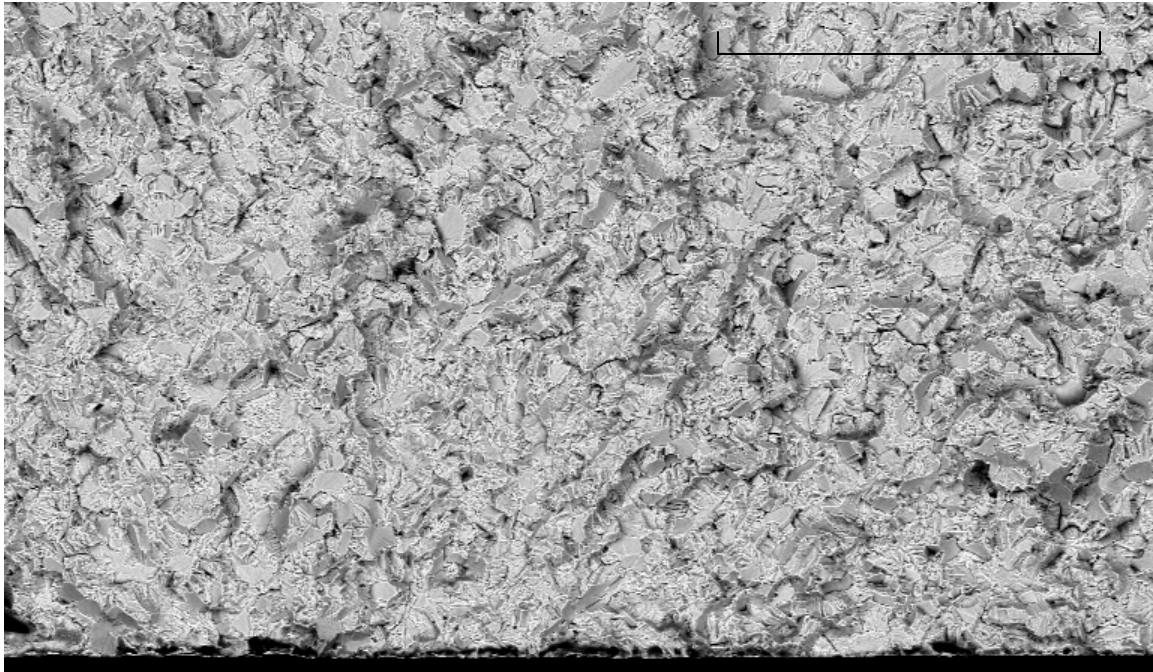
Figure 15.

200 µm
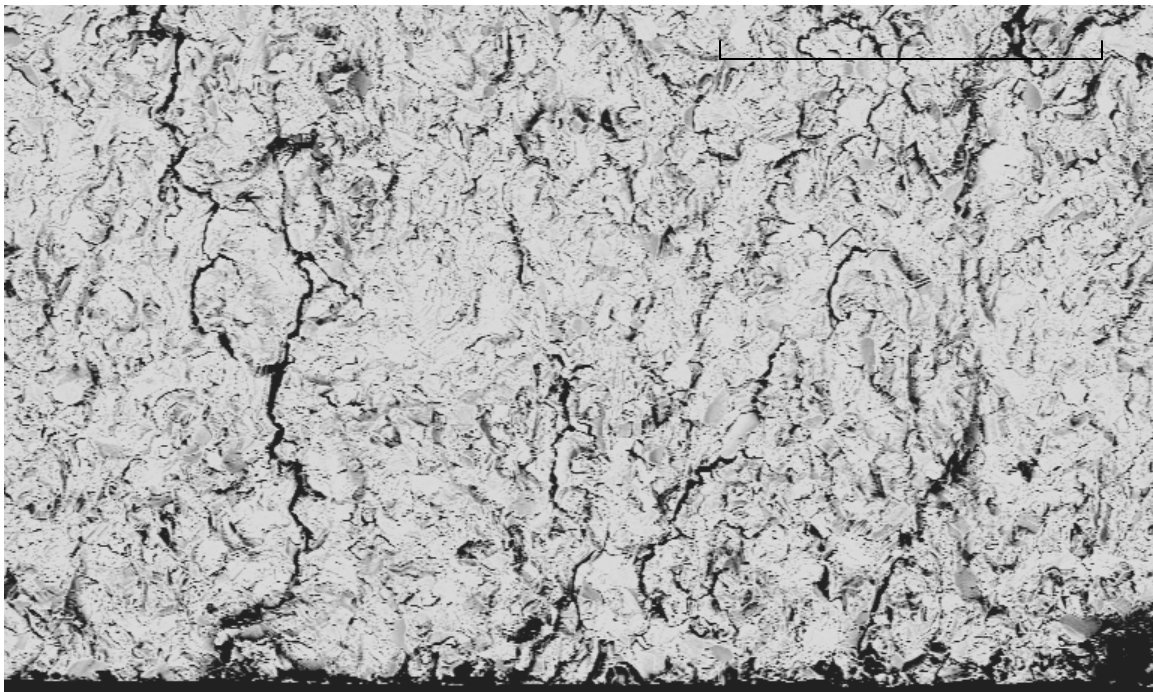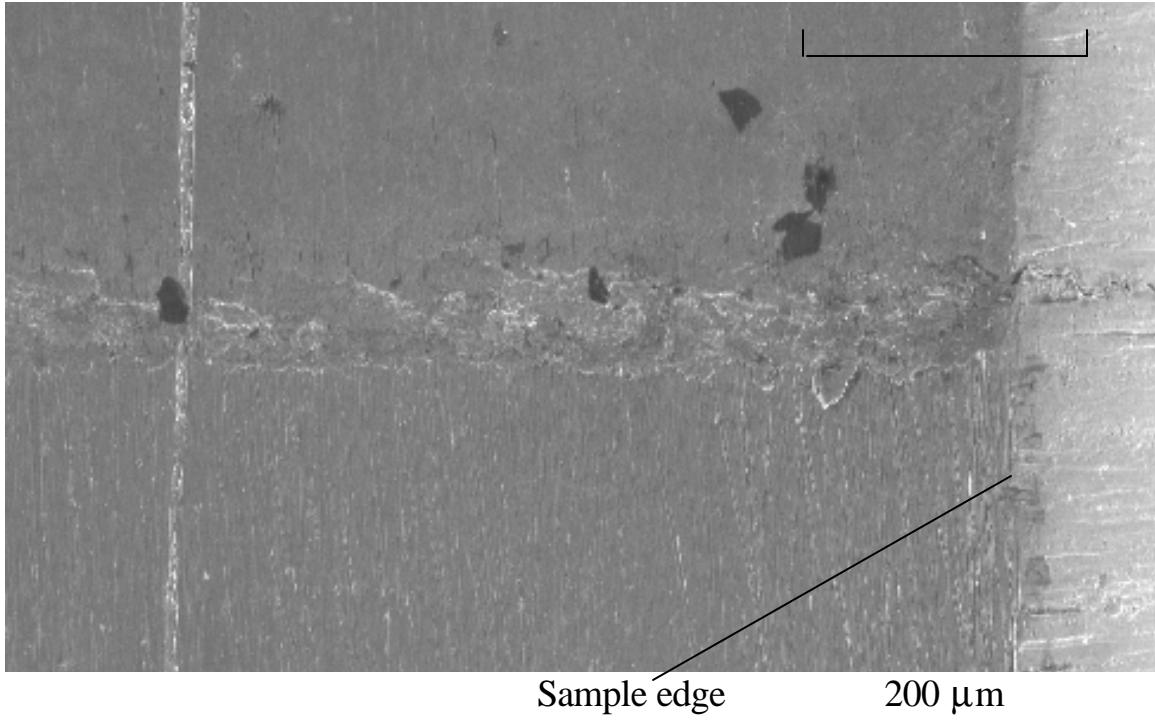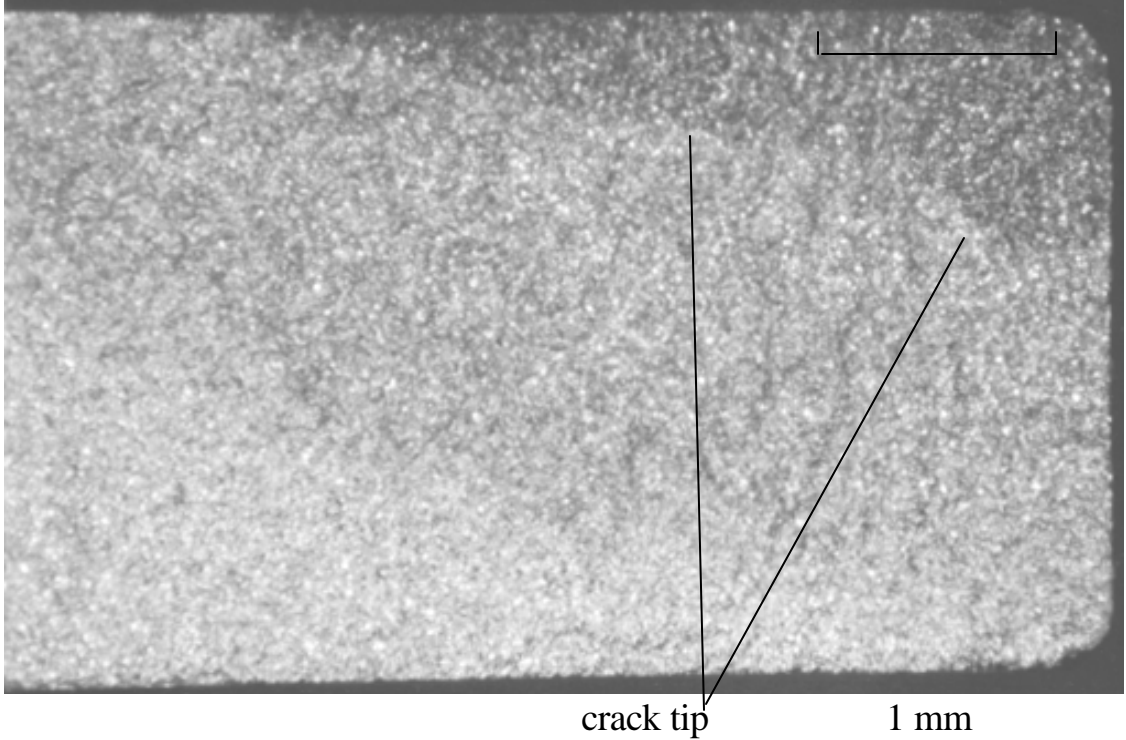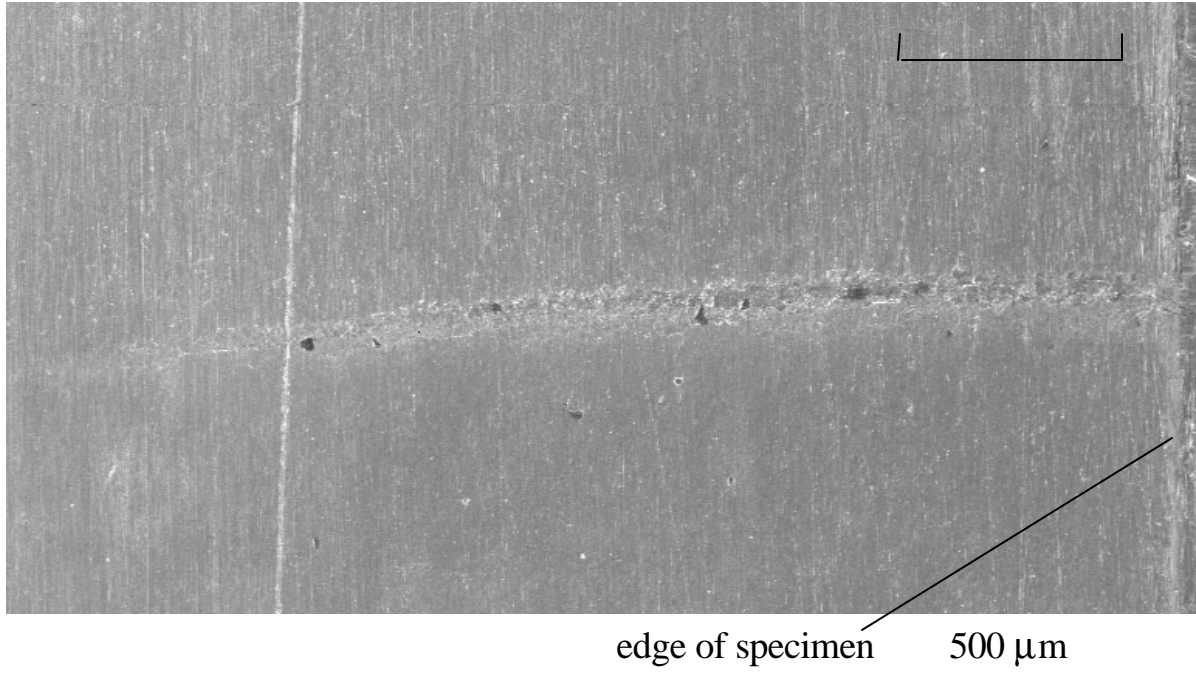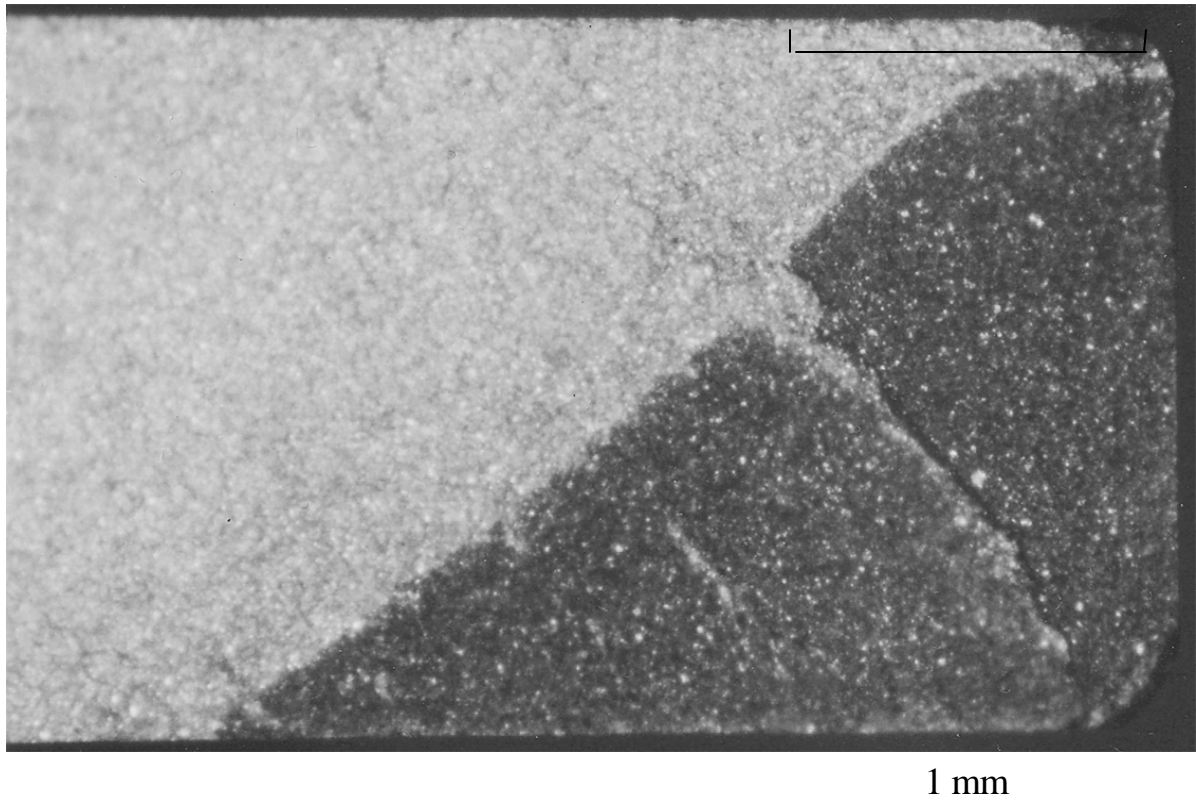
Figure 16.

200 µm

Figure 17.

Sample edge   200 µm

Figure 18.

crack tip   1 mm

Figure 19.

edge of specimen 　　 500 µm

Figure 20.

1 mm

Figure 21.

153

This page intentionally left blank.

An Investigation of Fretting Fatigue Crack Nucleation Life of Ti-6Al-4V Under Flat-on-Flat Contact

A. L. Hutson[1], N. E. Ashbaugh[1], and T. Nicholas[2]

[1]University of Dayton Research Institute, 300 College Park, Dayton, OH 45469-0128, U. S. A. Phone: +1-937-255-2708, Fax: +1-937-255-1363, E-mail: alisha.hutson@afrl.af.mil

[2]Metals, Ceramics & NDE Division, Materials and Manufacturing Directorate, Air Force Research Laboratory (AFRL/MLLMN), Wright-Patterson AFB, OH 45433-7817, U. S. A.

ABSTRACT

A study was conducted to investigate fretting fatigue damage of Ti-6Al-4V against Ti-6Al-4V under flat-on-flat contact with blending radii at room temperature. Both the location of and the time required to nucleate fretting fatigue cracks were investigated for two static average clamping stress values that are representative of those estimated for turbine engine blade attachments. The effect of fretting fatigue on uniaxial fatigue life was quantified by interrupting fretting fatigue tests, and conducting uniaxial residual fatigue life tests. Metalography, scanning electron microscopy and spectral analysis were used to characterize the level of fretting damage.

Fretting fatigue tests interrupted at 1 million cycles indicated significant fretting damage and reduction in residual uniaxial fatigue life for half of the specimens subjected to the higher clamping stress. Little observable damage and no reduction in residual uniaxial fatigue life was identified for the lower clamping stress. Stress distribution trends from the analysis supported experimental findings. Relative slip values determined from the analysis were lower than expected based on values reported in the literature. Results of the analysis were used to calculate the inherent bending moment in the experimental apparatus, which was determined to be small.

INTRODUCTION

Fretting fatigue is the phenomenon caused by localized relative motion between contacting components under vibratory load. The damage due to fretting fatigue can lead to premature crack initiation and failure. Such damage has been indicated as the cause of many unanticipated disk and blade failures in turbine engines, and as a result, has been the focus of numerous studies [1-5] over the years. Fretting fatigue often takes place in the presence of other types of damage, leading to confusion regarding the source of and micro-mechanisms responsible for premature failures. With the numerous conditions influencing the fretting fatigue phenomenon, a comprehensive understanding of how fretting fatigue occurs and subsequent accurate life prediction modeling has been elusive.

Many different test systems have been developed to aid in the search to understand the fretting fatigue phenomenon. Most research has been conducted on Hertzian [3,5], or square cornered punch-on-flat [3,5] geometries because of the availability of closed form analytical solutions for the resulting stress distributions. However, the applicability of these geometries to

real components is limited. Some work has been done to directly test real component geometries [1], but specimens are expensive, determination of the stress distribution is tedious and costly, and the results are difficult to model. A geometry that provides information at an intermediate level of complexity is required as the next step toward the development of an accurate life prediction model that bridges the gap between laboratory and service conditions.

The authors have published work on a novel test geometry that simulates the essential features of a turbine engine blade root attachment while maintaining the simplicity of a more generalized geometry. Previously published work established the viability of the test apparatus in investigating fretting fatigue behavior and documented preliminary results on the effect of several parameters critical to the fretting problem [6,7].

The purpose of the present investigation was to extend the scope of prior work and answer questions regarding the mechanisms of fretting fatigue crack nucleation in the current test geometry. Of interest to the current work were the location of and portion of life spent in fretting fatigue crack nucleation, and quantification of the effects of fretting fatigue damage on residual fatigue properties. Previous efforts by the authors to address these issues have produced less than conclusive results [6-8]. By extending the scope of testing from previous investigations to include characterization of damage at a small percentage of life, conclusive data may be obtained to address the issues of fretting fatigue crack location, crack nucleation life and the magnitude of fretting fatigue damage for the current contact geometry.

EXPERIMENTAL APPROACH

Fretting Fatigue Apparatus

The fretting experiments in this study were designed to simulate the primary loading conditions under which fretting fatigue damage occurs in turbine engine blade attachments. This was achieved by testing a flat specimen against a flat pad with blending radii at the edges of contact. Static clamping loads were imposed using instrumented bolts to quantify the clamping load. An electromagnetic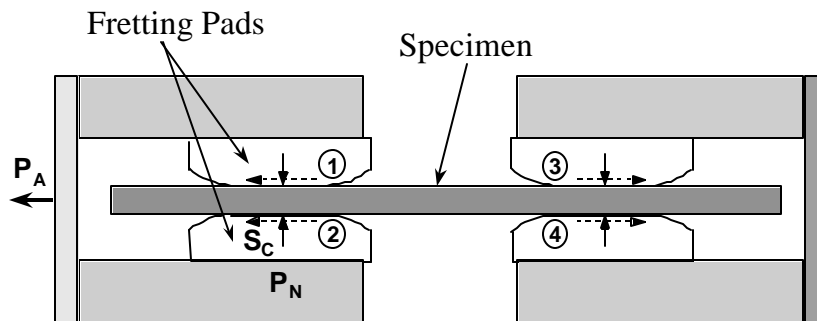 shaker system was used to apply the axial fatigue load. The test assembly produced two nominally identical fretting fatigue tests for each specimen (Figure 1), and imposed normal and internal shear loads as well as a negligible bending moment [9]. Additional details can be found in [6]. For this investigation, fretting fatigue cycles were applied at 300 Hz.

Figure 1. Test load train schematic. Numbers indicate edge of contact locations.

Uniaxial Fatigue Apparatus

For the tests conducted for this investigation, fretting fatigue conditions were removed after a small portion of total fretting fatigue life, and the residual fatigue properties were evaluated in uniaxial fatigue. Two test systems were used in the residual fatigue property portion of the investigation: one for tests in which residual fatigue life was evaluated and one for tests in which residual fatigue strength was evaluated. For the residual fatigue life tests, a servo-

hydraulic test system was used. The system was equipped with a 5000 lbf (22.24 kN) capacity load cell, an analogue controller operated in the load control mode, and hydraulic wedge grips with a 25 kN grip capacity and surfalloy inserts. Tests were conducted at 3 Hz. Residual fatigue strength tests were conducted using an electromagnetic shaker system like the one used for the fretting fatigue portion of the study [6]. Tests were conducted at 300 Hz. All test were conducted in lab air at room temperature.

Material and Machining Parameters

Fretting fatigue specimens and pads were machined from forged Ti-6Al-4V plates with a $\alpha+\beta$ duplex microstructure. Since no cracks were expected in the pads, orientation with respect to loading for the pads was not specified or identified. Axial specimens were machined with the fatigue axis oriented in the longitudinal direction. The material yield strength is 930 MPa; the tensile strength is 980 MPa, and the modulus is 120 GPa. Microstructure details are can be found in reference [10]. Specimens and pads were low stress ground to a RMS 8 μinch surface finish.

Test Condition Selection

Three objectives were defined for the current investigation: identify the location of fretting fatigue crack nucleation, identify the portion of life spent nucleating fretting fatigue cracks, and quantify the reduction of fatigue properties caused by fretting fatigue damage accumulated by 10% of fretting fatigue life. Attempts to conclusively identify primary crack nucleation sites and crack nucleation lives in prior work [6,7] have been inconclusive. The most recent effort by the authors involved attempts to detect fretting fatigue cracks *in situ* using ultrasonic Non-Destructive Inspection (NDI) techniques [8]. This effort produced partial answers to the questions regarding crack nucleation life and location for the conditions under investigation. For lower clamping stress (~200 MPa), crack nucleation required 95% of total life. The crack nucleation life for higher clamping stress (~620 MPa) was determined to be shorter, but no estimate was obtained. Crack nucleation sites were determined to be within 500 μm of the specimen edge using fractography, and this value was verified by inspecting cracks present on the unfailed end of specimens subjected to the higher clamping stress.

The experiments for this investigation were designed to build on the work described above. For these experiments fretting fatigue damage was applied for 1 million cycles at fatigue limit stresses corresponding to a 10^7 cycle fatigue life for two clamping stress conditions used in the earlier work [8]. Then the fretting condition was removed and residual fatigue property tests were conducted. These experiments are referred to as 10%-of-life tests, since the fretting fatigue damage is removed at 10% of the fretting fatigue life. The 10%-of-life damage level was selected, in part, to allow comparison to work in the literature [3,5,11,12], where significant damage progression up to 10% of life has been reported. Damage characterization was conducted through SEM (Scanning Electron Microscope) imaging and uniaxial residual fatigue property testing.

Geometry and loading conditions were the same as those used prior work. Fretting fatigue samples were 10 mm x 2 mm x 150 mm. Nominal fretting pad lengths were 12.7 mm and 25.4 mm. A contact radius of 3.2 mm was used, resulting in contact lengths of 6.35 mm and 19.05 mm. Clamping stresses, σ_N, of 140 MPa to 420 MPa were selected, and could be tested in the current apparatus with a single clamping load, P_N, of 26 kN. Actual clamping stresses achieved are approximately 30% higher than was intended due to the manner in which the clamping load was controlled; however, higher clamping stress conditions were consistent

throughout the testing for this study and are consistent with previous work by the authors, so that the comparisons made below are still valid. For this investigation the actual clamping stresses imposed were ~200 MPa and ~ 620 MPa. Fretting fatigue cycles were applied at 350 MPa for the lower clamping stress and 260 MPa for the higher clamping stress at a stress ratio, R, of 0.5. Three fretting fatigue specimens were tested for each condition.

In previous work interrupted samples were re-machined into dogbone samples in the vicinity of the fretting damage. The residual fatigue life test results obtained from those samples did not indicate a reduction in fatigue life compared to undamaged samples, except in the case of features that could not be attributed to fretting damage [7]. SEM inspection of these fretting scars prior to re-machining indicated that the highest levels of wear damage occurred at the sample edge. Thus, the results of these tests provided information on the location of the highest level of damage, which was not within the test sample.

In the current work, the region of highest wear damage was isolated by cutting straight sided specimens from the fretted regions, as shown in Figure 2. The resulting straight sided sample was 2 mm X 2.5 mm X 100 mm. To minimize grip failures, the ends of the specimen were covered with 0.127 mm (5 mil) thick copper tabs. Samples were tested at 950 MPa maximum stress at a stress ratio 0.5. This condition was selected because more appropriate test conditions required more time to complete than was available. Thus, several baseline tests were also conducted to compare against the fretted specimen data.
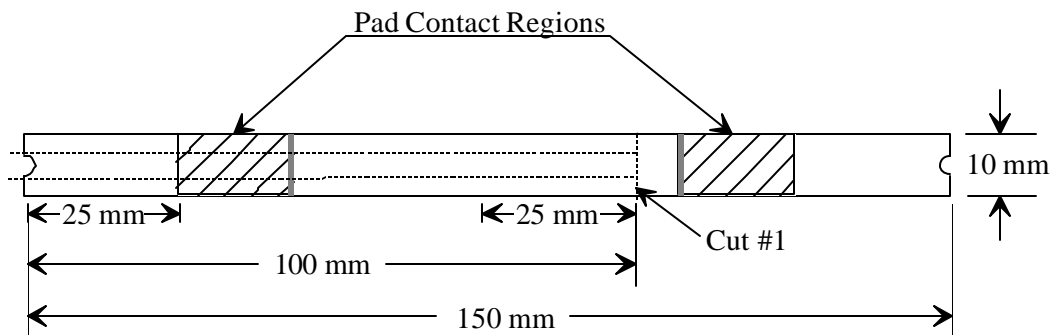

Figure 2. Machining schematic for residual fatigue life specimens.

Results from the straight sided specimen tests were inconclusive for reasons to be discussed later, so the fretting fatigue specimen geometry was re-designed, as shown in Figure 3. After application of fretting fatigue damage, these specimens were bisected to produce two dogbone specimens on which residual fatigue strength tests were conducted. These tests were completed using a step loading technique to obtain fatigue limit stresses for a 10^7 cycle fatigue life [6].
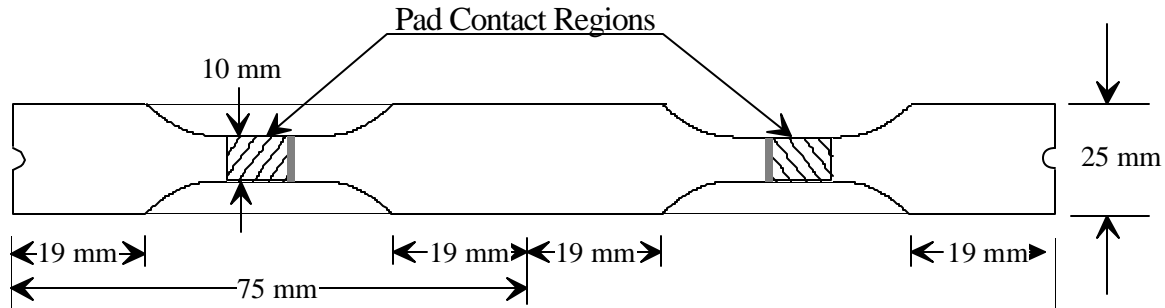
Figure 3. Double dogbone specimen schematic.

Characterization

Specimens were characterized in the SEM after the application of fretting damage to provide qualitative information on the level of damage generated in each test. The uniaxial fatigue specimens were also inspected in the SEM after fracture. Crack nucleation sites and causes were documented for all samples that fractured in the gage section. For specimens that failed in the gage, but away from the fretting damage, the distance of the fracture surface from the fretting pad edge of contact was measured.

The fretting fatigue damage was also characterized with a metalographic cross-section of a step load sample and with spectral analysis of representative samples of the fretting debris. The section was taken from the unfailed end of a failed sample with non-failure cracks. Similar sections taken from samples subjected to fretting fatigue under Hertzian or punch-on-flat contact conditions have been reported in the literature [2,4,5]. Those authors reported the presence of numerous non-propagating cracks and primary crack nucleation angles of approximately 45°. A similar cross-section from the current test geometry was cut to acquire information on the crack front location at the point at which the section was taken and to allow future comparison to other geometries. Spectral analysis of the fretting debris was conducted using Energy Dispersive Spectrometry (EDS) to identify elemental differences between fretting debris and the base material.

EXPERIMENTAL RESULTS

Results of the residual fatigue life tests on straight sided specimens are shown in Table 5 and Figure 4. Table 5 lists cycles to failure and the clamping stress under which each fretting specimen was tested. In addition, the "failure location" column indicates failure in the grip, at the fretting damage, or the distance from the fretting damage that failure occurred. Figure 4 presents all valid residual fatigue life test results in S-N form along with baseline data described below.

159

Table 5: Residual axial fatigue life test results at 950 MPa, R = 0.5.

Specimen	Ave. Normal Stress (MPa)	Cycles to Failure	Failure location
00-071	420	11,042	@ fretting
00-072	420	36,097	2.27 mm
00-073	420	30,343	86 μm
00-074	420	29,886	2.46 mm
00-075	420	3,055	@ fretting
00-076	420	25,357	@ fretting
00-077	140	32,680	grip
00-078	140	27,475	2.63 mm
00-081	140	21,794	grip
00-082	140	unknown	no failure
00-083	140	12,563	grip
00-084	140	16,282	grip
00-262	0	35,037	-

Of the six residual fatigue life specimens whose damage was generated with 200 MPa clamping stress and 350 MPa axial fatigue stress, only one failed in the gage section when subjected to uniaxial fatigue. The resulting fracture occurred ~ 2.6 mm away from the line of fretting damage and, thus, was not a fretting fatigue related fracture. No appreciable reduction in fatigue life was observed (note "◆"in Figure 4). Four of the remaining five samples failed in the grip and are invalid. The sixth specimen (00-082) is invalid due to a computer failure that resulted in loss of the cycle count data.

Of the six specimens subjected to fretting fatigue damage at 620 MPa clamping stress and 260 MPa axial fatigue stress, all six failed in the gage section when subjected to uniaxial fatigue. (note "(" symbol in Figure 4). One failed at approximately 3,000 cycles at the fretting damage due to a sizeable fretting nucleated crack. Two more specimens failed in less than 25,000 cycles at fretting damage where no obvious cracks were present. The remaining three specimens failed away from the fretting damage in the gage section, and produced residual lives of 30,000 cycles or greater. The five wear scars on which no cracks were identified appeared nominally identical from the SEM imaging.

Additional baseline data are provided in Figure 4 for comparison. These tests were conducted on as-received dogbone samples machined to the same surface condition as the fretting fatigue samples, and are represented by "O". One unfretted straight sided specimen was tested successfully, represented by "□". Only specimens that failed at the line of fretting damage showed a marked decrease in residual fatigue life compared to the baseline tests.

Residual fatigue strength tests are ongoing, but the results of completed tests indicate similar conclusions to the residual fatigue life tests. The specimens on which residual fatigue strength tests are being conducted have a K_t ~ 1.4. Thus, a reduction in strength of less than 30% cannot be quantified. Of the three completed tests, two (one for each clamping stress condition) indicated less than 30% reductions in strength. The scar on the third specimen contained a crack measuring 725 μm on the surface, and the resulting fatigue strength was ~ 50% of the unfretted material fatigue strength, which is 660 MPa. Further details of the crack and fretting scars are discussed below.
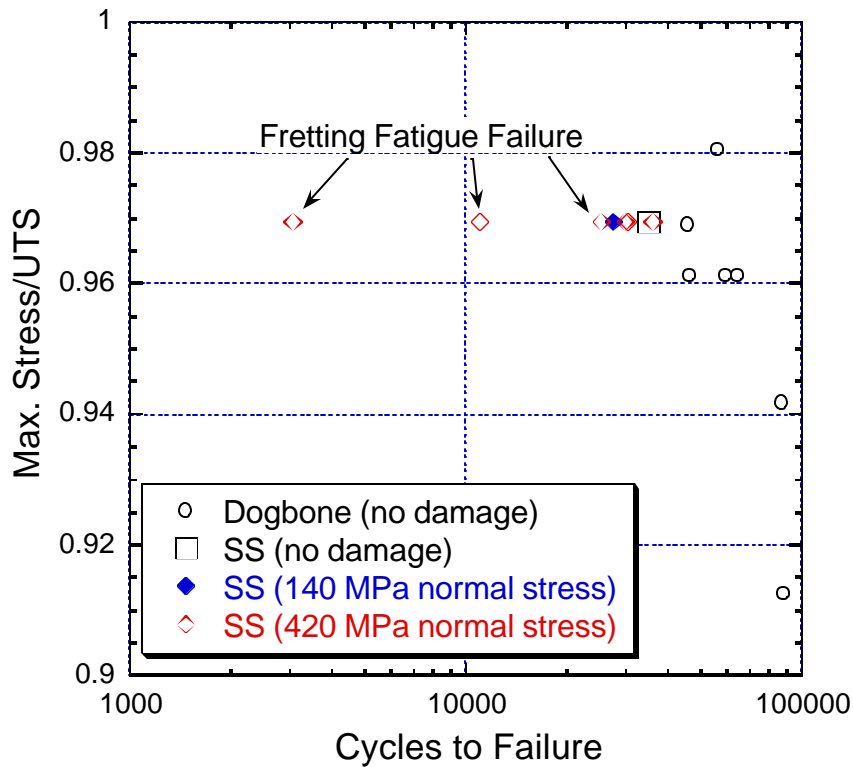
Figure 4. S-N results for residual fatigue life specimens with 10%-of-life damage.

CHARACTERIZATION RESULTS

Characteristic fretting scars from each clamping stress conditions are shown in Figures 5 and 6. Wear was minimal in the 200 MPa sample, and almost imperceptible in the 620 MPa sample, except in the presence of cracks, around which appreciable wear was observed. As with the specimens tested to fracture [8], the wear debris was spread over a larger area in the 200 MPa specimens than in the 620 MPa specimens. However, cracks of 1 mm or more in length were observed on all 620 MPa specimens at 10^6 cycles, indicating that cracks nucleate in less than 10% of life for this clamping stress condition. The crack nucleation life of specimens subjected to the lower clamping stress was greater than 95% [8].

The presence of cracks at 10% of life in the specimens subjected to the higher clamping stress condition provides an explanation for the residual fatigue life results discussed above. If crack nucleation required most of the fretting fatigue life for the tests conducted at the lower clamping stress, then reduction in residual fatigue life would not be expected. However, if crack nucleation occurred early in life, as with the specimens tested at the higher clamping stress, the reduction in residual fatigue life is plausible.

After residual fatigue life tests were completed, the resulting fracture surfaces were inspected in the SEM to determine if the fracture were fretting fatigue related. A representative fracture surface of a non-fretting fatigue gage section failure is shown in Figure 7 Only one such failure was obtained for the lower clamping stress condition. Two failures of this type were obtained for the higher clamping stress condition. This image was taken with the sample tilted at a 45° angle and includes both the fretting scar and the fracture surface. . In each non-fretting
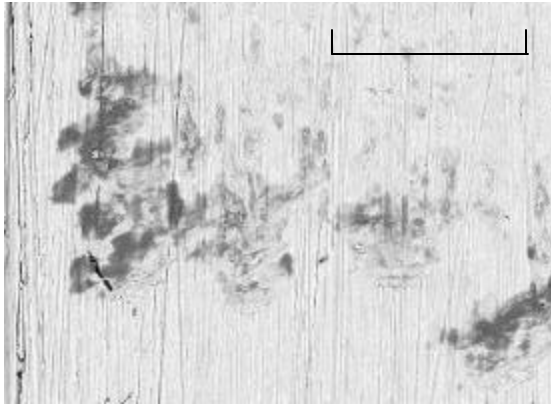
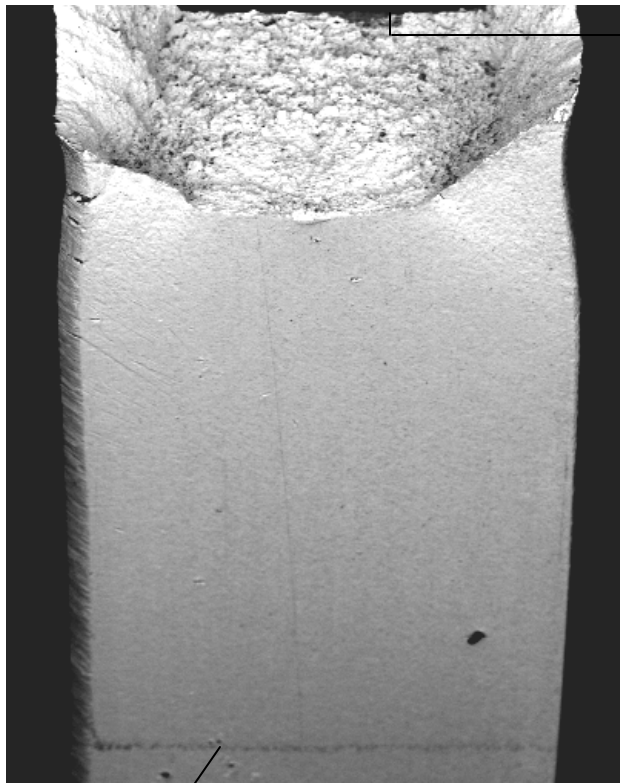*Figure 5. Damage for 10%-of-life sample at 200 MPa clamping stress. Fatigue loading axis is vertical.*

Figure 6. Non-crack damage for 10%-of-life sample at 620 MPa clamping stress. Fatigue loading axis is vertical.

Fretting   1 mm

Figure 7. Residual fatigue life sample with fracture surface and fretting scar shown simultaneously at 45° to the fatigue loading axis. (Nf = 36,097 cycles)

gage section failure an unintentional notch was identified as the cause of crack nucleation. Fretting damage was a sufficient distance from the crack nucleation site, as noted in Table 5, that fretting could not have played a role in the specimen fracture, except in one case. One specimen fractured under the pad contact area so that a conclusive cause of crack nucleation could not be determined. The fracture surface for this specimen is shown at a 45° angle in Figure 8. A notch was present at the crack nucleation site, but it occurred under the contact region in an area that would have been subjected to high tensile stresses during the application of fretting damage. Since the time of damage site introduction was unknown, determining if fretting played a role in crack nucleation was impossible. Two of the specimens failed at the fretting edge of contact without the presence of identifiable fretting nucleated cracking. A representative photo of one of the fracture surfaces is shown in Figures 9. In both cases crack nucleation occurred within the line of fretting fatigue damage, and without the presence of unintentional damage sites from other sources. The fretting "damage" that resulted in these failures was not noticeably different from the "damage" observed on specimens where fracture occurred away
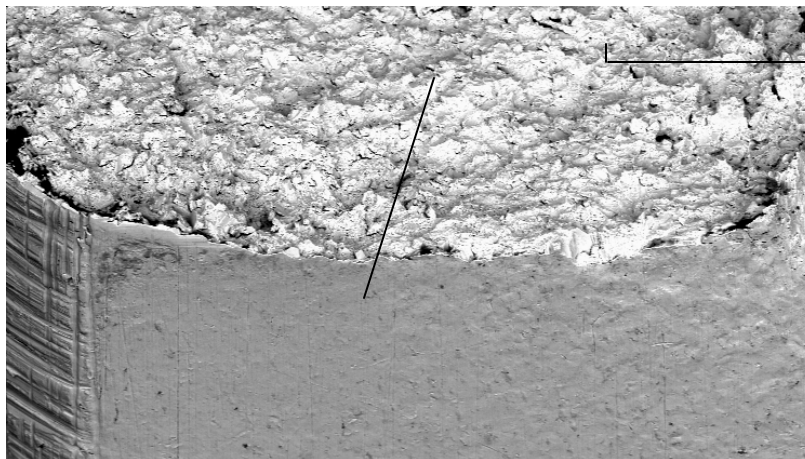
from the fretting site.
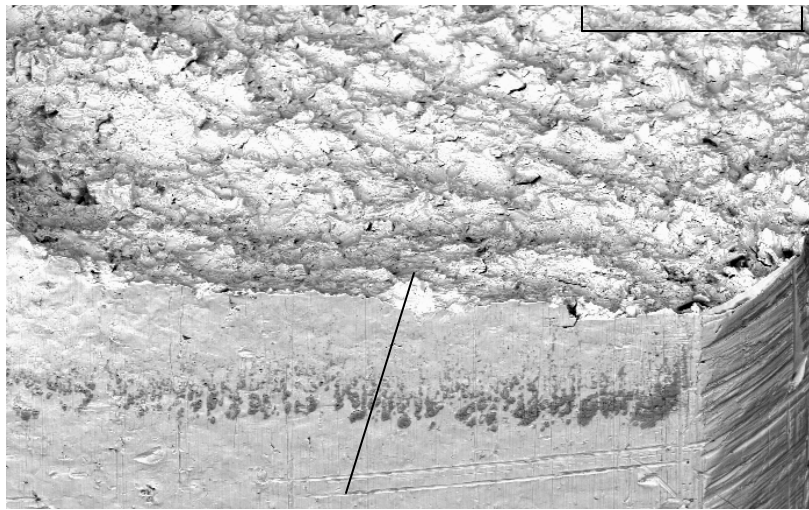
<center>nucleation site   200 μm</center>

Figure 8. Residual fatigue life sample with fracture surface shown at 45° to the fatigue loading axis. (Nf = 30,343 cycles – indeterminate failure)

<center>nucleation site   200 μm</center>

Figure 9. Residual fatigue life sample with fracture surface shown at 45° to the fatigue loading axis. (Nf = 11,042 cycles – fretting nucleated failure)

The last specimen failed at the fretting damage in the presence of a crack 400 μm long by 160 μm deep. The 45° view of the fracture surface is shown in Figure 10. Since the presence of the crack was known prior to uniaxial fatigue testing, the specimen was heat tinted to mark the location of the crack front. The crack was nearly elliptical, and nucleated within 50 μm of the specimen corner. Previous work indicated nucleation sites within 500 microns of edge, a distance that was the same for both clamping stress conditions [8]. This work verifies the crack nucleation location near, but not at the edge of the specimen.

<center>163</center>

One unfretted specimen was also tested for comparison purposes. Crack nucleation was caused by surface damage perpendicular to the fatigue loading axis. While the fatigue lives of
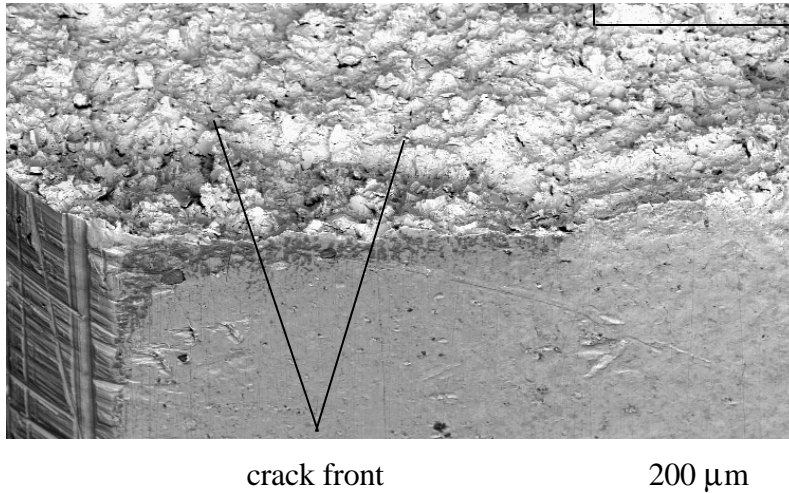

crack front   200 μm

Figure 10. Residual fatigue life sample with fracture surface shown at 45° to the fatigue loading axis. (Nf = 3,055 cycles – failure from fretting nucleated crack) Note location of crack tip prior to uniaxial fatigue testing.
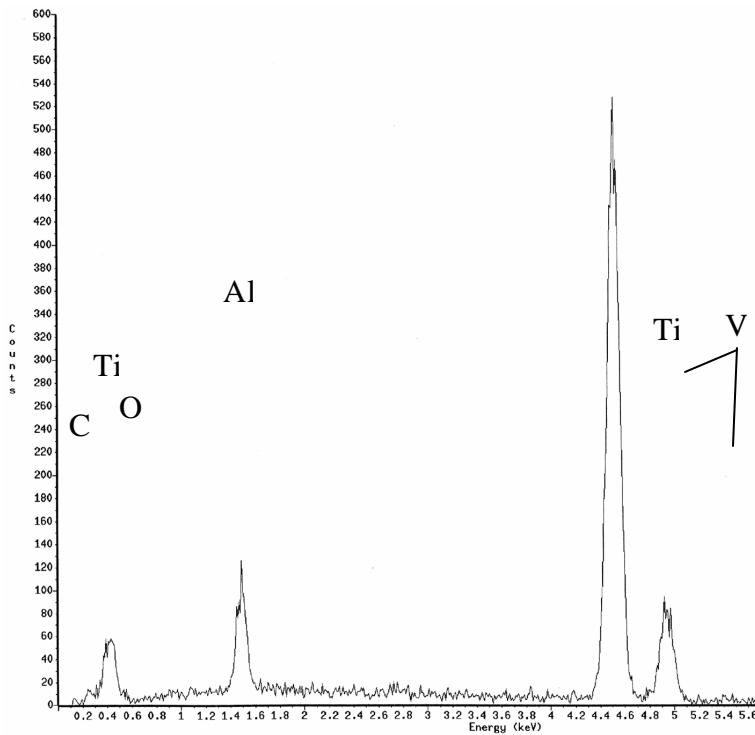
the straight samples did not differ in a statistically significant manner from the baseline tests on dogbone samples, some sort of stress riser was required to achieve a gage section failure. Thus the only conclusion to be drawn is that damage at 10% of fretting fatigue life obtained under 200 MPa clamping stress is less severe than a small damage site, such as might be incurred during machining or installation of the specimen into the test frame. Fretting damage obtained at 620 MPa clamping stress may be more severe than the types of incidental damage described here, but is not necessarily so.

Some characterization of the residual fatigue strength specimens is complete. In two of the tests fracture occurred at the location of highest stress concentration. SEM inspection of the fretting scars before and after the

Figure 11. As-received material element analysis results.

uniaxial portion of the test revealed no significant changes. Small pieces of oxide had fallen off during cycling, but no features that were thought to be very small cracks had changed size. Heat

tinting had been used to mark the crack front on the third specimen.
Inspection of the fracture surface revealed a crack depth of 200 μm crack.

The fretting debris from an un-cracked fretting scar was characterized for elemental content. The 200 MPa clamping stress condition was selected, since a greater volume of wear debris was available and the expected anomalous elements were small. Figure 11 shows an spectral analysis of the baseline material. Only titanium, aluminum, and vanadium are present in significant quantities. Carbon and oxygen are marked on the graph, but the amount present with respect to the primary alloy constituents is negligible. A representative scan of the fretting debris is shown in Figure 12. Titanium, aluminum and vanadium are still the primary constituents, but the oxygen and carbon peaks are more pronounced, and can no longer be described as noise.
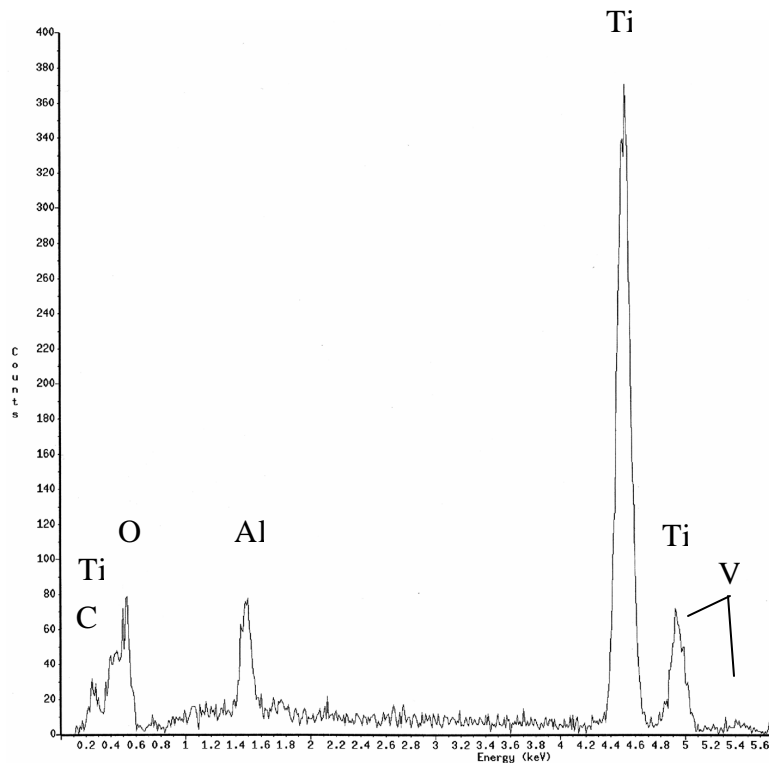

Figure 12. Fretted material analysis results.

Oxidation of the original material elements has been linked to premature crack nucleation in both fretting fatigue and fretting wear in other materials [13,14]. So the presence of significant levels of oxygen, as found here, presented a possible mechanism for crack nucleation in the specimens tested at the 200 MPa clamping stress. Brittle reaction products such as TiO_2 or Al_2O_3 could present ideal crack nucleation sites that would allow crack propagation into the bulk material, if the oxide were fixed firmly to the substrate. For each of the 200 MPa samples inspected in the SEM, the oxide was fixed firmly enough to the base material that it was left undisturbed by rigorous ultrasonic cleaning. This nucleation mechanism is not applicable to the higher clamping stress condition, based on the observed volume of wear debris in the absence of cracks.

A metalographic cross-section was cut in the region of a secondary crack on the unfractured end of a fractured specimen tested under the 620 MPa clamping stress condition. The crack extended ~ 1 mm from the specimen edge. Two nucleation sites were identified by the presence of relatively large amounts of fretting debris, and the crack appeared to propagate outward from both sites along a complex propagation path (figure 13). The crack was sectioned

165

to approximately 600 µm from the specimen edge near the second nucleation site (Figure 13 – note section line at right of photo).

The depth of the crack at the section location was ~ 500 µm. As shown in Figure 14, the dominant crack nucleated at ~ 45° to the loading axis, as reported by other researchers [4], and within 5-10 µm, turned perpendicular to the loading axis. Both propagating and non-propagating cracks are observed. In this case, very little material was removed from this part of the specimen face during the crack nucleation process. Also, the crack propagated across the $\alpha+\beta$ lath before turning perpendicular to the fatigue loading axis, indicating that the early stages of crack propagation under this contact condition are not heavily influence by environmental conditions such as oxidation or corrosion, as has been
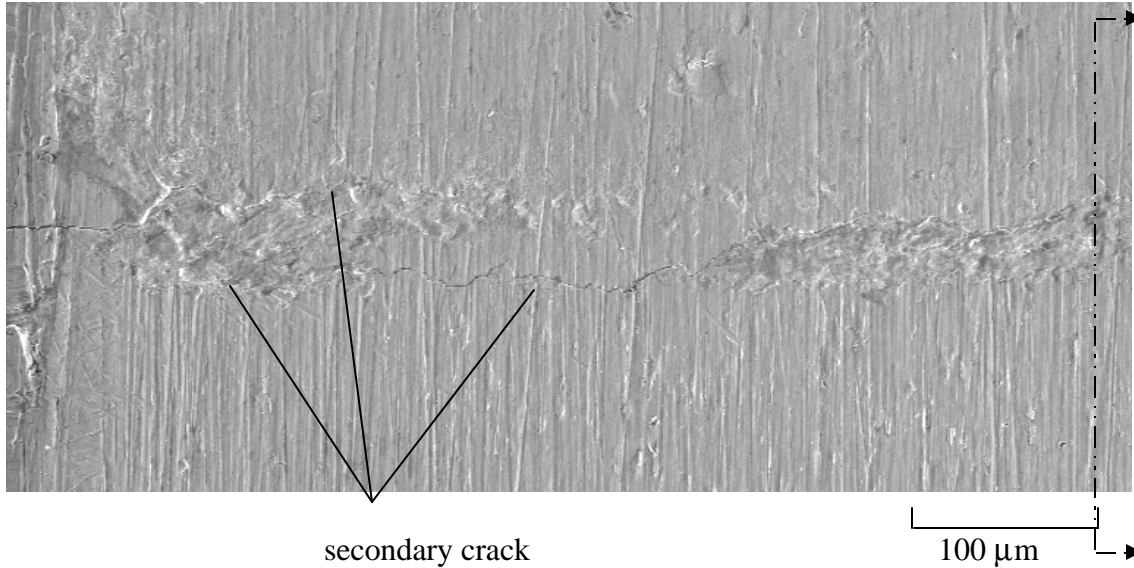

secondary crack   100 µm

Figure 13. Secondary fretting crack nucleated at 420 MPa clamping stress. Fatigue loading axis is vertical. (Nf ~ 4.1 million cycles)
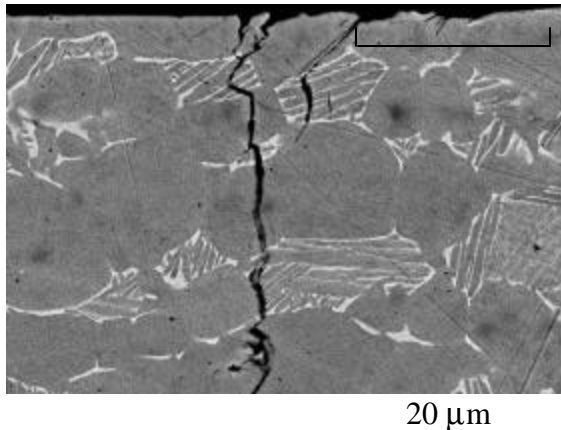

20 µm

Figure 14. Cross-section of secondary fretting crack ~600 mm from sample edge.

reported [13,14]. Since no secondary cracking was observed on specimens subjected to 200 MPa clamping stress, the role of environment on fretting fatigue nucleated cracks could not be verified.

SUMMARY & CONCLUSIONS

Taken together, the results from the different aspects of this investigation provide new insight into the fretting fatigue crack nucleation mechanisms for the current contact geometry. Two clamping stress conditions were investigated and two crack nucleation behaviors are verified.

1.   Cracks nucleated at or near specimen edges regardless of the applied normal stress.
2.   The number of cracks present on a single specimen is dependent on the clamping stress. The higher clamping stress produces multiple cracks, which nucleated early in life, while the

lower clamping stress produces one crack, which nucleated late in life.

3.   Fretting fatigue at 10% of life can reduce residual fatigue life for the 620 MPa clamping stress condition, even in the absence of detectable fretting nucleated cracks.

REFERENCES

15. Ruiz, C., Boddington, P. H. B., and Chen, K. C., "An Investigation of Fatigue and Fretting in a Dovetail Joint," *Experimental Mechanics*, Vol. 24, 1984, pp. 208-217.
16. Bryggman, U. and Söderberg, S., "Contact Conditions and Surface Degradation Mechanisms in Low Amplitude Fretting", *Wear*, Vol. 125, 1988, pp. 39-52.
17. *Fretting Fatigue, ESIS 18*, R.B. Waterhouse and T.C. Lindley, Eds., Mechanical Engineering Publications, London, 1994, pp. 219-238.
18. Zhou, Z. R. and Vincent, L., "Mixed Fretting Regime," *Wear*, Vol. 181-183, 1995, pp. 551-536.
19. *Standardization of Fretting Fatigue Test Methods and Equipment, ASTM STP 1159*, M. Helmi Attia, and R. B. Waterhouse, Eds., American Society for Testing and Materials, Philadelphia, 1992, pp. 153-169.
20. Hutson, A., Nicholas, T., and Goodman, R., "Fretting Fatigue of Ti-6Al-4V Under Flat-on-Flat Contact", *International Journal of Fatigue*, Vol. 21, No 7, 1999, pp. 663 – 670.
21. Hutson, A. and Nicholas, T., "Fretting Fatigue Behavior of Ti-6Al-4V against Ti-6Al-4V under Flat-on-Flat Contact with Blending Radii," *Fretting Fatigue: Current Technologies and Practices, ASTM STP 1367*, D.W. Hoeppner, V. Chandrasekaran, and C.B. Elliot, Eds., American Society for Testing and Materials, West Conshohocken, PA, 1999, pp. 308 - 321.
22. Hutson, A. L. and Stubbs, D., "Detection of Fretting Fatigue Cracks Using Ultrasonic Shear Wave NDT," submitted to International Journal of Fatigue, May 2001.
23. Hutson, A.L., "Fretting Fatigue of Ti-6Al-4V Under Flat-on-Flat Contact with Blending Radii," M.S. Thesis, School of Engineering, University of Dayton, Dayton, OH, August, 2000.
24. Haritos, G.K., Nicholas, T. and Lanning, D., "Notch Size Effects in HCF Behavior of Ti-6Al-4V," *International Journal of Fatigue*, Vol. 21, No 7, 1999, pp. 643 – 652.
25. Endo, K. and Goto, H., "Initiation and Propagation of Fretting Fatigue Cracks," *Wear*, Vol. 38, 1976, pp. 311-324.
26. Nix, K.J. and Lindley, T.C., "The Application of Fracture Mechanics to Fretting Fatigue," *Fatigue and Fracture of Engineering Materials Structures*, Vol. 8, No. 2, 1985, pp. 143-160.
27. Blanchard, P., Colombie, C., Pellerin, V., Fayeulle, S. and Vincent, L. "Material Effects in Fretting Wear - Application to Iron, Titanium, and Aluminum Alloys," *Metallurgical Transactions*, Vol. 22A, 1991, pp. 1535-1544.
28. Waterhouse, R.B., "Fretting Wear," *Wear*, Vol. 100, 1984, pp. 107-118.

This page intentionally left blank.

Effect of Normal to Shear Load Ratios on HCF Stress Limit Under Fretting Fatigue Conditions

Mrs. A. L. Hutson[1], Dr. T. Nicholas[2], Mr. S. E. Olson[1] and Dr. N. E. Ashbaugh[1]

[1]University of Dayton Research Institute, Dayton, OH, 45469
Tel: 937-255-2708, FAX: 937-255-1363, E-mail: alisha.hutson@afrl.af.mil

[2]Air Force Research Laboratory (AFRL/MLLN), Wright-Patterson AFB, OH 45433-7817
Tel: 937-255-1347, FAX: 937-656-4840, E-mail: theodore.nicolas@afrl.af.mil

INTRODUCTION

While fretting fatigue has been studied extensively, there are so many aspects to the problem [1] that it is still not a well understood phenomenon. Fretting fatigue, as described here, refers to the cyclic loading of a material that is subjected to clamping stresses normal to the direction of loading. What distinguishes fretting fatigue from wear or galling is rather subjective, but fretting fatigue is normally associated with small magnitudes of relative slip on the order of tens of microns and little if any material removal. Such damage has been indicated as the cause of many unanticipated disk and blade failures in turbine engines.

Under laboratory conditions, the synergistic effects of various parameters make determination and modeling of the mechanical behavior of fretting fatigue extremely difficult. The stress state in the contact region involves very high peak stresses, steep stress gradients, multi-axial stresses and differing mean stresses. Further, there is controversy over whether the problem is one primarily of crack initiation or a crack propagation threshold, and whether or not stress states rather than surface conditions play a major role in the observed behavior. There is also confusion related to the different stress distributions associated with those that occur in lab specimens versus what are present in real structures. Laboratory tests can involve thin plate samples contacted on both sides whereas real structures are more representative of contact with a half space. Finally, lab testing usually involves a constant clamping force while real hardware has cyclic contact loading.

While no single investigation is expected to answer all of the questions associated with fretting fatigue phenomena, an attempt is made here to shed some light on some of the issues regarding the relative roles of clamping force, ratio of shear to axial load in a specimen under contact fatigue, and contact pad geometry. An experimental determination of the conditions under fretting fatigue which are analogous to the fatigue limit stress under uniaxial fatigue loading corresponding to a 10^7 cycle fatigue life over a range of contact conditions is presented. Finite element analyses of the test apparatus are included to provide details of the stress distribution in the flat-on-flat geometry for representative sample thicknesses and contact lengths. From the analyses, both stress fields and stress intensity factors for specific cases were obtained in an effort to find some commonality, which may lead to development of parameters having broad application to fretting fatigue.

EXPERIMENTS

A unique, high frequency test system was used to conduct tests simulating the fretting fatigue damage that occurs in turbine engine blade attachments [2, 3, 4]. The apparatus uses flat fretting pads, with a radius at the edge of contact, against a flat specimen. Normal and shear loads are applied to the specimen as shown in figure 1. The test geometry restricts the maximum nominal shear stress to that which can be reached for a given nominal clamping stress before total slip occurs. A previous study has shown that the bending moment present in the apparatus is negligible relative to other parameters, and may be disregarded when designing the tests [5]. Therefore, the reported experimental data will only include the applied normal load and shear load.

The test geometry differs from conventional fretting fatigue tests [6,7] in two fundamental ways. First, the axial stress is transferred entirely to the fixture through shear. Resulting stresses in the specimen are zero on one end of the pad, thus the shear force into the pad is determined from the load applied to the specimen. Second, symmetry of the apparatus provides a specimen which breaks on one end, leaving the other end with a fretting scar and damage obtained under nominally identical conditions. As with a conventional fretting fatigue apparatus, the clamping force is constant and only the axial and shear loads are oscillatory.
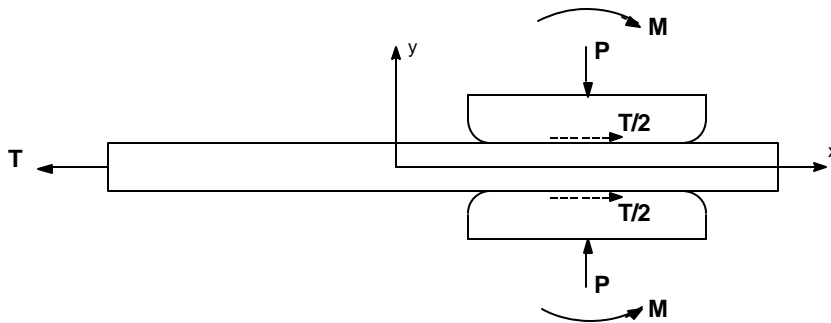

Figure 1: Test geometry and loading schematic (half specimen

All tests were conducted at 300 Hz under ambient lab conditions. Specimens and pads were taken from forged Ti-6Al-4V plates used in a series of investigations under a U.S. Air Force sponsored high cycle fatigue program. The processing and microstructure are reviewed in previous work [8,9]. Each specimen was subjected to uniaxial fatigue using a step-loading procedure [10] to determine a fatigue limit stress corresponding to 10^7 cycle fatigue life. Tests were conducted by incrementing the maximum axial stress by five percent of the initial value for various combinations of specimen thickness, pad length, and clamping force. The step loading technique was validated in earlier fretting fatigue studies using the same apparatus [2,11].

ANALYSIS

Analyses were conducted to determine the state of stress and the magnitude of relative slip of the pad with respect to the specimen at the edge of contact, and to provide a basis for stress intensity factor calculations, to be discussed later. ABAQUS was selected as the finite element modeling package. Eight node quadrilateral elements were used, with mesh refinement down to sizes of approximately 6.5 μm near the edges of contact. Quasi-static linear elastic

behavior under plane stress was assumed. Additional details of the finite element methods are presented in [5].

The geometry for the pads and specimen was treated as two-dimensional and, because of symmetry, only one pad and half the specimen thickness was modeled. A line of symmetry, defined along the x-axis corresponding to the middle of the specimen, limited translation in the y direction. In addition, the pad was prevented from rotation as shown in figure 2. The uniform x and y displacements were chosen to produce the desired axial force in the specimen and clamping force, respectively. Contact was defined for the entire top region of the specimen and the pad bottom including the full radius. The material was modeled as a Ti-6Al-4V pad against a Ti-6Al-4V specimen and the material parameters were defined as follows: Poisson's ratio = 0.3, Young's modulus = 120 GPa, ultimate tensile strength = 980 MPa, and yield strength = 930 MPa. For most of the conditions simulated numerically [2,4,5], the coefficient of friction, μ, was taken as 0.3. In two cases μ was increased to 1.0, to allow comparison of resulting stresses, relative displacements, and stress intensity values. Only the first half of the initial fatigue cycle was modeled.
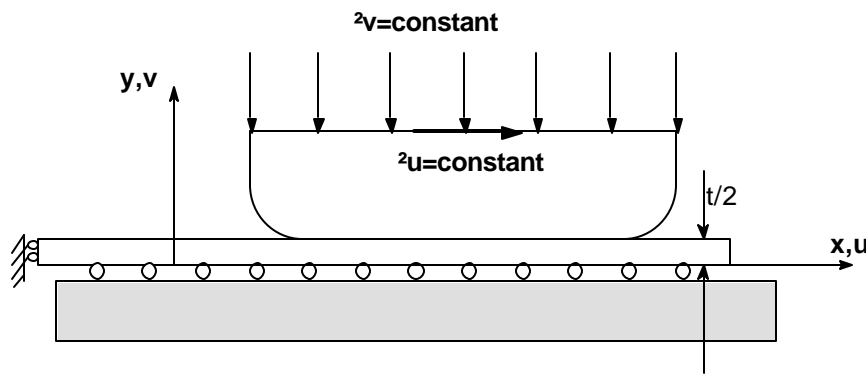

Figure 2: Finite Element Analysis geometry and loading schematic.

Clamping loads were taken as those used in the experiments: axial stress in the specimen was taken from experimental observations. Specimen thicknesses were modeled as either 1, 2, or 4 mm, thereby providing a broad range of shear forces over which the experimental axial stresses for 10^7 cycle fatigue lives were similar. Two pad total lengths were used, 25.4 mm and 12.7 mm, each one having a blending radius of 3.175 mm at both ends. Thus, the undeformed contact length was 6.35 mm for the short pad and 19.05 for the long pad. The clamping loads on the pads, which contacted the 10 mm wide specimens, were either 21, 26 or 35 kN. A summary of the test conditions simulated with the FEM analysis, indicating maximum loads and stresses, is given in Table 1.

TABLE 1
SUMMARY OF TEST CONDITIONS AND RESULTS FOR FINITE ELEMENT ANALYSIS.

Specimen thickness (mm)	Pad length (mm)	μ	Clamping Load (kN)	Applied σ_{axial} (MPa)	Average σ_y (MPa)	Average τ_{xy} (MPa)	Peak σ_x (MPa)	Max. Relative Displacement (μm)
1	12.7	0.3	35	275	551	21.7	1145	3.0
2	25.4	0.3	26	350	409	18.4	627	15.0
2	25.4	1.0	26	350	409	18.4	1186	3.2
4	25.4	0.3	21	275	110	28.9	481	24.0
4	25.4	1.0	21	275	110	28.9	945	6.3

After evaluating the stress fields and relative displacements from the FE simulations, the stresses were used to compute the stress intensity factor, K, as a function of crack length, assuming cracks normal to the specimen surface under pure mode I loading. The K distributions were calculated using a program developed to model a single edge tension (SE(T)) specimen geometry under a non-constant σ_x stress field [12]. Some success has been reported in modeling fretting fatigue behavior as an edge notch, since both conditions produce similar stress fields [13]. Characterization results from a prior investigation [5] indicated that cracks nucleated at or near the edges of contact in specimens tested in the existing apparatus. The objective of these calculations was to compare the K values from two different cases where the peak stresses were significantly different, yet the stress fields both matched conditions corresponding to failure in 10^7 cycles.

The K solution program required material and crack dimension input parameters in addition to the stress distribution data. Material parameters used in the K calculations were the same as those used in the FE simulations. The depth position of the final stress value given in the stress distribution, which was equal to half of the specimen thickness, was used for the final crack length. Stress intensity values are only reported for the first 100μm into the specimen thickness, although calculations were performed as far into the model specimen as possible.

RESULTS & DISCUSSION

Experimental Results:

Fatigue limit stresses were obtained for samples having one of the three thicknesses (1 mm, 2 mm and 4 mm) and fretting pads which we denote as short or long. The fatigue limit stress, obtained from the step loading tests, was normalized with respect to smooth bar fatigue limits. The normalized fatigue limits are plotted as a function of the average clamping stress, which is taken to be positive, for the 1mm and 4mm thick specimens over a range of contact conditions (figs. 3 and 4). A similar representation of the 2mm thick specimen data can be found in reference [4]. Two contact radii (CR = 0.4mm & 3.2mm) and two stress ratios (R = 0.1 & 0.5) are represented; the baseline uniaxial fatigue limits for this material are: 660 MPa @ R=0.5, 558

MPa @ R=0.1. Average clamping stress is computed based on the area of contact in the undeformed state, from the locations corresponding to the tangent of the radii to the flat portion of the pad. As will be shown later, this is a very good approximation to the deformed area of contact.

Initial data for the 4mm thick specimens [4] indicated no appreciable trend as a function of applied clamping stress. However, the data for the 1mm thick specimens show a trend of increasing fatigue strength with decreasing applied clamping stresses (Fig. 3), which was not noted previously for the 4mm or the 2mm thick specimens [4,5]. The trend is not significant and conducting tests with clamping stresses much below 100 MPa to verify the trend is not possible, since low clamping stress will result in the specimen pulling out of the grips in the current test apparatus. Also, the trend is obscured by experimental scatter in tests involving the smaller (0.4mm) contact radius. In comparing figures 3 and 4, an apparent effect of thickness is noted. The 4mm thick specimens produced much lower fatigue limit stresses than 1mm thick specimens under similar contact conditions, emphasizing the need to consider test specimen geometry in evaluating laboratory data.

The same data are presented in (figs. 5 through 8) to compare the behavior of the different specimen thicknesses. These plots present the normalized fatigue limits as a function of average applied clamping stress (figs. 5 & 6) or average shear stress (figs. 7 & 8) for tests conducted at either R=0.1 or 0.5. The numerical simulation conditions are also noted in figure 5. The R = 0.5 data are represented by power fit curves to indicate the overall trend of the data.
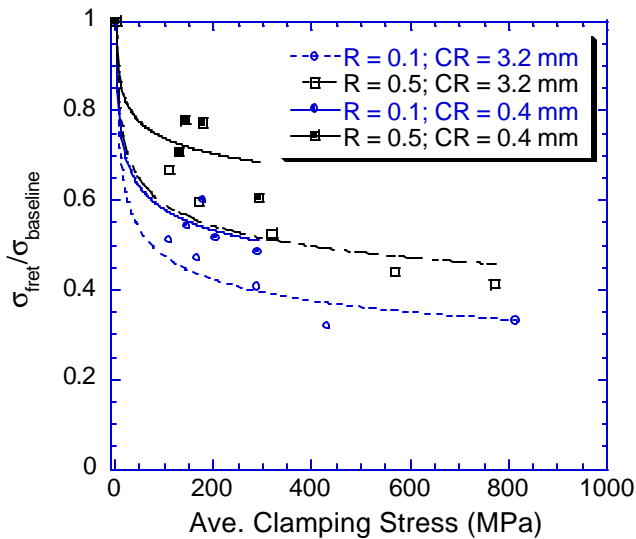

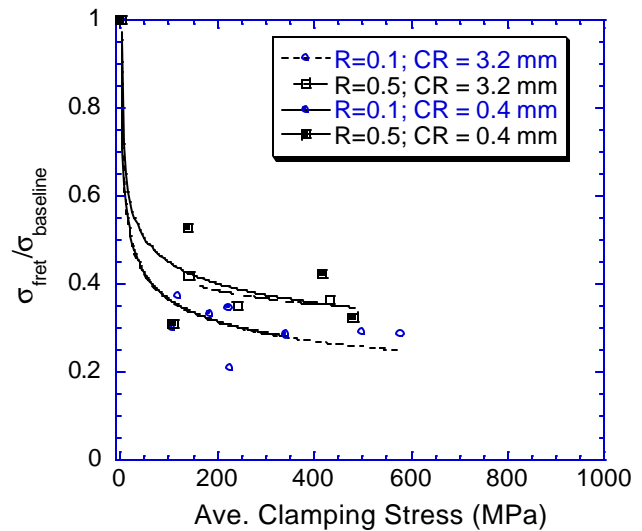*Figure 3: Experimental results for 1mm thick specimens and unfretted baseline conditions.*

Figure 4: Experimental results for 4mm thick specimens and unfretted baseline conditions.
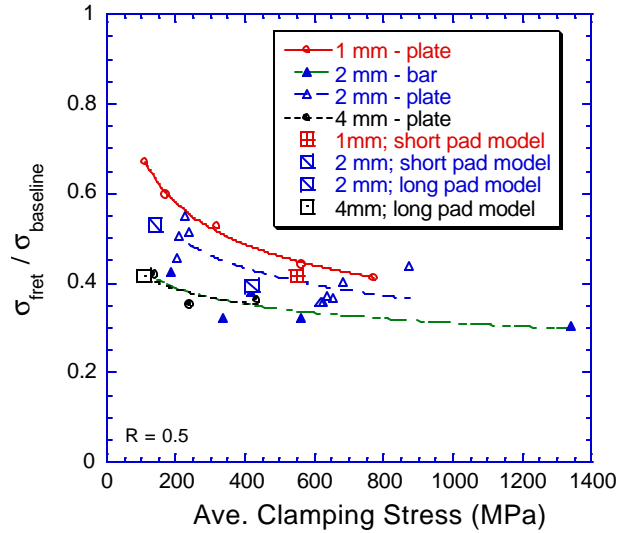
Figure 5: Normalized limit stresses for 1, 2, and 4 mm thick samples tested at R=0.5 vs. average applied normal stresses.
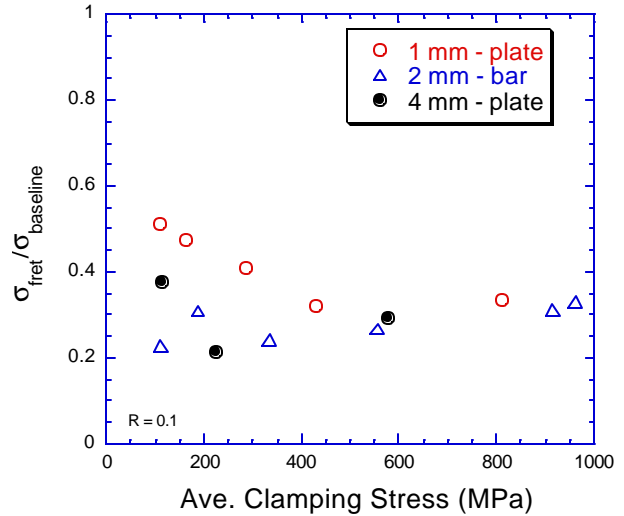

Figure 6: Normalized limit stresses for 1, 2, and 4 mm thick samples tested at R=0.1 vs. average applied normal stresses.

The figures show that there is a severe degradation of fatigue limit stress due to fretting fatigue, resulting in fretting fatigue limit stresses 30 to 80 percent lower than the corresponding smooth bar fatigue results for 10^7 cycle fatigue lives, depending on specimen thickness. It is also seen that the fatigue limit stress is rather insensitive to either average normal stress or average shear stress. The data at R=0.5 for the 1mm thick specimens (figs. 5 and 7) are characterized by a rather pronounced trend of increasing fatigue strength with decrease in applied normal or shear stresses and relatively little experimental scatter. The 2mm thick specimen data also show some trend as a function of both applied clamping stress and applied shear stress, but no real conclusions can be drawn due to significant scatter.
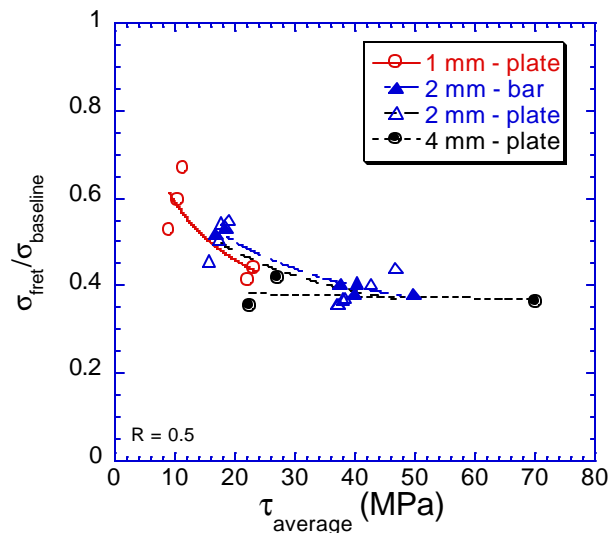

Figure 7: Normalized limit stresses for 1, 2, and 4 mm thick samples tested at R=0.5 vs. average applied shear stresses.
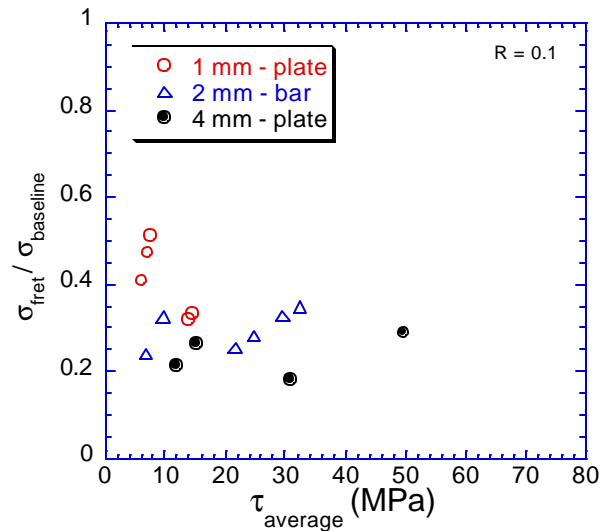

Figure 8: Normalized limit stresses for 1, 2, and 4 mm thick samples tested at R=0.1 vs. average applied shear stresses.

174

Analytical Results:

The distribution of stresses along the entire length of the pad is shown in figure 9, where x is normalized with respect to the half-length of the pad between the center and the position of undeformed contact (UEC). In this and all subsequent figures, the left end is the loaded one while the right end of the specimen is stress free outside the right edge of contact. The long pads show a slightly increasing σ_x as the loaded left end is approached while the short pad has σ_x in nearly uniform compression except near the edges of contact. The short pad has the highest compressive (clamping) stresses, σ_y, and the most variability with position along the pad. The stresses peak at the ends of contact; the stress distributions near the deformed edge of contact (DEC) are plotted in figures 10 and 11. In each plot, x=0 corresponds to the DEC as determined from the computer output. While the magnitudes of the stresses are different, the general shape of the stress distribution is the same and shows that peak stresses are very high and very localized near the DEC. The maximum tensile stress occurs just outside the DEC, but at a distance less than ~ 10 µm. Obviously, σ_y and τ_{xy} go to zero outside the contact region. Compared to σ_x and σ_y, the values of τ_{xy} are relatively small and spread out more while the compressive stresses, of the same order as σ_x, peak at ~ 50 µm inside the DEC for the long pad (Fig. 11) and at ~ 100 µm for the short pad (Fig. 10).

The stress gradients into the thickness are plotted for the 2 mm thick long pad in figure 12. Shown is σ_x at several distances into the thickness direction. The coordinate y=1 corresponds to the surface of the specimen in contact with the pad. The stress profiles show that the σ_x stresses decay rapidly, with stresses at 50µm below the surface being almost the same as those much deeper. Thus, stress gradients into the thickness are of the same order of magnitude as those along the surface. Similar observations were made for the other cases, which are not shown here.
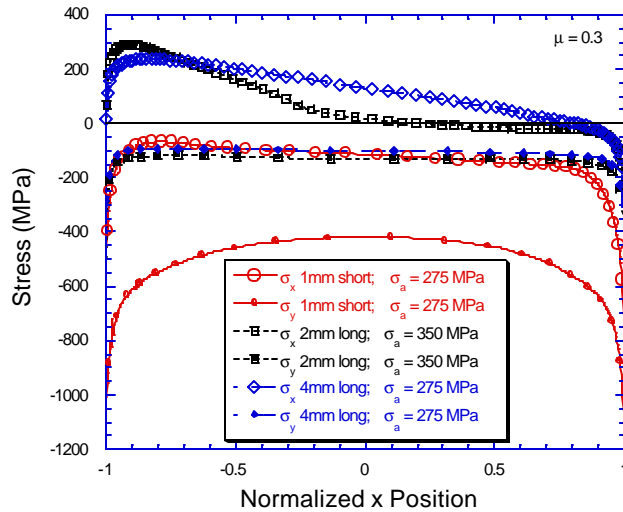

Figure 9: Maximum $\mathbf{s}_x$ and $\mathbf{s}_y$ distributions for 1, 2, and 4 mm thick samples vs. normalized x position. x=0 corresponds to the middle of the fretting pad. ($\mathbf{m}$= 0.3)
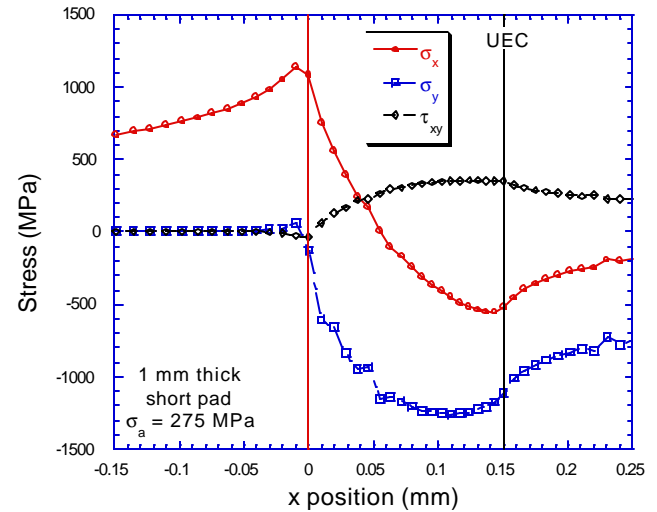
Figure 10: Maximum $\mathbf{s}_x$, $\mathbf{s}_y$, and $\mathbf{t}_{xy}$ distributions for the 1 mm thick sample against a short pad vs x position. x=0 corresponds to the DEC. ($\mathbf{m}$= 0.3)
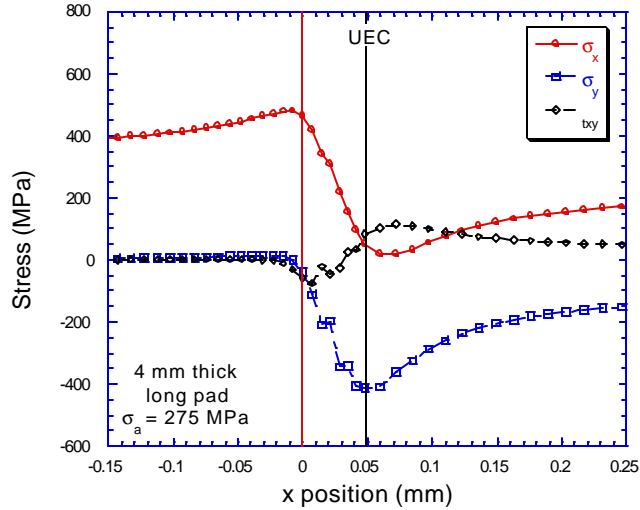
175

Figure 11: Maximum s_x, s_y, and t_{xy} distributions for the 4 mm thick sample against a long pad vs. x position. x=0 corresponds to the DEC. ($m= 0.3$)

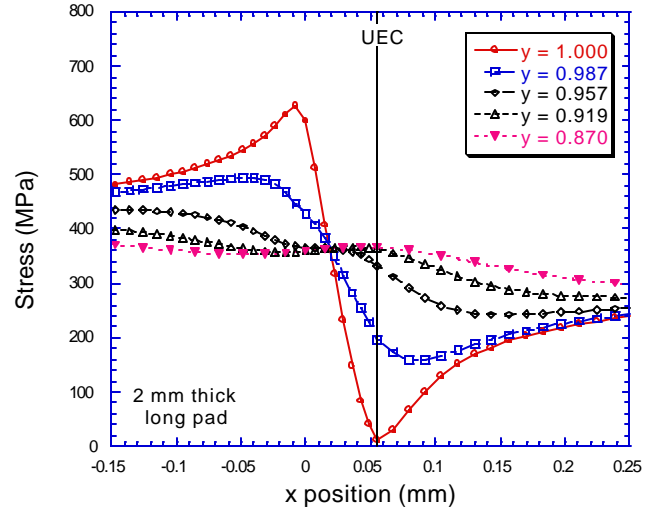*Figure 12: s_x stress gradient into the sample thickness calculated for the 2 mm thick sample against a long pad vs. x position. x=0 corresponds to the DEC. y=1 corresponds to the sample surface. ($m= 0.3$)*

Tensile stresses or maximum principal stresses are often associated with a fatigue initiation or failure criterion. Since all of the cases simulated correspond to the fretting fatigue limit for a 10^7 cycle fatigue life, it is of interest to compare the maximum tensile stresses (Figs. 10 and 11 and Table 1). The values of maximum σ_x can be seen to vary from about 600 MPa for the 2mm thick long pad case to about 1200 MPa for the 1mm thick short pad case to about 500 MPa for the 4mm thick long pad case. While this alone does not constitute a failure or initiation criterion, it points to the conditions under which fretting fatigue occurs at the applied fatigue limit.

Another parameter, which might enter such a failure criterion, is the relative slip between pad and specimen. The relative slip is plotted over the coordinates corresponding to the DEC, denoted by x=0, to x=2mm in figure 13. Also shown are the cases where μ is changed from 0.3 to 1.0, indicated by the solid symbols. This will be discussed later. The maximum slip distance occurs at the edge of contact, where the maximum tensile stresses occur. For the simulations discussed above, the maximum slip distances corresponding to maximum tensile stresses can be seen to be 15 μm (600 MPa), 3 μm (1200 MPa), and 25 μm (500 MPa). No clear trend between slip distance and maximum tensile stress is apparent. While the value of σ_y might also be expected to have an influence on a failure criterion, it is noted again that the the clamping stresses and the shear stresses approach zero near the DEC. Thus, a parameter such as the product $\sigma_y \tau_{xy} \delta$, proposed by Ruiz, et al. [11], where δ is the relative displacement, would not be applicable to these geometries where σ_y and τ_{xy} are zero and, further, the parameter varies widely inside the contact region.
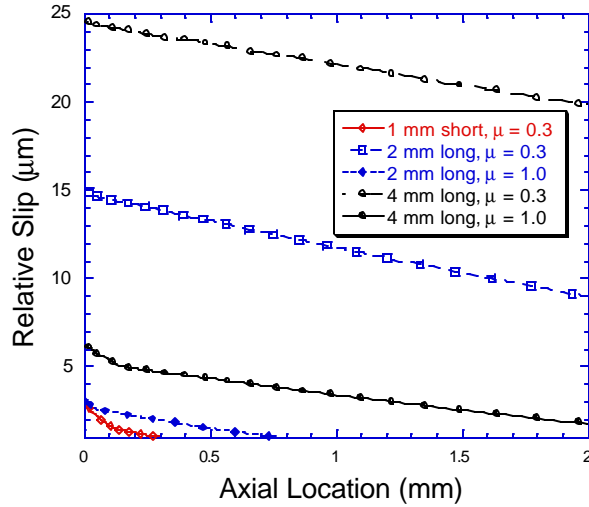
176

Figure 13: Comparison of relative displacements along the contact calculated for all three simulation conditions identified in Table 1.
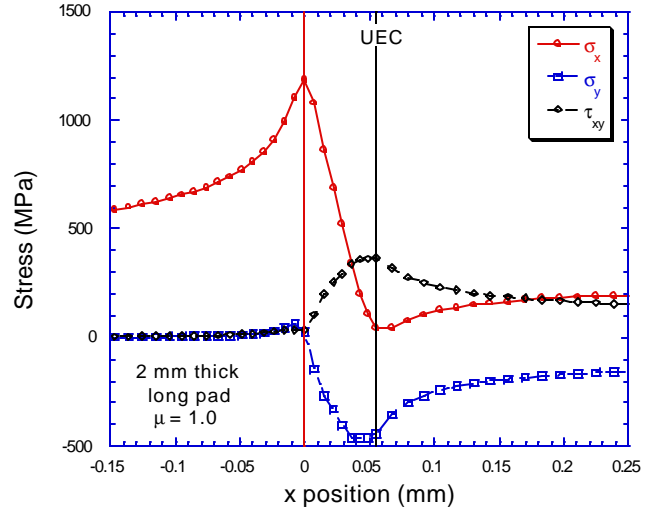

Figure 14: Maximum $\boldsymbol{s}_x$, $\boldsymbol{s}_y$, and $\boldsymbol{t}_{xy}$ distributions for the 2 mm thick sample against a long pad vs. x position. x=0 corresponds to the DEC. ($\boldsymbol{m}=1.0$)
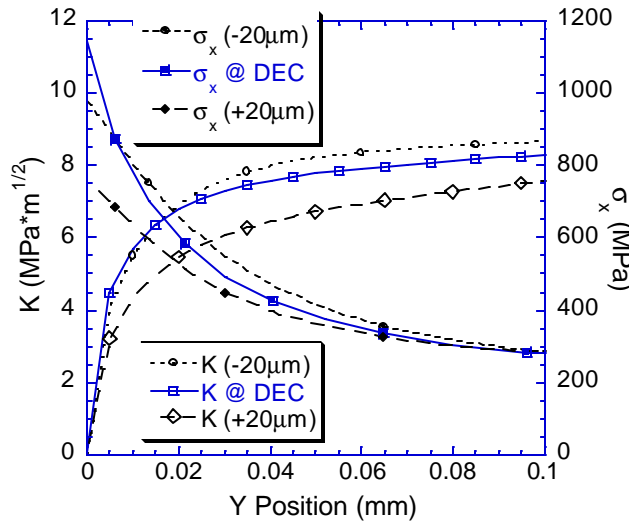

Figure 15: Stress distribution and resulting K solution for 1mm thick specimen case.
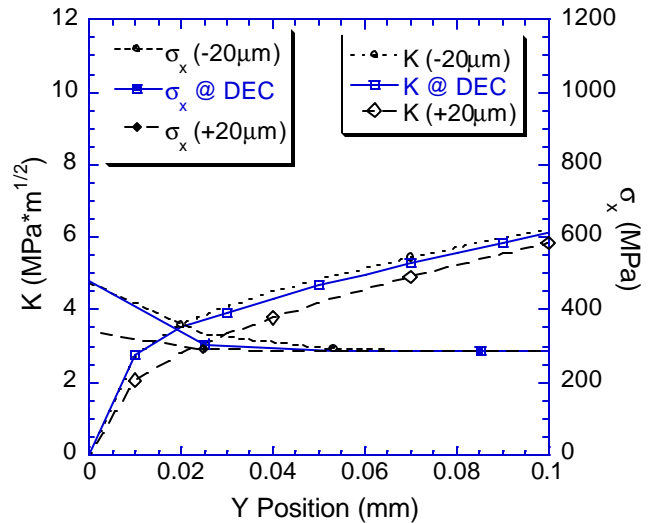

Figure 16: Stress distribution and resulting K solution for 4mm thick specimen, $\boldsymbol{m}=0.3$ case.

Some additional analysis was conducted to investigate the influence of μ on the calculated stresses and displacement. A value of μ=1.0 was chosen arbitrarily for the long pad cases. The maximum tensile stresses at the left end can be compared to the stresses for the identically loaded case where μ=0.3 (see Table 1 for results summary). It can be seen that increasing the μ from 0.3 to 1.0 doubles the peak tensile stress from about 600 MPa to 1200 MPa for the 2mm thick specimen case. The compressive stresses, σ_y, are nearly the same and are governed primarily by the clamping load which is unchanged in the two comparative cases. However, the shear stresses just inside the DEC are increased from almost 150 MPa to almost 400 MPa by increasing μ [4]. Finally, the maximum slip value at the DEC is reduced drastically from 15 to

3.2 µm (figs. 13) when increasing µ. The sensitivity of the stresses and displacements near the edge of contact to the value of µ between pad and specimen is apparent from these observations.

Stress Intensity Factor Results:

The next results presented are the K solutions plotted as a function of depth into the specimen (figs. 15 through 17) for the deformed edge of contact (DEC) location and two adjacent locations 20µm on either side of the DEC. In figures 15, 16, and 17, y=0 corresponds to the surface of the specimen in contact with the pad. Each plot also includes the axial stress σ_x, illustrating the extent of the gradients into the specimen thickness for the corresponding K curve. The K values peak at the DEC, as do the stresses on the specimen surface. Other cases (not shown) for locations farther beyond the DEC indicated K values decaying proportional to the stress field. However, K distribution trends at the DEC show a continuous increase in K with crack length, and point to crack propagation to failure and not crack arrest, as reported for other geometries [6].
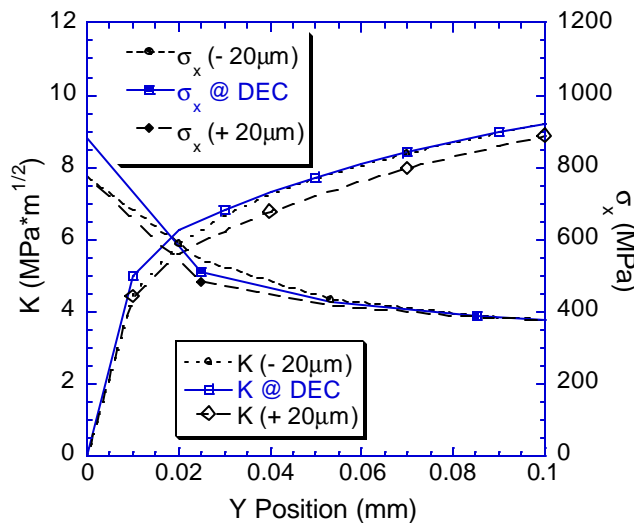

Figure 17: Stress distribution and resulting K solution for 4mm thick specimen, μ=1.0 case.

In comparing the various cases modeled here, we first address the cases where µ is taken as 0.3, a value which represents an average of values corresponding to gross slip over the entire pad length [4]. Data for the 1mm thick specimen and short pad case are shown in figure 16; data for the 4mm thick specimen and long pad are shown in figure 17. The values of maximum σ_x, shown in Table 1, vary from ~500 MPa for the 4mm thick long pad case (Fig. 16) to ~1200 MPa for the 1mm thick short pad case (Fig. 15). Since K depends strongly on the stress field, the calculated K values are higher for the case with the higher stresses, namely the 1mm thick specimen and short pad case. Variations of stress gradients into the depth from one case to another are not too great and have little effect on the nature of the variation of K with crack length.

The experimental results for these two cases indicate nearly identical fatigue limits (Fig. 5). One would expect similar peak stresses and stress intensity factors in cases reflecting similar fatigue limits for the same fatigue life. As reported previously [4], differences in applied shear stress and average applied clamping stress at the contact for these two cases do not adequately explain the marked differences in the stresses from the numerical simulations. One possible explanation lies in the value of µ used in the analyses. Work by other researchers has indicated pronounced changes in µ over time under fretting fatigue conditions [14,15], and as stated above, overall fretting fatigue behavior is extremely sensitive to µ.

Also discussed earlier was that the maximum relative displacement (see Table 1) at the edge of contact was considerably different for the cases studied. This observation, coupled with the observation that increasing the value of µ results in increasing values of σ_x, leads to

consideration of increasing μ for the case of the 4 mm thick specimen, which showed both lower stresses and higher relative displacements. While there is no physical basis for this assumption, the concept of higher μ for higher slip displacements is not totally without merit. It is also of interest to note that an early fretting parameter [11] contained the product of the stress and relative displacement. Perhaps the theory proposed here has the same effect by increasing the stress through an increase in μ rather than through multiplying by relative displacement.

For the conditions modeled here, we hypothesize that initial slip conditions corresponding to μ=0.3 change over time to conditions of increasing μ, thus increasing σ_x and corresponding K values. As shown above, higher tensile stresses and the resulting K values may be produced either by imposing a high clamping stress or by increasing μ. An equilibrium condition may exist for μ, which is dependent on the resultant relative displacement. If such a condition exists, an iterative method would be required to determine the final condition.

COMMENTS & CONCLUSIONS

Some final comments are in order in interpreting the numerical results presented above. Of importance is that the numerical values correspond to maximum load on the first cycle at R = 0.5. To evaluate both maximum and minimum stress and stress range, the calculations should be carried out over several cycles until steady state is achieved [14]. Further, it would be desirable to study how steady state is achieved under a changing value of μ as has been observed experimentally [15]. Of importance, additionally, is the observation that comparisons have been made for maximum stress at a point. If an approach is taken using stresses at a critical distance or stresses averaged over a critical distance [16], and this distance is not small compared to the distance over which the stresses decay rapidly, then the peak stresses will be of lesser importance. Such an approach is analogous to that used for very sharp notches where the equivalent of a short crack effect has to be taken into account [16]. In the present study, as noted earlier, peak stresses decay rapidly over distances of tens of microns.

Changes in μ over time for various fretting fatigue conditions vastly compound the problem of accurate life prediction for fretting fatigue, since it is very difficult to determine how μ will change over time. Further, such a change will be different for each combination of pad material, specimen material, applied loads, surface modification, and environment. Since fretting fatigue behavior is so profoundly influenced by μ which, in turn, may depend on relative displacements, additional research in how μ changes under fretting fatigue conditions is recommended.

Within the constraints of the geometry and test configuration and loading conditions examined in this investigation and under the assumptions made in the analyses, particularly that of μ being 0.3, the following conclusions can be drawn.

1. The fatigue limit stress corresponding to 10^7 cycles, under fretting fatigue, is only 20 to 60 percent of that of a smooth bar. Thus, fretting fatigue is highly detrimental to the fatigue properties of Ti-6Al-4V.
2. The debit in fatigue limit stress is rather insensitive to the average shear stress or average clamping stress.
3. Stress and relative displacement (slip) fields are very sensitive to the value of μ used in analysis.

4. Stress and slip fields, determined under a range of conditions corresponding to a fretting fatigue life of 10^7 cycles, show no clear pattern from which a fatigue limit criterion can be deduced.
5. High levels of slip may produce increases in μ, which might have to be revised to produce higher stresses and smaller displacements.
6. Under the assumption of a Mode I crack normal to the surface, if a crack nucleates, it will continue to propagate to failure.

References
1. Dobromirski, J.M., *Fretting Fatigue, ESIS 18*, R.B. Waterhouse and T.C. Lindley, Eds., Mechanical Engineering Publications, London, 1994, pp. 60-66.
2. Hutson, A., Nicholas, T., and Goodman, R., *Int. J. Fatigue*, 21, 7, 1999, pp. 663 – 670.
3. Hutson, A. and Nicholas, T., *Fretting Fatigue Current Technologies and Practices, ASTM STP 1367*, D.W. Hoeppner, V. Chandrasekaran, and C.B. Elliot, Eds., American Society for Testing and Materials, West Conshohocken, PA, 1999, pp. 308-321.
4. Hutson, A.L., Nicholas, T., Olson, S.E., and Ashbaugh, N.E. *Submitted to Int. J. Fatigue* September 2000.
5. Hutson, A.L., "Fretting Fatigue of Ti-6Al-4V Under Flat-on-Flat Contact with Blending Radii," M.S. Thesis, School of Engineering, University of Dayton, Dayton, OH, August, 2000.
6. *Fretting Fatigue, ESIS 18*, R.B. Waterhouse and T.C. Lindley, Eds., Mechanical Engineering Publications, London, 1994, pp. 171-182.
7. *Standardization of Fretting Fatigue Test Methods and Equipment, ASTM STP 1159*, M. H. Attia, and R. B. Waterhouse, Eds., American Society for Testing and Materials, Philadelphia, 1992.
8. Peters, J.O. and Ritchie, R.O., *Submitted to Int. J. Fatigue* September 2000.
9. Moshier, M.A., Nicholas, T. and Hillberry, B.M., *Submitted to Int. J. Fatigue* September 2000.
10. Maxwell, D., and Nicholas, T., *Fatigue and Fracture Mechanics: 29th Vol., ASTM STP 1321*, T. L. Panotin and S. D. Sheppard, Eds. American Society for Testing and Materials, 1999, pp. 626-641.
11. Ruiz, C., Boddington, P.H.B., and Chen, K.C., *Experimental Mechanics*, Vol. 24, 1984, pp. 208-217.
12. John, R., Weight Function Analysis for a Single Edge Cracked Specimen, Unpublished work, Air Force Research Laboratory (AFRL/MLLN), Wright-Patterson AFB, OH.
13. Giannakopoulos, A.E., Lindley, T.C., Suresh, S., and Chenut, C. *Submitted to Fatigue Frac. Eng. Mat. Structures.*
14. Szolwinski, M.P., Matlik, S.F. and Farris, T.N., *Int. J. Fatigue*, 21, 1999, pp. 671-677.
15. Farris, T.N., Harish, G., McVeigh, P.A., and Murthy, H., Proc. of the 5th National Turbine Engine High Cycle Fatigue (HCF) Conference on CD, Session 13, Chandler, AZ, March 2000.
16. Taylor, D., *Int. J. Fatigue*, 21, 1999, pp. 413-420.

Effect of sample thickness on local contact behavior in a flat-on-flat fretting fatigue apparatus

Alisha L. Hutson[1], Ted Nicholas, Steven E. Olson and Noel E. Ashbaugh

Metals, Ceramics & NDE Division, Materials and Manufacturing Directorate,
Air Force Research Laboratory (AFRL/MLLN), Wright-Patterson AFB, OH 45433-7817

[1] Phone: 937-255-2708, FAX: 937-656-4840, E-mail: alisha.hutson@afrl.af.mil

Abstract

Thin plate samples of Ti-6Al-4V contacted on both sides with pads of the same material were used to simulate contact conditions in real structures subjected to fretting fatigue. Laboratory tests on specimens of varying thicknesses were used to determine the stresses that correspond to a fatigue life of 10^7 cycles using a step-loading procedure. For the specific apparatus used in this study, changes in thickness produced changes in the ratio of shear load to clamping load for a specific fretting pad geometry. Specimen thicknesses of 1 mm, 2 mm, and 4 mm, and stress ratios of R = 0.1 and R = 0.5 were investigated for two different contact pad lengths. Fatigue limit stresses in the specimen were found to be relatively insensitive to the average clamping or shear stress. Finite element analyses of the test geometry were used to provide details of the stress distribution in the contact region for the flat-on-flat geometry with blending radius. Results show that stress and displacement fields for a variety of test conditions corresponding to a fatigue life of 10^7 cycles vary widely and do not provide any clear indication of the existence of a simple parameter equivalent to a uniaxial fatigue limit stress. The stress and displacement fields are also shown to be very sensitive to the coefficient of friction used in the analysis.

---

[1] University of Dayton Research Institute, 300 College Park, Dayton, OH 45469-0128.

1. Introduction

While fretting fatigue has been studied extensively, there are so many aspects to the problem [1] that it is still not a well understood phenomenon. Fretting fatigue, as described here, refers to the cyclic loading of a material that is subjected to clamping stresses normal to the direction of loading. In this geometry, the contact region undergoes relative slip near the edge of contact. Terminology such as contact fatigue is also used for this situation. What distinguishes fretting fatigue from wear or galling is rather subjective, but fretting fatigue is normally associated with small magnitudes of relative slip on the order of tens of microns and little if any material removal.

The damage due to fretting fatigue can lead to premature crack initiation and failure. Such damage has been indicated as the cause of many unanticipated disk and blade failures in turbine engines. As a result, it has been the focus of numerous studies involving experimental techniques [2,3,4,5], analyses [6,7,8] and mechanisms [9,10,11,12,13] over the years. Several symposia have also focused on the topic of fretting fatigue [14,15].

Failures occur in the contact region between the disk and a blade and are normally found near the end of the contact zone. The blade and disk are in contact over part of the region, but relative slip can occur near the edge of contact. While it has not been clearly established whether fretting fatigue is primarily due to small amplitude, high cycle fatigue (HCF) vibratory loading, large amplitude low cycle fatigue loads, or a synergistic combination of the two, it is felt to be important to address the HCF aspect of the problem. Towards this end, the need exists to define the limits of applied loads on a given contact geometry beyond which HCF failure will occur, and to establish criteria for determining such loads. Thus, the objective is to find the conditions under fretting fatigue which are analogous to the fatigue limit stress under uniaxial fatigue loading corresponding to a chosen HCF life, 10^7 cycles, for example.

Even under laboratory conditions, the synergistic effects of various parameters make determination and modeling of the mechanical behavior of fretting fatigue extremely difficult. The stress state in the contact region involves very high peak stresses, steep stress gradients, multi-axial stresses and differing mean stresses. Further, controversy exists whether the problem is one primarily of crack initiation or a crack propagation threshold, and whether or not stress states rather than surface conditions play a major role in the observed behavior. Confusion also

exists regarding the different stress distributions associated with those that occur in lab specimens versus what are present in real structures. Laboratory tests can involve thin plate samples contacted on both sides to simulate contact conditions whereas real structures are more representative of contact with a half space. Finally, lab testing usually involves a constant clamping force while real hardware has cyclic contact loading. While no single investigation is expected to answer all of the questions associated with fretting fatigue phenomena, an attempt is made here to shed some light on some of the issues regarding the relative roles of clamping force, ratio of shear to axial load in a specimen under contact fatigue, and contact pad geometry. In addition, finite element analyses of the test apparatus are presented to provide details of the stress distribution in the flat-on-flat geometry for representative sample thicknesses and contact lengths.

2. Experiments

2.1 Test apparatus

A unique, high frequency test system was used to conduct tests that simulate the fretting fatigue damage that occurs in turbine engine blade attachments [16,17]. The test apparatus simulates many of the essential features of a typical blade root geometry by employing flat fretting pads, with a radius at the edge of contact, against a flat specimen. Normal and shear loads are applied to the specimen in the test apparatus as shown in Fig. 1. Although a bending moment is present, a prior investigation has shown that it is relatively small and can be neglected when designing the tests [18]. The reported experimental data, therefore, will only include the applied normal load and shear load, which was equal to one half of the applied axial load as shown in Fig. 1.

This test geometry differs from the conventional fretting fatigue test with a fretting pad [2,3] in that the axial stress in the specimen is transferred completely through the pads. Thus, the shear force into the pad is known without any other measurements being made beyond the applied stress in the specimen. The clamping force is applied with instrumented bolts and can be controlled with reasonable accuracy. The test geometry restricts the maximum nominal shear stress to be that which can be reached for a given nominal clamping stress before total slip

occurs in the contact region. Likewise, the axial stress is transferred completely to the fixture through shear, unlike conventional fixtures where partial transfer occurs. As in a conventional test, only the axial and shear loads are oscillatory: the clamping load is static. Finally, the symmetry of the apparatus provides a specimen, which breaks on one end typically, leaving the other end with a fretting scar and damage obtained under nominally identical conditions corresponding to 100 percent of the fretting fatigue life.

The test machine used in this investigation has the capacity for fatigue testing at frequencies of up to 500 Hz. [16,17]. An electro-dynamic shaker applies oscillatory loads while a pneumatic chamber fitted in the rigid fatigue test frame produces the mean load. The air cylinder is very compliant for the high frequency, low amplitude loading allowing a very large fraction of the oscillatory load from the shaker to be transferred to the specimen instead of the load frame. Tests for this study were conducted at 300 Hz in lab air at room temperature. The choice of frequency was dictated by a need to avoid system resonance and by a desire to have as high a frequency as possible with the available hardware, since vibratory modes in engine hardware often exceed 1 kHz.

2.2 Material

The material used for both the pads and the specimens in this investigation was Ti-6Al-4V, taken from forged plates which have been used in a series of investigations under a U.S. Air Force sponsored high cycle fatigue program. The processing and microstructure are described in other investigations within this volume [19,20]. The material was machined using conventional low stress grind procedures for titanium and finished by hand polishing. No surface treatments were applied, even though it is recognized that many applications involve the use of coatings or surface treatments such as shot peening.

2.3 Test procedure

For various combinations of specimen thickness, pad length, and clamping force, specimens were subjected to uniaxial fatigue to determine the fatigue limit stress corresponding to 10^7 cycles to failure. The step-loading procedure of Maxwell and Nicholas [21], used and

validated in earlier fretting fatigue experiments using the same apparatus [8,16], was employed. In this method, blocks of 10^7 cycles were applied at constant R of continually increasing magnitudes until failure occurred. The procedure is outlined in the paper by Thompson, et al. in this volume [22]. For each test, a fatigue limit stress was obtained unless the starting load was too large and failure occurred within the first load block. The load level was incremented by five percent of the first load block until failure occurred.

3. Analysis

Analyses were conducted to determine the state of stress and an estimate of the relative slip of the pad with respect to the specimen at the edge of contact. ABAQUS was selected as the finite element modeling package with PATRAN as the pre- and post-processor. The geometry for the pads and specimen was treated as two-dimensional and, because of symmetry, only one pad and half the specimen thickness was modeled. Eight node quadrilateral elements were used, with mesh refinement down to sizes of approximately 6.5 μm near the edges of contact.

The analyses were quasi-static linear elastic analyses under plane stress. A line of symmetry was defined along the x-axis corresponding to the middle of the specimen, which limits translation in the y direction. In addition, the pad was prevented from rotation as shown in Fig. 2. The uniform x and y displacements were chosen to produce the desired axial force in the specimen and clamping force, respectively. First, the y displacement, Δv, was imposed to generate the clamping force. Then, the x displacement, Δu, was added to produce the axial force. Contact was defined for the entire top region of the specimen and the pad bottom including the full radius. Contact elements were used throughout the defined contact region with the pad set as the master surface and the specimen set as the slave surface. The material was modeled as a Ti-6Al-4V pad against a Ti-6Al-4V specimen and assumed to be linear elastic with a Poisson's ratio of 0.3 and a Young's modulus of 120 GPa. The material in the experiments had an ultimate tensile strength of 980 MPa, and a yield strength of 930 MPa. For the interface conditions, a constant coefficient of friction of 0.3 was assumed. Only the first half of the initial fatigue cycle was modeled. Details of the finite element methods are presented in [18].

Clamping loads were taken as those that were used in the experiments while the axial stress in the specimen was taken from the experimental observations. Specimen thicknesses were

either 1, 2, or 4 mm, thereby providing a broad range of shear forces since the shear force is half of the axial force and, as will be shown later, axial stresses for 10^7 cycles to failure did not vary widely throughout all of the experiments. Tests were conducted at stress ratios of either R=0.1 or R=0.5. Two pad total lengths were used, 25.4 mm and 12.7 mm, each one having a blending radius of 3.175 mm at both ends. Thus, the undeformed contact length was 6.35 mm for the short pad and 19.05 for the long pad. The clamping loads on the pads, which contacted the 10 mm wide specimens, were either 21, 26 or 35 kN. A summary of the test conditions simulated with the FEM analysis, indicating maximum loads and stresses, is given in Table 1.

Several test conditions were simulated numerically to compare stress fields and slip displacements for cases which all correspond to the conditions when the fatigue limit of 10^7 cycles is achieved. As in the earlier work, the coefficient of friction that was observed under gross slip conditions [16,18] was taken as 0.3. The first two conditions in Table 1 were simulated in a prior investigation [18] using a slightly less refined mesh than used here. Nonetheless, it was shown that peak tensile stresses in the specimen occurred at the surface at the deformed edge of contact and decayed rapidly in both the axial and thickness directions over distances of tens of microns.

For the long pad case, the maximum value of σ_x was approximately 700 MPa while for the short pad the maximum was about 1000 MPa. In the same comparison, the relative displacement between pad and specimen (maximum slip) was about 13 μm for the long pad and 3 μm for the short pad. In the refined analysis used in this investigation, the same conditions for the long pad produced an axial stress of 630 MPa and a relative displacement of 15μm. The numerical simulations discussed below cover three cases of the four in Table 1. First, the 2 mm thick specimen with a long pad is evaluated. Comparisons with the case of a 2 mm thick specimen with a short pad have been made elsewhere [18]. The remaining two cases, 4 mm thick with long pad and small clamping load, and 1 mm thick with short pad and large clamping load, cover the extremes of average clamping stresses used in this investigation. Note that the maximum shear forces (= half the maximum axial forces) are determined from the experimental observations and cannot be arbitrarily assigned when attempting to cover the broadest range of conditions corresponding to the ratio of normal to shear loads for a fatigue life of 10^7 cycles.

The clamping stresses in the experimentation are ~ 30% higher than was originally estimated. Since the clamping stresses used in the analysis were selected based on the original

estimates of experimental conditions, the analytical and experimental conditions used in the comparisons are not exactly the same (note analytical conditions identified in Figure 3). However, differences of this order in clamping stress have little effect on the resulting fatigue limit and therefore, will not affect overall results or conclusions.

4. Results and Discussion

Fatigue limit stresses were obtained for samples having one of the three thicknesses (1 mm, 2 mm and 4 mm) and fretting pads which we denote as short or long. The fatigue limit stress, obtained from the step loading tests, was normalized with respect to smooth bar fatigue limits. The normalized fatigue limits are plotted as a function of the average normal (clamping) stress or average shear stress for tests conducted at either R=0.1 or 0.5 in Figs. 3 through 6. The average stress is computed based on the area of contact in the undeformed state, from the locations corresponding to the tangent of the radii to the flat portion of the pad. As will be shown later, this approximation to the deformed area of contact is relatively accurate. Additional data points from a prior investigation are included, and represent tests that used pads with the same total lengths.

The first observation to note is the severe degradation of fatigue limit stress due to fretting. Fretting fatigue under the conditions imposed in this investigation degrades the maximum fatigue limit stress corresponding to 10^7 cycles from approximately 40 to 80 percent. The second major observation is that the fatigue limit stress is rather insensitive to either average normal stress or average shear stress. Only the data at R=0.5, Figs. 3 and 5, show a slight trend of increasing fatigue strength with decrease in applied normal or shear stresses. In all cases, the limiting value of normalized fatigue strength is 1.0 for normal or shear stresses, since this represents the smooth bar fatigue strength. Practically, however, such a limit cannot be obtained experimentally in the existing apparatus since normal stress has to be applied to keep the specimen from pulling out of the grips. To approach zero shear stress, an arbitrarily thin specimen would have to be used in the experimental configuration utilized here.

The distribution of stresses along the entire length of the contact is shown in Fig. 7, where x is normalized with respect to the half-length of the pad between the center and the position of undeformed contact. In this and all subsequent figures, the left end is the loaded one

187

while the right end of the specimen is stress free outside the right edge of contact. The long pads show a slightly increasing σ_x as the loaded left end is approached while the short pad has σ_x in nearly uniform compression except near the edges of contact. The short pad has the highest compressive (clamping) stresses, σ_y, and the most variability with position along the pad. The stresses peak at the ends of contact where the variation cannot be seen in Fig. 7. To observe the stress distribution near the deformed edge of contact (DEC), the stresses for the three cases studied are plotted in Figs. 8, 9, and 10. In each plot, x=0 corresponds to the DEC as determined from the computer output, and the vertical line identified with UEC refers to the undeformed edge of contact. While the magnitudes of the stresses are different, the general shape of the stress distribution is the same. The maximum tensile stress occurs just outside the DEC, but at a distance not exceeding about 10 μm. Obviously, σ_y and τ_{xy} are zero outside the contact region. Compared to σ_x and σ_y, the values of τ_{xy} are relatively small and spread out more while σ_y, of the same order as σ_x, peak at about 50 μm inside the DEC for the long pad, Figs. 8 and 10, and at about 100 μm for the short pad, Fig. 9. From these plots, the relative magnitude and localization of peak stresses near the DEC can be seen.

The stress distributions into the thickness are plotted for the 2 mm thick long pad in Fig. 11. Shown is σ_x at several distances into the thickness direction. The coordinate y=1 corresponds to the surface of the specimen in contact with the pad and the corresponding stress profile is identical to that shown in Fig. 8. The stress profiles show that the σ_x stresses decay rapidly, with stresses at 50 μm below the surface being almost the same as those much deeper. Thus, stress gradients into the thickness are of the same order of magnitude as those along the surface. Similar observations were made for the other cases, which are not shown here.

Tensile stresses or maximum principal stresses are often associated with a fatigue initiation or failure criterion. Since all three cases simulated here correspond to the fretting fatigue limit for 10^7 cycles, comparison of the maximum tensile stresses shown in Figs. 8 to 10 is of interest. The values of maximum σ_x can be seen to vary from about 600 MPa for the 2 mm thick long pad case (Fig. 8) to about 1200 MPa for the 1 mm thick short pad case (Fig. 9) to about 500 MPa for the 4 mm thick long pad case (Fig. 10). Clearly, this does not constitute a

failure or initiation criterion by itself in determining the conditions under which fretting fatigue occurs at the applied fatigue limit stress.

Another parameter that could enter such a failure criterion would be the relative slip between pad and specimen. The relative slip is plotted over the coordinates corresponding to the DEC, denoted by x=0, to the end of the slip/stick zone in Figs. 12 and 13. Two plots are used because of the need to show the details of the magnitude and x-distribution of slip distances, which take place over a significant portion of the contact length. Shown also in Fig. 13 is a case where the coefficient of friction is changed to $\mu=1.0$ from $\mu=0.3$ which is used for all the other calculations. The effects of this change will be discussed below. The maximum slip distance occurs at the edge of contact, which is where the maximum tensile stresses occur. For the three cases discussed above, the maximum slip distances corresponding to maximum tensile stresses can be seen to be 15 μm (600 MPa), 3 μm (1200 MPa), and 25 μm (500 MPa). No clear trend between slip distance and maximum tensile stress is apparent. While the value of σ_y might also be expected to have an influence on a failure criterion, note that at the DEC, or slightly outside, the clamping stresses as well as the shear stresses are zero. Thus, a parameter such as the product $\sigma_y \tau_{xy} \delta$, proposed by Ruiz, et al. [8], where δ is the relative displacement, would not be applicable to these geometries where σ_y and τ_{xy} are zero and, further, the parameter varies widely inside the contact region.

Stress peaks at both ends of the fretting pad were noted earlier in Figure 7. While failure in the specimen occurred in all tests at the loaded (left) end of the pad, examination of the local stresses at the unloaded (right) end of the pad in the vicinity of the DEC is of interest as these stresses provide an upper limit of a stress distribution that can lead to failure. The details of such a stress distribution are shown in Fig. 14 for the case of the 2mm thick specimen and long pad. In the figure, x=0 represents the DEC, thus σ_y and τ_{xy} are zero for positive values of x. The small values of σ_x at x=0 represent a combination of a non-zero equilibrium stress distribution and numerical oscillations because the total axial force is zero in this region. The σ_y stresses are nearly the same as at the left end (Fig. 8) and are due primarily to the clamping load and the slight bending moment which results from equilibrium and the assumed boundary condition of no rotation of the pad [18].

Of greater interest are the stresses at the right end for the short pad where average clamping stresses are the highest. Such a stress distribution is shown for the 1 mm thick pad in Fig. 15. While shear stresses are generally small, the axial and clamping stresses, both of which are compressive, are fairly significant. At maximum load, σ_y is approximately -1300 MPa and σ_x from about -600 to -700 MPa over a slightly longer distance, about 0.1 mm, than for the long pad (see also Fig. 9). While the clamping stresses at the right end are not cyclic, the other two stress components are cyclic and are shown only for the peak loads in R=0.5 fatigue testing.

It can only be speculated about what combined cyclic σ_x in compression and a large static σ_y in compression might do to initiate a crack. A detailed examination of possible damage or cracks has not been made yet on these specimens. Of greatest interest is the observation from the numerical simulations that there is no slip at the right end of contact in any of the cases studied. This is consistent with experimental observations, which did not indicate any fretting scars in that location on the specimen.

The last analysis conducted was to investigate the influence of coefficient of friction on the calculated stresses and displacement. Choosing a value of $\mu=1.0$ for the 2 mm thick specimen and long pad, the stresses at the left end, shown in Fig. 16, can be compared to the stresses for the identically loaded case shown in Fig. 8 where $\mu=0.3$. Note that increasing the coefficient of friction from 0.3 to 1.0 doubles the peak tensile stress from about 600 MPa to 1200 MPa. The compressive stresses, σ_y, are nearly the same and are governed primarily by the clamping load which is unchanged in the two comparative cases. However, the shear stresses just inside the DEC are increased from almost 150 MPa to almost 400 MPa by increasing μ. Finally, the maximum slip value at the DEC is reduced drastically from 15 to 3.2 μm (Figs. 12 and 13) when increasing the coefficient of friction. It is clearly seen from these observations that stresses and displacements near the edge of contact are very sensitive to the coefficient of friction between pad and specimen.

5. Closure

Some final comments are in order in interpreting the numerical results presented above. The loads on the specimen for the FEA correspond to maximum load on the first loading cycle at

R = 0.5. To evaluate both maximum and minimum stress and stress range, the calculations should be carried out over several cycles until steady state is achieved [23]. Further, it would be desirable to study how steady state is achieved under a changing value of μ as has been observed experimentally [24]. Of importance, additionally, is the observation that comparisons have been made for maximum stress at a point. If an approach is taken using stresses at a critical distance or stresses averaged over a critical distance [25], and this distance is not small compared to the distance over which the stresses decay rapidly, then the peak stresses will be of lesser importance. Such an approach is analogous to that used for very sharp notches where the equivalent of a short crack effect has to be taken into account [25]. In the present study, as noted earlier, peak stresses decay rapidly over distances of tens of microns. Finally, fracture mechanics criteria could be evaluated for the complex stress states obtained by assuming that cracks initiate in all cases studied and that a threshold crack growth criterion exists in order for the crack to continue to propagate. This approach would treat the problem in a manner such as that of a worst case fret [26]. These studies were beyond the scope of the present investigation and will be pursued in the future.

6. Conclusions

Within the constraints of the geometry and test configuration and loading conditions examined in this investigation and under the assumption made in the analyses, particularly that of the coefficient of friction being 0.3, the following conclusions can be drawn.

1. The fatigue limit stress corresponding to 10^7 cycles, under fretting fatigue, is only 20 to 60 percent of that of a smooth bar, depending on stress ratio. Thus, fretting fatigue is highly detrimental to the fatigue properties of Ti-6Al-4V.

2. The debit in fatigue limit stress is relatively insensitive to the average shear stress or average clamping stress.

3. Stress and relative displacement (slip) fields are very sensitive to the value of coefficient of friction chosen for analysis.

4. Stress and slip fields, determined under a range of conditions which each correspond to a fretting fatigue life of 10^7 cycles, show no obvious pattern from which a fatigue limit criterion can be deduced.

References

[1]   Dobromirski, J.M., "Variables of Fretting Processes: Are There 50 of Them?," Fretting Fatigue, ESIS 18, R.B. Waterhouse and T.C. Lindley, Eds., Mechanical Engineering Publications, London, 1994, pp. 60-66.

[2]   Attia, M.H., "Fretting Fatigue Testing: Current Practices and Future Prospects for Standardization," *Standardization of Fretting Fatigue Test Methods and Equipment, ASTM STP 1159*, M. Helmi Attia and R. B. Waterhouse, Eds., American Society for Testing and Materials, Philadelphia, 1992, pp. 263-275.

[3]   Hills, D.A. and Nowell, D., "A Critical Analysis of Fretting Fatigue Experiments", *Fretting Fatigue, ESIS 18*, R.B. Waterhouse and T.C. Lindley, Eds., Mechanical Engineering Publications, London, 1994, pp. 171-182.

[4]   Del Puglia, A., Pratesi, F., and Zonfrillo, G., "Experimental Procedure and Parameters Involved in Fretting Fatigue Tests," *Fretting Fatigue, ESIS 18*, R.B. Waterhouse and T.C. Lindley, Eds., Mechanical Engineering Publications, London, 1994, pp. 219-238.

[5]   *Standardization of Fretting Fatigue Test Methods and Equipment, ASTM STP 1159*, M. H. Attia, and R. B. Waterhouse, Eds., American Society for Testing and Materials, Philadelphia, 1992.

[6]   Fouvry, S., Kapsa, P., and Vincent, L., "Quantification of Fretting Damage," *Wear*, Vol. 200, 1996, pp. 186-205.

[7]   Vingsbo, O. and Schon, J., "Gross Slip Criteria in Fretting," *Wear*, Vol. 162-164, 1993, pp. 347-356.

[8]   Ruiz, C., Boddington, P.H.B., and Chen, K.C., "An Investigation of Fatigue and Fretting in a Dovetail Joint," *Experimental Mechanics*, Vol. 24, 1984, pp. 208-217.

[9]   Bryggman, U. and Söderberg, S., "Contact Conditions and Surface Degradation Mechanisms in Low Amplitude Fretting", *Wear*, Vol. 125, 1988, pp. 39-52.

[10]   Fellows, L.J., Nowell, D., and Hills, D.A., "On the Initiation of Fretting Fatigue Cracks," *Wear*, Vol. 205, 1996, pp. 120-129

[11]   Hoeppner, D.W., "Mechanisms of Fretting Fatigue," *Fretting Fatigue, ESIS 18*, R.B. Waterhouse and T.C. Lindley, Eds., Mechanical Engineering Publications, London, 1994, pp. 3-19.

[12]   Fayeulle, S., Blanchard, P., and Vincent, L., "Fretting Behavior in Titanium Alloys," *Tribology Transactions*, Vol. 36, No. 2, 1993, pp. 267-275.

[13] Waterhouse, R.B., "Effect of Material and Surface Conditions on Fretting Fatigue," *Fretting Fatigue, ESIS 18*, R.B. Waterhouse and T.C. Lindley, Eds., Mechanical Engineering Publications, London, 1994, pp. 339-349.

[14] *Fretting Fatigue, ESIS 18*, R.B. Waterhouse and T.C. Lindley, Eds., Mechanical Engineering Publications, London, 1994.

[15] Fretting Fatigue: Current Technologies and Practices, ASTM STP 1367, D.W. Hoeppner, V. Chandrasekaran, and C.B. Elliot, Eds., American Society for Testing and Materials, West Conshohocken, PA, 1999.

[16] Hutson, A., Nicholas, T., and Goodman, R., "Fretting Fatigue of Ti-6Al-4V Under Flat-on-Flat Contact", *International Journal of Fatigue*, Vol. 21, No 7, 1999, pp. 663 – 670.

[17] Hutson, A. and Nicholas, T., "Fretting Fatigue Behavior of Ti-6Al-4V against Ti-6Al-4V under Flat-on-Flat Contact with Blending Radii," *Fretting Fatigue Current Technologies and Practices, ASTM STP 1367*, D.W. Hoeppner, V. Chandrasekaran, and C.B. Elliot, Eds., American Society for Testing and Materials, West Conshohocken, PA, 1999, pp. 308-321.

[18] Hutson, A.L., "Fretting Fatigue of Ti-6Al-4V Under Flat-on-Flat Contact with Blending Radii," M.S. Thesis, School of Engineering, University of Dayton, Dayton, OH, August, 2000.

[19] Peters, J.O. and Ritchie, R.O., "Foreign-Object Damage and High-Cycle Fatigue: Role of Microstructure in Ti-6Al-4V," Int. J. Fatigue (this volume).

[20] Moshier, M.A., Nicholas, T. and Hillberry, B.M., "Determining a True Material Fatigue Crack Growth Threshold," Int. J. Fatigue (this volume).

[21] Maxwell, D., and Nicholas, T., "A Rapid Method for Generation of a Haigh Diagram for High Cycle Fatigue, "Fatigue and Fracture Mechanics: 29th Vol., ASTM STP 1321, T. L. Panotin and S. D. Sheppard, Eds. American Society for Testing and Materials, 1999, pp. 626-641.

[22] Thompson, S.R., Ruschau, J.J. and Nicholas, T., "Influence of Residual Stresses on High Cycle Fatigue Strength of Ti-6Al-4V Leading Edges Subjected to Foreign Object Damage," Int. J. Fatigue (this volume).

[23] Szolwinski, M.P., Matlik, S.F. and Farris, T.N., "Effects of HCF Loading on Fretting Fatigue Crack Nucleation," Int. J. Fatigue, 21, 1999, pp. 671-677.

[24] Farris, T.N., Harish, G., McVeigh, P.A., and Murthy, H., "Prediction and Observation of Fretting Fatigue of Ti-6Al-4V Subjected to Blade/Disk Type Contacts," Proc. of the 5th National Turbine Engine High Cycle Fatigue (HCF) Conference on CD, Session 13, Chandler, AZ, March 2000.

[25]   Taylor, D., "Geometrical Effects in Fatigue: A Unifying Theoretical Model," <u>Int. J. Fatigue</u>, **21**, 1999, pp. 413-420.

[26]   Chan, K.S., Lee, Y-d, Davidson, D.L. and Hudak, S.J., Jr., "A Fracture Mechanics Approach to High Cycle Fretting Fatigue Based on the Worst Case Fret Concept, <u>Eng. Fract. Mech.</u>, 2000 (submitted for publication).

<u>Figure Captions</u>

Figure 1: Schematic of experimental specimen loading configuration (symmetrical half of specimen shown $\approx$ 75 mm).

Figure 2: Schematic of geometry and loading conditions for finite element analysis. Characteristic dimensions are given in Table 1.

Figure 3: Normalized limit stresses for 1, 2, and 4 mm thick samples tested at R=0.5 vs. average applied normal stresses.

Figure 4: Normalized limit stresses for 1, 2, and 4 mm thick samples tested at R=0.1 vs. average applied normal stresses.

Figure 5: Normalized limit stresses for 1, 2, and 4 mm thick samples tested at R=0.5 vs. average applied shear stresses.

Figure 6: Normalized limit stresses for 1, 2, and 4 mm thick samples tested at R=0.1 vs. average applied shear stresses.

Figure 7: σ_x and σ_y stress distributions along specimen surface in contact with fretting pad calculated for the first half cycle for 1, 2, and 4 mm thick samples vs. normalized x position, where zero corresponds to the middle of the fretting pad.

Figure 8: σ_x, σ_y and τ_{xy} stress distributions along specimen surface for the 2 mm thick sample against a long pad, where zero corresponds to the deformed edge of contact (DEC) identified from the analysis.

Figure 9: σ_x, σ_y and τ_{xy} stress distributions along specimen surface for the 1 mm thick sample against a short pad, where zero corresponds to the DEC.

Figure 10: σ_x, σ_y and τ_{xy} stress distributions along specimen surface for the 4 mm thick sample against a long pad, where zero corresponds to the DEC.

Figure 11: σ_x stress distribution at various depths from specimen surface for the 2 mm thick sample against a long pad. x=0 corresponds to the DEC identified from the analysis. y=1 corresponds to the sample surface.

Figure 12: Relative slip for 2 and 4 mm thick samples against long pad. x=0 corresponds to the DEC.

Figure 13: Relative slip calculated for a 1 mm thick sample against a short pad and a 2 mm thick sample against a long pad. x=0 corresponds to the DEC.

Figure 14: σ_x, σ_y and τ_{xy} stress distributions along specimen surface for the unloaded end of a 2 mm thick sample against a long pad. x=0 corresponds to the DEC.

Figure 15: σ_x, σ_y and τ_{xy} stress distributions along specimen surface for the unloaded end of a 1 mm thick sample against a short pad. x=0 corresponds to the DEC.

Figure 16: σ_x, σ_y and τ_{xy} stress distributions along specimen surface for a 2 mm thick sample against a long pad vs. x position. x=0 corresponds to the DEC.

Specimen thickness, t (mm)	Pad length, l (mm)	Clamping load (kN)	Applied axial stress, σ_a (MPa)	Average σ_y (MPa)	Average τ_{xy} (MPa)
2	25.4	26	350	136	18.4
2	12.7	26	260	409	40.9
4	25.4	21	275	110	28.9
1	12.7	35	275	551	21.7

Table 1. Summary of test conditions selected from R=0.5 experimental data for FEM analysis.

Figure 1

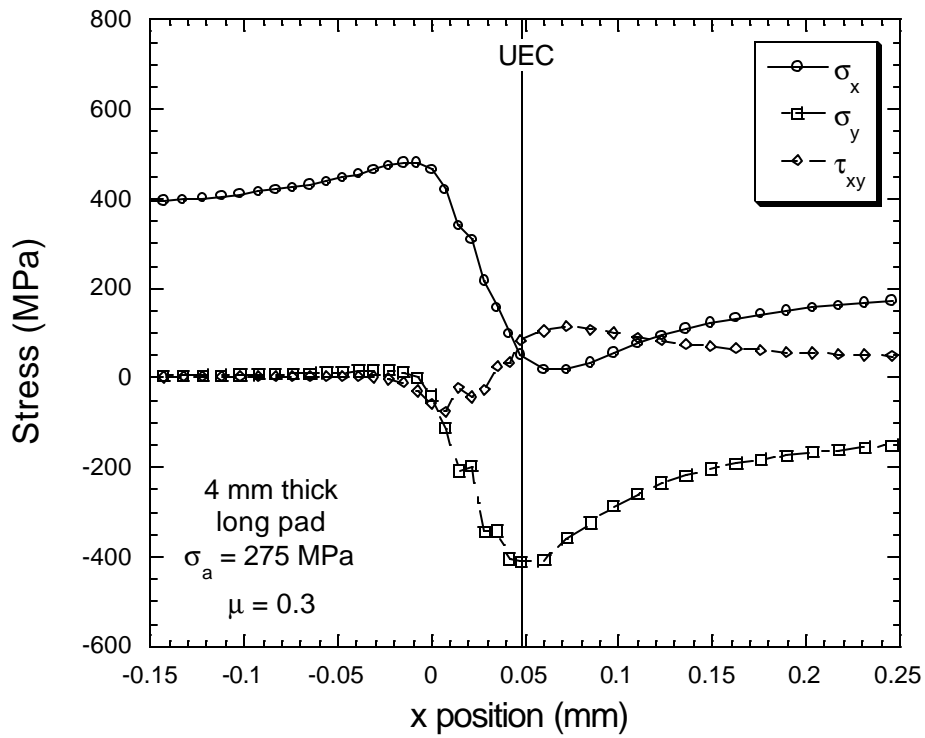Figure 2

Figure 3

Figure 4
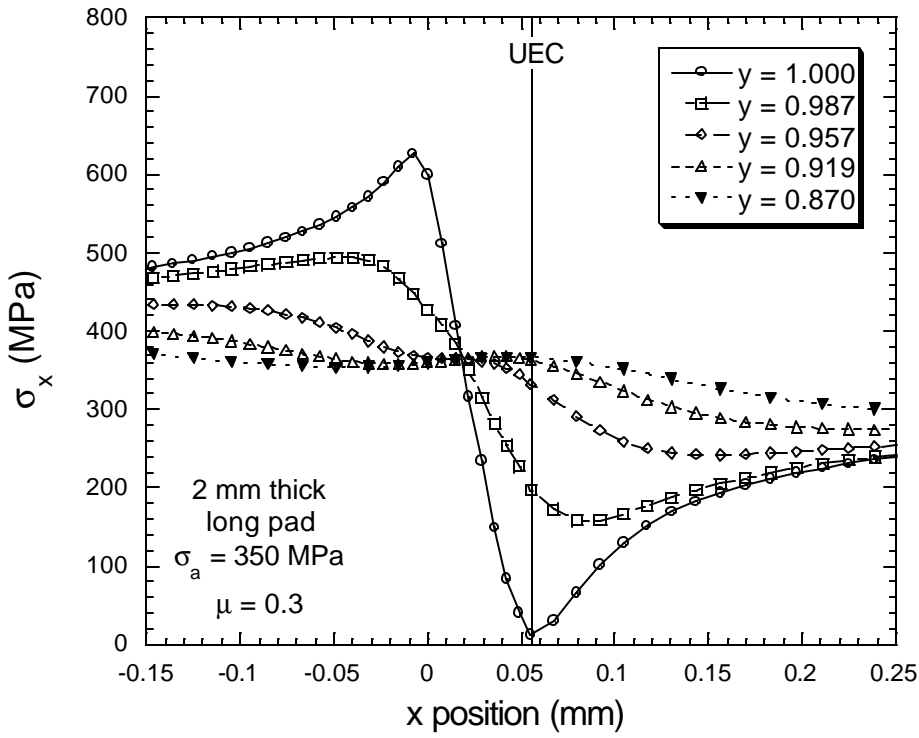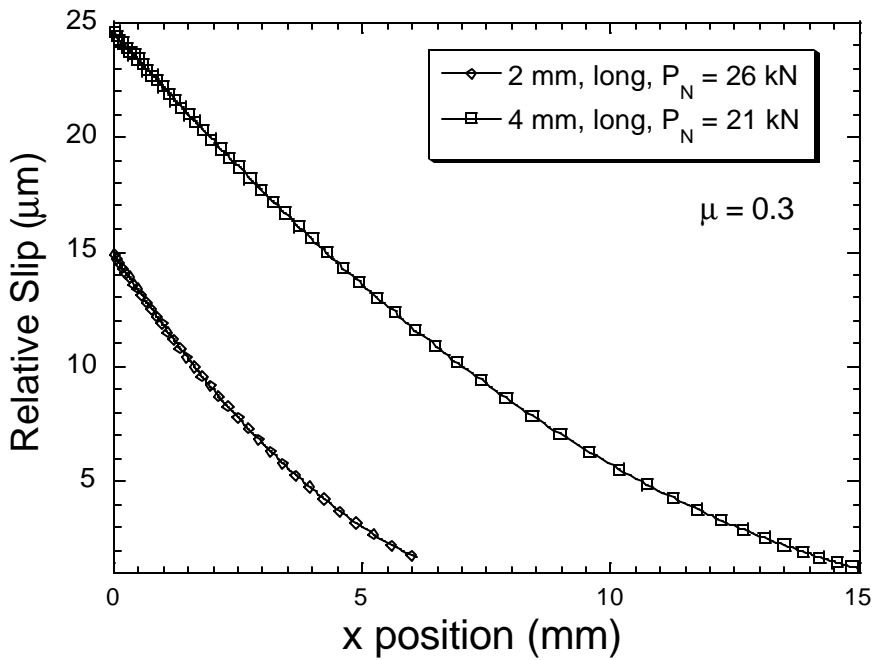
197
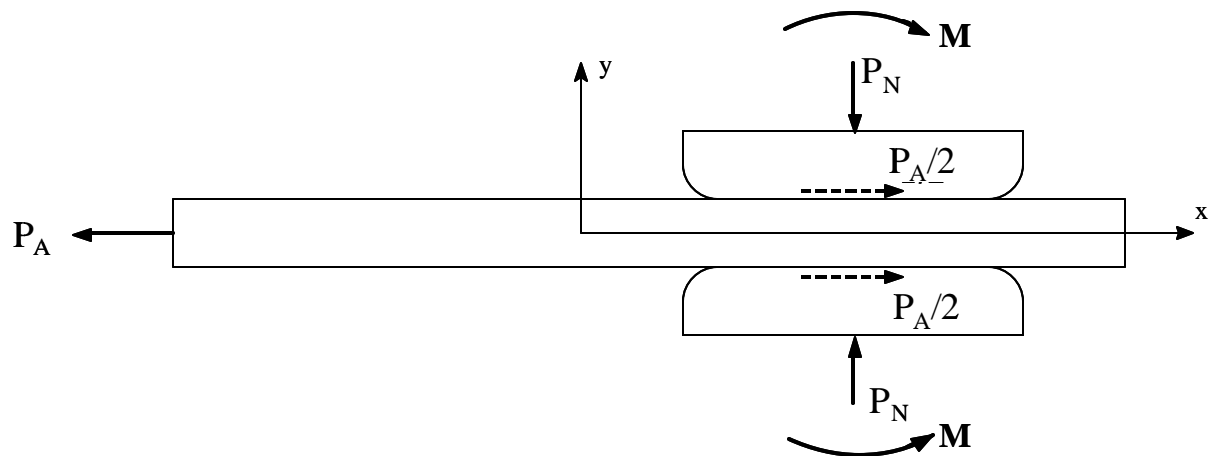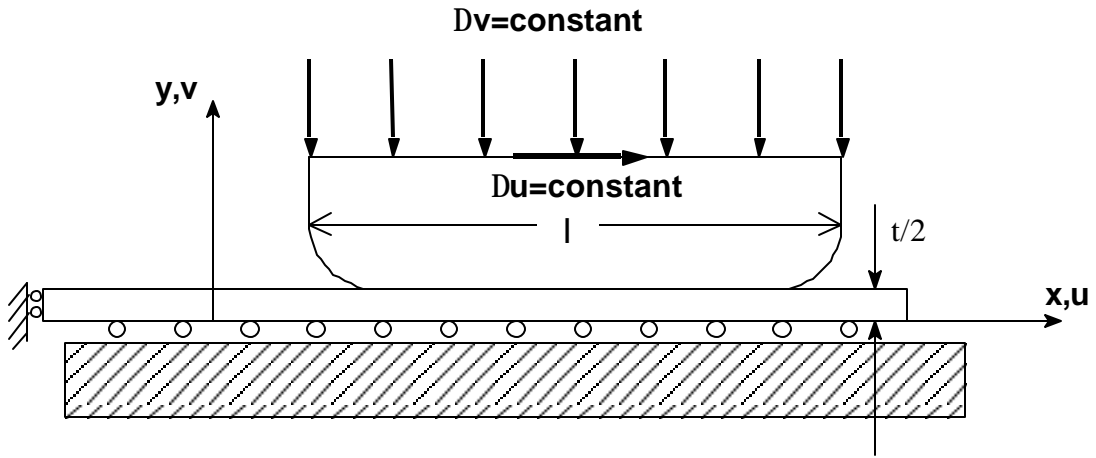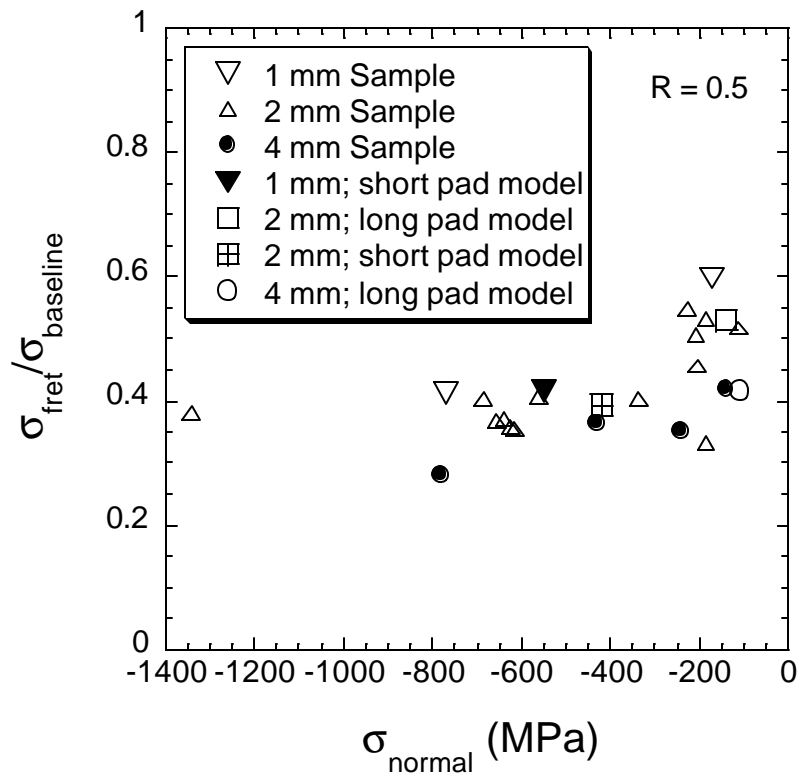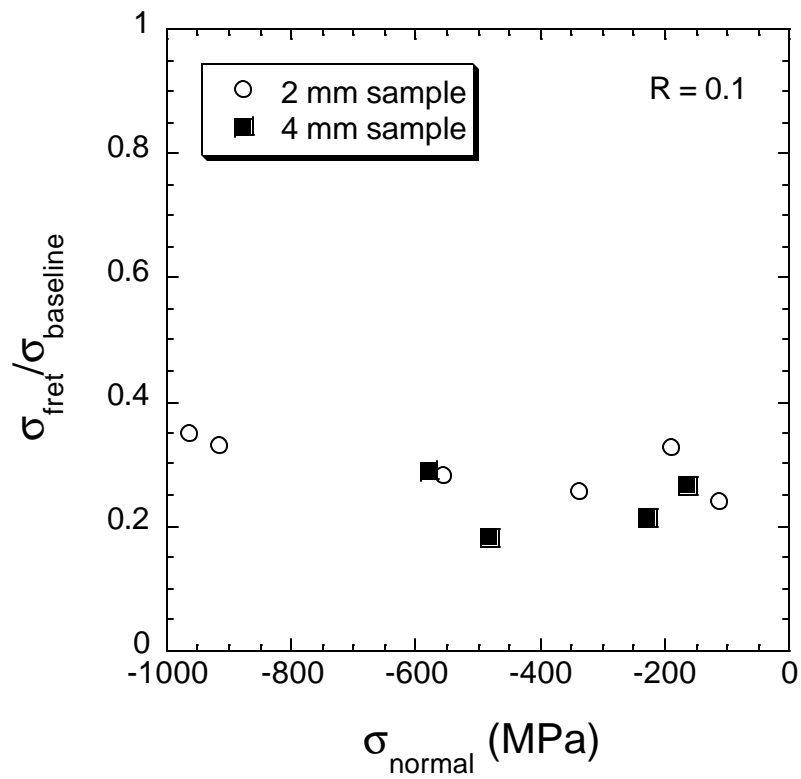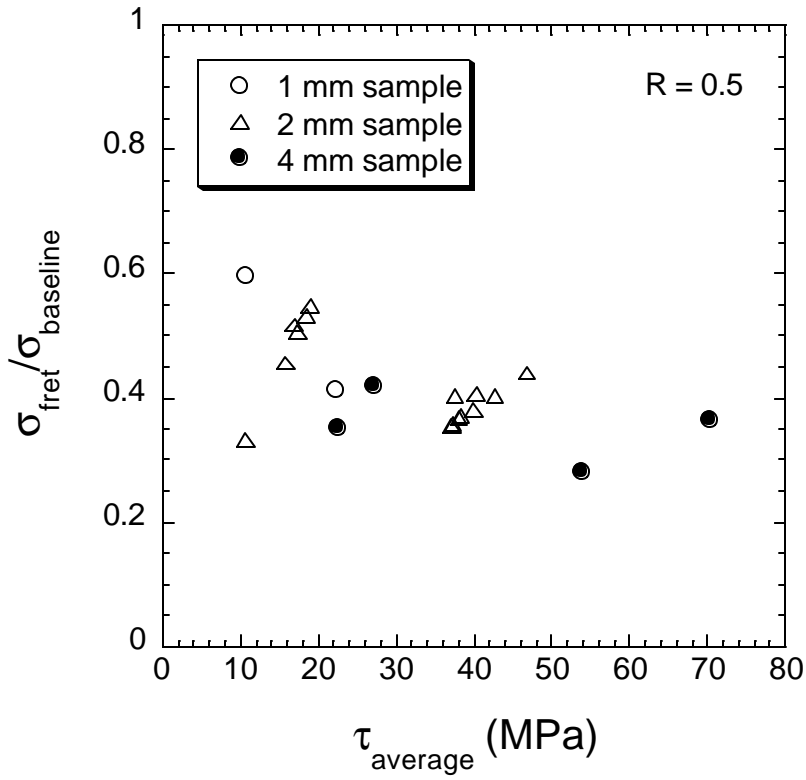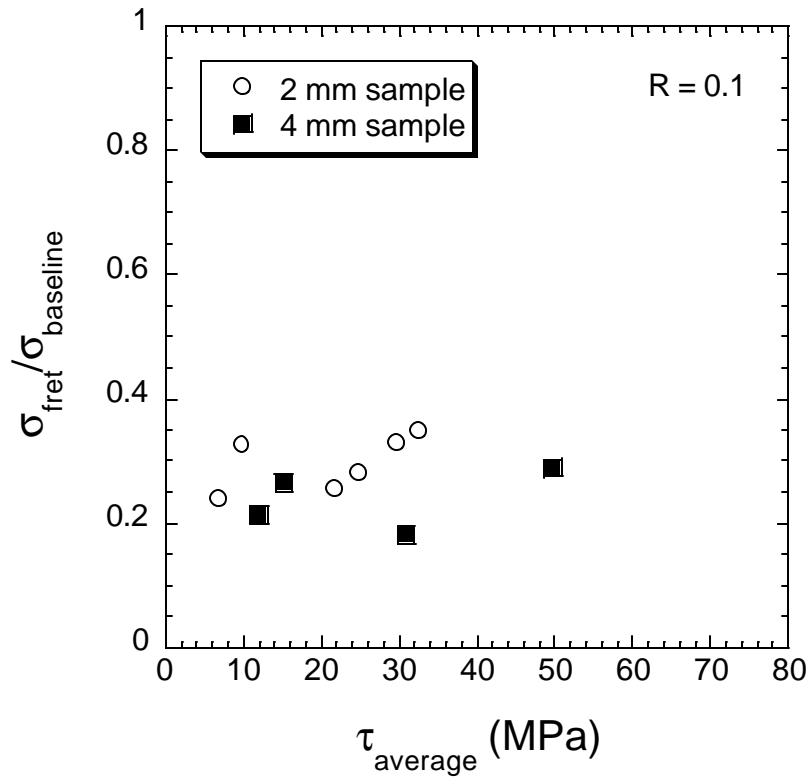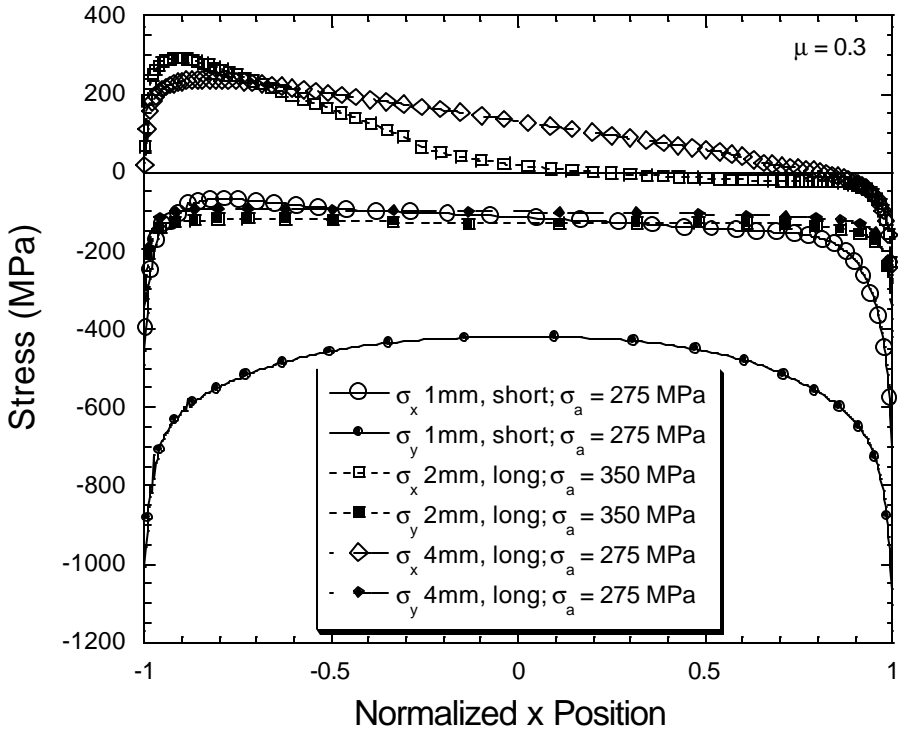
Figure 5

Figure 6

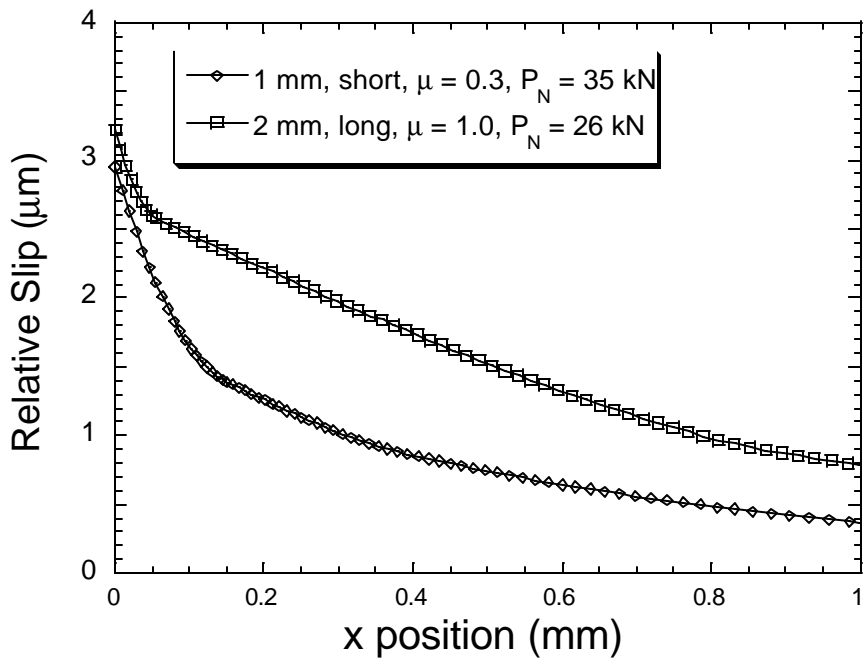Figure 7
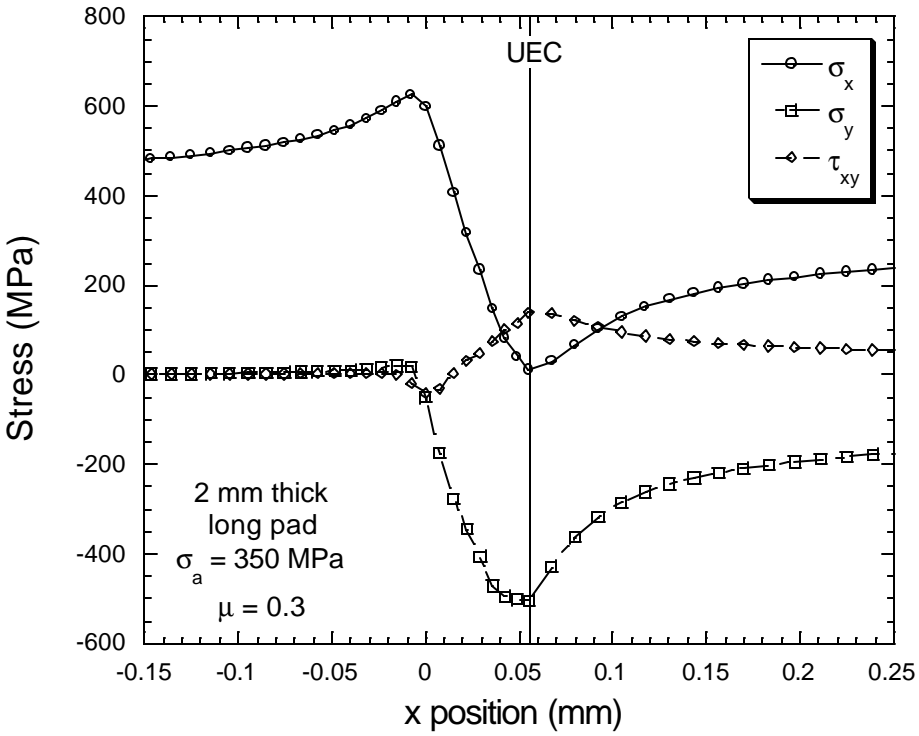
Figure 8
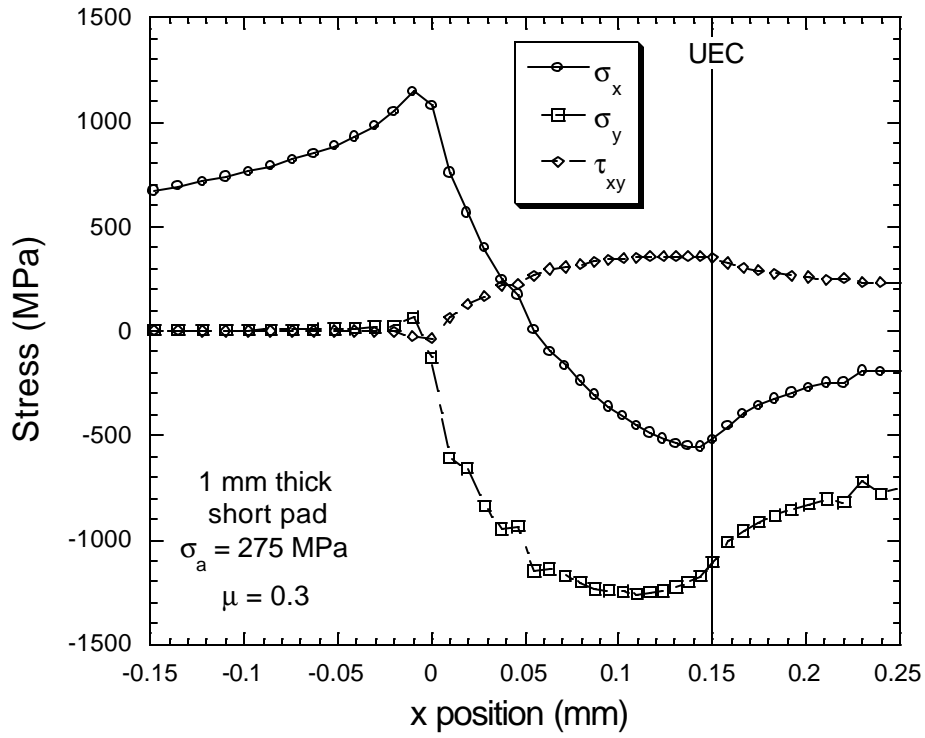
Figure 9
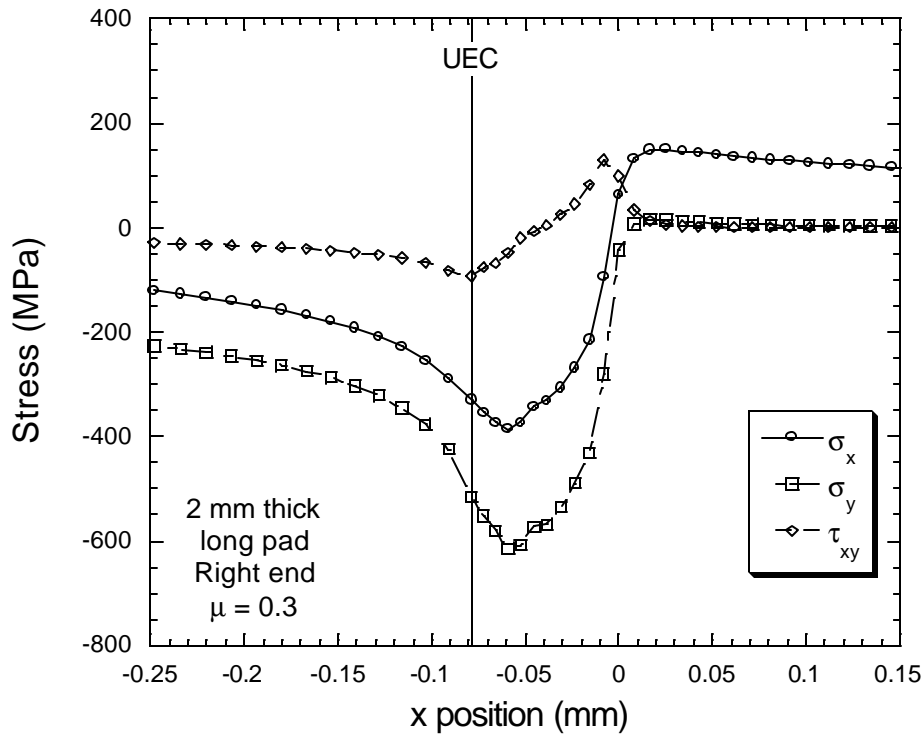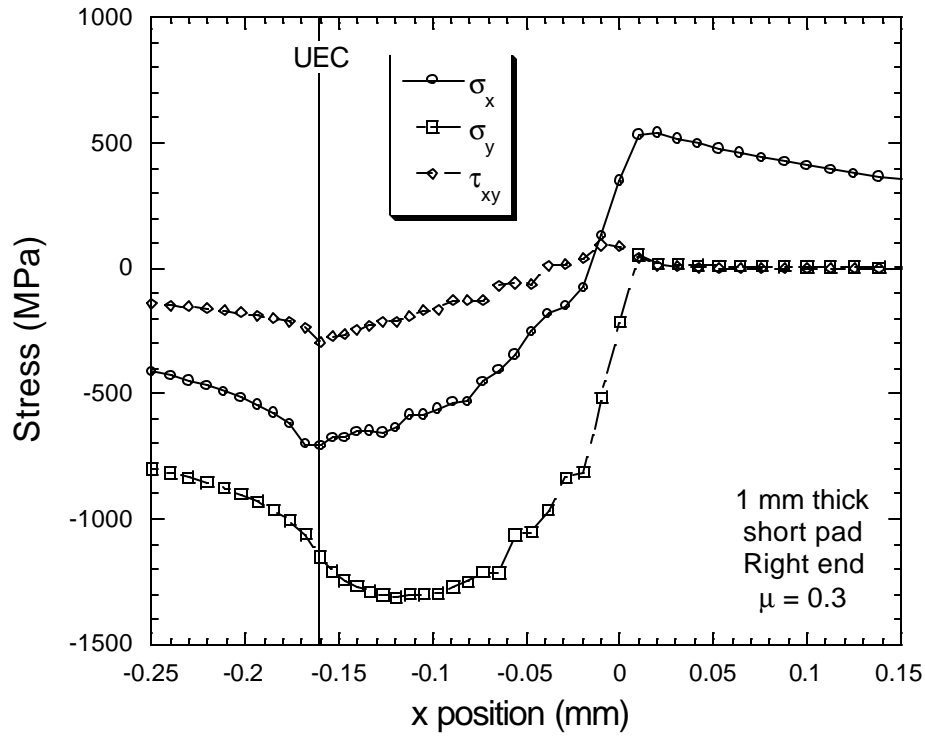

Figure 10

Figure 11

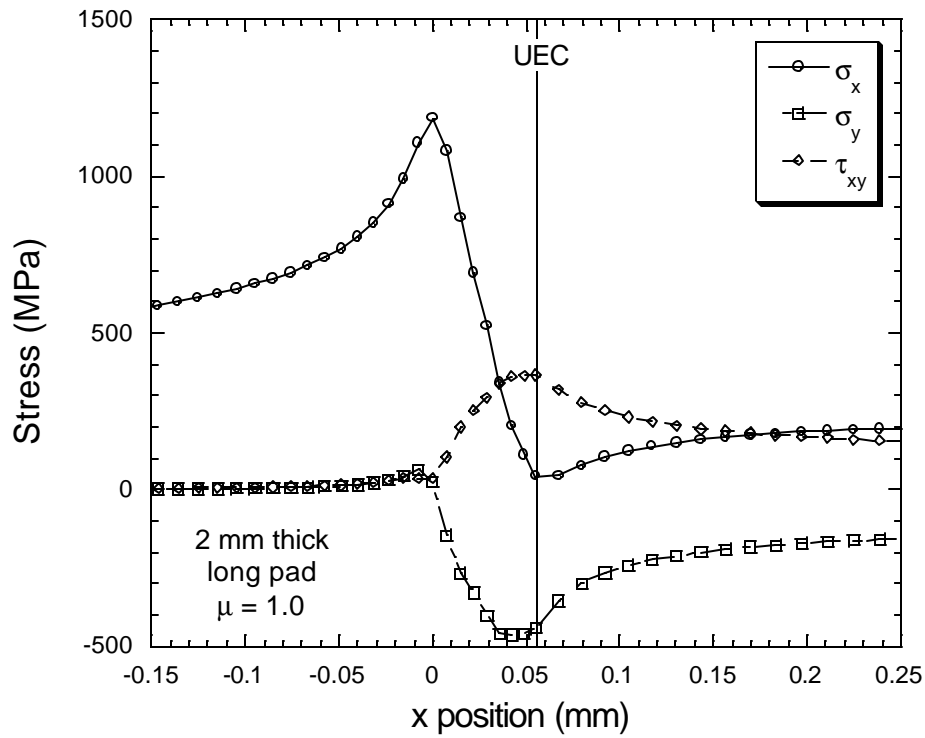Figure 12

Figure 13

Figure 14

Figure 15

Figure 16

203

This page intentionally left blank.

IN SEARCH OF A PARAMETER FOR FRETTING FATIGUE

A. L. Hutson[2], T. Nicholas[1], S. Olson[2] and N. Ashbaugh[2]

[1]Air Force Research Laboratory, AFRL/MLLMN, Wright Patterson AFB, OH 45433, USA

[2] University of Dayton Research Institute, Dayton, OH 45469-0128, USA

ABSTRACT

Fretting fatigue experiments were conducted to determine the fatigue limit stress at 10^7 cycles for Ti-6Al-4V. A step-loading procedure was used to determine the fatigue limit stress that, in turn, was applied to the test geometry in numerical simulations using finite elements. Several fretting pad geometries and specimen thicknesses were used to obtain a range of normal and shear forces that produced the stress and displacement fields in the specimen. An evaluation was made of the conditions near the edge of contact where peak stresses occur to deduce parameters which lead to fretting fatigue failures at 10^7 cycles. However, no simple combination of stresses and slip displacements could be used to correlate all of the experimental data. A fracture mechanics methodology was also employed in order to determine the conditions for propagation or non-propagation of cracks that initiate in the edge of contact region. While no parameters were found which could uniquely predict the fretting fatigue failure, adjustment of the coefficient of friction based on computed slip displacements was shown to have a substantial effect on the stress and stress intensity factors. A correlation of friction coefficient with slip displacement is proposed as a possible method for consolidating data from fretting fatigue experiments conducted under different conditions.

## KEYWORDS

fretting, fatigue, fracture mechanics, titanium

INTRODUCTION

Fretting fatigue is a type of damage occurring in the presence of contacts in which at least one of the components is subjected to bulk loading. It is normally associated with small magnitudes of relative slip, on the order of tens of microns, and little if any material removal and can lead to premature crack initiation and failure. Such damage has been indicated as the cause of many unanticipated disk and blade failures in turbine engines.

Under laboratory conditions, the synergistic effects of various parameters make determination and modeling of the mechanical behavior of fretting fatigue extremely difficult. The stress state in the contact region involves very high peak stresses, steep stress gradients, multi-axial stresses and differing mean stresses. Further, there is controversy whether the problem is primarily one of crack initiation or a crack propagation threshold, and whether or not stress states rather than surface conditions play a major role in the observed behavior. The parameters which govern the initiation and subsequent propagation of fretting fatigue cracks is still not well established. Thus the objectives of this investigation are to find several different fretting fatigue conditions analogous to the fatigue limit stress under uniaxial fatigue loading corresponding to a chosen high cycle fatigue (HCF) life. From these, both stress fields and stress intensity factors for specific cases can be obtained in order to find some commonality which may lead to development of parameters having broad application to fretting fatigue.

EXPERIMENTS

Tests were conducted using a high frequency test system to simulate the fretting fatigue loading conditions that occur in turbine engine blade attachments [1,2,3]. The apparatus uses flat fretting pads, with a radius at the edge of contact, against a flat specimen. Normal and shear loads are applied to the specimen as shown in Figure 1. A previous study has shown that the bending moment present in the apparatus is negligible relative to other parameters, and may be disregarded when designing the tests [4].
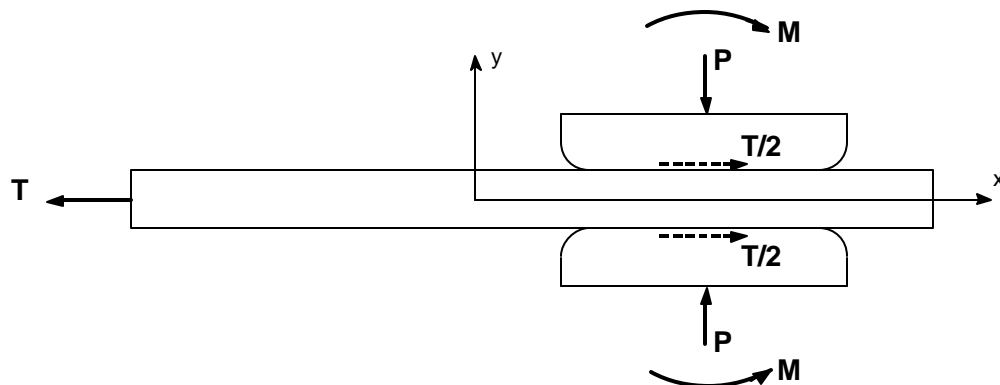
Figure 1: Test geometry and loading schematic.

The test geometry differs from conventional fretting fatigue tests [5,6] in two fundamental ways. First, the axial stress is transferred entirely to the fixture through shear. Resulting stresses in the

specimen are zero on one end of the pad, thus the shear force into the pad is determined from the load applied to the specimen. Second, symmetry of the apparatus provides a specimen which breaks on one end, leaving the other end with a fretting scar and damage obtained under nominally identical conditions. As with a conventional fretting fatigue apparatus, the clamping force is constant and only the axial and shear loads are oscillatory.

All tests were conducted at 300 Hz under ambient lab conditions. Specimens and pads were taken from forged Ti-6Al-4V plates used in a series of investigations under a U.S. Air Force sponsored high cycle fatigue program. The processing and microstructure are reviewed in previous work [7,8]. Each specimen was subjected to uniaxial fatigue using a step-loading procedure [9] to determine a fatigue limit stress corresponding to 10^7 cycle fatigue life. Tests were conducted by incrementing the maximum axial stress by five percent of the initial value for various combinations of specimen thickness, pad length, and clamping force. The step loading technique was validated in earlier fretting fatigue studies using the same apparatus [3,10], and is outlined in reference [11].

ANALYSIS

Finite element analysis (FEA) results from a prior investigation [1] and additional computation provided stress fields through the specimen thickness and along the length of the specimen in the vicinity of the edge of contact. Load conditions were selected to cover a range of combinations of pad and specimen geometry, which produce average shear stresses typical of those tested in the experimental portion of the study. Conditions used in the numerical analysis are summarized in Table 1 along with some of the results for comparison. Axial stresses applied to the specimens in the model were taken from experimental observations. The model included pads with a 3.175 mm blending radius at both ends, resulting in an undeformed contact length of 6.35 mm for the short pad and 19.05 mm for the long pad. In two of the three test conditions simulated numerically [1,3,4], the coefficient of friction, μ, was taken as 0.3. The third case was run with $\mu=1.0$, to allow comparison of results where only μ was changed.

Assuming cracks normal to the specimen surface under pure mode I loading, and using the stresses from the FEA, the stress intensity factor, K, was computed as a function of crack length. The K distributions were calculated using a program developed to model a single edge tension (SE(T)) specimen geometry under a non-constant σ_x stress field [12]. Some success has been reported in modeling fretting fatigue behavior as an edge notch, since both conditions produce similar stress fields [13]. Characterization results from a prior investigation [4] indicated that cracks nucleated at or near the edges of contact in specimens tested in the existing apparatus. The objective of these calculations was to compare the K values from two different cases where the peak stresses were significantly different, yet the stress fields both matched conditions corresponding to failure in 10^7 cycles.

The K solution program required material and crack dimension input parameters in addition to the stress distribution data. 120 GPa was used for the material modulus. The depth position of the final stress value given in the stress distribution, which was equal to half of the specimen thickness, was used for the final crack length. Stress intensity values are only reported for the

first 100μm into the specimen thickness, although calculations were performed as far into the model specimen as possible using the available stress data from the FEA simulation.

TABLE 1

SUMMARY OF TEST CONDITIONS AND RESULTS FOR FINITE ELEMENT ANALYSIS.

| Specimen thickness (mm)	Pad length (mm)	μ	Clamping Load (kN)	Applied σ_{axial} (MPa)	Average σ_y (MPa)	Average τ_{xy} (MPa)	Peak σ_x (MPa)	Max. Relative Displacement (μm)
1	12.7	0.3	49	275	770	21.6	1300	4.0
4	25.4	0.3	34	275	140	28.9	540	19.0
4	25.4	1.0	34	275	140	28.9	1100	3.4

RESULTS & DISCUSSION

The first results presented are the Haigh stresses corresponding to a 10^7 cycle fatigue life for the 1 mm and 4 mm thick specimens over a range of contact conditions (Figs. 2 and 3). The data are presented as a function of average applied clamping stress, which is taken to be positive. Two contact radii (CR) and two stress ratios are represented, and the baseline uniaxial fatigue limits for this material: 660 MPa @ R=0.5, 558 MPa @ R=0.1, are included. The numerical simulation conditions area also noted.

Much of the data for the 4 mm thick specimens was reported earlier [1] and seemed to indicate no appreciable trend as a function of applied clamping stress. However, the data for the 1 mm thick specimens do show a trend of increasing fatigue strength with decreasing applied clamping stresses, which was not noted in previous investigations [1,4]. The trend is not marked and conducting tests with clamping stresses much below 100 MPa to verify the trend is not possible, since clamping stress has to be applied to keep the specimen from pulling out of the grips in the current test apparatus. Also, the trend is obscured by experimental scatter in tests involving the smaller (0.4 mm) contact radius. Another feature to note in comparing Figures 2 and 3 is an apparent effect of thickness. The 4 mm thick specimens produced much lower fatigue limit stresses than 1 mm thick specimens under similar contact conditions, emphasizing the need for investigators to consider test specimen geometry issues closely in the development of life prediction models for service components.
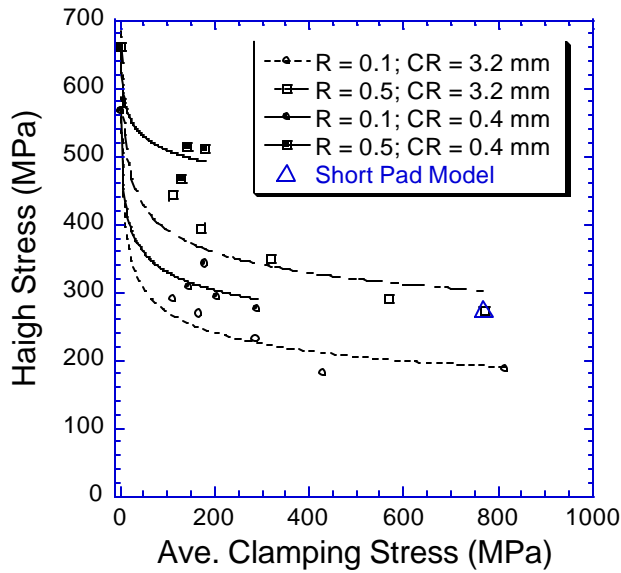
Figure 2: Experimental results for 1 mm thick specimens and unfretted baseline conditions.
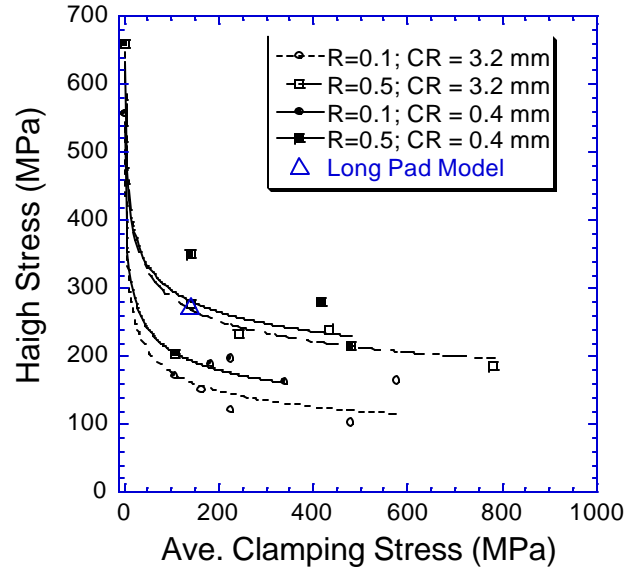
Figure 3: Experimental results for 4 mm thick specimens and unfretted baseline conditions.

The next results presented are the K solutions plotted as a function of depth into the specimen (Figs. 4 through 6) for the deformed edge of contact (DEC) location and two adjacent locations 20 μm on either side of the DEC. In Figures 4, 5, and 6, y=0 corresponds to the surface of the specimen in contact with the pad. Each plot also includes the axial stress σ_x, illustrating the extent of the gradients into the specimen thickness for the corresponding K curve. The K values peak at the DEC, as do the stresses on the specimen surface. Other cases (not shown) for locations farther beyond the DEC indicated K values decaying proportional to the stress field. However, K distribution trends at the DEC show a continuous increase in K with crack length, and point to crack propagation to failure and not crack arrest, as reported for other geometries [5].

In comparing the various cases modeled here, we first address the cases where μ is taken as 0.3, a value which represents an average of values corresponding to gross slip over the entire pad length [1]. Data for the 1 mm thick specimen and short pad case are shown in Figure 5; data for the 4 mm thick specimen and long pad are shown in Figure 6. The values of maximum σ_x, shown in Table 1, vary from ~500 MPa for the 4 mm thick long pad case (Fig. 5) to ~1300 MPa for the 1 mm thick short pad case (Fig. 4). Since K depends strongly on the stress field, the calculated K values are higher for the case with the higher stresses, namely the 1 mm thick specimen and short pad case. Variations of stress gradients into the depth from one case to another are not too great and have little effect on the nature of the variation of K with crack length.

The experimental results for these two cases indicate nearly identical fatigue limits (Figs. 2 and 3). One would expect similar peak stresses and stress intensity factors in cases reflecting similar fatigue limits for the same fatigue life. As reported previously [1], differences in applied shear

stress and average applied clamping stress at the contact for these two cases do not adequately explain the marked differences in the stresses from the numerical simulations. One possible explanation lies in the value of μ used in the analyses. Work by other researchers has indicated pronounced changes in μ over time under fretting fatigue conditions [14, 15], and as our previous work indicated, overall fretting fatigue behavior is extremely sensitive to μ.

Another observation from the previous work [1] was that the maximum relative displacement (see Table 1) at the edge of contact was considerably different for the two cases studied. This observation, coupled with the observation that increasing the value of μ resulting in increasing values of σ_x, lead to consideration of increasing μ for the case of the 4 mm thick specimen, which showed both lower stresses and higher relative displacements. While there is no physical basis for this assumption, the concept of higher μ for higher slip displacements is not totally without merit. It is also of interest to note that an early fretting parameter [10] contained the product of the stress and relative displacement. Perhaps the theory proposed here has the same
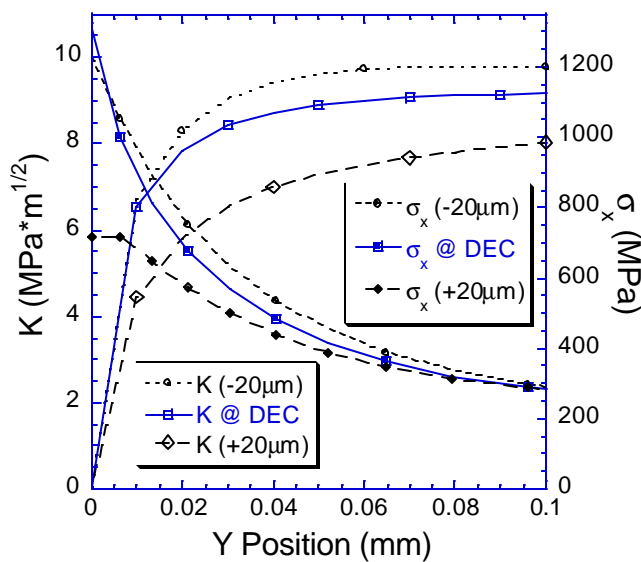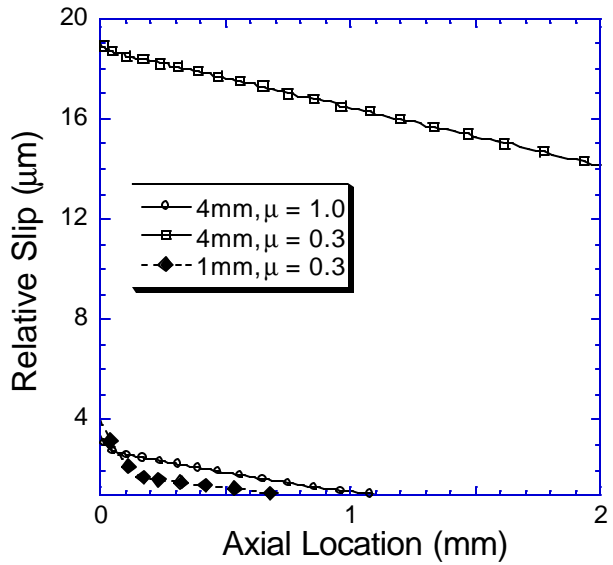

Figure 4: Stress distribution and resulting K solution for 1 mm thick specimen case.
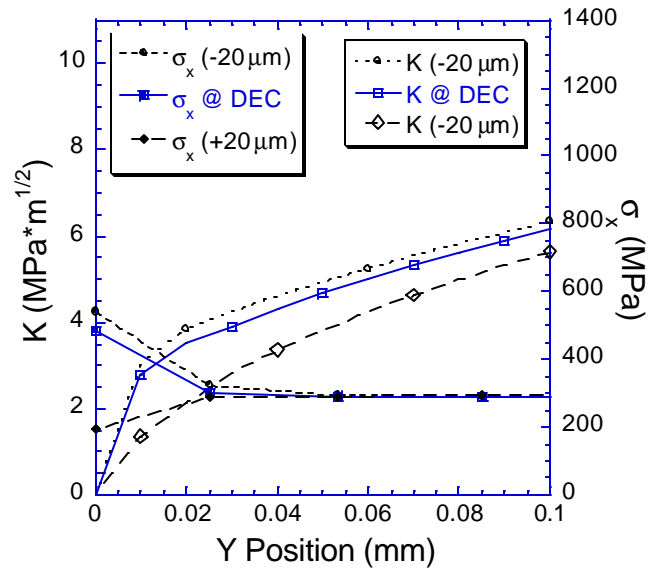
Figure 5: Stress distribution and resulting K solution for 4 mm thick specimen, μ=0.3 case.
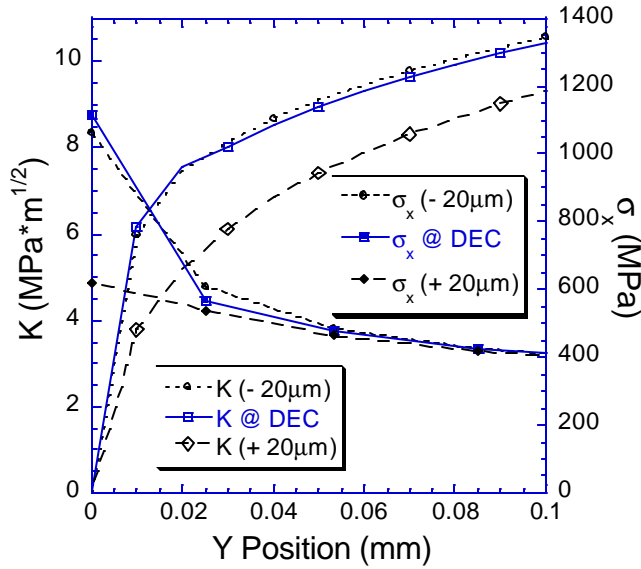
Figure 6: Stress distribution and resulting K solution for 4 mm thick specimen, μ=1.0 case.

Figure 7: Comparison of relative displacements along the contact calculated for all three simulation conditions identified in Table 1.

effect by increasing the stress through an increase in μ rather than through multiplying by relative displacement. To explore this concept the next comparison is of the two cases in which a 4 mm thick specimen with a long pad was modeled with two different values of μ. Increasing μ arbitrarily from 0.3 to 1.0 results in an increase in the maximum σ_x from ~ 500 MPa (Fig. 5) to 1100 MPa (Fig. 6). A similar increase was noted in the previous investigation of a 2 mm thick specimen [1]. Corresponding increases in maximum shear stresses were also noted for increases in μ, which are not discussed here. As with the previous comparison, the case with μ=1.0 resulting in higher tensile stresses also produced higher K values.

Changes in μ also produce changes in relative slip between the pad and specimen. In Figure 7, relative slip is plotted from the DEC, denoted by x=0, to x=2.0 mm under the fretting pad. Maximum slip distance occurs at the edge of contact, which is where the maximum tensile stresses occur. For the 4 mm thick specimen and long pad cases discussed above, the maximum slip distances corresponding to maximum tensile stresses is reduced from 19 μm (500 MPa) to 3.4 μm (1100 MPa). By comparison, the 1 mm thick specimen and short pad case produced a maximum relative slip of 4.0 μm (1300 MPa). These results are consistent with findings from the previous investigation, which concluded that stresses and displacements near the edge of contact are very sensitive to the value of μ between pad and specimen [1].

For the conditions modeled here, we hypothesized that initial slip conditions corresponding to μ=0.3 change over time to conditions of increasing μ, and thus increasing σ_x and corresponding K values. As shown above, higher tensile stresses and the resulting K values may be produced either by imposing a high clamping stress or by increasing μ. An equilibrium condition may exist for μ, which is dependent on the resultant relative displacement. If such a condition exists, an iterative method would be required to determine the final condition.

211

COMMENTS & CONCLUSIONS

Changes in μ over time for various fretting fatigue conditions vastly compound the problem of accurate life prediction for fretting fatigue, since it is very difficult to determine how μ will change over time. Further, such a change will be different for each combination of pad material, specimen material, applied loads, surface modification, and environment. Since fretting fatigue behavior is so profoundly influenced by μ which, in turn, may depend on relative displacements, additional research in how μ changes under fretting fatigue conditions is recommended.

Within the constraints of the geometry and test configuration and loading conditions examined in this investigation and under the assumptions made in the analyses, particularly that of μ being 0.3, the following conclusions can be drawn.

1. High levels of slip may produce increases in μ, which might have to be revised to produce higher stresses and smaller displacements.
2. Stress and relative displacement (slip) fields are very sensitive to the value of μ chosen for analysis.
3. Under the assumption of a Mode I crack normal to the surface, if a crack nucleates, it will continue to propagate to failure.

REFERENCES

1. Hutson, A.L., Nicholas, T., Olson, S.E., and Ashbaugh, N.E. *Submitted to Int. J. Fatigue.*
2. *Fretting Fatigue: Current Technologies and Practices, ASTM STP 1367*(1999). D.W. Hoeppner, V. Chandrasekaran, and C.B. Elliot (Eds). American Society for Testing and Materials, West Conshohocken, PA.
3. Hutson, A., Nicholas, T., and Goodman, R.(1999) *Int. J. Fat.* 21, 7, 663.
4. Hutson, A.L.(2000). MSc Thesis, University of Dayton, USA.
5. *Fretting Fatigue, ESIS 18*(1994). R.B. Waterhouse and T.C. Lindley (Eds). Mechanical Engineering Publications, London.
6. *Standardization of Fretting Fatigue Test Methods and Equipment, ASTM STP 1159*(1992). M. Helmi Attia, and R. B. Waterhouse (Eds). American Society for Testing and Materials, Philadelphia.
7. Peters, J.O. and Ritchie, R.O., *Submitted to Int. J. Fat.*
8. Moshier, M.A., Nicholas, T. and Hillberry, B.M., *Submitted to Int. J. Fat.*
9. Maxwell, D., and Nicholas, T.(1999). In: *Fatigue and Fracture Mechanics: 29th Vol., ASTM STP 1321,* pp. 626-641, T. L. Panotin and S. D. Sheppard (Eds), American Society for Testing and Materials, West Conshohocken, PA.
10. Ruiz, C., Boddington, P. H. B., and Chen, K. C.(1984) *Experimental Mechanics* 24, 208.
11. Thompson, S.R., Ruschau, J.J. and Nicholas, T. *Submitted to Int. J. Fat.*
12. John, R., Weight Function Analysis for a Single Edge Cracked Specimen, Unpublished work, Air Force Research Laboratory (AFRL/MLLN), Wright-Patterson AFB, OH.
13. Giannakopoulos, A.E., Lindley, T.C., Suresh, S., and Chenut, C. *Submitted to Fat. Frac. Eng. Mat. Structures.*
14. Szolwinski, M.P.. Matlik, S.F. and Farris, T.N.(1999). *Int. J. Fat.* 21, 671.
15. Farris, T.N., Harish, G., McVeigh, P.A., and Murthy, H.(2000). In: Proc of the 5th National Turbine Engine High Cycle Fatigue (HCF) Conference on CD, Session 13, Chandler, AZ.

FATIGUE VOIDS AND THEIR SIGNIFICANCE   C13

R. Sunder[1], W.J. Porter & N.E. Ashbaugh
University of Dayton Research Institute, Dayton, OH 45469
Work Conducted and Supported by: Air Force Research Laboratory, Materials and
Manufacturing Directorate, Wright-Patterson AFB, OH 45433.
[1]BiSS Research, Bangalore, 560 094, India

ABSTRACT

Fatigue voids form in Al-alloys as a consequence of the separation of non-coherent secondary particulates from the matrix in early fatigue. The process of their formation is through the initiation, growth and coalescence of multiple interfacial cracks around the particulate. Such voids become visible on the fatigue fracture surface if and when the crack front advances through them. In the event the dominant crack forms and grows slowly, as in vacuum, each fatigue void is the potential source of an embedded penny-shaped crack. In air, the dominant crack forms and grows faster, giving less opportunity for multiple internal cracks to spawn off from the innumerable voids in the fatigue process zone. In vacuum, fatigue voids appear to be the potential origins of the dominant crack. In air, fatigue voids do not appear to affect the fatigue process at low and intermediate growth rates. At high crack growth rates involving considerable crack tip shear, angular planes of particulate concentration offer the path of least resistance. This explains the increasing density of fatigue voids with growth rate. Very high growth rates signal the onset of a quasi-static crack growth component that manifests itself through growing clusters of micro-void coalescence associated with static fracture. Micro-voids have nothing in common with fatigue voids.

KEYWORDS

 fractography, fatigue crack growth, fatigue voids, particulates, air and vacuum fatigue.

INTRODUCTION

Micro-void formation and their coalescence is associated with the static fracture process[1,2]. Voids are also noticed on fatigue fractures of Al-alloys. Fig. 1 [2] provides the background for this investigation. Previous investigations [3,4] describe the near-circular 'pits' in the pictures as 'micro-voids' initiating at precipitates and constituent particles in the crack-tip process zone. Riddel and Piascik [3] isolated the effect of stress-ratio (or R) on fatigue crack growth rate under closure-free conditions and associated this effect with the kinetics of voids. They relate the varying density of the voids in Fig. 1a-d to applied stress ratio and the crossing of a certain threshold K_{max}, beyond which, void formation is promoted. For convenience of identification and association with the fatigue process, we refer to these voids as 'fatigue voids'.

The current study addresses the question of what causes the so-called 'fatigue' voids to form and in turn, what is their interaction, if any, with the crack growth process.

EXPERIMENTAL PROCEDURE

Specimen details and loading conditions used in this investigation are described in detail in [5,6]. A large amount of available and largely unpublished fractographic data from previous work was also used. The experiments were on Al-alloys 2014-T6511 and 2024-T351. The tests were conducted under programmed load conditions involving the application of steps of 2,000 or more high-R (>0.42) cycles separated by markers of low-R (0-0.1) cycles of large magnitude. Each

step was at a different stress ratio to investigate the effect of R-sequence. Most experiments were performed in air. Some reference data were obtained under air-vacuum-air transition.

RESULTS AND DISCUSSION

Fatigue Voids

Fatigue voids form around secondary, non-coherent particulates. Secondary particulates are from the same alloy constituents, but are non-coherent with respect to the matrix. They are known to have a higher modulus than the matrix. The matrix around them is stretched into yield and flows during the rolling process. In the course of the matrix stretching, the particulates fragment with the crushing transverse action of rolling, and flow along with the matrix, forming strings of beads. In view of the nature of their formation as a consequence of breakup of a larger particle, they appear in clusters [7]. The number of particulates exposed to observation will depend on the plane of metallography or crack growth. This is shown in Fig. 2. Fig. 2a is a micrograph of 2014-T6511. Fig. 2b shows clusters of fatigue voids on a fatigue fracture surface under programmed loading. Fig. 2c shows clusters of voids including un-sheared (a), sheared voids (b) and fractured particulates still in their cavity (c). The fractured particulates (Fig. 2c) are featureless. Also, they may be shaped and/or interconnected in a manner that prevented them from falling out during fracture as most others do.

The sheared void (labeled 'b') in Fig. 2c indicates a shift of at least 2 microns between the sheared quarters bisected by a secondary crack normal to the main crack (solid black arrow, top left in Fig. 2c). However, the striation bands crossing this crack appear to be better aligned, creating the impression that the crack occurred before the main crack front advanced to this point. Secondary cracking normal to the main crack front is likely at high stress ratio. Plane strain conditions in the mid-thickness area, combined with the flat crack plane normal to loading direction, enhance transverse cyclic stresses, which tend to locally 'disbond' the material through secondary cracking.

The bands between markers in Figs. 2b,c are from up to 2000 low amplitude cycles. This is essentially a low growth rate regime. Typical of this regime is absence of visible fatigue striations. In the absence of the programmed markers, the primary features on the fracture surface would have been the voids and the river patterns in the direction of crack growth, with no indication of local crack-front shape. Note also, that at low crack growth rates, the presence of the voids (particulates) appears to have no discernible effect on the process of crack growth. There is no local distortion of crack front and no sign of local acceleration or retardation. It would follow that in the low and intermediate range crack growth rate is a matrix-resistance-driven process, quite unrelated to secondary particulate density.

With an increase in crack growth rate, fatigue void density increases dramatically. This is highlighted in Fig. 2d from the same material. From the evidence in Fig. 2b-d, one may conclude that void density as observed on the fracture surface depends only on crack path. At high crack growth rate, the associated extent of slip may not be accommodated by the material in view of the large number of particulates likely to lie along the slip plane. This in turn leads to preferential crack growth along shear planes. As the crack pursues this path of least resistance, clusters of particulate voids get connected to show an increasing density as seen in Fig. 2d.

The above evidence agrees with the presumed correlation of secondary, non-coherent particulate density with resistance to crack growth under periodic overloads (see Fig. 3) [8, 9]. It would appear from Fig. 3 that particulate density begins to affect crack growth rate when crack tip cyclic

shear strains (slip) cross a certain threshold, associated with shear fracture of multiple particulates and coalescence of the shear cracks thus formed.

One may conclude that void density as observed on the fracture surface is related to the mechanism associated with current crack growth rate rather than to applied load level and/or stress ratio. Fig. 4 supports this argument. We see two adjoining bands of crack growth from similar K_{max}, but different ΔK. The high ΔK loading (right) over 10 cycles produces high growth rate and the associated 'rough', void-rich fracture surface, while the preceding low ΔK loading (left) over 2000 cycles produced a comparatively flat surface with fewer voids. Fatigue void density appears to increase with growth rate (ΔK), rather than with K_{max} or with R.

As K_{max} approaches K_{Ic}, the quasi-static component of crack extension steadily gains in proportion. As fatigue crack extension is accompanied by localized bursts of quasi-static crack extension, the crack growth rate over this interval increasingly exceeds striation spacing. A typical fractograph from this interval appears in Fig. 5a. It shows large clusters of micro-void coalescence around fatigue voids along with what appear to be a few striations at the bottom spaced about 2 microns apart.

Fig. 5b shows a zoomed-in view of high growth rate fatigue with a rare view of a fractured particulate that did not fall out of its cavity to leave a void. At top left are striations bands spaced about 2 microns apart (black arrows). The vertical arrow points to a sharp edge on the particulate suggestive of a rupture surface. The particulate has rounded edges. The horizontal arrows point to the trail of the edges from the fractured half of the particulate. The void appears to have 'opened up', perhaps from the shear-mode-ductile rupture that carried the other half away. It would appear that the matrix has 'held on' to the particulate even though separation is evident all around it. The bottom and right is clear evidence of ductile fracture caused by microvoid coalescence.

Fig. 5c is a high magnification photo from the static fracture, which shows the well-known micro-void coalescence. The clusters of microvoid coalescence in Figs 5a,b are identical to that in static fracture (Fig. 5c). Fig. 5 confirms the distinction between fatigue voids and micro-voids. The latter occur in the matrix and are unrelated to non-coherent particulates. Micro-voids are sub-micron in size and always appear in coalesced clusters. Fatigue voids represent signatures of the crack bisecting pre-existing cavities formed by the separation of secondary particulates from the matrix. Just as striations mark the progress of the fatigue crack, fatigue voids mark the location of secondary particulates.

To reconstruct the process of early fatigue, one needs to address certain fundamental academic questions: When and how do fatigue voids form? What is their influence on the fatigue process? Enclosed void formation is confirmed by Fig. 6, which shows the matching halves of a fatigue fracture. For convenience of comparison, the images on the right have been flipped to overcome the 'mirror' image effect of matching fracture halves. From Fig. 6, one may conclude that the void formed as a consequence of separation of an inclusion or constituent particulate from the matrix. A closer observation of the inset at left bottom, reveals concentric striation like marks that appear to mark the progress of multiple interfacial cracks that eventually led to particulate-matrix separation. The origin of each of these interfacial cracks appears to be a penny-shaped discontinuity about 100 nm in diameter, that may have also formed in fatigue. The interfacial crack is marked by a concentric, near-perfect circular front limited only by the edge of a particulate face. The striation bands marking the progress of this front appear to have been caused by the programmed load sequence used in our experiments and represent evidence of fatigue separation *prior* to the crack front bisecting the void. The separated particle may have

'rolled out' during the test as soon as local crack opening displacement provided adequate clearance, or, may have been washed out during the ultrasonic surface cleaning process in preparation for scanning electron microscopy (SEM).

As the concentric striation bands are visible on the void surface one may assume that the interfacial cracking occurs within the matrix layer adjoining the particulate and closely follows the latter's contour. Further, the particulate shape may or may not be spherical. Therefore, the striation pattern surface takes the shape of the matching particulate face.

The fatigue test specimen was loaded in axial tension-tension fatigue. However, interfacial cracks appear to form all around the particulate, including its sides which are located around the particulate and oriented *along* the plane of nominal loading. These sides should actually see compression-compression fatigue under the test conditions used. Cracking in compression-compression is possible given Mode II or III conditions, but is unlikely in Mode I. Mode III for circular interfacial crack fronts (around the particulate) requires triaxial torsional action that seems implausible. Mode II for such a crack requires its penny-shaped origin to serve as a cyclic source / sink for slip, which appears even less likely. Besides, Mode II and Mode III, even if found plausible, could not have possibly left behind such clear striation bands. Quite to the contrary, the presence of Mode II/III components would have obliterated them. Given that crack extension / disbond is unlikely in compression-compression Mode I, the only remaining possibility is tension-tension Mode I all around the particulate, with momentary Mode II during the marker cycles causing mixed-mode crack extension along a conical plane. Such a possibility may be explained by the presence of high tensile residual stresses in the matrix all around the particulate. Given this possibility, applied cyclic loading, whether tensile or compressive when superposed on the high tensile residual stresses, can lead to tensile fatigue. This is schematically described in Fig. 7.

Interfacial cracking is locally, a strain-controlled process. Progress of the interfacial crack *relieves* local stresses because local displacements are driven by matrix macro response. This may explain why all the fatigue interfacial cracks appear to grow in 'near-perfect' harmony as indicated by near-constant circumferential striation band spacing. This may represent a near constant-K environment which may be partly attributed to local displacement control.. The multiple cracks around the particulate eventually coalesce to separate it from the matrix, leaving in their wake, an enclosed fatigue fracture surface forming a void, which we have termed as a 'fatigue void'.

In the case of a spherical particulate, one may expect six interfacial cracks (top, bottom and at 90° intervals around the circumference) to coalesce in order to separate the particulate from matrix. However, if the particulate has several faces forming sharp edges, one is likely to see more cracks. This is seen in the two halves of the void in Fig. 6 (insets). Also, the particulate in Fig. 5b indicates more than 6 faces.

In view of substantial tensile residual stresses around the particulate, one may expect that when elastic stresses are relieved by separation, the matrix void 'expands' around the enclosed particulate. This may explain why the fatigue striations from particulate-matrix interfacial cracking are amazingly well preserved in spite of the particulate falling out or being wrenched out fracture.

Fig. 8 is a good example of near-spherical fatigue void formation in 2014-T6511 with well-defined concentric striations. At the center of the photo, a very small, 0.1 μm (10^{-7} m) penny-shaped fatigue crack that grew at or near constant growth rate is shown. Each concentric step

may have occurred over 2000 cycles, which was the duration of cycling at each step between markers. The band spacing corresponds to a growth rate of about 5×10^{-11} m/cycle. At the top of the photo, we see growth bands from another penny-shaped crack.

Figures 9a-s are close-ups of a variety of typical voids in different 2014-T6511 specimens. Micron scale bars on individual pictures indicate that all the voids are more or less the same size, but of varying shape. This collection appears to represent overwhelming evidence that particulate-matrix separation can occur before the major crack front crosses over. Figs. 9p,r are high magnification views of fatigue striation bands in Figs. 9m and 9q, respectively. The apparent near perfect concentricity of the pattern, the striking contrast of the markers and the clear penny-shaped crack origin Fig. 9r appear remarkable. From the tilted projection of this particular interfacial crack, it would appear that the change in band elevation causing the contrast may not be more than ten angstroms.

Clearly, most voids show signs of multiple penny-shaped interfacial cracks that grow in near-perfect concentric circles. Further, the concentric crack fronts abruptly stop at face edges without extending to the neighboring face and also without distorting the crack-front shape towards the edge. The latter is in contrast to the major crack front that curves backwards at grain boundaries and level transitions. Crack growth rates appear to go down to about 10^{-12} m/cycle, assuming each band corresponds to 2000 cycles.

The degree of contrast associated with the concentric growth bands may be attributed to changes in crack extension mode (plane) between the marker cycles and the low amplitude, high-R cycles. It would follow that the crack extension mode is sensitive to load magnitude even in small interfacial cracks that grow in vacuum. Further, an estimated stress-intensity range of under 0.2 MPa assuming a penny-shaped crack of 0.1 μm diameter and applied stress range equal to near yield stress suggests the absence of threshold (or fatigue limit) in this material.

The fatigue nature of particulate void formation precludes change in void size beyond that of the enclosed particulate. This is in stark contrast to micro-voids associated with the ductile fracture process, which grow to coalescence.

One may conclude that fatigue voids form as a consequence of interfacial fatigue cracking that eventually separates secondary non-coherent particulates from the matrix. Thousands of such voids form in the early stages of fatigue, though many particulates may remain un-separated from the matrix at failure. Each fatigue void serves as a potential initiation point for a penny-shaped fatigue crack whose initial size will be equal to particulate size. It would now appear that even in a simple laboratory coupon, the fatigue process is not merely about the formation of a dominant crack at a surface stress riser.

The process of fatigue damage involves thousands of potential sites of void formation, followed by growth from the void of a penny-shaped crack whose initial size may be assumed to be particulate size. It effectively generates a competitive process of fatigue damage. Two factors retard the process. One is the vacuum environment. The second is the constraint due to the lack of a free edge. The moment a penny-shaped internal crack breaks to the free edge of a specimen, the constraint is removed, thus promoting both environmental action as well as increased stress intensity due to the presence of a free edge. This crack is more likely to grow at a faster rate than the others. In the course of its growth to catastrophic failure, it will slice through voids in its path and merge with cracks growing out of them. In the event the planes of the two cracks are different, a ridge will be formed in an arc preceding the bisected void indicating the size of the

penny-shaped crack at the moment of merger. Obviously, the through and large dominant crack exposed to the environment will grow much more rapidly than individual embedded cracks.

In air fatigue, embedded cracks will barely be able to grow out of their voids before they are 'consumed' by the dominant crack. In vacuum however, the embedded cracks will offer some competition because even the dominant crack is retarded by absence of environmental action. While embedded cracks form early in fatigue, competition between void-initiated embedded cracks and surface crack growth will essentially depend on the life to formation of the dominant crack. This is illustrated by Figs.10-12. Fig. 10 shows void and near-void topography in a fatigue fracture obtained in air-vacuum-air cycling. The dominant crack formed early in air from the notch root at left and progressed across the voids shown before embedded cracks could grow to appreciable proportions from them.

Fig.11 shows the progress of a dominant crack growing towards bottom right in vacuum. The ridge around the void is at a distance of about 1 μm from the void edge at a level lower than the plane of the dominant crack. This is indicative of a pre-existing penny-shaped fatigue crack, which had grown to a depth of about 1 μm from the edge of the void, before the dominant crack 'consumed' it. Obviously, such growth was made possible by the slow progress of the dominant crack, something less likely to happen in air.

The displaced ridge around the void in Fig. 11 also explains why most voids on the fatigue fracture surface appear to be sliced exactly in half even though perfect orientation of the fracture plane with their plane of symmetry is improbable. One may conclude that most voids will have a rim around them whose width will be equal to embedded crack extension up to the point of dominant crack convergence. On one half of the fracture, the rim will appear as a ridge while on the matching half, it will appear as a wall. The height of this wall (and the depth of the ridge) will reflect the separation of dominant and the embedded crack planes. This observation is supported by the matching halves in Fig. 6, where the ridge is seen around the void at the top right and a wall rings the void at the bottom left.

Fig. 12 provides more evidence on distinct change in fatigue void appearance depending on the relative progress of the dominant crack. In air, the dominant crack originating at the top left 'races' across the large number of voids before embedded cracks can grow to appreciable lengths. In vacuum, the crack growing from bottom left merges with reasonably large embedded cracks up to 15 μm in diameter (indicated by circles).

To investigate the reproducibility of voids reported in [3], a keyhole notch C(T) specimen was tested under programmed loading with markers. Fig. 13 shows typical fatigue voids from the 2024-T351 fatigue fracture surface with the anticipated marker bands. This appears to support the possibility that the voids reported in [3] are also fatigue voids that formed around particulates and pre-existed at the time the dominant crack bisected them. One may conclude that the increasing density of voids may be attributed to the change in crack plane that now 'pursues' particulate clusters that constitute the weak link in the event of increased shear associated with higher growth rates. The presence of particulates obviously represents a barrier to slip, leading to strain localization and shear along planes connecting multiple particulates [7-9].

Fatigue Voids in Fracture

The fatigue process is associated with negligible lateral (Mode II) movement of the fracture surfaces against each other. This also explains why the voids are so well preserved and appear to

conform to the shape of the particulate that formed them. The ductile (static) fracture process however, is associated with considerable lateral displacements, well in excess of void dimensions. As a consequence, void shape suffers deformation as seen in the case of quasi-static fracture around a particulate in Fig. 14. In the process of ductile shear in the direction of the arrow, the particulate appears to have crushed the wall of its cavity. The harder secondary particulate tends to flatten out the void when wrenched out in shear. Seen all around the void is micro-void coalescence associated with the ductile fracture process. These pictures highlight once again, the difference between fatigue voids and micro-voids.

CONCLUSIONS

1. A fractography study using SEM was performed on voids observed on the fatigue fracture surface in Al-Cu alloys. These are referred to as 'fatigue voids' in view of the nature of their formation and to distinguish them from microvoids in fracture.
2. Fatigue voids are distinct from micro-voids associated with quasi-static fracture. While the former match the shape, size and random location of secondary particulates that they enclosed, the latter are sub-micron in size and always form as innumerable, closely-connected (coalesced) cavities.
3. Fatigue voids are formed by fatigue separation of secondary non-coherent particulates from the matrix. The process of particulate-matrix separation occurs early in fatigue through the initiation and growth to coalescence of multiple cracks in the interface surrounding the particulate.
4. The initial interfacial crack size can be as small as 100 nm. The circular front of interfacial fatigue cracks grow with near-perfect concentricity and at even growth rate of about 10^{-11} - 10^{-12} m/c. Microscopic imprints of concentric markers were produced by the marker-banding program employed in the loading sequence. These markers appear to indicate that crack extension mode even of microscopic cracks is sensitive to the magnitude of loading. Also, the apparent crack extension even at small, applied load amplitude appears to confirm the virtual absence of a threshold stress intensity (or fatigue limit) for the interfaces within the material studied.
5. In the event the dominant crack grows slowly as in vacuum, embedded penny-shaped cracks grow out of fatigue voids to a noticeable size, before they merge with the dominant crack. In air, the environmentally-accelerated dominant crack crosses fatigue voids before noticeable penny-shaped cracks can form around them.
6. There appears to be no tangible evidence of fatigue voids influencing the progress of the dominant crack at low and intermediate crack growth rates. Their increasing density at high crack growth rate may be an indication of crack plane re-orientation through particulate clusters as a path of least resistance.

REFERENCES
1. Gurson, A.L., Continuum Theory of Ductile Fracture by Void Nucleation and Growth, Journal of Engineering Materials and Technologies, Vol. 99, 1977, pp. 2-15.
2. C.F. Shih, Fracture Analysis in the Ductile/Brittle Regime: A Predictive Tool Using Cell Models, Fatigue and Fracture Mechanics: Twenty-Ninth Volume, ASTM STP 1332, T.L. Panontin and S.D. Sheppard, Eds., American Society for Testing and Materials, West Conshohocken, PA 1999, pp. 9-14.
3. Riddell, W.T. and Piascik, R.S., Stress Ratio Effects on Crack Opening Loads and Crack Growth Rates in Aluminum Alloy 2024, Fatigue and Fracture Mechanics, Twenty-Ninth Volume, ASTM STP 1332, T.L. Panontin and S.D. Sheppard, Eds., American Society for Testing and Materials, West Conshohocken, PA, 1999, pp. 407-425.

4.   Bretz, P.E., Vasudevan, A.K, Bucci, R.J., Malcom, R.C., Fatigue Crack Growth Behavior of 7XXX Aluminum Alloys under Simple Variable Amplitude Loading, Fracture Mechanics: Fifteenth Symposium, ASTM STP 833, R.J. Sanford, Ed., American Society for Testing and Materials, Philadelphia, PA, 1984, pp.242-265.

5.   Ashbaugh, N.E., Porter, W.J., Prakash, R.V., and Sunder, R, A Fractographic Study of Load Sequence – Induced Mixed-Mode Fatigue Crack Growth in an Al-Cu Alloy, Mixed-Mode Crack Behavior, ASTM STP 1359, K.J. Miller and D.L. McDowell, Eds., American Society for Testing and Materials, West Conshohocken, PA, 1999, pp. 258-278.

6.   Sunder, R., Porter, J., Ashbaugh, N.E., The effect of stress ratio on fatigue crack growth rate in the absence of closure, Int. J. Fatigue, Vol. 19, Supp. No 1, pp. s211-S221, 1997.

7.   Starke, E.A., Lutjering, G., Cyclic Plastic Deformation and Microstructure, Fatigue and Microstructure, American Society for Metals, Metals Park, OH, 1978, pp. 205-244

8.   Sanders T.H., Jr., and Staley, J.T., Review of Fatigue and Fracture Research on High-Strength Al-Alloys, Fatigue and Microstructure, American Society for Metals, Metals Park, OH, 1978, pp. 467-516

9.   Staley, J.T., How Microstructure Affects Fatigue and Fracture of Aluminum Alloys, Presented at the International Symposium on Fracture Mechanics, George Washington University School of Engineering and Applied Science, Washington, D.C., Sep. 11-13, 1978.

(a) *R* = 0.1   (b) *R* = 0.6

(c) *R* = 0.8   (d) tearing
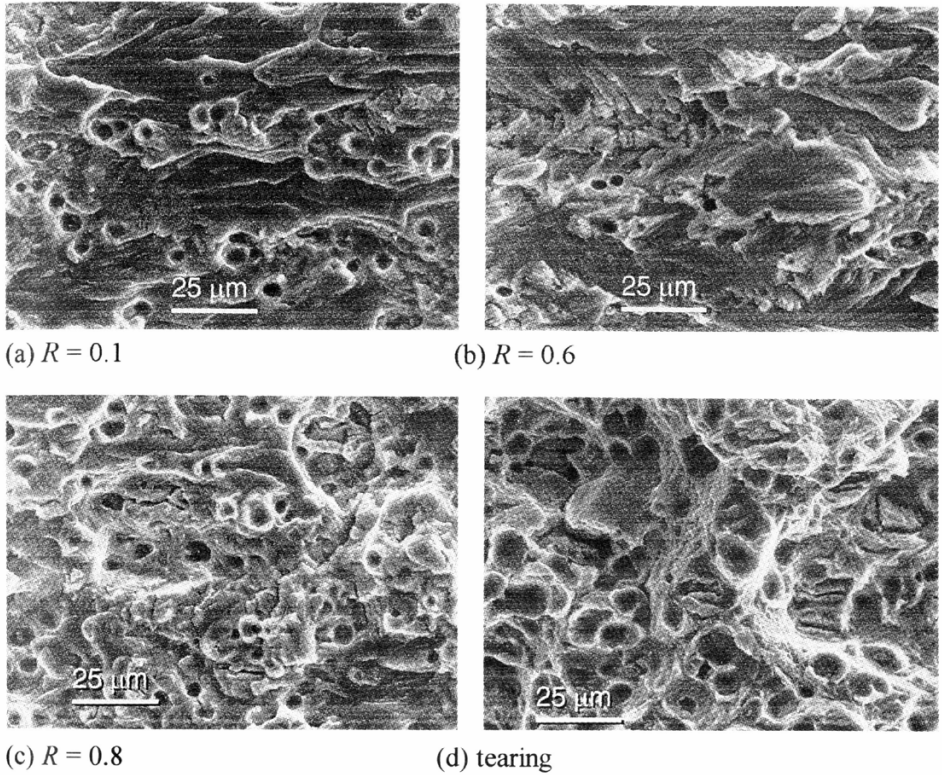
Figure 1 - Micrographs of fatigue fracture surfaces obtained on 2024-T3 at identical ΔK = 5.5 MPa/m and different stress ratios [3]. Note that void density in (a) vastly exceeds that in (b) indicating stress ratio may not be primary controlling variable.
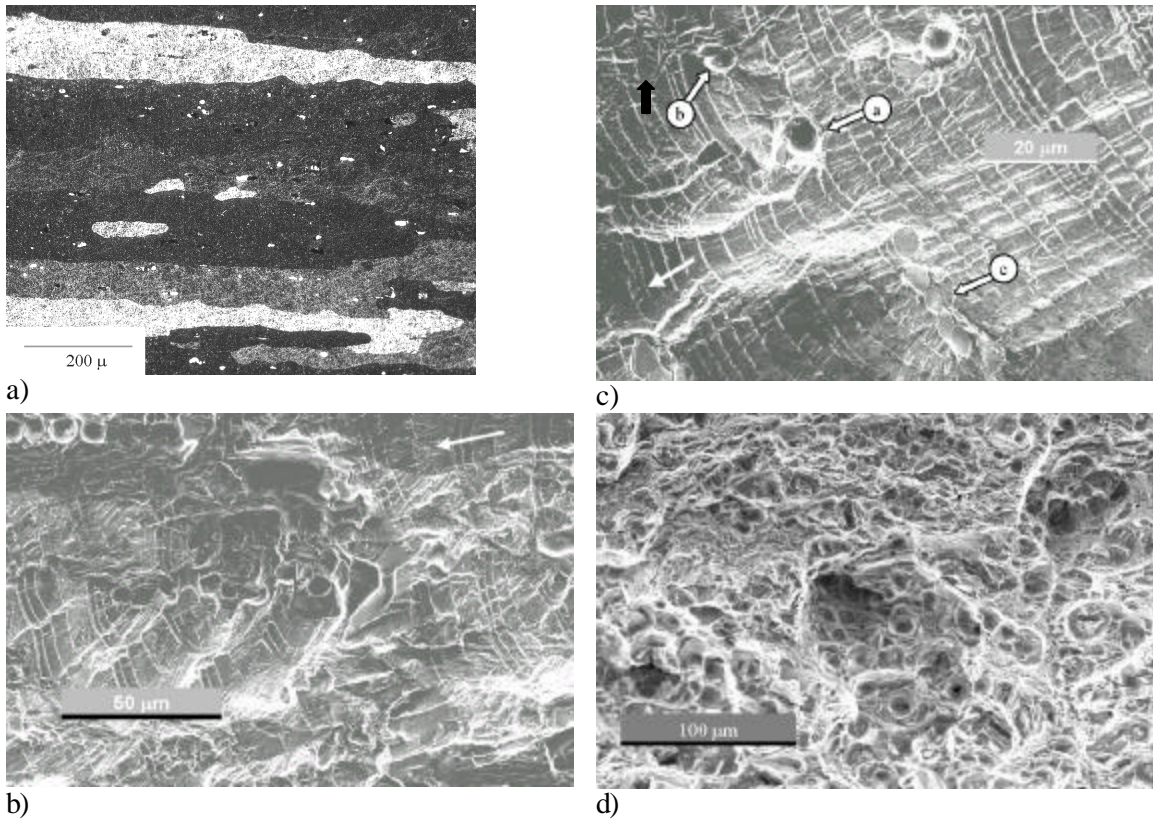
Figure 2 - Secondary particulates and voids from them in 2014-T6511. a) Metallograph b) Strings of fatigue voids on fracture obtained under programmed loading. c) Different views of particulate fracture: a:- fatigue void from particulate separation, b:- fatigue void quarters displaced by shear and c: sheared particulates retained in cavities and d) Clusters of fatigue voids formed in high rate (quasi-static) fatigue crack growth.
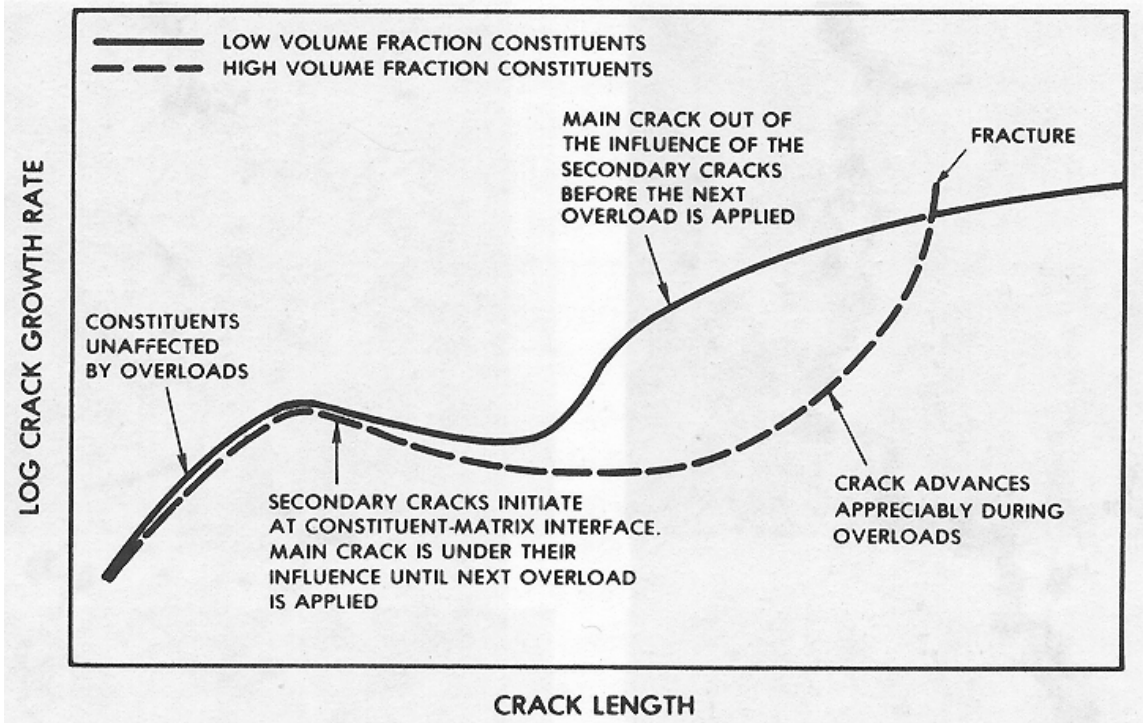
Figure 3 - Schematic of crack growth rate under periodic overloads [8]. Microcracks form at particle-matrix interface during overload and upon resumption of baseline loading, additional time is required for the microcracks to link up and re-form the primary crack. The time to re-form the main crack is reflected in the crack growth retardation shown.
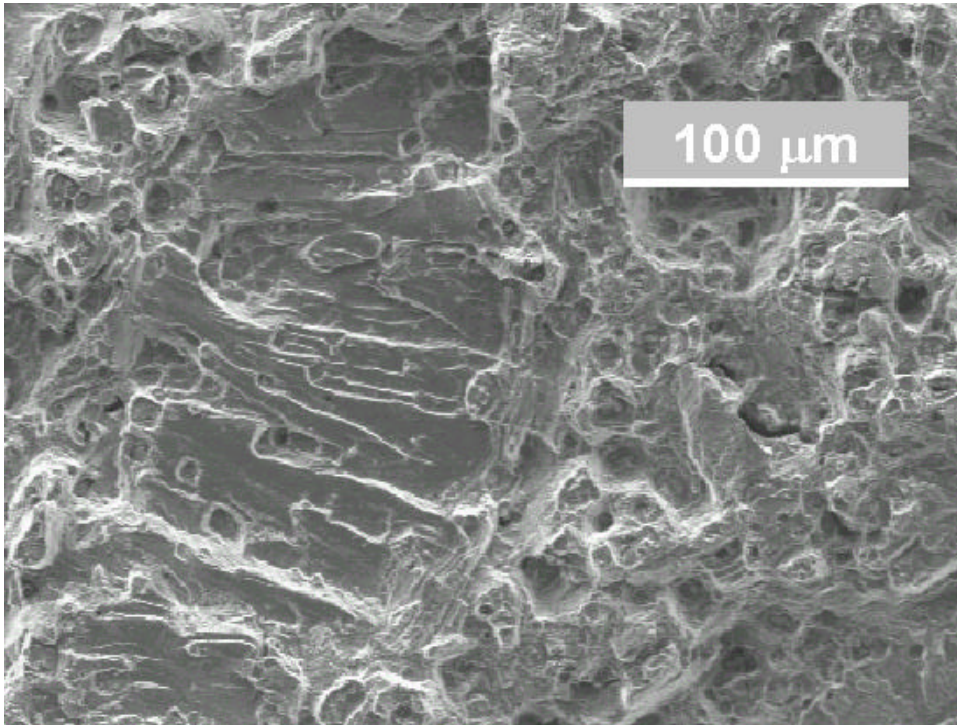
Figure 4 - Fatigue fracture in 2024-T351 C(T) specimen under programmed loading. Crack growth is from left to right. The two distinct fracture regions were obtained under identical Kmax and different ΔK
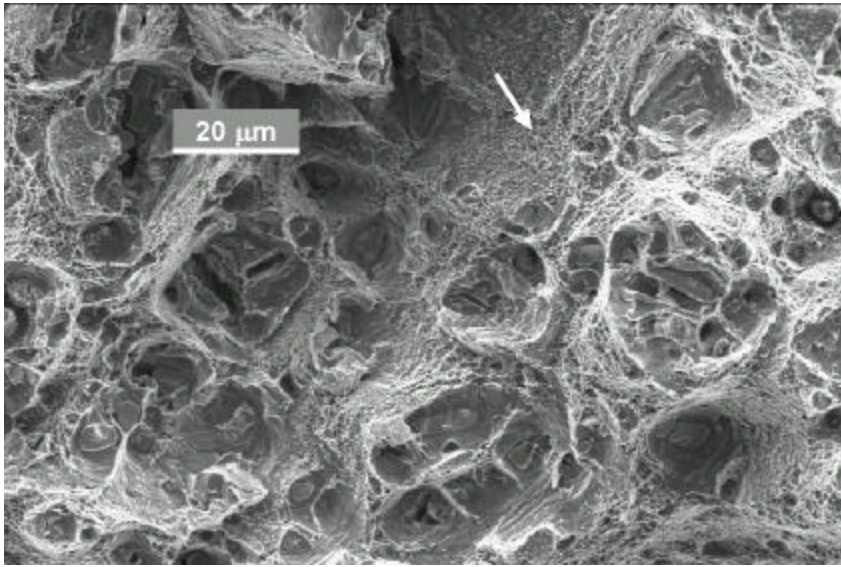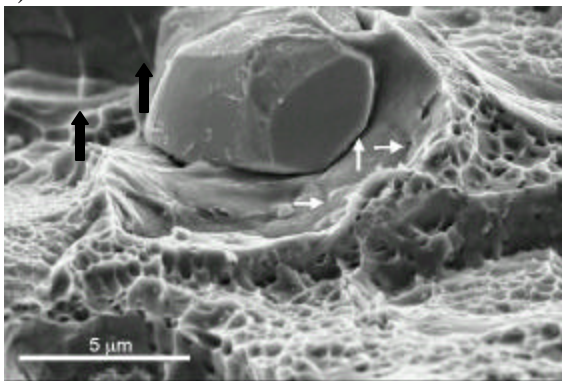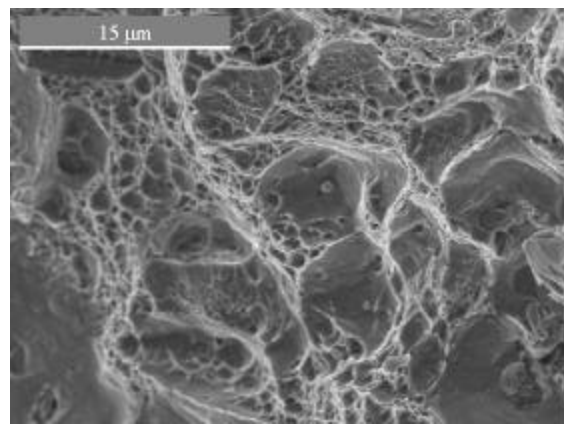
Figure 5 - The contrast between fatigue voids and micro-voids. a) quasi-static extension at high crack growth rate. Note bursts of micro-void coalescence indicating local, quasi-static crack extension. b) A rare picture of a particulate that did not totally separate from matrix, surrounded by micro-void coalescence c) Zoomed in view of micro-void coalescence
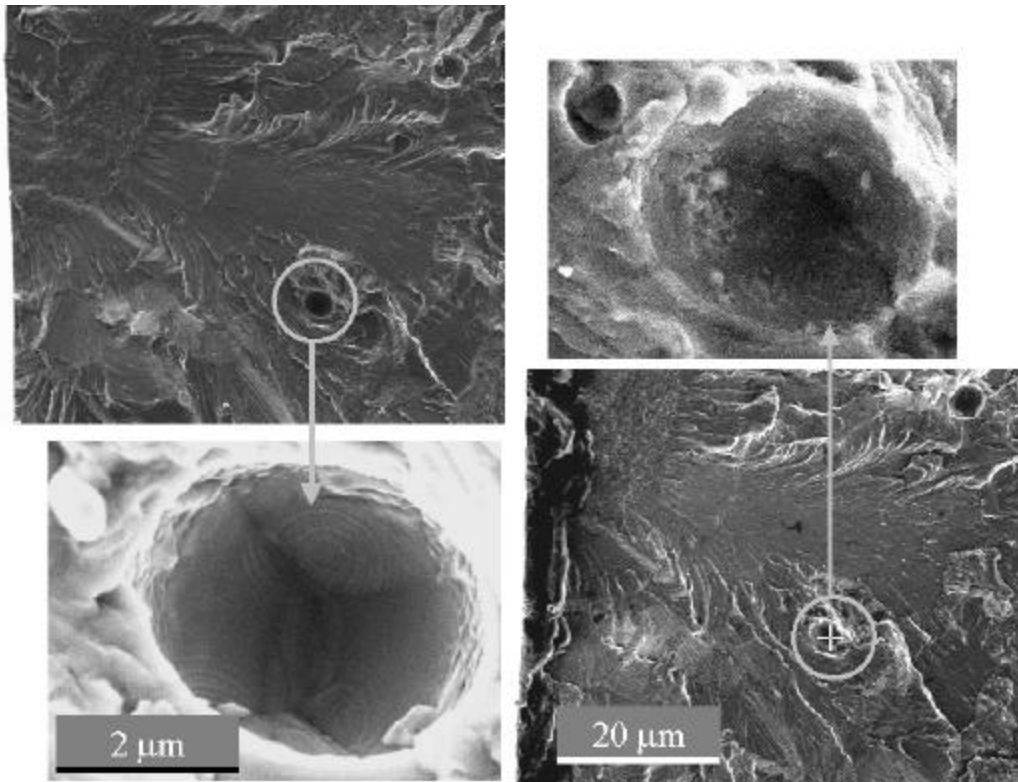
Figure 6 - Matching halves of fatigue fracture with zoomed-in view of fatigue void (insets). Pictures from one half have been flipped to avoid mirror-image effect and assist comparison. Note 'wall' around void at left that matches ridge at right. The height of this wall indicates the difference in elevation of major crack plane and plane of void separation. Also note concentric marker bands indicating progress of interfacial cracks that eventually coalesced to separate particulate from matrix.
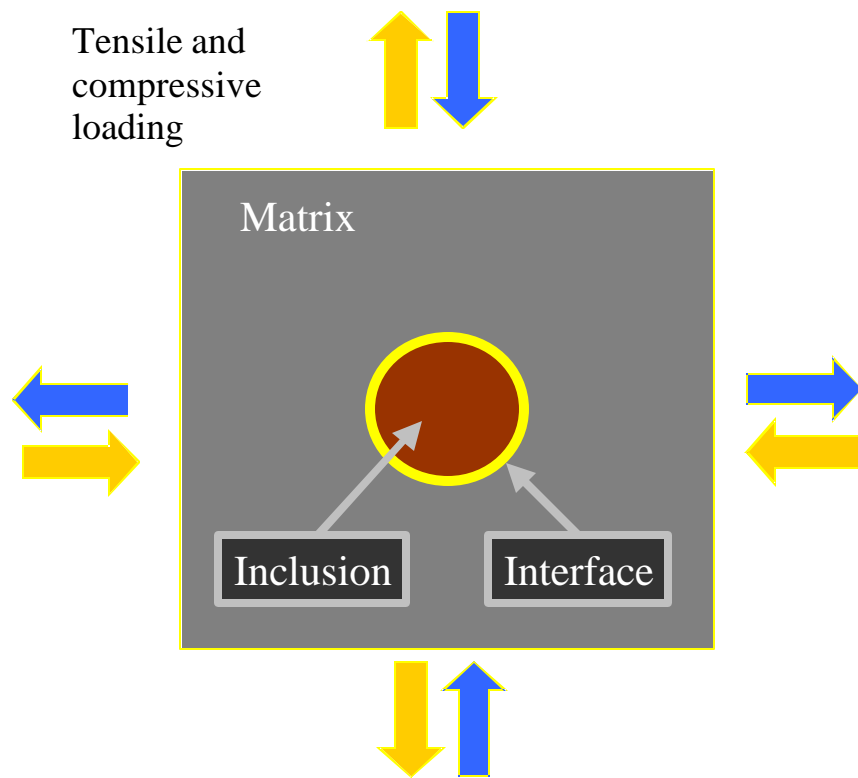
Figure 7 - Schematic of loading on secondary particulate. Fractographic evidence points to tensile fatigue stresses acting all around the particulate to promote multiple interfacial crack formation and growth. This is indicative of high residual tensile radial stresses around the particulate.
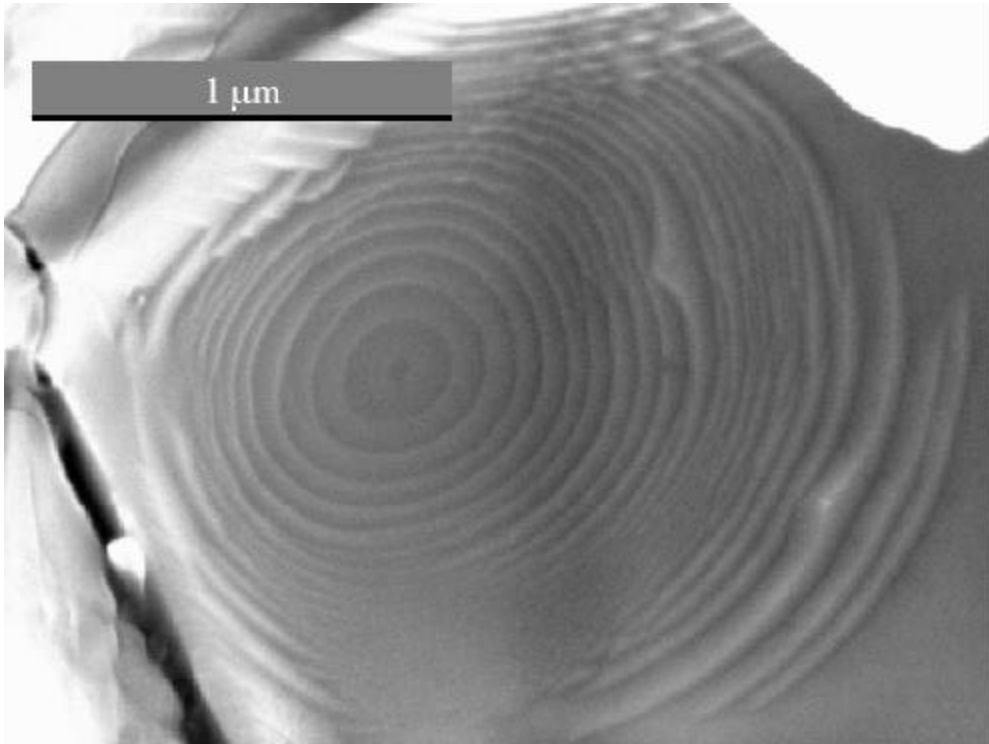
Figure 8 - Near perfect concentric circles mark the progress of a particulate-matrix interfacial crack. Smallest discernible penny-shaped crack size is about 100 nm.
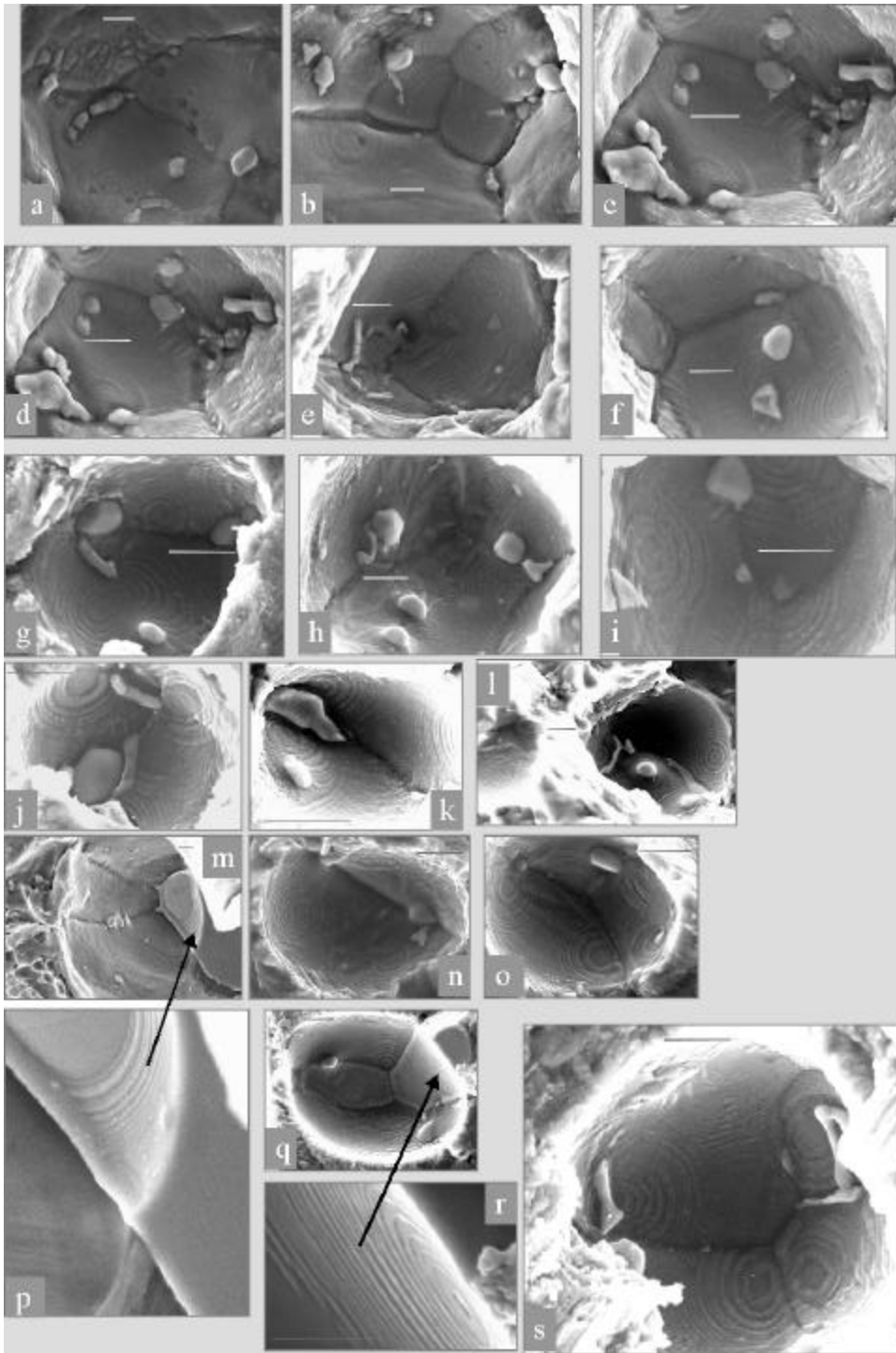
Figure 9 - Close-ups of a variety of typical fatigue voids in 2014-T6511. Each scale marker is one micron in length. Note the consistency in penny-shaped interfacial crack formation and growth.
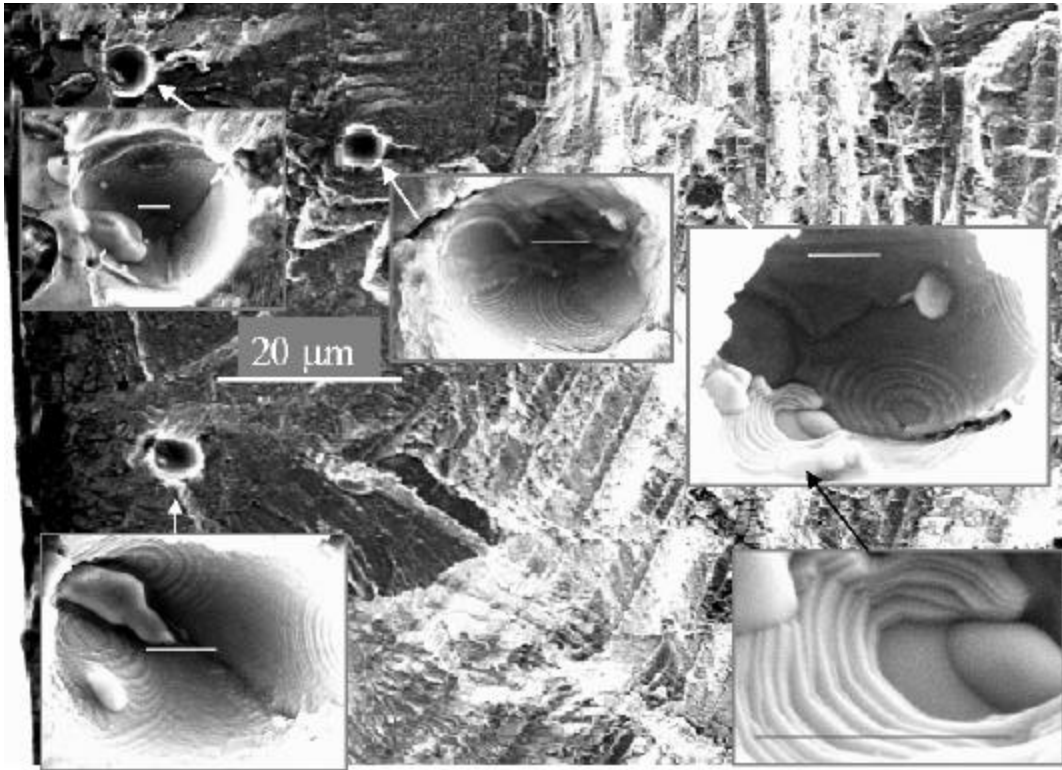
Figure 10 - Fatigue void characteristics appear identical in air as well as vacuum fatigue fracture. Picture from testing with vacuum-air transition. Fracture surface from cracks grown in vacuum appear in the upper left of figure (dark contrast) and the fracture surface from cracks grown in air appear in the lower right of figure (light contrast). Each scale marker in inset pictures is one micron in length.
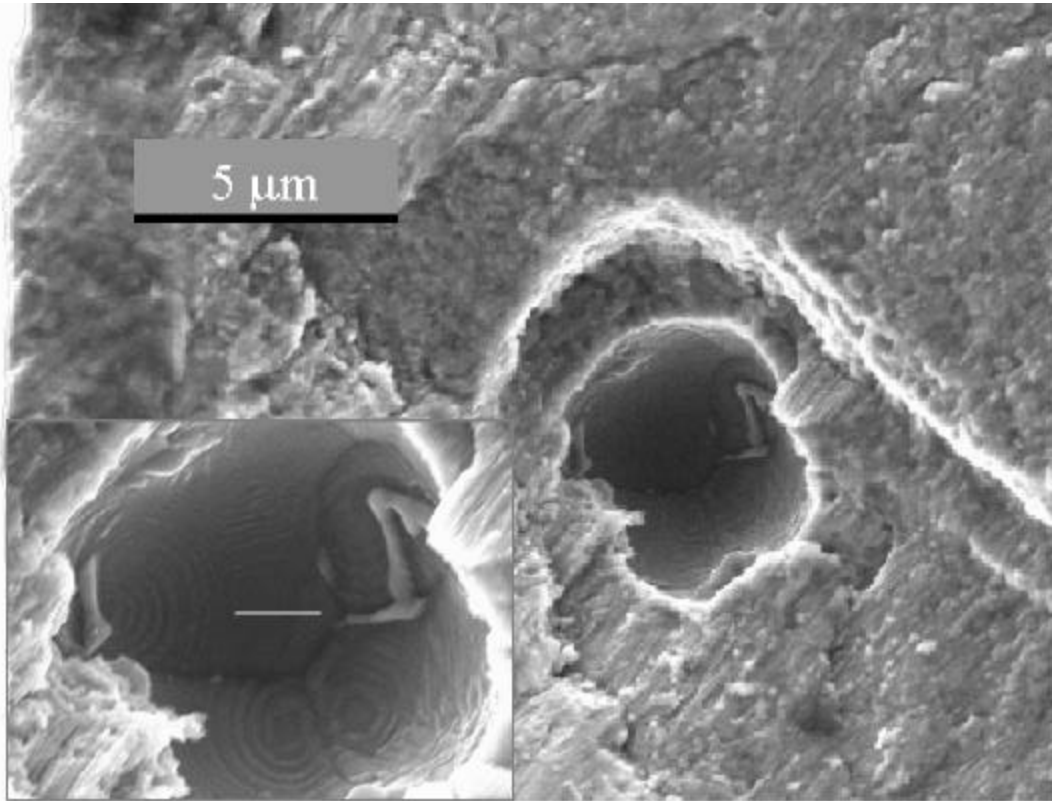
Figure 11 - Typical fatigue fracture surface in vacuum crack growth. Note sizeable growth (in excess of one micron) of embedded penny-shaped crack out of fatigue void before dominant crack advance. Inset confirms nature of fatigue void formation. Difference in height of the two crack planes is apparent. The region of the ridge around the void will appear as a wall on the matching half of fracture. The scale marker in the inset picture is one micron in length.
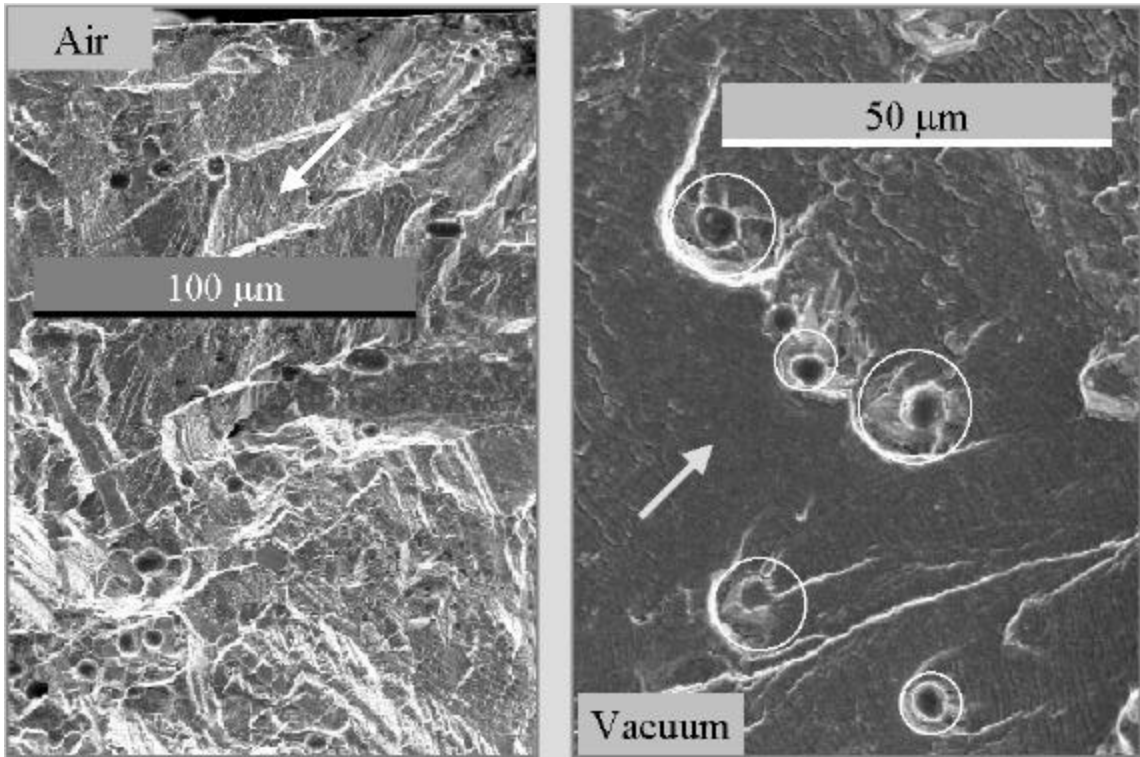
Figure 12 - Fatigue void appearance in air and vacuum fatigue. Note the substantial growth of multiple internal penny-shaped cracks around fatigue voids in vacuum. This confirms the possibility of internal sources of crack formation in vacuum as opposed to air.
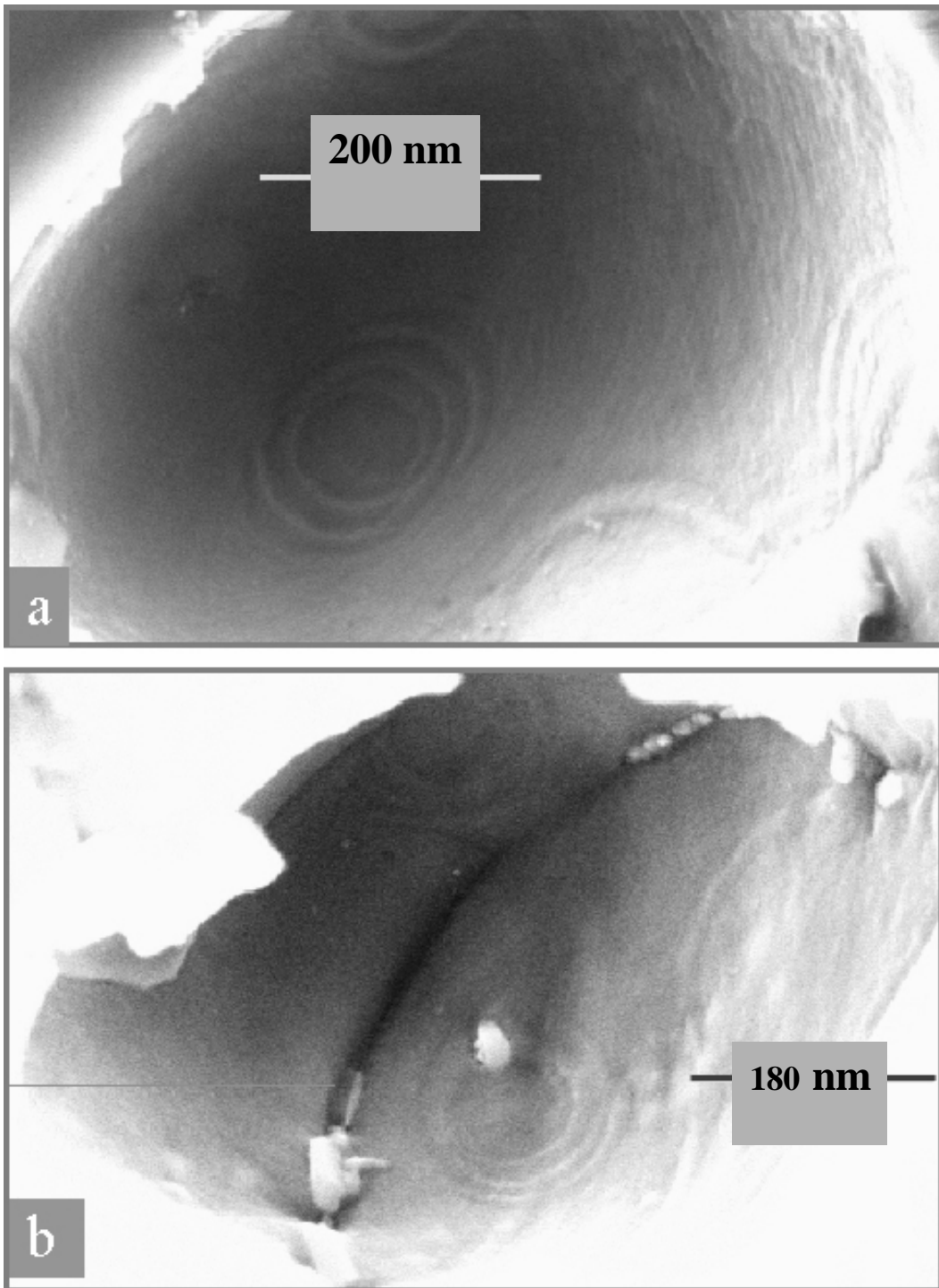
Figure 13 - Fatigue voids from 2024-T351 C(T) keyhole specimen tested under programmed loading. Concentric marker bands confirm similarity of mechanism of interfacial fatigue cracking leading to particulate-matrix separation in 2024-T351 and 2014-T6511.
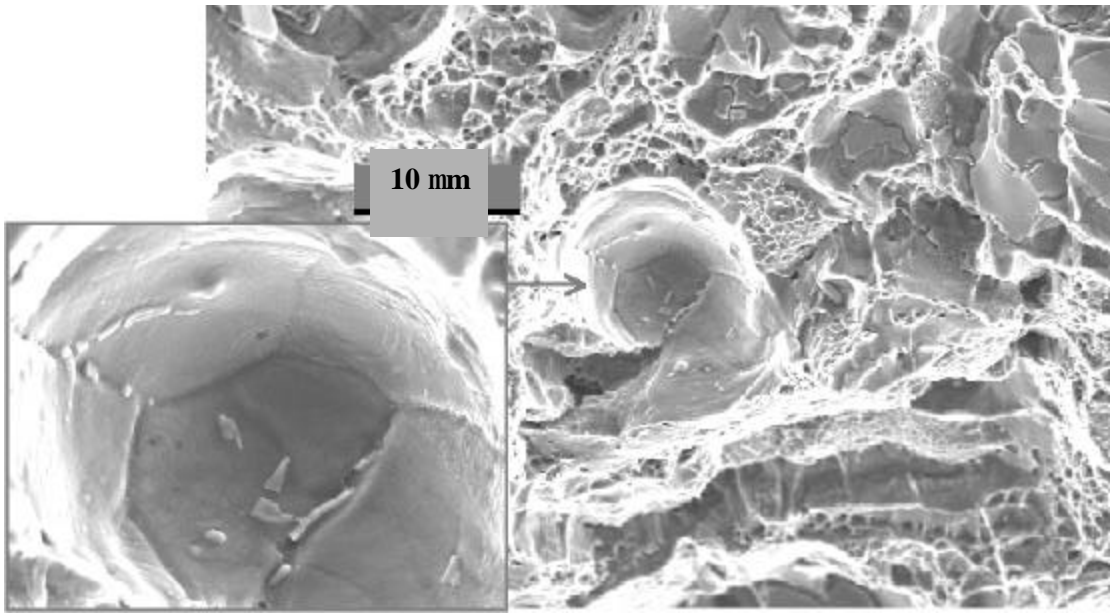
Figure 14 - Evidence of pre-existing fatigue void in ductile fracture area. Inset shows distinct circular marker bands. Particulate appears to have 'pushed down' the wall of its cavity in the process of being sheared. The fatigue void stands in contrast with micro-void coalescence around it.

Microscopic Markers Reveal Root of the Fatigue Process in Al-Alloys   C14

R. Sunder, BiSS Research, Bangalore, India, and
University of Dayton Research Institute, 300 College Park, Dayton, OH 45469
Research conducted at: Air Force Research Laboratory, Materials and Manufacturing
*Directorate, Wright-Patterson AFB, OH*

When metals are subject to cyclic loading, they eventually fail. Failure occurs through the formation and growth of fatigue cracks that gradually reduce residual strength. The kinetics of crack growth is described by the relationship between rate of crack growth per cycle, da/dN, and stress intensity range, ΔK. Fracture Mechanics defines the stress intensity factor, K as the parameter that describes the severity of the crack tip stress field. K is uniquely related to crack size, applied stress and the geometry of the crack as well as the body containing it.

Critical stress intensity, K_c, is a measure of fracture toughness that qualifies materials for resistance to defects. It aids in the qualification of structures for fail-safety – the ability to tolerate damage sustained in usage. A wide range of design exercises including airworthiness, structural integrity of bridges and leak-before-break (burst safety) of piping rely on Fracture Mechanics analyses.

Material constants that determine the da/dN versus ΔK relationship are established through laboratory testing conforming to prevailing standards such as ASTM E-647. The relationship typically covers growth rates ranging from 10^{-7} to 10^{-2} mm/cycle and is the accepted input for analyses to determine Safe Life (to formation of finite crack size) and inspection period (life for growth of detectable crack to critical size). Crack sizes handled by such analyses typically range from long cracks subject to visual observation down to barely detectable small cracks about 100 microns in size. Conventional inspection technology restricts our ability to track cracks that may be less than 50 to 100 microns in size.

Cycle-by-cycle crack extension may be accompanied by the formation of discernible 'striations' on the fracture surface that mark the progress of the fatigue crack. Electron fractography using high-resolution Scanning Electron Microscopes (SEMs) is used to quantify crack size and growth rate from striation spacing. However, the distinguishing features of striations simply 'fade away' at growth rates less than about 10^{-5} mm/cycle. This corresponds to a magnification of under x10,000 which is much less than what an SEM may be capable.

Conventional research techniques are inadequate in the study of cracks smaller than 0.1 mm and growth rates less than 10^{-7} mm/cycle. Recent collaborative research at the Air Force Research Laboratories (AFRL) focused on extending electron fractography to track naturally forming notch-root cracks in Al-alloys used in airframes. The objective was to reach down to extremely small cracks and extremely low growth rates and do so in a reproducible manner. Specially programmed fatigue load sequences were designed to 'mark' the progress of the fatigue process. The idea was to build a 'zoom-in' capability by inserting striation forming marker loads between large steps of baseline loading. Thus, the baseline loading grows the crack, while the marker loads merely mark the crack front by enforcing an instantaneous *microscopic switch* in crack extension mode that leaves a high contrast, *striation-like* mark on the fracture surface. The markers were carefully designed so as not to influence the fatigue process through overload effects, or, by themselves contributing to discernible crack extension.
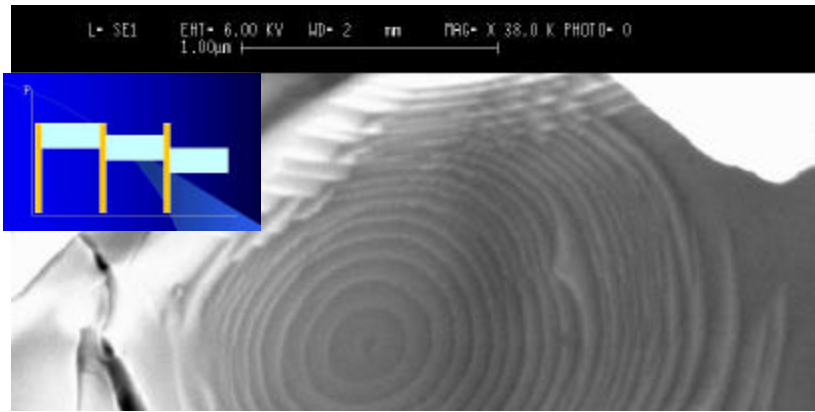
Fig. 1 Inclusion void formed by interfacial fatigue cracking. Load sequence used in the test appears at the left top. The switch in loading to and from the few marker cycles (yellow) caused the concentric circles that mark the progress of the interfacial crack. When zoomed out, this appears as one of the voids in Fig.2

Experiments on notch root fatigue under programmed loading using the above technique revealed several interesting facets of the fatigue process:

Fatigue crack formation occurs through two competing processes: (a) Interfacial fatigue cracking through formation and coalescence of multiple, embedded penny shaped cracks around

inclusions at grain boundaries and (b) Cyclic slip at the notch root rendered irreversible by environmental action (oxidation) that prevents re-fusing of exposed surface. Being internal to the material, process (a) is *always* in vacuum and leads to fatigue separation of inclusions from the matrix. Thus, the fatigue process in Al-alloys can be initiated by the formation of thousands of inclusion-voids. The fatigue fracture surface will typically reveal these voids if the dominant crack happens to pass through them.
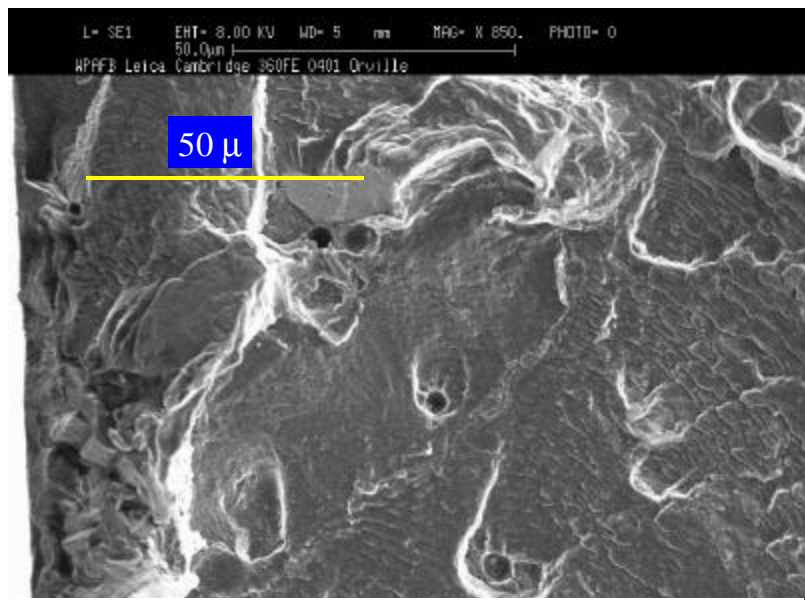
Fig. 2 Crack formation and growth at notch area in vacuum. Voids such as those seen here appear on close-up like the one in Fig. 1. Note the circular ridge and absence of striations in the vicinity of the voids. This indicates embedded penny shaped crack growth around the void prior to advancement of the dominant crack from the notch root at left.

In vacuum, process (a) is followed by the growth of an embedded penny shaped crack whose initial diameter is defined by inclusion size (Fig.2). Obviously, such cracks can potentially grow out of every inclusion-void. However, the one closest to the notch root will on reaching the surface, serve as the dominant crack in view of the increased stress intensity from the free edge (edge crack effect).
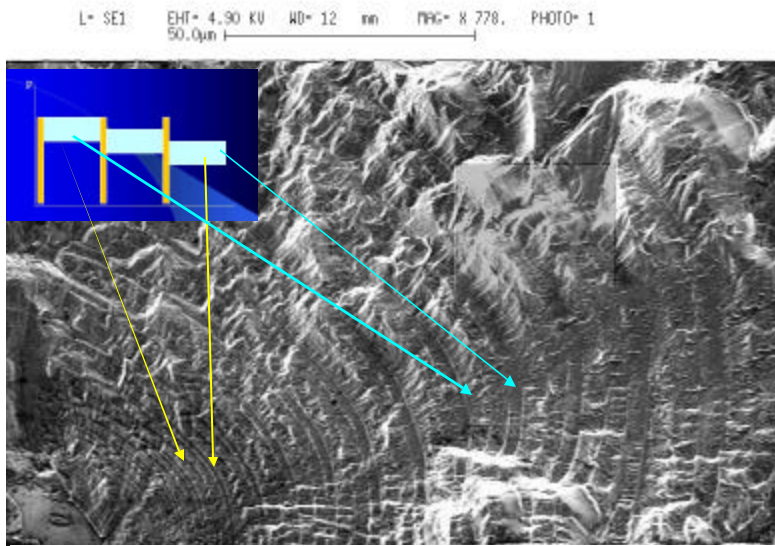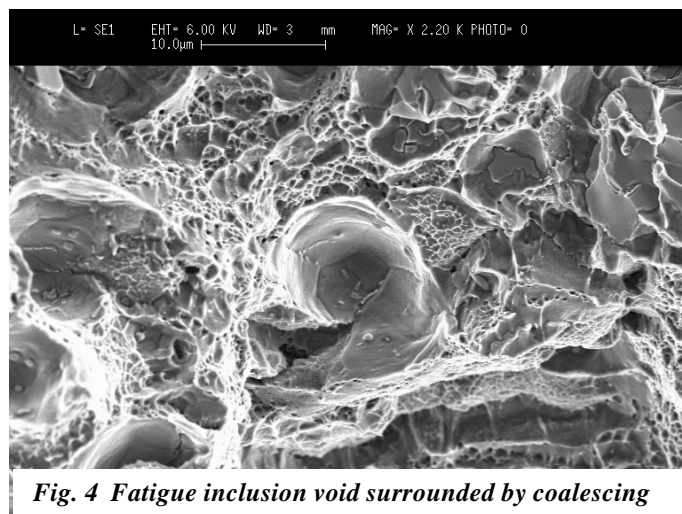
Fig. 3 Notch root crack formation and growth in air. The dominant crack from the notch edge forms and grows much faster than embedded cracks can at inclusion voids.

In air (Fig. 3), the process of notch root crack formation from irreversible slip occurs simultaneously with the fatigue separation of inclusions from the matrix. One or more cracks can form along the notch surface. These will coalesce into a dominant crack well before embedded cracks can grow out of inclusion-voids.

The results of this research permit clear distinction of inclusion-voids that are a consequence of the fatigue process from *micro-voids* associated with the fracture process. This is brought out in Fig. 4, where we see a fatigue inclusion void in the midst of coalescing micro-voids. In principle, such a picture would emerge if a test coupon is fatigue pre-cycled (under the programmed sequence described above) and then pulled apart as shown on the cover.

These pictures bear evidence to the reproducible nature of crack growth behavior down to extremely small crack size and at growth rates several orders of magnitude less than assumed material thresholds. It would appear that penny-shaped cracks as small as 0.1 microns in size can grow in perfect concentricity and at reproducible growth rates as low as 10^{-12} mm/cycle. It may not necessarily follow that Linear Elastic Fracture Mechanics (LEFM) extends to microscopic scale. However, the ability to track the process down to its microscopic origins can be expected to bring in its wake, the ability to

Fig. 4 Fatigue inclusion void surrounded by coalescing micro-voids. The latter are associated with static ductile fracture.

also model and perhaps one day, predict the process of fatigue crack formation.

Understanding how cracks form and grow in the early stage of fatigue is crucial to improved life prediction technology. This is particularly so for those components that may not be subject to routine inspection and those, such as high r.p.m. engine rotaries, that see substantial fatigue cycling in their lifetime.

LIST OF SYMBOLS, ABBREVIATIONS, AND ACRONYMS

ABBREVIATION	DEFINITION
γ-TiAl	Gamma Titanium Aluminide
A/D	Anolog-to-Digital
AE	Acoustic Emission
CMC	Ceramic Matrix Composites
COF	Coefficient of Friction
COTS	Commercial Off-the-Shelf
CTE	Coefficient Thermal Expansion
CVI	Chemical Vapor Infiltrated
DCPD	Direct Current Potential Difference
DE(T)	Double-notched Tension Specimen
DEH(T)	Semicircular Double-notched Tension Specimen
EBSP	Electron Back-Scattered Diffraction Patterns
ERLE	Engine Rotor Life Extension
FCC	Face-Centered Cubic
FOD	Foreign Object Damage
FY	Fiscal Year
HCF	High Cycle Fatigue
IDDS	Infrared Damage Detection System
IHPTET	Integrated High Performance Turbine Engine Technology
IPF	Intensity Pole Figure
LCF	Low Cycle Fatigue
LE	Leading Edge
LVDT	Linear Variable Differential Transformer
MH(T)	Middle Hole Tension Specimen
MI	Melt Infiltrated
MLLM	Metals Branch
MLLMN	Behavior/Life Prediction Section
MLOC	Government Computer Support
NDE	Nondestructive Evaluation
NDI	Nondestructive Inspection
NTED	National Turbine Engine Durability
OIM	Orientation Imaging Microscopy
PIN	Physically Isolated Networks
PLAT	Probabilistic Life Analysis Technique
PM	Powder Metallurgy
PST	Poly Synthetically Twinned
SBIR	Small Business Innovation Research
SE(T)	Single Edge Hole Tension Specimen
SEM	Scanning Electron Microscopy
Ti	Titanium
TMF	Thermo-mechanical Fatigue
TPRL	Thermophysical Properties Research Laboratory
USAF	United States Air Force
UMAT	User Material
WANS	WinMATE Analytical and Numerical Solutions